Title

The Governing Interactions in Fuel-Cell Catalyst-Layer Inks

Author

Berlinger, Sarah A

Publication Date

2021

Peer reviewed|Thesis/dissertation

The Governing Interactions in Fuel-Cell Catalyst-Layer Inks

By

Sarah A. Berlinger

A dissertation submitted in partial satisfaction of the

requirements for the degree of

Doctor of Philosophy

in

Chemical Engineering

in the

Graduate Division

of the

University of California, Berkeley

Committee in charge:

Dr. Adam Z. Weber, Co-Chair
Professor Bryan D. McCloskey, Co-Chair
Professor Clayton J. Radke
Professor Ashok Gadgil

Summer 2021

The Governing Interactions in Fuel-Cell Catalyst-Layer Inks

Sarah A. Berlinger

Abstract

The Governing Interactions in Fuel-Cell Catalyst-Layer Inks

by

Sarah A. Berlinger

Doctor of Philosophy in Chemical Engineering

University of California, Berkeley

Dr. Adam Z. Weber, Co-Chair
Professor Bryan D. McCloskey, Co-Chair

It is increasingly and urgently obvious that the world needs to move toward green, renewable energy sources. Key in realizing this infrastructure are energy-conversion devices such as hydrogen fuel cells and water electrolyzers. As their name suggests, these devices allow energy to be converted from one form (a fuel) to another (electricity), and vice versa, enabling a distributed and modular energy network. The efficiency and cost of these devices have vastly improved over the last few decades, but those gains (in particular for fuel cells) have stagnated in recent years due to performance limitations and high costs associated with their catalyst layers (CLs). This dissertation focuses on fuel-cell CLs, although the fundamental principles and insights gained are applicable to electrolyzers and other energy-conversion devices that rely on similar CL paradigms and architectures.

CLs are heterogeneous porous electrodes comprised of agglomerates of catalyst particles (typically platinum supported on carbon), ion-conducting polymer (ionomer), and void space. The microstructure of the CL, including the size of the agglomerates, the ionomer coverage, porosity/tortuosity, *etc*. controls the complex gas, liquid, ion, and electron transport networks and impacts the overall kinetic, ohmic, and mass-transport performance of these devices. Characterization efforts have spanned micro-, meso-, and macro-scale techniques to probe structure-property-performance relationships of the CL.

CLs are made from precursor CL inks, which are colloidal dispersions of the ionomer and catalyst particles, dispersed in solvent. CL studies are complicated by the multiple material types used (varying ionomer chemistry, catalyst loading, carbon support type, solvents) and disparate ink deposition and drying methods that render no two CLs alike; this makes it difficult to compare across these different studies. Additionally, within the community, CL fabrication has traditionally been treated as a black art, and the details of the fabrication process (ink composition, casting method, *etc.*) are typically inconsistently reported, because emphasis has been placed on understanding CL properties and performance and not the forces controlling that formation process. However, it is increasingly clear that simply being able to characterize CLs is not enough.

To enable predictive control and rational design of CLs, it is vital to understand *how* and *why* (in addition to *what*) specific microstructures form.

This dissertation sets out to uncover systematically the underlying fundamental interactions between the ink components in solution, which ultimately govern CL microstructure (agglomerate structures and sizes, ionomer coverages, *etc.*) and performance once cast. We begin by introducing all relevant parameters in the CL ink fabrication process and conducting a literature-based parameter screening to test correlation between ink variables and performance metrics. The analysis reveals that while no single parameter is controlling, solvent identity and ionomer-to-catalyst-particle ratio correlate well with performance metrics. This suggests ionomer/solvent, ionomer/particle, and ionomer/solvent/particle interactions merit further investigation.

To probe the specifics of these interactions, we build our understanding piecewise. The first part of this dissertation is dedicated to the investigation of ionomer/solvent interactions. We use a range of water/propanol ratios to probe the influence of solvent on these interactions. Water/propanol ratios are chosen because they are (1) the most commonly used solvents, (2) represent a range of water contents (relevant for studying hydrophobic/hydrophilic interactions), and (3) encompass a wide range of dielectric permitivities. We first explore the solution structure of ionomer dispersed in various water/propanol ratios, and how these different conformations affect the *in situ* evolution of thin-film morphology via x-ray scattering. Higher-water-content dispersions exhibit enhanced ordering of primary ionomer aggregates, and fewer secondary aggregates, which affect the final structure of the films; this results in thin films and membranes with improved transport.

Having established a strong link between ionomer/solvent dispersion interactions and the cast state, this dissertation focuses on additional details of the ionomer/solvent interaction and how it may influence catalyst-particle aggregation behavior. We uncover that solvent has a strong effect on the acidity of these dispersions, and that this acidity change is likely due to solvent-induced conformational differences. Additionally, this ionomer/solvent interaction is sensitive to ionomer concentration, wherein acidity does not scale linearly with ionomer concentration, again suggesting it is in part attributed to conformational differences (*i.e.* aggregation) across the different compositions. The increased acidity with increasing water content propagates to alter particle interactions: acidity strongly influences the electrostatic interactions between the ionomer and catalyst particles in an ink. These pH measurements are then used to probe a third dimension to this solvent/ionomer parameter space by considering the temporal stability of these dispersions. The ionomer slowly equilibrates to new solvent environments over the course of many days: lower ionomer concentrations and water/propanol composition extremes affect this change more drastically. Once again, these conformations persist to membranes upon casting and annealing.

To study ionomer/particle interactions further, isothermal titration calorimetry measurements are used to extract quantitative binding affinities of ionomer to both platinum and carbon nanoparticle surfaces as a function of ionomer charge density. There exists a nonmonotonic relationship between the number of charged groups in the ionomer and its binding affinity. The binding affinity is modeled to extract the entropic and enthalpic contributions to the binding free energy, critically revealing that binding to both platinum and carbon surfaces is governed by a similar entropy-dominated mechanism. This finding is counter to the prevailing hypothesis in literature that

ionomer/particle ink association is due to inherent, strong specific-ion (enthalpic) interactions between the ionomer and platinum, and it reveals that ink interaction mechanisms operate in different modes than those occurring *operando* in the fuel cell. Therefore, extrapolation from well-studied fuel cell systems to ink systems should be avoided because of differences in charge states of the platinum surface; this leads to a new reinterpretation of existing data.

We compliment the calorimetry results with a wide parameter screening using quartz crystal microbalance: we probe ionomer adsorption from solution onto crystal surfaces with a range of different surface functionalities (varying hydrophobicity, metal type, and surface chemistry). Importantly, the findings from the above ionomer/solvent interaction studies inform this ionomer/particle interaction investigation by considering adsorption to these different surfaces both as a function of ionomer charge density as well as water/propanol ratio. In inks (under no applied potential) data reveal that higher-water-content dispersions promote adsorption to all surface types, and adsorption to hydrophobic surfaces (like carbon) is higher than adsorption to platinum. In sum, these ionomer/particle interaction investigations suggest that the ionomer/catalyst particle interactions in inks are dominated by ionomer/carbon interactions, rather than ionomer/platinum interactions.

Finally, the results of the preceding sections are used to inform a case study examining the influence of platinum versus carbon nanoparticle surface area on ink interactions, CL microstructure, and fuel-cell performance. Catalysts with varying platinum loadings are used to explore the zeta potential of inks with varying ionomer-to-particle ratios. A direct correlation between ink zeta potential and CL local-transport resistance is established. Furthermore, we demonstrate that particles with higher carbon surface areas can support more ionomer, likely leading to more uniform coverage and lower CL transport resistance.

The fundamental ink interactions uncovered here provide insights into CL performance and lay the groundwork for design rules to select for desired CL microstructures by manipulating ink parameters not only for fuel cells, but similar energy-conversion technologies from CO_2 electrolysis to chemical synthesis to water treatment.

Table of Contents

Abstract **1**

List of Figures ..... **vi**

List of Tables ..... **xiv**

Acknowledgements ..... **xv**

1 Introduction **1**

1.1 Background 1

1.2 Ink Parameters 4

1.2.1 Catalyst Particles 4

1.2.2 Ionomers 4

1.2.3 Solvents 6

1.2.4 Processing 6

1.2.5 Interactions 6

1.3 Parameter Screening 7

1.4 Dissertation Outline 10

1.5 Supplementary Information 12

1.5.1 Feature Selection 12

1.5.2 Statistical Modeling 14

2 Impact of Dispersion Solvent on Ionomer Thin Films and Membranes **17**

2.1 Abstract 17

2.2 Introduction 17

2.3 Experimental Methods 19
2.3.1 Dispersions 19
2.3.2 Thin Films 19
2.3.3 Membranes 20
2.4 Results & Discussion 22
2.4.1 Structure 22
2.4.2 Properties 30
2.4.3 Structure-Property Implications 34
2.5 Summary 35
2.6 Supplementary Information 36
2.6.1 *In situ* GISAXS and Dispersion Properties 36
2.6.2 Rheology 40
2.6.3 Teubner-Strey Fitting 41
2.6.4 Membrane Structure and Properties 42
3 Inherent Acidity of PFSA Dispersions and Implications for Ink Aggregation 44
3.1 Abstract 44
3.2 Introduction 44
3.3 Experimental Methods 45
3.3.1 Materials 45
3.3.2 pH Measurement 46
3.3.3 Inks 47
3.4 Results & Discussion 47
3.4.1 Dispersion pH 47
3.4.2 Ink Aggregation 51

3.5 Summary 55
3.6 Supplementary Information 55
3.6.1 pH Measurement Corrections 55
3.6.2 Inks 56
3.6.3 Dispersion Aggregate Structure 57
4 Aging Influences Structure and Properties of Ionomer Dispersions 59
4.1 Abstract 59
4.2 Introduction 59
4.3 Experimental Methods 60
4.3.1 Dispersions 60
4.3.2 Membranes 61
4.4 Results & Discussion 62
4.4.1 Dispersions 62
4.4.2 Membranes 65
4.5 Summary 67
5 Probing Ionomer Interactions with Electrocatalyst Particles in Solution 69
5.1 Abstract 69
5.2 Introduction 69
5.3 Experimental Methods 72
5.3.1 Ionomers 72
5.3.2 Quartz Crystal Microbalance (QCM) Experiments 72
5.3.3 Isothermal Titration Calorimetry (ITC) Experiments 76
5.4 Results & Discussion 78

5.4.1 Adsorption Screening 78
5.4.2 Thermodynamics of Binding 82
5.4.3 Additional Parameters 84
5.5 Summary 85
5.6 Supplementary Information 86
5.6.1 QCM Model Sensitivity Analysis 86
5.6.2 Adsorption Behavior 88
5.6.3 ITC Fitting 91
5.6.4 Molar Conversion of ITC Data 93
5.6.5 Dispersion Ageing 94
6 Fuel-Cell High-Current-Density Performance and Platinum Loading: Insights from Catalyst/Ionomer Ink Interactions 97
6.1 Abstract 97
6.2 Introduction 97
6.3 Experimental Methods 99
6.4 Results & Discussion 102
6.4.1 Particle Description 102
6.4.2 Ink Characterization 104
6.4.3 CL Investigation 107
6.5 Summary 111
6.6 Supplementary Information 113
6.6.1 Ink Zeta Potential and pH 113
6.6.2 ECSA Correction 117
6.6.3 CL Thickness Measurement 118

6.6.4 H^+ Transport Resistance Correction 118

7 Summary & Outlook 119

7.1 Ionomer/Solvent Interactions 120

7.2 Ionomer/Particle Interactions 121

7.3 Concluding Remarks 123

8 References 124

List of Figures

Figure 1.1. Two-dimensional schematic of a hydrogen fuel cell. 2

Figure 1.2. Pictorial representation of ink and catalyst-layer structure (not meant to be exact or drawn to scale) and associated relevant important parameters that govern these structures/properties. Parameter list is not exhaustive. These parameters guided the database collection and regression analysis (see Section 1.5). 3

Figure 1.3. Left: general schematic of PFSA ionomer, depicting the polytetrafluoroethylene backbone and pendant sidechains terminating in hydrophilic sulfonic acid groups. The repeat density of these sidechains is inversely proportional to its equivalent weight (EW, $g_{polymer}/moles_{SO3-}$), as depicted in the top and bottom right images. 5

Figure 1.4. Structure of three common PFSA ionomers with varying chain lengths: Nafion, 3M, and Aquivion. n denotes the polymer repeat length, and x determines the equivalent weight of the polymer (*i.e.* the number of tetrafluoroethylene groups in the backbone). 5

Figure 1.5. Data from References[23, 46-47, 50-52, 60, 67-81] that displays the effect solvent dielectric constant (ε) has on (A,B) ink interaction descriptors (agglomerate diameter, d, and zeta potential) and (C,D) catalyst layer parameters (limiting current density, i_{lim}, and electrochemical surface area, ECSA). The left and right panels of each subplot categorize similar data based on ionomer type (left) or carbon support type (right). The shaded region represents one standard error of the regression fit (dotted line). 9

Figure 1.6. Data from References[23, 46-47, 50-52, 60, 67-81] that displays the effect ionomer-to-carbon (I:C) ratio has on (A,B) ink interaction descriptors (agglomerate diameter, d, and zeta potential) and (C,D) catalyst layer parameters (limiting current density, i_{lim}, and electrochemical surface area, ECSA). The left and right panels of each subplot categorize similar data based on ionomer type (left) or carbon support type (right). The shaded region represents one standard error of the regression fit (dotted line). 10

Figure S1.7. Example scatter plots relating each input variable to each output variable. 13

Figure S1.8. Example data showing how certain "continuous" variables are limited by commercial suppliers (evidenced by vertical lines at discreet points along the x-axis). 14

Figure S1.9. Data were categorized by ionomer identity and carbon type before fitting the regression models. 15

Figure S1.10. Categorized data sets before filtering for outliers. 15

Figure S1.11. Final data sets used to fit the regression models. 16

Figure 2.1. Schematic depicting a summary of Chapter 2: dispersion solvent affects the structure and properties of dispersions, thin films, and membranes. 17

Figure 2.2. Left: In-plane linecuts describing intensity (I) as a function of the scattering vector (q_p) obtained from *in situ* GISAXS experiments of the dispersions immediately upon casting. Right: Same data on the left, with dashed lines showing the core-shell form factor fit to the data. Lines are offset from one another for clarity. Labels describe the weight percentage of water that makes up the dispersion solvent composition (the balance is *n*-propanol). 22

Figure 2.3. Effective structure factor (Seff) time evolution of the sol-gel transformation both (a)-(d) in-plane and (e)-(h) through-plane for the dispersions after casting for dispersion solvents containing (a, e) 90%, (b, f) 70%, (c, g) 50%, and (d, h) 30% water (balance *n*PA). Note the 90% sample has a different y-scale. Dashed white line indicates gel formation. 24

Figure 2.4. Measured viscosity of 4 wt. % Nafion dispersions (η) divided by the pure solvent viscosity (η_s) as a function of the water concentration in the dispersion (balance *n*-propanol) at ~12 Hz (the shear rate used to print the films for the *in situ* casting experiments). 25

Figure 2.5. Tuebner-Strey fitting parameter apparent time to equilibrium versus weight percentage of water (the balance is *n*-propanol). κ^{-1} is the hydrophilic domain spacing and ξ represents the correlation between the domains. 27

Figure 2.6. (a) Through-plane and (b) in-plane linecuts (offset for visual clarity) taken at the conclusion of film formation showing intensity (I) as a function of the scattering vector (q). Labels describe the weight percentage of water that makes up the dispersion solvent composition (the balance is *n*-propanol) from which these films were cast. 28

Figure 2.7. Inter-crystalline peak position (in reciprocal and real space) of the membranes as a function of the dispersion water concentration (balance *n*-propanol) at 2452 eV. Error bars are smaller than data points. 29

Figure 2.8. Proposed schematic depicting conclusions of data for dispersion aggregation, thin films, and membranes for high- and low-water concentrations. Features are not drawn to scale. Membrane diagram zooms into possible nanoscale/mesoscale structure (not meant to depict the entire membrane). 30

Figure 2.9. Thin-film (~145 nm thick on silicon) swelling measurements displaying water content (λ, mol water/mol SO_3^-) (a) as a function of relative humidity (RH). Labels describe the weight percentage of water that makes up the dispersion solvent composition (the balance is *n*-propanol) from which these films were cast. (b) Shows the swelling at 90% RH as a function of the dispersion solvent. Closed symbols (●) denote annealed (Ann) films, and open symbols (○) denote unannealed (Un) films. 31

Figure 2.10. Membrane swelling measurements displaying water content (λ, mol water/mol SO_3^-) as a function of relative humidity (RH). Labels describe the weight percentage of water

that makes up the dispersion solvent composition (the balance is *n*-propanol) from which these films were cast. Error bars are smaller than data points. 32

Figure 2.11. In-plane conductivity of membranes prepared from dispersions of varying water concentration (balance *n*-propanol). 33

Figure S2.12. Through-plane intensity I(q) as a function of q linecuts obtained from GISAXS experiments of the dispersions immediately upon casting. Labels describe the weight percentage of water that makes up the dispersion solvent composition (the balance is *n*-propanol). Dashed lines show the core-shell form factor fit to the data. Lines are offset from one another for clarity. 36

Figure S2.13. Shell thickness from core-shell form factor fit of initial linecuts. Error bars represent one standard deviation in fit uncertainty. 37

Figure S2.14. Initial effective structure factors (S_{eff}) of the dispersions immediately upon casting. This was obtained by dividing the line cuts in Figure 2.2 by the core-shell form factor. Labels describe the weight percentage of water that makes up the dispersion solvent composition (the balance is *n*-propanol). Lines are offset from one another for clarity. . 38

Figure S2.15. 2D GISAXS images for each water:*n*PA solvent ratio at select times. The sol-gel transition times shown are 88 s, 42 s, 22 s, and 27s for 90%, 70%, 50%, and 30%, respectively. 39

Figure S2.16. Measured viscosity of the dispersions (η) divided by the pure solvent viscosity (ηs) as a function of shear rate. Labels describe the weight percentage of water that makes up the dispersion solvent composition (the balance is *n*-propanol). 40

Figure S2.17. Gel to final film through-plane Teubner-Strey fitting parameters as a function of time, with error bars. Labels describe the weight percentage of water that makes up the dispersion solvent composition (the balance is *n*-propanol). Note the 90% goes out to 300 seconds. 41

Figure S2.18. Inter-crystalline WAXS peak of the membranes at 2452 eV. Labels describe the weight percentage of water that makes up the dispersion solvent composition (the balance is *n*-propanol). 42

Figure S2.19. Residual water from membrane swelling measurements, as a function of the dispersion water concentration (balance *n*-propanol) from which the membranes were cast. 43

Figure 3.1. Schematic depicting a summary of Chapter 3: dispersion acidity is impacted by the solvent. 44

Figure 3.2. Measured pH of Nafion as a function of Nafion and water concentrations. 48

Figure 3.3. Measured proton divided by corrected theoretical proton concentration as a function of water concentration. 49

Figure 3.4. Schematic of 2D slice of potential structure representing individual chains and aggregates of Nafion, showing the sidechain orientation differences (pH differences) as a function of aggregation and solvent content. 50

Figure 3.5. Titration of a 0.1 wt% XC72 Vulcan carbon particle solution by the addition of Nafion (plotted as measured proton concentration) at different water:*n*PA ratios. 52

Figure 3.6. (a) The diameter as measured by dynamic light scattering and (b) zeta potential of the carbon/ionomer aggregates at different water percentages for Ionomer:Carbon (I:C) ratios between 0 and 1.5, without adjusting pH. (c)-(e) The average diameter of inks made by first adjusting the dispersion pH to 0, 2.5, and 9, respectively. (f)-(h) The average zeta potential of the same inks in (c)-(e). 53

Figure S3.7. Uncorrected data of percent protons measured of acids and different Nafion loadings as a function of water concentration. 56

Figure S3.8. The average diameter and zeta potential of the aggregates in inks adjusted to pH 1. Comparing no ionomer to higher ionomer-to-carbon (I:C) ratios shows that ionomer stabilizes the dispersions. 57

Figure S3.9. cryo-TEM images of 0.2% Nafion solutions in (a)-(c) 50, 70, and 90% water, respectively. 57

Figure 4.1. Schematic depicting a summary of Chapter 4: dispersion conformation changes with age, propagating to affect the properties of dispersions, thin films, and membranes. 59

Figure 4.2. pH of (A.) 0.5, (B.) 2, and (C.) 4% Nafion dispersions, dispersed in various water to *n*-propanol ratios, reported as the percentage water in the figures (30 to 90%). Panels (D.-F.) correspond to (A.-C.) respectively, transforming the pH data into percentage increase in proton concentration as calculated from the pH measurement, normalized to the initial day 0 concentration. 63

Figure 4.3. pH of (A.) 0.5, (B.) 2, and (C.) 4% Nafion dispersions prepared from Nafion D521, dispersed in various water to *n*-propanol ratios, reported as the percentage water in the figures (30 to 90%). Panels (D.-F.) correspond to (A.-C.) respectively, transforming the pH data into percentage increase in proton concentration as calculated from the pH measurement, normalized to the initial day 0 concentration. 64

Figure 4.4. Small-angle x-ray scattering linecuts of Nafion membranes cast from 4% Nafion dispersions in (a.) 30, (B.) 50, (C.) 70, or (D.) 90% water (balance *n*-propanol). The same dispersions were used to cast membranes on the initial day and 7 days later. 65

Figure 4.5. In-plane conductivity of Nafion membranes cast from 4% Nafion dispersions in various water to *n*-propanol ratios (reported as a function of water content). The same dispersions were used to cast membranes on the initial day (0) and 7 days later. Error bars represent the values of multiple unique samples. 67

Figure 5.1. Schematic depicting a summary of Chapter 5: ionomer adsorption onto nanoparticles is affected by the charge density of the ionomer, the particle surface chemistry, and the surrounding solvent environment. 69

Figure 5.2 Ink-to-electrode progression, depicting that ionomer adsorption to catalyst particles impacts electrode structure. In this chapter, we probe these interactions with both isothermal titration calorimetry (adsorption thermodynamics) and quartz crystal microbalance (QCM, to screen the influence of solvent, surface type, and ionomer charge density parameters on adsorption) as illustrated. 71

Figure 5.3. Water droplets (~100 μL) used to determine water-contact angles on the five QCM surfaces studies. Platinum and gold surfaces were supplied by the manufacturer. Hydroxyl, carboxyl, and alkane surfaces were prepared by creating self-assembled monolayers on the gold surface of 11-mercapto-1-undecanol (hydroxyl-modified), 11-mercaptoundecanoic acid (carboxyl-modified), and 1-decanethiol alkane-modified). 73

Figure 5.4. Example raw QCM data (for 3M 1000 on a gold crystal adsorbing from 100% water) depicting the frequency shift at the third overtone (Δf_3) relative to the pure solvent (here water) frequency and dissipation. Dashed vertical lines around 38 and 98 minutes indicate where feed solution was changed. 75

Figure 5.5. Example ITC data of 3M 1000 binding to platinum black. (a.) Raw ITC data, before background subtraction. The first injection is omitted in the fitting to ensure no air bubbles/diffusion of polymer during equilibration impacts the measurement. Minimal baseline drift (baseline indicated by dashed gray line) is observed. (b.) The same data, and the independent binding model isotherm fit to that data, as a function of mass ratio of polymer to particle. 78

Figure 5.6. Frequency change (Δf) measured at the third overtone and associated mass change (Δm) due to ionomer adsorption in solution (as compared with pure solvent) on (a.) alkane-thiol and (b.) platinum model surfaces, respectively, for ionomers with EWs of 620 and 1000 g/mol SO_3^- dispersed in a range of water:*n*-propanol ratios, reported as weight percentage water. 79

Figure 5.7. Frequency change (Δf) measured at the third overtone and associated mass change (Δm) due to ionomer adsorption in solution (as compared with pure solvent) for a range of EWs on surfaces with alkane ($-CH_3$), platinum (Pt), gold (Au), hydroxyl (-OH), and carboxyl (-COOH) functionality in (a.) 50:50 (wt%) water:*n*-propanol and (b.,c.) 100% water. 81

Figure 5.8. Association constants (K_A) of ionomer binding to (a.) carbon or (b.) platinum nanoparticles for freshly prepared (New) or older (Aged) dispersions as a function of ionomer EW in water. Note quantitative comparisons should not be made between (a.) and (b.) because K_A is on a gram basis. (c.) Stacked plot displaying the absolute value of the enthalpic and entropic contributions to the positive binding free energy for the New dispersions (all values indicate spontaneous adsorption). 83

Figure 5.9. (a.) Association constants (K_A) of 3M 1000 versus Nafion 1100 binding on carbon and platinum black nanoparticles from ITC measurements. (b.) Frequency change (Δf) measured at the third overtone and associated mass change (Δm) due to ionomer adsorption (3M 1000 or Nafion 1100) in 100% water onto alkane-thiol-modified and platinum QCM surfaces. 85

Figure S5.10. Calculated deviation from the Sauerbrey model as a function of layer thickness for a thin polymer layer immersed in an infinite liquid overlayer. (a.) Varies the value of shear modulus, while holding the shear viscosity constant at 2×10^{-1} Ns/m^2. The overlayer properties are that of water. (b.) Examines the effect of changing the solvent overlayer using the properties of water and *n*-propanol mixtures (water percentages are balanced by propanol), setting the polymer layer properties to $\mu = 17 \times 10^6$ N/m^2 and $\eta = 2 \times 10^{-1}$ N/m^2. Density of the PFSA film was assumed to be 2 g/cm^3.[113-114] 88

Figure S5.11. Frequency change (Δf) measured at the third overtone and associated mass change (Δm) due to ionomer adsorption in solution (as compared with pure solvent) on (a.) alkane-thiol and (b.) platinum model surfaces, respectively, for ionomers with EWs of 620 and 1000 g/mol SO3- dispersed in a range of water:*n*-propanol ratios, reported as weight percentage water. 89

Figure S5.12. Frequency change divided by maximum frequency change (normalized Δf) for fifteen representative experiments encompassing all solvents, equivalent weights, and surfaces studied as a function of time from which dispersion is introduced. 90

Figure S5.13. The calculated mass change (Δm) for adsorption of 3M PFSA of different EWs in pure water, as a function of the water contact angle of the surface it adsorbs to. 91

Figure S5.14. Data of sequential injections of ionomer (3M 1000) into carbon nanoparticles, as a function of the ionomer-to-carbon (I:C) weight ratio in the sample cell. The dotted light blue line is the independent binding model fit to the data. The total energy (enthalpy) change is indicative of the binding mechanism, the slope of the curve gives the binding affinity (K_A) and the concentration to reach 50% saturation gives the binding stoichiometry, n. 92

Figure S5.15. Association constants (K_A) of ionomer binding to (a.) carbon or (b.) platinum nanoparticles for freshly prepared (New) or older (Aged) dispersions as a function of ionomer EW in water. 94

Figure S5.16. The enthalpic and entropic contributions to the binding free energy to carbon and platinum for aged dispersions of varying EW. 95

Figure S5.17. pH of 3M 1000 and 3M 825 in either (a) 100% water or (b) 50% water/50% *n*-propanol measured as a function of the days after sample preparation. 96

Figure 6.1. Schematic depicting a summary of Chapter 6: as platinum primary particle loading increases, ionomer coverage on the particle's surface becomes patchier thus increasing transport resistance in catalyst layers. 97

Figure 6.2. Zeta potential of inks of varying ionomer-to-carbon (I:C) ratios, containing (A.) 0 wt.% Pt (bare carbon) (B.) 10 wt.% Pt, or (C). 30 wt.% Pt-on-carbon catalyst particles. The dashed light blue vertical line indicates where the marginal ionomer added switches from adsorbing to the catalyst-particle surface (because the surface is unsaturated, Uns) versus no longer adsorbing (because the surface is saturated, Sat). (B.) and (C.) are reproduced with permission from Anamika Chowdhury.[212] 104

Figure 6.3. Measured pH titrating in ionomer of an ink containing either bare carbon (C), 30, or 46 wt.% platinum on carbon (Pt/C) as a function of the measured pH of ionomer-solvent dispersions of the same composition containing no particles. Dashed lines are meant to guide the eye. The dotted gray line indicates a one-to-one correlation. 106

Figure 6.4. (A.) Gas-transport resistance of catalyst layers (CLs) containing the same total platinum loading (0.05 mg/cm^2), but varying primary particle platinum loading. The zeta potentials of the inks used to cast these CLs are also shown. Scanning electron microscopy images of CLs manufactured with (B.) 10 wt% Pt/C and (C.) 46 wt% Pt/C (the same samples measured in (A.)). 108

Figure 6.5. Fractional (A.) carbon and (B.) platinum double-layer capacitance due to ionomer coverage on those respective surfaces. (C.) Bulk catalyst layer (CL) sheet resistance (R_{CL}), normalized by thickness of the CL (L_{CL}). All data are for electrodes containing 0.1 mg/cm^2 platinum loading, achieved while varying the Pt PPL. 109

Figure 6.6. H2-Air polarization curves obtained from CLs using different PPL on the WE, with a total Pt loading of 0.1 mg/cm^2. Operating conditions were 80^{o}C, 150 kPa backpressure, and either (A.) 40% relative humidity (RH) or (B.) 75% RH. The voltage is corrected for high-frequency ohmic resistance (HFR), and the current density is normalized to Pt specific surface area. 111

Figure S6.7. (A.) Zeta potential of 0 wt% Pt/Carbon (bare carbon) inks containing 0.1 wt% nanoparticles as a function of ionomer to carbon weight ratio, exhibiting U-shaped behavior (B.) Zeta potential of 0 wt% Pt/Carbon (bare carbon) inks with constant I:C ratio of 1 and additional electrolyte/acid to increase ionic strength (corresponding to the range enclosed by the dashed gray box in Figure A). Figure A. data is plotted for reference. All ink dispersions show similar behavior of increasing zeta potential (decreasing magnitude)

with higher ionic strength. Ionic strength for the ionomer dispersions was calculated assuming all charges contribute to the ionic strength. The dashed boxes in (B.) are used in further analysis below. 113

Figure S6.8. ζ versus $1/I$, normalized by reference point $\zeta 0$ and $I0$ (highlighted in Figure S6.7). The dashed grey line represents 1:1 correlation. 114

Figure S6.9.The measured pH titrating in ionomer of an ink containing either bare carbon (C), 30 wt%, or 46 wt% platinum on carbon (Pt/C) as a function of the added ionomer, reported as ionomer-to-carbon weight ratio (I:C). Dashed lines are meant to guide the eye. 116

Figure S6.10. Freeze-fractured cross-sectional SEM images of CLs with varying primary particle Pt wt% loadings, and a total loading of 0.1 mg/cm^2. Cross-sectional thickness is indicated by black arrow in images. CL thickness measurements were averaged from three different locations. Results are reported in Table S6.4. 118

List of Tables

Table 1.1 List of input and output variables present in the database. Continuous parameters (*i.e.* encompassing a range of values, rather than discreet points) with sufficient data are chosen for further data analysis. Categorical variables were also analyzed separately. Inconsistently reported parameters, or those with insufficient data were not..... 8

Table 2.1. Final film thicknesses of the dried films from the casting experiments as measured by ellipsometry. At least 7 points are averaged over the width of the film. 27

Table S2.2. Core-shell form factor fitting parameters. 37

Table 4.1. domain (d) spacing and full-width half max (FWHM) of the ionomer peak, and FWHM of the inter-crystalline peak calculated from SAXS membrane experiments. Some cells are empty (--) because the peak was to weak to fit, as seen in Figure 4.4..... 66

Table 5.1. Parameter matrix of the 3M EWs studied (+ Nafion) in each solvent (reported as wt% water, balance *n*-propanol) per QCM surface type studied. Equilibrium water contact angles of the five surfaces are also reported in the last row. 73

Table 5.2. The composition of the final dispersion solvent, and the associated name used. Components are reported in weight percentages of the total solvent, rounded to the nearest half percent..... 74

Table 5.3. Parameter matrix of the 3M EWs studied (+ Nafion) per nanoparticle type studied with ITC. 77

Table 6.1. Relative platinum and carbon surface area estimates, assuming zero percent internal porosity. 103

Table 6.2. Relative platinum and carbon surface area estimates, assuming 30% internal porosity. 103

Table 6.3. CL thickness (L_{CL}) measured from CL cross-sectional SEM..... 110

Table S6.4. r_f (ECSA normalized to CL geometric area) at various total Pt loadings of WE.. 117

Acknowledgements

This work was mainly funded under: the Million Mile Fuel Cell Truck (M2FCT) Consortium (https://millionmilefuelcelltruck.org) and the Fuel Cell Performance and Durability Consortium (FC-PAD), technology managers Greg Kleen and Dimitrios Papageorgopoulos, which are supported by the U.S. Department of Energy, Office of Energy Efficiency and Renewable Energy, Hydrogen and Fuel Cell Technologies Office, under contract number DE-AC02-05CH1123. Parts of this work were conducted at: beamline 7.3.3 at the Advanced Light Source (ALS), supported by the Office of Science, Office of Basic Energy Sciences, of the U.S. Department of Energy (Contract No. DE-AC02-05CH11231); the Soft Matter Interfaces (SMI) Beamline 12-ID of the National Synchrotron Light Source II, a U.S. Department of Energy (DOE) Office of Science User Facility operated for the DOE Office of Science by Brookhaven National Laboratory under Contract No. DE-SC0012704; the Molecular Foundry supported by the Office of Science, Office of Basic Energy Sciences, of the U.S. Department of Energy under Contract No. DE-AC02-05CH11231. I would also like to acknowledge support from the Graduate Research Fellowship Program by the National Science Foundation under Grant No. DGE 1752814.

Now, on to the more important acknowledgements. First, I would like to thank my advisors, Adam Weber and Bryan McCloskey, for their support over the last five years. Thank you for giving me the freedom to take this work in directions that interested me. Adam: thank you for the always twice-as-long-as-scheduled meetings filled with hard questions, interesting tangents, and good conversation. Bryan: thank you for providing very important external perspective and insight and for the many helpful career discussions. I'd also like the thank my unofficial advisor, Clay Radke, for teaching me how to argue back, defend my work, and ask questions. Thank you also for the many laughs. Working with the three of you has made me into an undoubtedly better scientist and stronger person than I was five years ago.

The contents of this dissertation would also have not been possible without some incredible labmates in both the Energy Conversion Group and McCloskey Lab. I would especially like to acknowledge Andrew Crothers, Meron Tesfaye, Anamika Chowdhury, Douglas Kushner, Ashley Bird, Ahmet Kusoglu, Peter Dudenas, Kyle Diederichsen, Kara Fong, and Helen Bergstrom for their many important conversations, collaborations, and research contributions. I have thoroughly enjoyed working with all of you and admire you all so much as scientists. I would also like to thank my undergraduate mentees: Xunkai Chen, Nicholas Dagan, Samay Garg, Jiwoo Choi, and Aiden Grahame. Thank you for teaching me how to be a better mentor; it was a pleasure working with you.

Graduate school was a journey, beyond just research. There were just as many lows as there were highs. (Actually, there were probably more lows than highs.) In my third year, I was not entirely sure that I would be able to finish this PhD. I'd like to again thank Meron and Kyle; I really hope you know how much those early pep talks meant to me. Thank you for showing me that I should stay. Similarly, thank you to greater Energy Conversion Group and McCloskey Lab: grad school would have been a much less enjoyable process without the many laughs, distractions, lunches, happy hours, and group trips that made the day-to-day experience memorable. In particular, I'd like to thank my officemates (Doug, Yagya Regmi, and Johnny Petrovick) and very first lab friend,

Julie Fornaciari, for always being there to chat (more often about non-research than research). While I will not miss the lack of windows or temperature control at all, Building 70 was a true community.

To the 2016 cohort: thank you for going on this adventure and eating many tacos with me. You are all incredible scientists, and I am so excited to follow your careers. Special shout-out to Eric McShane for teaching me about value. I'd of course also like to acknowledge Rebecca Pinals. While we are not actually the same person (despite what some might think), I love being part of Team Bearah. Thank you for being my best friend throughout the last five years, pushing me both as a scientist and as a person to believe in myself.

I'd also like to acknowledge the Alligator House in its many iterations: Rebecca, Andrew, Peter, Kyle, Matthew Whitman, Constance Visser Whitman, Parbir Grewal, Tammy Hsu, Julie Rorrer, and Kitty Friend. Thank you for being my Berkeley family and an incredible community of humans (except for Kitty Friend – while he might think he is a human, he is not). I think our house was pretty unique and special.

Finally, I'd like to thank some people that inspired this PhD dream. I decided sophomore year of high school that I wanted to get a PhD in Chemical Engineering. This was kind of a crazy thing to do because I didn't really know what chemical engineering was, nor what a PhD entailed. Regardless, thank you to Gregory Horrace and Mary Couzis for their encouragement to pursue this path. Similarly, I'd like to thank Alan West for agreeing to mentor a first-year college student who knew absolutely nothing about electrochemistry, but somehow knew that was what she wanted to study.

Of course, these dreams would be nothing without my family. Thank you to my mom, dad, and sister Maya for their endless support and encouragement, and for being my constant cheerleaders. I am so incredibly lucky to have you all and truly appreciate everything you do for me.

Last but certainly not least, thank you, Pete. To put it simply, I wouldn't have wanted to do this with anyone else by my side.

1 Introduction[‡]

1.1 Background

Proton-exchange-membrane (PEM) fuel cells are promising energy-conversion devices that have made great technological progress over the past few decades. When coupled with hydrogen produced from a renewable power source, these devices offer green electricity with applications in a wide variety of sectors. There is fast-growing interest in a hydrogen-based energy economy[1]: estimates indicate that by 2050, hydrogen could meet up to 24% of the world's energy needs.[2] Similarly, hydrogen-economy roadmaps suggest the addition of over five thousand hydrogen fueling stations in the Unites States by 2030.[3] With this distributed hydrogen network, fuel cells are particularly good candidates to replace both internal-combustion-engine- and battery-powered vehicles due to zero emissions and fast (hydrogen) refueling times. Indeed, heavy-duty fuel-cell electric vehicles have garnered much attention lately;[4] the United States Department of Energy has recently funded a multi-million-dollar research consortia focused on heavy-duty vehicles (Million Mile Fuel Cell Truck), as part of their larger hydrogen at scale (H2@Scale) vision for wide-scale hydrogen production and utilization.[5]

PEM fuel cells operate by taking in reactant gases (hydrogen and oxygen) into gas flow channels. These gases diffuse across carbon-based gas-diffusion layers, where they then react at catalyst layers (electrodes). At the anode catalyst layer, hydrogen is oxidized to protons and electrons. These protons travel across an ion-conducting polymer (ionomer) membrane, where they combine with oxygen on the cathode side to produce water. A schematic of a PEM fuel cell is shown in Figure 1.1.

The electrochemical heart of PEM fuel cells is their catalyst layers (CLs): heterogeneous porous electrodes composed of agglomerates of catalyst particles, ion-conducting polymer (ionomer), and void space. The ionomer serves both to bind the CL together and provide a pathway for ion transport.[6-7] Similarly, void space is crucial for gas and water transport, while the catalyst particles provide reaction sites and electron conduction pathways. These structures are necessarily complex, and characterization is nontrivial.[8-10] As such, there have been decades of research into CLs.[6, 11-24] However, the majority of studies have focused on relating structure to performance. Indeed, with the recent push for improved fuel-cell durability, much characterization effort has focused on structural changes and associated performance losses over time.[25-26] While this is certainly an

[‡] Portions of this chapter were previously published as "Berlinger, S. A.; Garg, S.; Weber, A. Z., Multicomponent, multiphase interactions in fuel-cell inks. *Current Opinion in Electrochemistry* **2021,** *29*, 100744," and are adapted with permission from all co-authors.

important problem, fundamental understanding of how these CL structures originally form is also missing: CL fabrication processes have relied mostly on empiricism. This gap poses challenges for the community: if we are to engineer next-generation optimized CLs in an efficient manner, knowledge of how CL structures arise is crucial.[27]

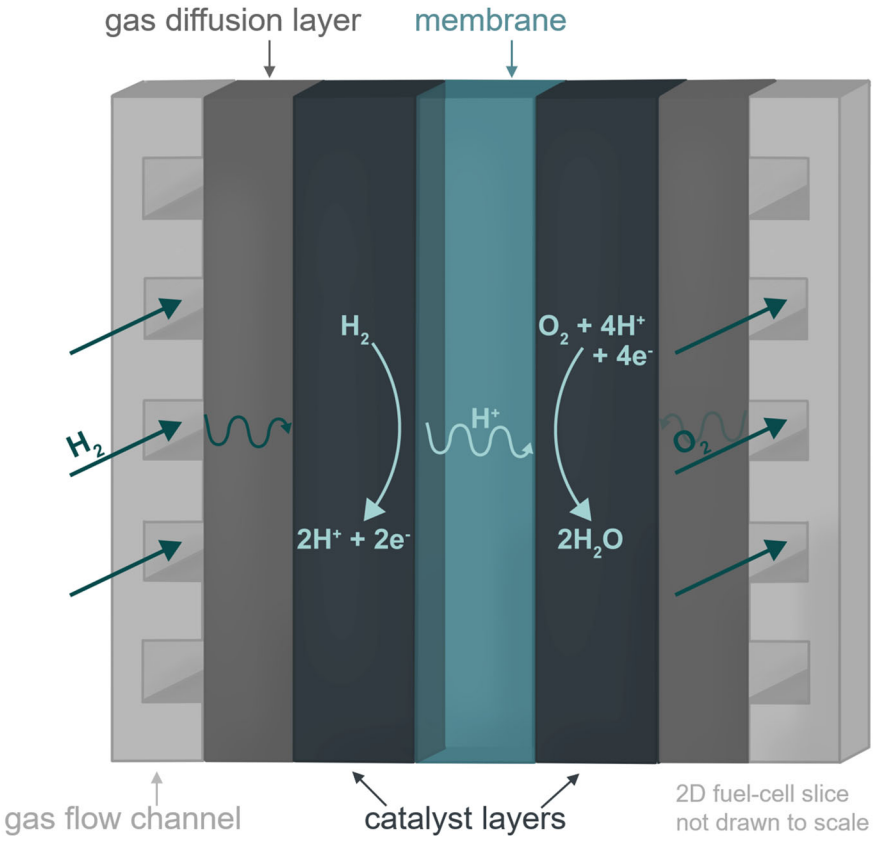

Figure 1.1. Two-dimensional schematic of a hydrogen fuel cell.

CLs are fabricated from inks that contain the catalyst particles and ionomer, dispersed in a solvent.[27] The particles and ionomer form agglomerates (on the order of 100's of nanometers) in the ink[6, 11] that eventually determine the final CL microstructure. Important parameters that impact (or are impacted by) this ink-to-CL progression are listed in Figure 1.2. Ultimately, one desires to know how inputs (ink parameters) affect measurable outputs (CL parameters). Different ink parameters result in different interactions; these interactions modulate CL microstructure and performance. For example, the ionomer/solvent interaction controls the ionomer conformation in solution. These different conformations will affect the ionomer/particle interaction, which dictates how the ionomer adsorbs to the catalyst particles in the ink. This ionomer/particle ink interaction

modifies the ionomer/particle interface in the CL. Multicomponent interactions between all three determine the agglomerate sizes and structures that self-assemble. Clearly, unraveling these interactions is key for understanding the final microstructures. Metrics of ink properties that reveal these different interactions are listed as interaction descriptors in Figure 1.2.

By understanding how ink parameters affect ink properties/interactions (which in turn dictate CL structure/performance), we can engineer inks to control and direct specific CL microstructures rather than rely on empirical and time-consuming optimization. With that goal in mind, this chapter first explicitly details ink parameters (Section 1.2), and then investigates the impact these parameters have on device performance through a parameter regression screening (Section 1.3).

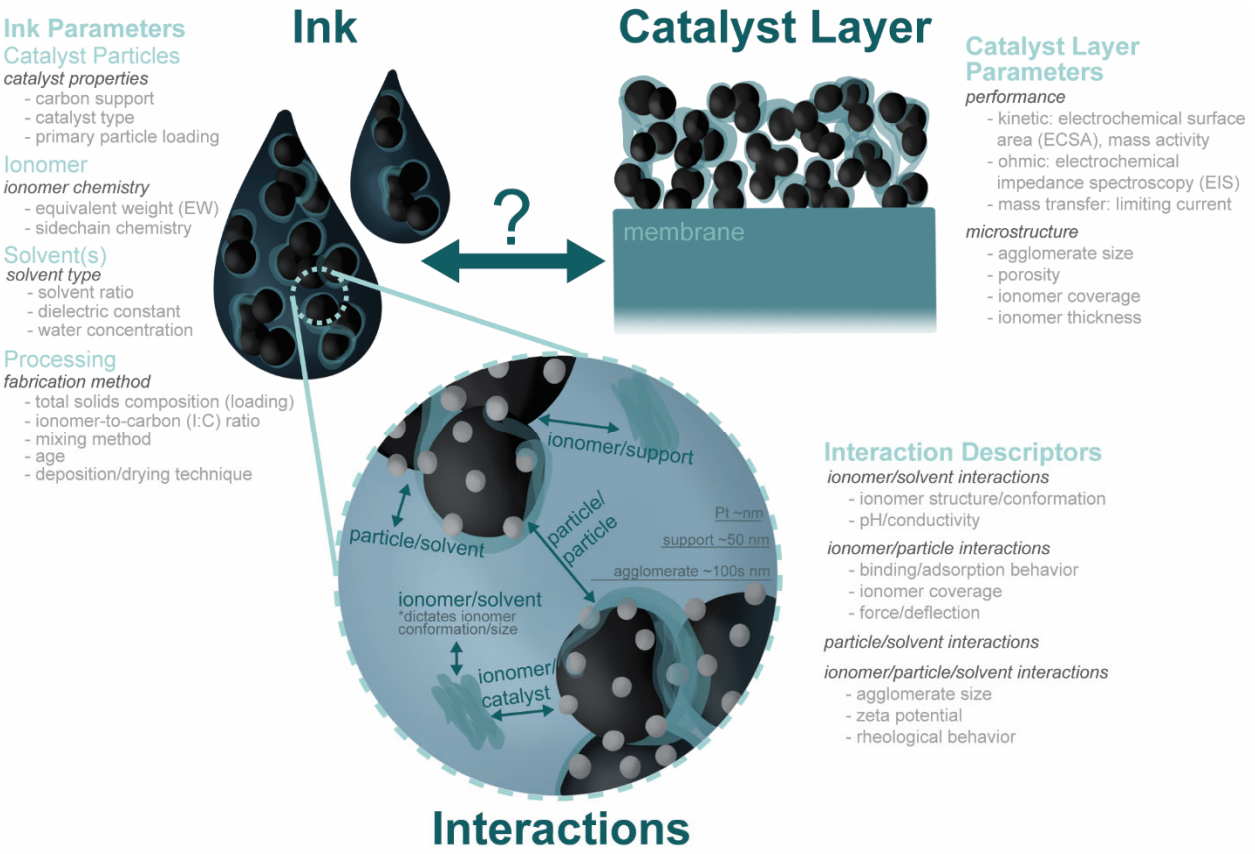

Figure 1.2. Pictorial representation of ink and catalyst-layer structure (not meant to be exact or drawn to scale) and associated relevant important parameters that govern these structures/properties. Parameter list is not exhaustive. These parameters guided the database collection and regression analysis (see Section 1.5).

1.2 Ink Parameters

While there has been much CL research, the literature is full of contradictory data, partly because the properties or values of the ink parameter categories in Figure 1.2 (catalyst particles, ionomer chemistry, solvent type, and fabrication method) can be drastically different. Each of these will be detailed in the following subsections.

1.2.1 Catalyst Particles

Catalyst particles are typically platinum or platinum-alloy nanoparticles supported on larger carbon nanoparticles (although some efforts are focused on non-platinum-group-metal catalyst development [28-30]). The platinum particles are on the order of a few nanometers (~1 to 5 nm) and the primary carbon particles are typically 30 to 50 nm in diameter. The platinum loading on these carbon supports can vary (termed primary particle loading); a catalyst particle is typically 10 to 50% platinum by weight (*i.e.* 30% Pt/C). Multiple carbons support types are used throughout different studies: two common commercial types are Vulcan and high-surface-area carbon (HSC), although novel carbon and even noncarbon supports have been explored.[31-33] Vulcan is more graphitic (and hydrophobic) than HSC. Bare Vulcan has a Brunauer–Emmett–Teller (BET) surface area of ~200 m^2/g, whereas HSC is upwards of 800 m^2/g.[34] Due to Vulcan's lower internal porosity, most platinum decorates the external surface in Vulcan-supported catalysts. In contrast for HSC-supported catalysts, most of the platinum is located in internal nanopores within the carbon.[35]

1.2.2 Ionomers

Many ionomer chemistries are studied in fuel cells. The most ubiquitous class of cation-conducting ionomers is perfluorosulfonic-acid ionomers (PFSAs), which consist of Teflon-like backbones and pendant sidechains that terminate in sulfonic-acid groups (see Figure 1.3). Notably, these sidechains are highly acidic (solid PFSA membranes have a pKA around -6).[36]

Within PFSA chemistries, there is wide variability of ionomer types. The sidechain spacing, or charge density of the ionomer can vary. This is defined by the ionomer's equivalent weight (EW, grams polymer/mole sulfonate). EW is inversely proportional to ion-exchange capacity and dictates the number of CF_2 groups associated per sidechain in the monomer (x in Figure 1.4). Additionally, the sidechain length is variable; three common commercial ionomer chemistries with different sidechains are shown in Figure 1.4. Of these, Nafion is historically the most prevalent in the literature and in fuel cells. Both EW and sidechain length alter the intrinsic ionomer properties (conductivity, crystallinity, swelling, *etc.*)[7] When comparing different chemistries (*i.e.* Nafion to 3M) it is often better to compare at the same CF_2 backbone spacing (x) rather than the same EW since the sidechain molecular weight is also changing.[7] Ionomers used in the preparation of fuel-

cell inks are often diluted from commercial stock dispersions of the ionomer dispersed in water/alcohol mixtures.

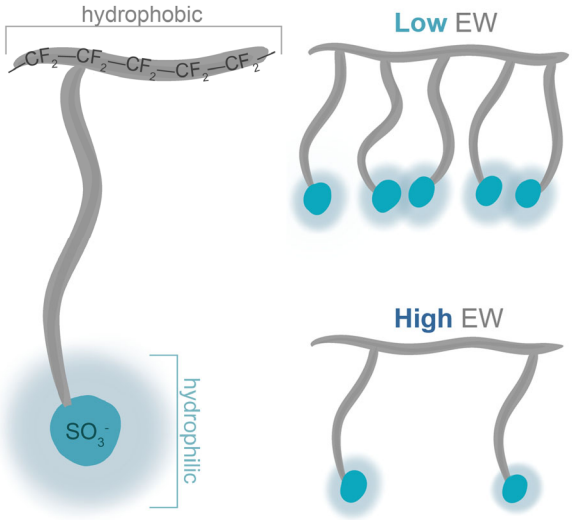

Figure 1.3. Left: general schematic of PFSA ionomer, depicting the polytetrafluoroethylene backbone and pendant sidechains terminating in hydrophilic sulfonic acid groups. The repeat density of these sidechains is inversely proportional to its equivalent weight (EW, $g_{polymer}/mole_{SO3-}$), as depicted in the top and bottom right images.

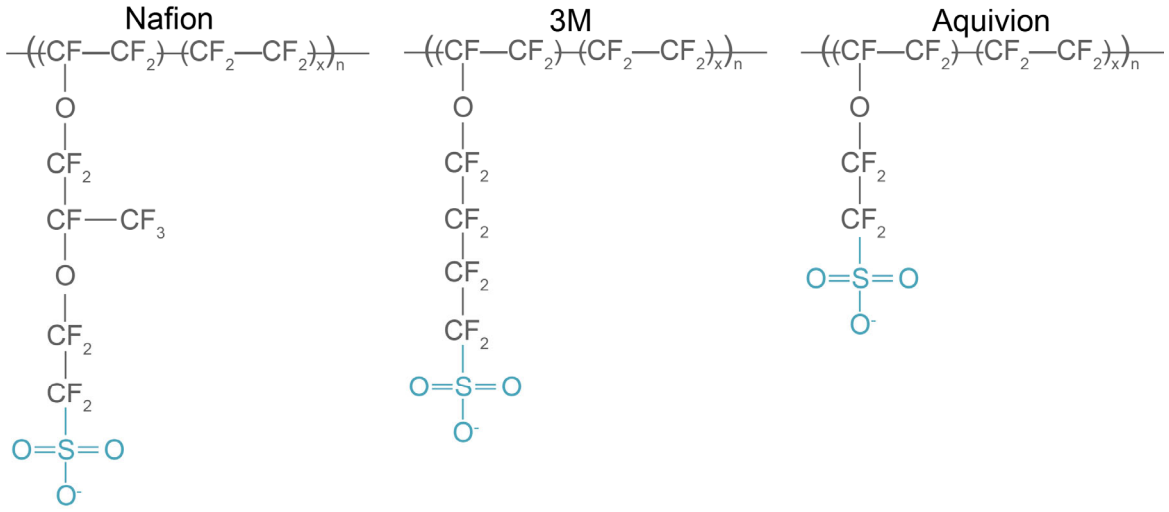

Figure 1.4. Structure of three common PFSA ionomers with varying chain lengths: Nafion, 3M, and Aquivion. n denotes the polymer repeat length, and x determines the equivalent weight of the polymer (*i.e.* the number of tetrafluoroethylene groups in the backbone).

1.2.3 Solvents

The solvents in fuel-cell inks function to disperse the ionomer and nanoparticles. Their properties (viscosity, boiling point) also control the deposition process, and alter how the ionomer and particles interact with each other (*e.g.* through media of varying dielectric permittivity depending on solvent choice). These solvents are not standardized: while alcohol-water mixtures are the most common, various others have been investigated.[37-41] Additionally, even when considering the same solvent system, the composition may vary (*i.e.* the ratio of alcohol to water).

1.2.4 Processing

To complicate matters further beyond just material selection, fabrication choices can influence final properties. The method[42] and length of mixing[43] may differ. The ratio of components (namely ionomer-to-carbon, I:C) can be modified, as well as the total solids loading, which is often set by the processing method: different techniques have different viscosity requirements. Ultrasonic-spray coating,[44-46] doctor blading,[47] screen printing,[23] and roll-to-roll[48] processing of electrodes can occur either on the membrane to form a catalyst-coated membrane (CCM), on diffusion media to form a gas-diffusion electrode (GDE) or on a decal[49-51] and later transferred. GDEs and decals are often also hot-pressed to the membrane to form the membrane-electrode assembly (MEA).

1.2.5 Interactions

As mentioned above, all of these parameter choices will control the interactions between components. Particle/solvent interacts are perhaps the simplest to understand. When dispersed in a solvent, these catalyst particles are typically weakly negatively charged due to functional groups on their surface.[52] The dielectric permittivity of the solvent will control (screen) the electrostatic interactions between these particles, and modify the Hamaker term in the van der Waals attractive interaction energy. These two opposing energies (attractive and repulsive) are described by classical Darjaguin-Landau-Verwey-Overbeck (DLVO) theory. In addition, carbon is hydrophobic (when fabricating these inks, one readily observes that the nanoparticles do not easily disperse/wet). When changing the ratio of water:alcohol, this will also tune hydrophobic interactions between the particles and solvent, inducing aggregation. These three interaction energies control the nanoparticle aggregate size in solution: for Vulcan carbon, it has been observed that higher ratios of water:propanol yield more stable inks, with aggregate diameters on the order of 300 to 500 nm, as measured in dilute conditions by Dynamic Light Scattering (DLS).[53]

Ionomer/solvent interactions control the ionomer conformation in solution. Additionally, because molecular-weight distributions are difficult to characterize for PFSAs, most PFSA solution analysis has relied explicitly on characterizing these structures in solution (often termed "aggregate" structure). Scattering[37, 54-55] and molecular-dynamics (MD) simulations[56-59] reveal that in many polar solvents, PFSA forms cylindrical bundles, although swollen spheres and random

coils have also been observed.[37] This solvent-induced conformation is driven by competing preferences for hydrophobic backbone aggregation and electrostatic sidechain repulsion. The solvent/ionomer interaction has been described using solubility parameters that have been measured for both the backbone and the sidechains.[60] Of note, this aggregate structure/size is dependent on both the concentration and solvent environment, and because the molecular weight is unknown, it is unclear how many chains make up one aggregate (in the dilute limit it could actually be only one, but is still termed an aggregate because it is not strictly dissolved and the molecular weight is unknown).

As one might imagine, the conformation the ionomer adopts in solution may impact how it adsorbs and interacts with nanoparticles. Unfortunately, the ink ionomer/particle interaction has received very little attention. In contrast, because the ionomer/platinum interface controls electrochemical reactions, the ionomer/platinum interaction in *operando* has received much attention in the literature. During fuel-cell operation, many researchers have noted that the PFSA sulfonate moieties interact with the platinum catalyst surface, effectively poisoning the catalyst by blocking active sites.[61-65] This is also evidenced by increased oxygen transport resistance.[17, 66] A number of groups have hypothesized that this platinum/sulfonate interaction extends to ink systems, and that this is what drives ionomer adsorption onto catalyst particles in inks.

1.3 Parameter Screening

The disparate and massive parameter space of differing nanoparticles, ionomer, solvents, and processing conditions makes it exceedingly difficult to compare studies directly to each other. Additionally, within the literature there are two main types of papers: catalyst-layer-focused and ink-focused. The majority of papers fall into the former category, and often report incomplete ink parameters, as their emphasis is on characterizing CL structure and performance. On the other hand, ink-focused papers systematically vary one ink parameter, but typically investigate its impact on only one or two CL parameters. This yields collective information rich on either end of the ink-to-CL spectrum, but lacks information connecting the two states. In an attempt to connect ink and CL parameters, we gathered data from ink-focused papers[23, 46-47, 50-52, 60, 67-81] that had sufficient detail about the ink parameters listed in Figure 1.2, and classified the data as either inputs (ink parameters) or outputs (ink interaction descriptors and catalyst layer (CL) parameters). The full list of inputs and outputs we collected in the database (available as an Excel file online[82]) are shown in Figure S1.7. To limit the scope, only papers using PFSA and Pt-based catalysts, and those that investigated at least three variations of one parameter (*e.g.* three different solvents, I:C ratios, *etc.*) were chosen. We then performed a linear regression to test correlation between these parameters and both ink interaction descriptors and CL parameters. Input parameters chosen for subsequent analysis were continuous variables (possessing more than three discreet values) that were consistently reported, and output variables were chosen based on prevalence of data available. From these criteria, we selected I:C ratio, solvent dielectric constant (ε), zeta potential (effective surface potential in solution), agglomerate size, electrochemical surface area (ECSA, in contrast to geometric surface area and measures the connectivity/coverage of electrically active regions), and limiting current density ($i_{lim,}$ the maximum current density achievable) as variables

to perform the regression. More details on data collection/analysis, additional parameter plots, and parameter selection can be found in Section 1.5.

Table 1.1 List of input and output variables present in the database. Continuous parameters (*i.e.* encompassing a range of values, rather than discreet points) with sufficient data are chosen for further data analysis. Categorical variables were also analyzed separately. Inconsistently reported parameters, or those with insufficient data were not.

Inputs		**Outputs**	
Parameter	**Comments**	**Parameter**	**Comments**
Solvent Identity (solvent(s) chemistry, *i.e*. propanol, water, mixed propanol/water)	Reported as dielectric constant, ε Continuous	**Agglomerate Size** (of the ink)	Sufficient
Solvent Concentration (the concentration of each solvent used, *i.e* 50% propanol, 50% water)		**Zeta Potential** (of the ink)	Sufficient
Catalyst Particle Concentration (primary particle catalyst concentration, *i.e.* 50% Pt on carbon)	Not continuous	**Viscosity (at 100 Hz)** (of the ink)	Insufficient
Ionomer-to-carbon (I:C) Ratio	Continuous	**Limiting current density** (of the catalyst layer)	Sufficient
Ionomer Type (ionomer identity, *i.e*. Nafion, Aquivion)	Not continuous, categorical	**Current density at 0.8V** (of the catalyst layer)	Inconsistent
Ionomer Equivalent Weight (EW) (grams polymer/mol SO_3^-)	Not continuous	**Porosity** (of the catalyst layer)	Insufficient
Ionomer Concentration (total ionomer concentration in the stock solution)	Not continuous	**Electrochemical surface area (ECSA)** (*i.e.* from CO-stripping experiments)	Sufficient
Catalyst Metal (catalyst chemistry, *i.e* Pt, Pt-Co)	Not continuous	**Charge Transfer Resistance** (from electrochemical impedance spectroscopy data)	Insufficient
Catalyst Loading (in the catalyst layer*, i.e.* 0.4 mg/cm^2)	Inconsistent	**Catalyst Layer Resistance**	Insufficient
Carbon Support Type (*i.e.* Vulcan, HSC)	Not continuous, categorical	**High frequency resistance (HFR)** (from electrochemical impedance spectroscopy data)	Insufficient
Age of Ink (from preparation)	Inconsistent	**Conductivity** (of the catalyst layer)	Insufficient
Sonication Time	Inconsistent		
Fabrication method (*i.e.* ultrasonic spray, roll-to-roll)	Inconsistent		
Technique to Measure Agglomerate Size	Not continuous		

Figure 1.5 examines the influence of ε on interaction descriptors (agglomerate diameter and zeta potential) and CL parameters (i_{lim} and ECSA). Because a wide range of solvents and solvent mixtures have been explored, solvent identity and mixture composition are jointly represented by ε to compare more easily the influence of these two parameters across different studies. This was calculated by computing the average of the pure component ε weighted by relative concentration. Figure 1.6 plots the same properties, now as a function of I:C ratio. The first thing to note is that no parameter of the ones studied is controlling; there are certainly correlations, but outcomes cannot be predicted solely from one parameter (or groupings of parameters). Spread in the data is due to variability in all of the other ink parameters. Additionally, particularly for the I:C data, there are clusters of points located at one value (*e.g.* I:C 1); variability in the y-value is again due to differences in the other parameters not held constant. That being said, a few general trends are observed. First, there is no strong correlation between agglomerate diameter and zeta potential as a function of ε, suggesting that the primary forces controlling the aggregation process are not electrostatic in nature. However, CL performance does seem to be related to ε: Figure 1.5 shows ECSA and i_{lim} increasing with ε. This is in agreement with recent studies[46] that demonstrated the impact of water:propanol ratio on CL performance and ionomer coverage of the agglomerate.

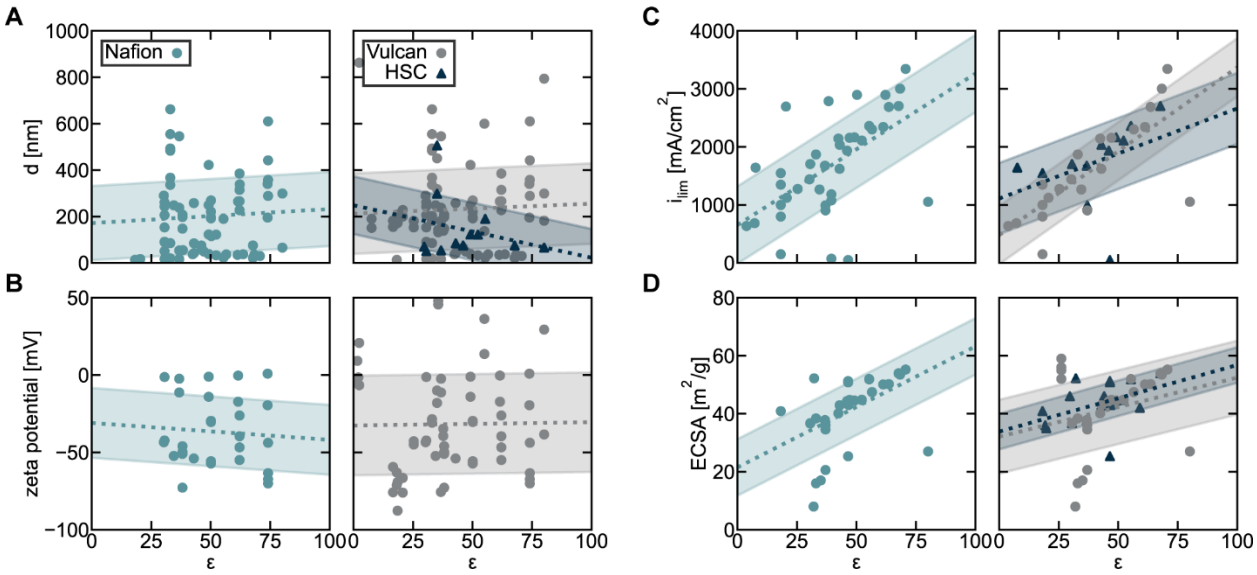

Figure 1.5. Data from References[23, 46-47, 50-52, 60, 67-81] that displays the effect solvent dielectric constant (ε) has on (A,B) ink interaction descriptors (agglomerate diameter, d, and zeta potential) and (C,D) catalyst layer parameters (limiting current density, i_{lim}, and electrochemical surface area, ECSA). The left and right panels of each subplot categorize similar data based on ionomer type (left) or carbon support type (right). The shaded region represents one standard error of the regression fit (dotted line).

In Figure 1.6, we see that the zeta potential generally becomes more negatives as I:C increases, likely due to greater ionomer adsorption to the agglomerate surface. We also see CL parameters

are impacted by I:C ratio, which has been the focus of a number of studies[23, 80, 83-84]. Electrochemical performance is controlled by how much ionomer is in contact with the catalyst sites: too much results in high transport resistances and catalyst poisoning, while too little ionomer coverage yields insufficient ion conduction.[17, 61, 65, 85-87] The lack of consensus on an optimal I:C value indicates that it is material/processing-dependent; this is evidenced by the different I:C trends for HSC and Vulcan in Figure 1.6. Most probably, optimal I:C also depends on parameters like solvent, EW, *etc*. While these trends are complex, it is clear solvent choice and I:C alter ink interactions and CL parameters.

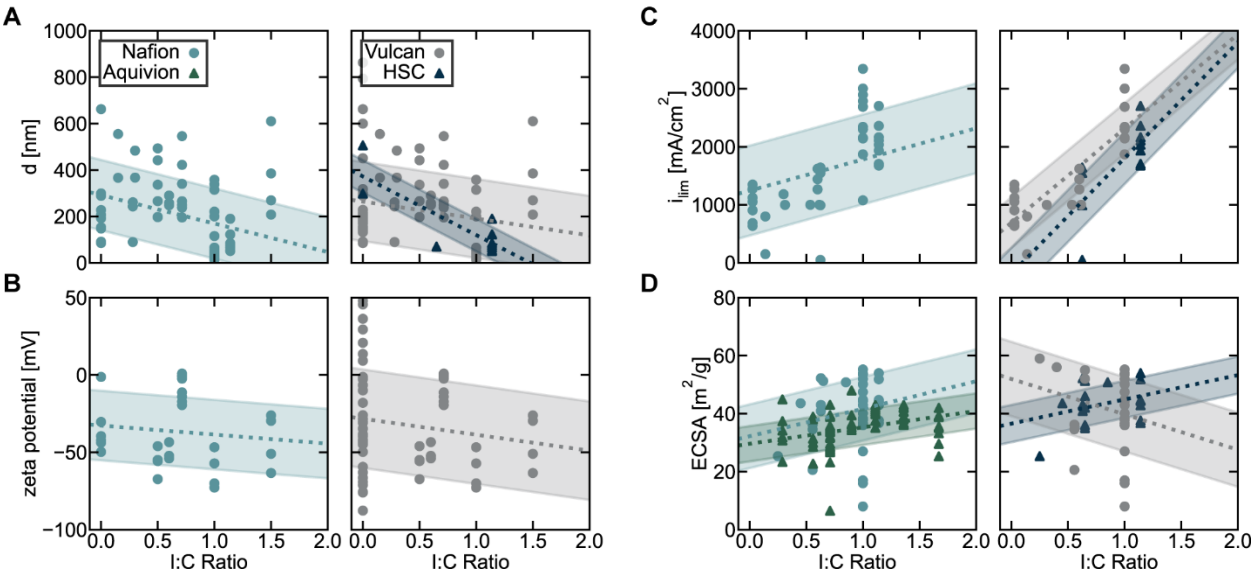

Figure 1.6. Data from References[23, 46-47, 50-52, 60, 67-81] that displays the effect ionomer-to-carbon (I:C) ratio has on (A,B) ink interaction descriptors (agglomerate diameter, d, and zeta potential) and (C,D) catalyst layer parameters (limiting current density, i_{lim}, and electrochemical surface area, ECSA). The left and right panels of each subplot categorize similar data based on ionomer type (left) or carbon support type (right). The shaded region represents one standard error of the regression fit (dotted line).

1.4 Dissertation Outline

In the above section, it is evident that ink parameters such as I:C and solvent choice impact CL metrics. However, because there are so much spread in the data, it is not entirely clear how or why they do. Also as discussed, the existing data is difficult to make use of because so many variables change across different studies. To understand this ink-to-CL progression, fundamental understanding of these interactions is required beyond the simple correlations above and empiricism currently observed in literature.

As such, the central question we would like to pose throughout this dissertation is: how and why do these components interact within an ink, and how do these interactions affect measurable outcomes? To make this problem more tractable, we tackle this question piecewise to understand different aspects of this complex, multicomponent ink phenomena.

This dissertation is generally broken up into two sections: Chapters 2 thru 4 discuss ionomer/solvent interactions, while Chapters 3, 5, and 6 detail ionomer/particle interactions. Throughout this work, the term "dispersion" refers to an ionomer and solvent system, and an "ink" means with particles (either platinum/carbon catalyst particles or bare carbon support particles). The term ionomer "dispersion" is chosen to be consistent with literature, especially given the fact that the ionomer backbone is not fully solubilized in most relevant solvent systems. However, as detailed in Chapters 3 and 6, the ionomer also behaves like a solution able to distribute uniformly and affect properties such as pH and the zeta potential of catalyst-particle agglomerates.

Beginning with Chapter 2, we explore how water:alcohol impacts ionomer dispersion properties. We then detail how these different dispersion structures induce altered coalescence pathways during the drying process, and how this affects the final structures of both thin films and membranes. Importantly, these solvent differences persist even after post processing (*i.e.* thermal annealing). Structure-property relationships as a function of casting solvent are explored for both thin films and membranes, by measuring conductivity and swelling of the ionomer films.

Chapter 3 investigates the inherent acidity of PFSA dispersions, and how that acidity changes as a function of water:alcohol ratio and ionomer concentration. Importantly, these acidity changes do not scale in a predicted manner, suggesting they are in large part due to ionomer conformation changes (and whether sidechains are exposed or buried). This has important implications for both electrostatic and hydrophobic interactions the ionomer may have with nanoparticles in solution. Therefore, we study how the bulk ink behavior (aggregate size and zeta potential) changes as a result of these altered ionomer/solvent and ionomer/particle interactions. We consider limiting cases with added acids and altered pH values to elucidate observed behavior.

Chapter 4 builds upon the results of Chapter 2 by introducing another variable to the solvent ratio matrix: time. These dispersions are inherently unstable, with slow equilibration times. Temporal stability (or lack thereof) obviously has important practical manufacturing ramifications. Here, we explore the ionomer's response to new solvent environments, via both dilution of the ionomer and altered environment (both of which tune the ionomer/solvent interaction). Using the techniques established in Chapter 3, we probe the pH and structure of the dispersions over a matter of weeks, and then cast membranes from each different solvent ratios at multiple time points, to see how the ionomer/solvent interaction is affected by both time and water:alcohol ratio. Properties of the final membranes are again measured and correlated with structure.

Chapter 5 explores the ionomer/particle and ionomer/solvent/temporal interactions established in Chapters 3 and 4, respectively, in greater depth from a more fundamental level. Using model functionalized surfaces to encompass a range of substrate hydrophobicities and metal types, we use quartz crystal microbalance (QCM) adsorption to probe ionomer/particle interactions, by

measuring ionomer adsorption from solution. We do this for both a range of EWs and solvent ratios, to understand how ionomer charge density and conformation (as a result of both differing solvents) impact the adsorption interaction. We then use isothermal titration calorimetry (ITC) measurements to extract thermodynamic binding information (including association constants, and enthalpies and entropies of binding) of the same ionomers (with varying EWs) onto both Vulcan and platinum nanoparticles. The ITC data confirm the QCM trends while also providing quantitative interaction strengths.

Building off the results of Chapter 5 that revealed platinum and carbon have different interaction strengths with ionomer in an ink, in Chapter 6 we ask: how does changing platinum loading on a catalyst particle (*i.e.* the ratio of platinum to carbon surface area available for the ionomer to interact with) impact both ink properties and CL performance? We establish a direct correlation between ink zeta-potential measurements and CL transport resistance measurements and demonstrate how ink properties propagate to affect CL microstructure and performance. This provides additional insights linking ink and CL properties that were missing from the simple correlations of Figure 1.6.

Finally, in Chapter 7, we conclude by discussing remaining challenges and future directions. In sum, this dissertation provides a fundamental exploration into the governing interactions in fuel-cell inks and shines a light into the black box of CL fabrication. Importantly, these results can be used to control and direct CL morphology. Moreover, they can be extended to other systems that utilize such ink-based processing techniques, such as electrolyzers, CO_2 reduction devices, *etc.*

1.5 Supplementary Information

1.5.1 Feature Selection

Once the database was created, we next needed to analyze the data. Figure S1.7 shows the results of the entire database, relating inputs to outputs. Before performing any statistical modeling, we selected an appropriate subset of input and output variables from the complete feature space on which to conduct our analysis. Several input variables including sonication time, sonication method, fabrication method, age of ink, and catalyst loading were inconsistently reported by the references included in the database, so they were removed from the list of candidate features for subsequent analysis. Catalyst identity was also not considered further because all references apart from one used Pt/C catalysts. Another issue arose with variables such as the ionomer EW and the catalyst particle concentration. These are theoretically continuous variables that could take any positive numerical value; in practice however, these variables are limited to several discrete values based on commercial availability, as illustrated in Figure S1.8. Because of this, ionomer EW, ionomer concentration, and catalyst concentration were also not analyzed further. Ultimately, the dielectric constant and I:C ratio were chosen as the final two quantitative input variables. Carbon type (Vulcan vs. HSC) and ionomer identity (Nafion vs. Aquivion) were also maintained as categorical variables.

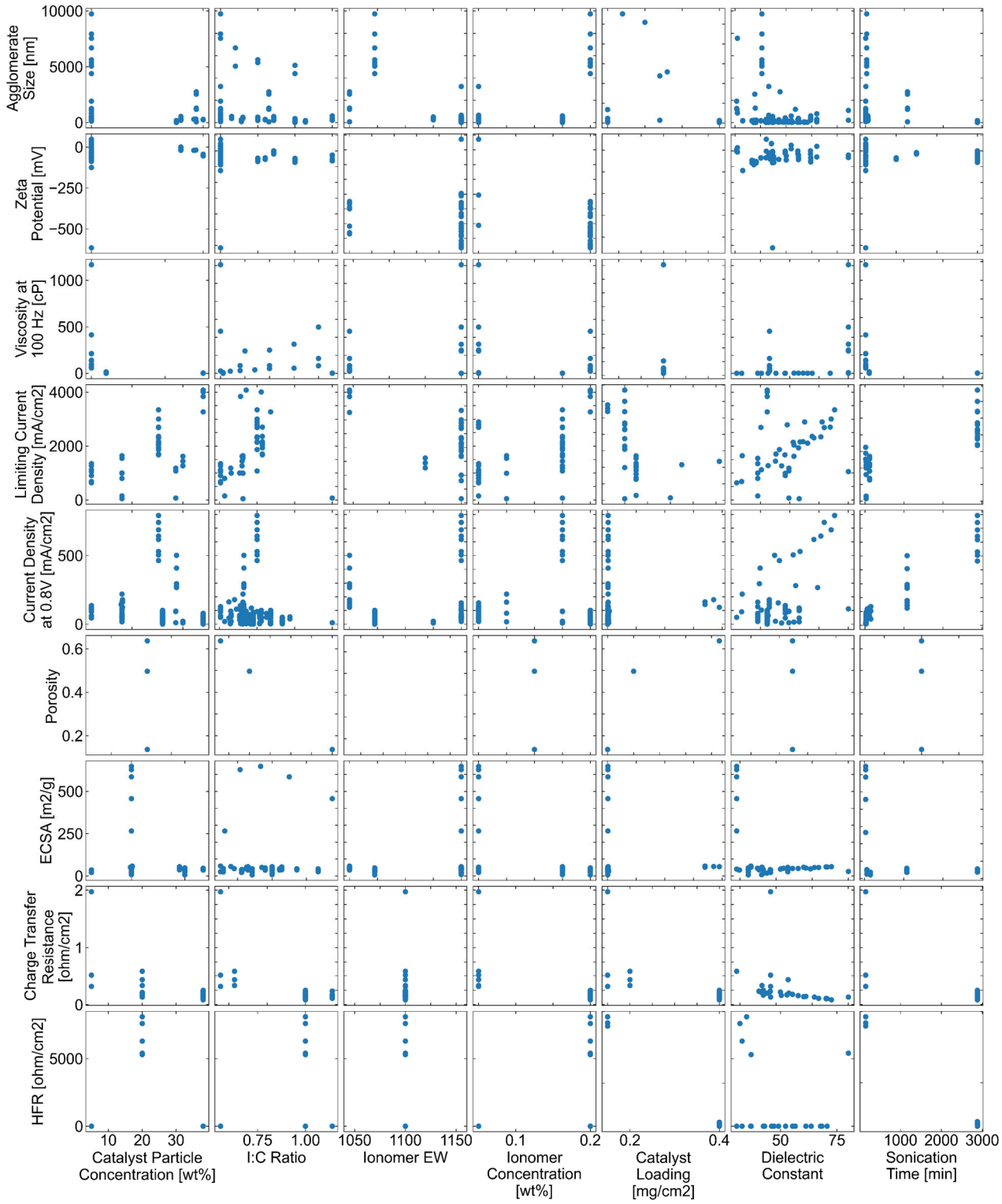

Figure S1.7. Example scatter plots relating each input variable to each output variable.

Output variables were selected primarily based on reporting consistency and prevalence across multiple sources. Current density at 0.8 V was dropped from the set of candidate output variables because it was inconsistently reported, while CL porosity, charge transfer resistance, high-frequency resistance (HFR), viscosity, and conductivity did not have large enough sample sizes to be included in the final set of output variables. Therefore, agglomerate size, zeta potential, limiting current density, and ECSA were chosen as the final output variables. The reasoning for each parameter is listed in Table 1.1.

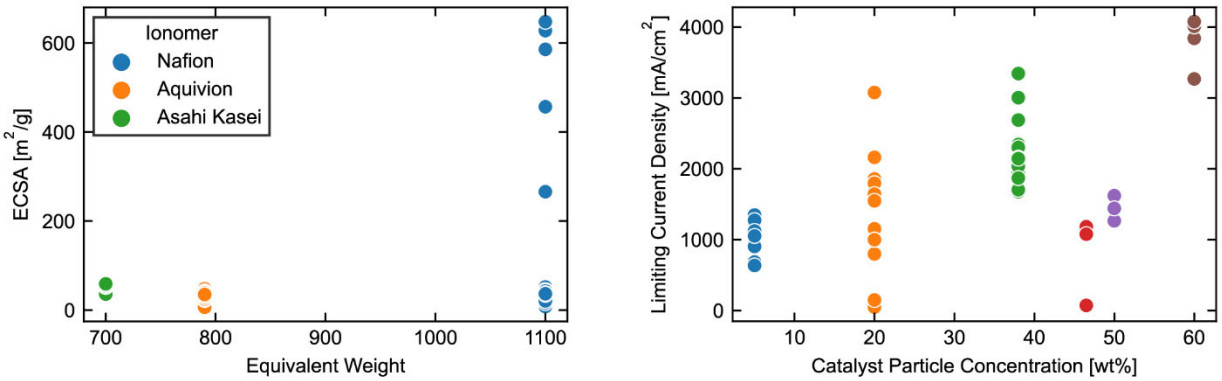

Figure S1.8. Example data showing how certain "continuous" variables are limited by commercial suppliers (evidenced by vertical lines at discreet points along the x-axis).

1.5.2 Statistical Modeling

Several modeling frameworks were considered for performing a statistical analysis of the catalyst ink data. These included purely statistical models, such as simple linear regression and regularization, as well "black-box" models, such as random forest regression and neural networks. By their nature, black-box models preclude any physical interpretation of the results, so they were not suitable for this work. Furthermore, the sample size (order of 50 to 100 data points) of the data sets being analyzed was not large enough to develop a sufficiently robust and generalizable complex regression model or black-box model without significantly bootstrapping or otherwise artificially augmenting the data. Therefore, univariate regression models were used to analyze the data. To preserve the effects of ionomer chemistry and carbon structure, the data were categorized by ionomer identity or carbon type, and a separate regression model was fit to each category (as seen in Figure 1.5 and Figure 1.6). Categories with five or fewer data points were also filtered out to avoid overfitting limited data. The data and analyses are intended to be a starting point from which more complex models can be created.

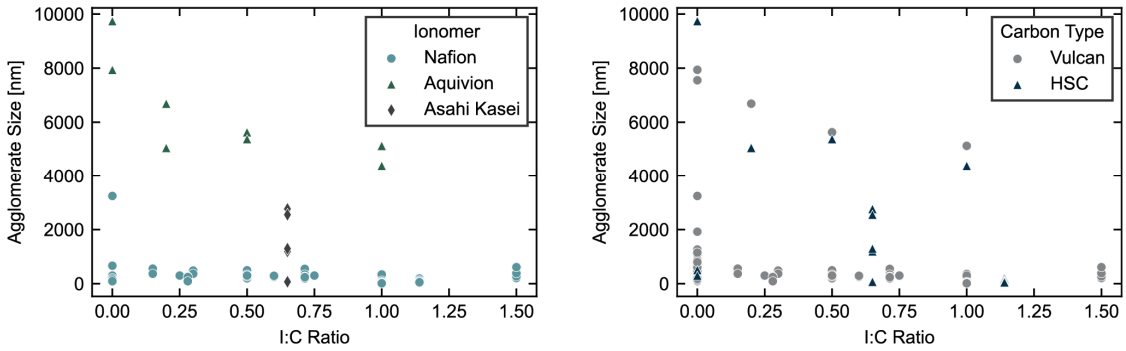

Figure S1.9. Data were categorized by ionomer identity and carbon type before fitting the regression models.

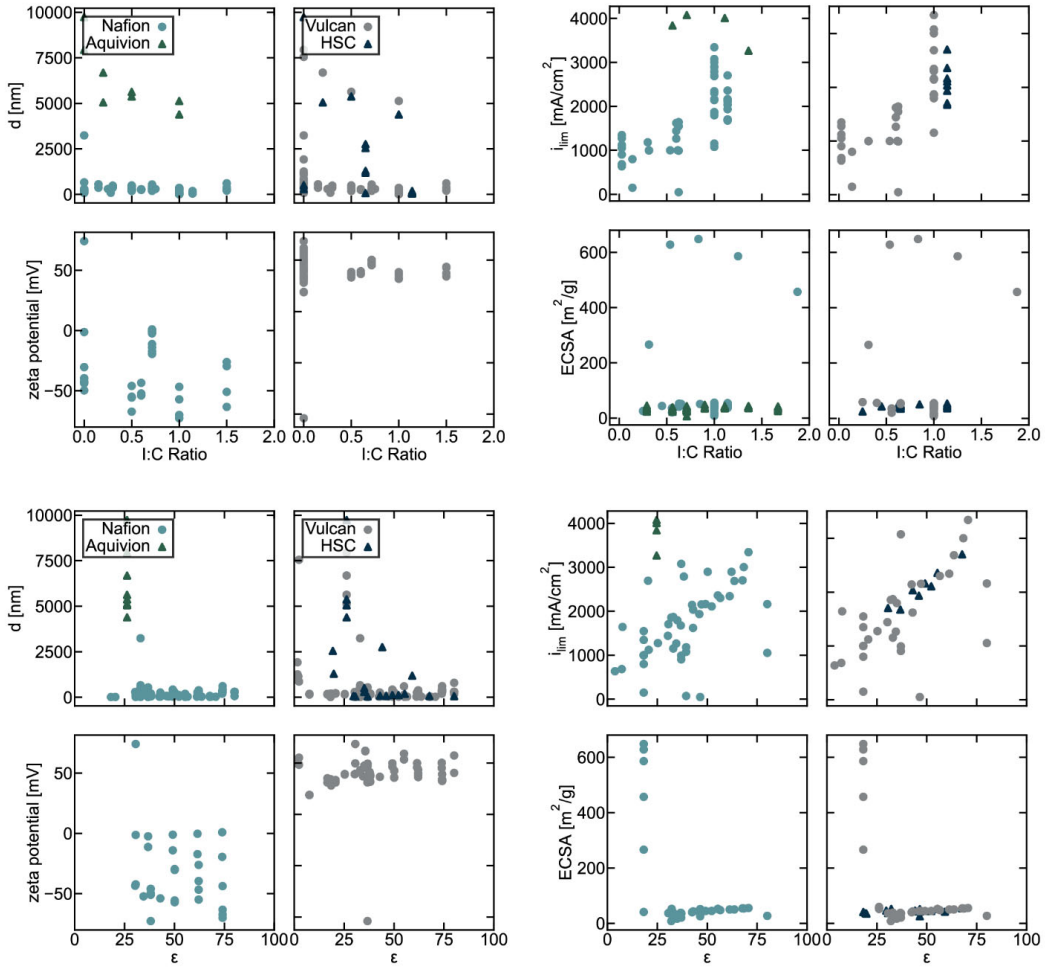

Figure S1.10. Categorized data sets before filtering for outliers.

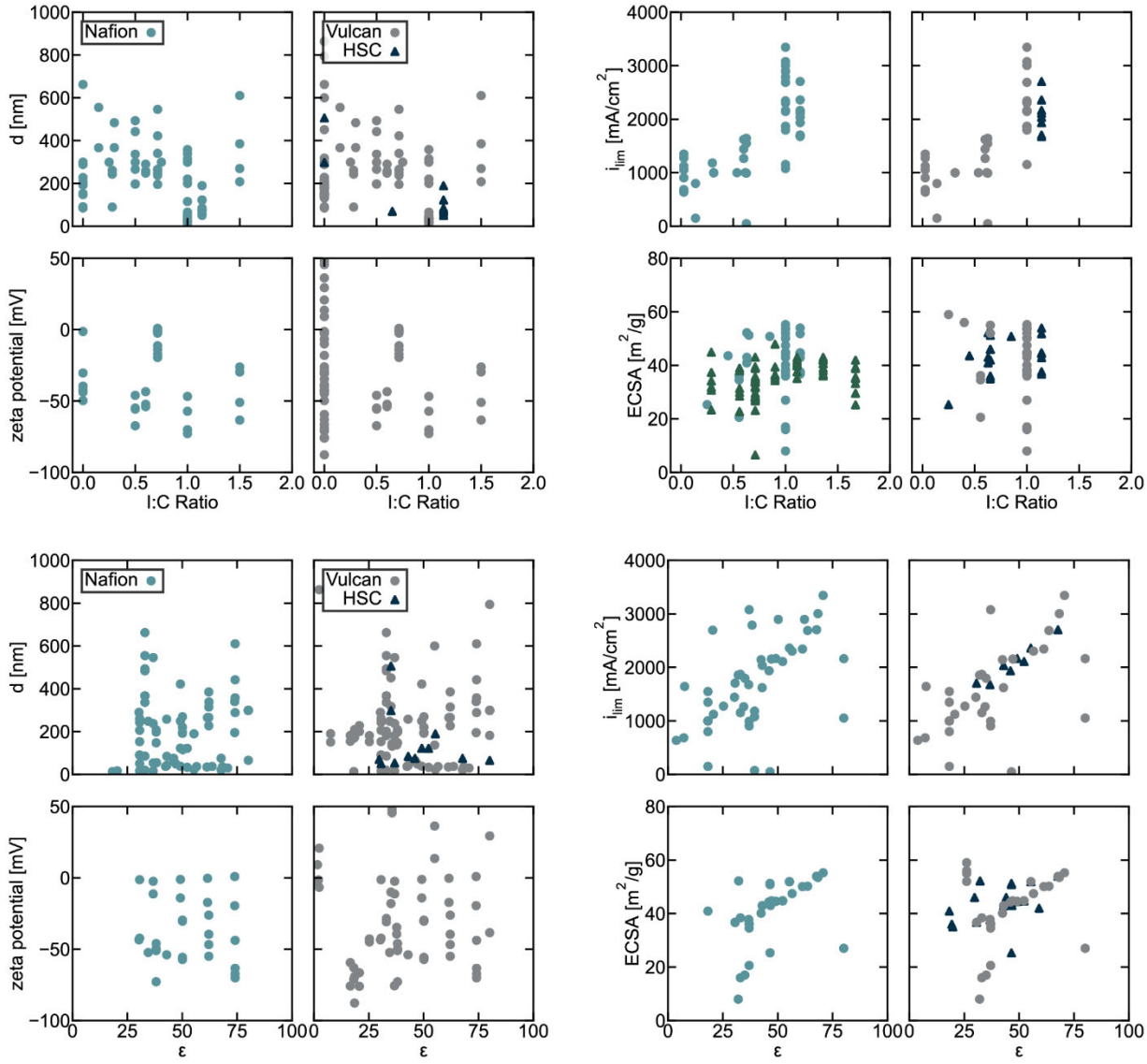

Figure S1.11. Final data sets used to fit the regression models.

2 Impact of Dispersion Solvent on Ionomer Thin Films and Membranes‡

2.1 Abstract

Perfluorosulfonic-acid (PFSA) ionomers are an important class of materials that many electrochemical devices rely on as their ion-conducting electrolyte. Often, PFSA films are prepared through solution-processing techniques. Previous research has demonstrated that the solvent environment affects PFSA dispersion conformation, but it is not clear to what extent (if at all) these conformational effects persist for thin films and membranes upon casting, nor how dispersion solvent impacts film formation during the drying process. Here, we explore these questions by systematically examining the effect of water and *n*-propanol mixtures on PFSA thin-film formation and structure, membrane structure, and resulting properties. Using a combination of *in situ*, time-resolved Grazing Incidence X-ray Scattering and tender Wide Angle X-ray Scattering, it is shown that films prepared from high-water-concentration dispersions exhibit stronger interactions and arrangement upon drying and possess larger network domain sizes than those prepared from low-water-concentration dispersions. These stronger interactions likely manifest in greater network connectivity as evidenced by enhanced conductivity for membranes and decreased water uptake for thin films. Significantly, these solvent-induced differences persist even after thermal annealing. It is clear dispersion solvent choice is a critical parameter controlling PFSA nano- and mesoscale structure and presents an important dial with which to tune PFSA macroscale properties.

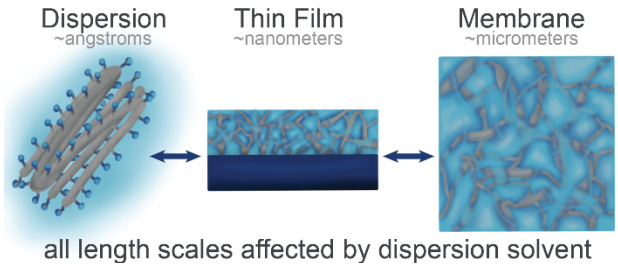

Figure 2.1. Schematic depicting a summary of Chapter 2: dispersion solvent affects the structure and properties of dispersions, thin films, and membranes.

2.2 Introduction

Despite the wealth of literature investigating perfluorosulfonic acid (PFSA, structure shown in Figure 1.4) membrane properties, the impact of solution processing on PFSA has received considerably less attention. Understanding how various solution parameters affect cast (dried)

‡ This chapter was previously published as "Berlinger, S. A.; Dudenas, P. J.; Bird, A.; Chen, X.; Freychet, G.; McCloskey, B. D.; Kusoglu, A.; Weber, A. Z., Impact of Dispersion Solvent on Ionomer Thin Films and Membranes. *ACS Applied Polymer Materials* **2020,** *2* (12), 5824-5834" and is adapted with permission from all co-authors.

PFSA films has significant implications for device performance, particularly as it relates to the catalyst layers (CLs). CLs are manufactured through solution-based colloidal slurry (ink) techniques, in which the ionomer and catalyst particles are dispersed in a solvent, and then cast and dried to form the resulting electrode.[27] The properties of the ink directly impact the CL; the strong effect of changing ink solvent on device performance has been demonstrated for proton-exchange-membrane (PEM) fuel-cell CLs.[12, 47, 50, 60, 72, 78-79, 88-93] These solvent effects are attributed to changing ionomer/catalyst particle interactions within the ink; ionomer aggregation behavior and coverage on the catalyst surface changes as a function of ink solvent.[88-89] Clearly, solvent impacts PFSA behavior. Additional ink-level studies have explored this phenomenon: solvent type alters ink properties, affecting important metrics such as aggregate size, zeta potential, and rheological behavior due to changing ionomer/solvent/particle interactions.[27, 67, 70, 94-95]

These studies are important steps toward understanding how solvent affects CL microstructure and performance. However, the multi-component interactions present within an ink are incredibly complex, and ink-level studies provide limited information as it pertains to the ionomer. For example, some unanswered questions are: How is the ionomer changing as a function of solvent, and why? How does solvent control film formation? How do these differences manifest upon casting? Many of the fundamental challenges in the CLs are associated with the ionomer/catalyst-particle interface. Elucidating how the ionomer is affected by solvent during the casting process is crucial to understand and control this interface. Additionally, beyond CLs, polymer-solution processing across all fields is becoming increasingly utilized due to the ease of manufacturing and scalability (especially with aqueous solvents).

Several studies have recognized the need to understand ionomer/solvent interactions and have focused on PFSA dispersion properties. In most solvent systems, PFSA can be thought of as a colloidal dispersion due to solvent/backbone incompatability.[37] A few PFSA chains will come together to form primary aggregates, the structure of which is dictated by the solvent environment. These primary aggregates (~angstroms to nanometers) determine the primary Nafion particle shape. These can then aggregate further into secondary aggregates (~100's of nanometers). In polar solvents, PFSA aggregates into rod-like structures, with radii on the order of tens of angstroms.[54-55, 96] Secondary aggregation modes then vary depending on solvent, even when considering only polar solvents. Small-angle neutron-scattering work revealed that water/alcohol mixtures yield very different ionomer secondary aggregate conformations (swollen particles) than alcohol alone (bundles), and solvents like N-Methyl-2-pyrrolidone produce a more classical random coil characterized by a radius of gyration.[37] Water/alcohol mixtures are particularly relevant for CL applications, and as such have been the focus of a few studies.[59-60, 67, 97-98] pH measurements suggest that as the proportion of water relative to alcohol increases, the ionomer sidechains extend into solution and the backbone clusters in the middle of the secondary aggregate much like a micellar structure,[67] as confirmed by molecular-dynamics simulations.[59] These pH measurements will be discussed at length in Chapter 3.

Other studies have focused on how solvent affects solution-cast PFSA membranes,[38, 99-102] and have shown that the degree of aggregation in the dispersion (due to the ionomer conformation that is affected by dielectric constant and solubility parameters)[100] impacts the membrane's structure, and the degree of phase separation when cast.[99] However, these studies rarely use industrially-

relevant solvents (water-alcohol mixtures are often preferred industrially due to ease of use, cost, and safety), and have little understanding about the mechanism of film formation or impact of solvent on thin films. Important recent work probes PFSA thin-film formation;[103] however, the effects of solvent remain unknown.

In this chapter, we systematically study the impact of dispersion solvent (varying water to alcohol ratios) on the *in situ* evolution of film morphology from dispersion to thin film via Grazing Incidence Small Angle X-ray Scattering (GISAXS). We extend this information across length scales, looking at the final structures of both thin films and membranes, and how these structures impact important metrics such as swelling/water uptake and ionic conductivity. Finally, we investigate whether these differences are retained after high-temperature processing. In this way, we correlate important structure-property-processing relationships that govern PFSA thin films and membranes.

2.3 Experimental Methods

2.3.1 Dispersions

All dispersions used in this study contained 4 wt.% Nafion (the prototypical PFSA) dispersed in varying ratios of water to *n*-propanol (*n*PA) ranging from 90 wt.% water to 30 wt.% water (balance *n*PA) except where noted. The dispersions were prepared by diluting stock 20 wt.% dispersion (D2021, equivalent weight 1100 g polymer/mol sulfonic-acid groups, with 46% water and 34% alcohols, Ion Power, Inc.) to the appropriate concentration using water and *n*PA, considering the native solvent in the stock dispersion. Upon dilution, dispersions were mechanically mixed and then sonicated for 30 minutes in a bath sonicator (Branson) equipped with a custom temperature control system to maintain room temperature. Dispersion rheology was measured using a 40 mm parallel plate geometry with an 800 μm gap on a Discovery Hybrid Rheometer 2 (TA Instruments).

2.3.2 Thin Films

In situ casting experiments of thin films were conducted at beamline 7.3.3 of the Advanced Light Source at Lawrence Berkeley National Laboratory as previously established.[103] Dispersions used here were prepared at 2 wt.% Nafion in an identical manner as described above. Dispersions were cast *in situ* using a custom-built mini slot-die printer.[104] After priming the line with solution, the films were cast from the slot-die head onto a silicon wafer with a head-substrate gap height of 200 μm and an injection rate of 5 μL/s, such that a similar volume of dispersion was dispensed for each sample. Silicon was chosen as a model substrate.[7] The print head was stationary while the substrate was translated underneath at a rate of 5 mm/s for the 90, 70, and 50% water dispersions and 2.5 mm/s for the 30% water dispersion. The X-ray energy was 10 keV (λ=1.24 A^{-1}) with a monochromator energy resolution E/ΔE of 100, and the patterns were acquired with a Dectris Pilatus 2M CCD area detector (172 μm x 172 μm pixel size) at a sample-to-detector distance of

2.515 m. GISAXS images were collected at grazing incidence angles (α_i) of 0.16° with 1 sec exposure under ambient atmosphere. Through-plane linecuts were averaged at q_p=0.3 ± 0.05 nm^{-1}, and horizontal linecuts were averaged at q_z=0.25 ± 0.05 nm^{-1}. Linecuts were fit to a core-shell model using the NCNR SANS Toolbox.[105] The Teubner-Strey model[106-107] was fit using scripts written in python, and error bars on the extracted parameters represent one standard deviation. Exposure times and total dose were selected to mitigate x-ray induced damage to the sample, while capturing the relevant drying dynamics.

Swelling (water-uptake) measurements were conducted on thin films. The thin films were prepared by spin casting the dispersions on silicon wafers (as in the casting experiments). The wafers were first cleaned with UV/ozone for twenty minutes to make them more hydrophilic prior to spin casting. Initial film thickness for all samples was measured with spectroscopic ellipsometry (J. A. Woollam alpha-SE) to be roughly 140 to 150 nm. Both annealed and unannealed samples were prepared. Annealed samples were placed in a 150°C vacuum oven for one hour before being removed. Unannealed samples were similarly dried in a vacuum oven for one hour, but at 30°C before being removed, and measured immediately for the swelling measurements. These measurements were conducted by monitoring the transient thickness as a function of relative humidity (RH) using a spectroscopic ellipsometer at an incident angle of 70°. The wave amplitude (Ψ) and phase shift (Δ) were measured over a spectral range of 400-900 nm and fit to a three-layer optical model (Si, native SiO_2, and Cauchy layer). The samples were exposed to nitrogen saturated at various RHs flowing at 500 cm^3/min: first with a conditioning cycle of 0 to 100 to 0% RH for 1 hour each at each step, then an absorption cycle of 10 to 100% RH, in increments of 10%, for a half hour each. Two of these absorption runs were measured for each sample to test repeatability. Data was averaged over multiple films. Swelling (ΔL) was determined by calculating the change in thickness at each RH step relative to the thickness at the end of the second 0% RH step in the conditioning cycle (L_0). To convert swelling data to water content (λ, moles of water per mole sulfonate groups), one-dimensional swelling was assumed (*i.e.* that the films swell only in the thickness direction because they are confined to the substrate)[108]; assuming no significant excess free volume or macroscale voids exist and additive partial molar volumes is valid[108-112] yields

$$\lambda = \frac{mol\ H_2O}{mol\ SO_3^-} = \frac{\Delta L}{L_0}\frac{\rho_W/MW_W}{\rho_N/EW} \tag{2.1}$$

where subscripts W and N denote water and Nafion, respectively, ρ is dry density, MW is molecular weight and EW is the equivalent weight of Nafion (here 1100 g polymer/mol sulfonic-acid groups). A dry density of 2.1 g/cm^3 was used for Nafion.[113-114]

2.3.3 Membranes

Membranes were fabricated from the same dispersions as described above. The dispersions were poured into custom-made glass wells such that the same mass of ionomer was added to each. They

were then heated at 35°C for 1 hour and annealed at 150°C for an additional hour, before slowly cooling back to room temperature overnight. They were then carefully removed from the glass, and the dry thickness of all membranes was measured at 16 +/- 2 μm with a thickness gauge (Heidenhain). Separate membranes were measured with tender x-ray scattering to quantify structure, and to measure water uptake and conductivity. For the property measurements, the membranes were cut in half: one portion was stored in air for water-uptake measurements, and the other was immersed in MilliQ (18 MΩ de-ionized) water to equilibrate for liquid-water conductivity measurements.

Sulfur K-edge scattering measurements were performed at the Soft Matter Interfaces (SMI, Beamline 12-ID) at the National Synchrotron Light Source II.[115] Samples were measured in transmission mounted perpendicular to the beam. X-ray scattering patterns were recorded on a Pilatus 300K-W detector, consisting of 0.172 mm square pixels in a 1475 × 195 array, mounted at a fixed distance of 0.275 m from the sample position. To cover the range of scattering angles desired, the vertically oriented elongated detector was moved horizontally on a fixed arc, from 0 to 26 degrees with 6.5 deg steps. Scattering patterns, recorded in-vacuum, were measured at 2542 eV. Images were later visualized in Xi-CAM software[116] and stitched using custom python code. The spot size at the sample was 20 μm by 200 μm.

Membrane water uptake as a function of RH was measured with a dynamic vapor-sorption (DVS) analyzer (Surface Measurement Systems, UK) at 25°C.[117-118] The samples were first dried at 25°C and 0% RH for 2 hours to determine the dry mass of the membrane M_0. The water uptake (ΔM_W) was then continuously measured as RH increased from 0 to 98% with a 10% RH interval using a pre-humidified nitrogen feed. Membranes were equilibrated at each RH step until the mass change with respect to the initial mass ($\frac{\Delta M_W}{M_0}$) had less than 0.005% change per minute. The water content was calculated from the water uptake according to

$$\lambda = \frac{\Delta M_W / MW_W}{M_0 / EW} \tag{2.2}$$

The residual water (λ_{res}) present in the membrane at 25°C and 0% RH was calculated in the same way, by comparing the mass change after 2 hours at 120°C relative to the initial mass at 25°C.

Membranes used for the conductivity measurements were equilibrated in DI-water for 24 hours before their wet thickness and width were measured. The resistance of the membranes was then measured using a four-point probe (BekkTech) and potentiostat (BioLogic) to sweep the voltage from −0.1 to 0.1 V and record the current as described previously.[119] Conductivity was calculated from the resistance measurement using the dimensions of the cross-sectional area of the membrane and the spacing between the electrodes. Four different membranes for each solvent ratio were measured.

2.4 Results & Discussion

2.4.1 Structure

2.4.1.1 Thin-Film Evolution

To understand the effect of dispersion solvent on film formation, structure, and properties across length scales, four different ratios of water:*n*-propanol (*n*PA) are used throughout this study. All samples are made from Nafion (a prototypical PFSA) dispersions that have a solvent composition of 90:10, 70:30, 50:50, or 30:70 all given as wt.% water:wt.% *n*PA and hereafter referred to as 90, 70, 50, and 30% water samples, respectively. The thin-film morphological formation investigations were accomplished by *in situ* GISAXS experiments, in which the Nafion dispersion is cast onto a silicon substrate via a slot-die printer and the structure monitored with time.

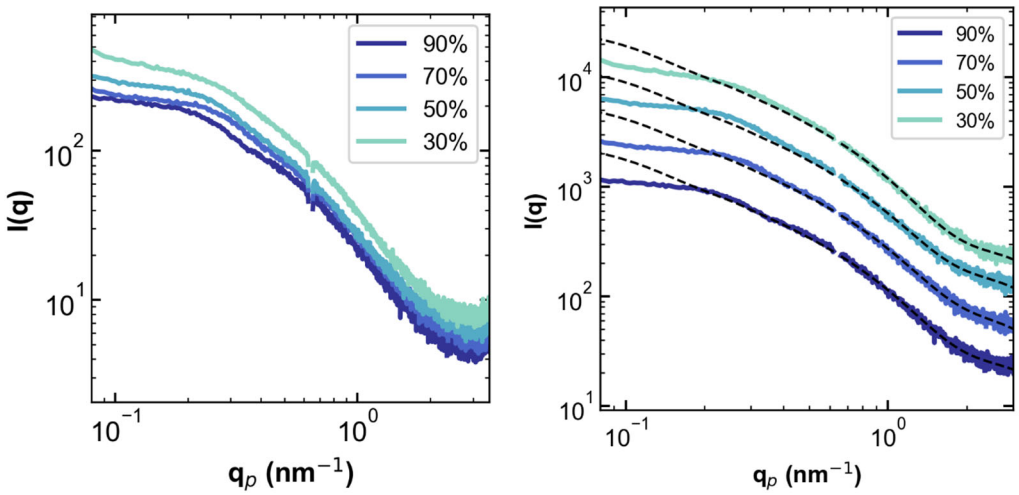

Figure 2.2. Left: In-plane linecuts describing intensity (I) as a function of the scattering vector (q_p) obtained from *in situ* GISAXS experiments of the dispersions immediately upon casting. Right: Same data on the left, with dashed lines showing the core-shell form factor fit to the data. Lines are offset from one another for clarity. Labels describe the weight percentage of water that makes up the dispersion solvent composition (the balance is *n*-propanol).

The left panel of Figure 2.2 shows the initial horizontal intensity linecuts obtained immediately after printing the dispersions, plotted versus the in-plane scattering vector (q_p). Similar results were obtained for the through-plane scattering and are shown in Figure S2.12 in Section 2.6. Previous work showed that the primary particle adopts a rod-like conformation in similar solvents.[96, 103] Using the same modeling/analysis approach, these initial linecuts are fit to a cylindrical core-shell form factor in the high-q region ($q_p > 0.7$ nm^{-1}), where the structure factor is expected to approach

one. The form-factor fit is shown on the right in Figure 2.2 with excellent agreement (fit parameters are shown in Table S2.2 in Section 2.6). The core-shell form factor is not expected to change much with drying (*i.e.* the primary particle should remain intact due to the highly hydrophobic PTFE core) and the form factor is therefore held constant during subsequent analysis. Changes in the core-shell length may occur, but the form factor is relatively insensitive to length in this q-range.

There are small differences in the shell thickness with water:*n*PA ratio, but this change is mostly within error of the fit (Figure S2.13 in Section 2.6). To further reduce the error and determine a clear trend in shell thickness with water:*n*PA ratio, wide-angle x-ray scattering would need to be done to access q = 4-10 nm^{-1}. Greater differences in the scattering for each of the samples is observed at lower q. The upturn in intensity at $q_p < 0.1$ nm^{-1} varies between water:*n*PA ratios, and indicates differences in the formation of larger length scale secondary aggregates of Nafion in all dispersions, as suggested by many previous studies.[37, 67] Between $q_p = 0.1$ and 0.7 nm^{-1}, differences in the scattering suggest differences in intermediate length scale aggregation and the structure factor.

These initial linecuts can be divided by the form factor to generate an effective structure factor. The scattering intensity is proportional the electron density contrast, $\Delta\rho$, the structure factor, *S(q),* and the form factor intensity, *P(q):*

$$I(q) \propto \Delta\rho^2 P(q) S(q) \tag{2.3}$$

where

$$P(q) = \langle |F(q)|^2 \rangle \tag{2.4}$$

We define the effective structure factor, $S_{eff}(q)$, as the observed scattering intensity divided by P(q)

$$S_{eff}(q) = \frac{I_{obs}(q)}{P(q)} \tag{2.5}$$

We call it an effective structure factor because it is not known *a priori*, but instead is derived from scattering. Initial structure factors for all solvent ratios are shown in Figure S2.14 in Section 2.6. The primary structure-factor peak around 0.3-0.4 nm^{-1} is evident for all dispersions. This same calculation is performed for the rest of the time-resolved data: S_{eff} is analyzed at all time points during the drying process. The intensity of the in-plane and through-plane structure factor peaks is shown in Figure 2.3 as a function of time during the initial portion of the drying process.

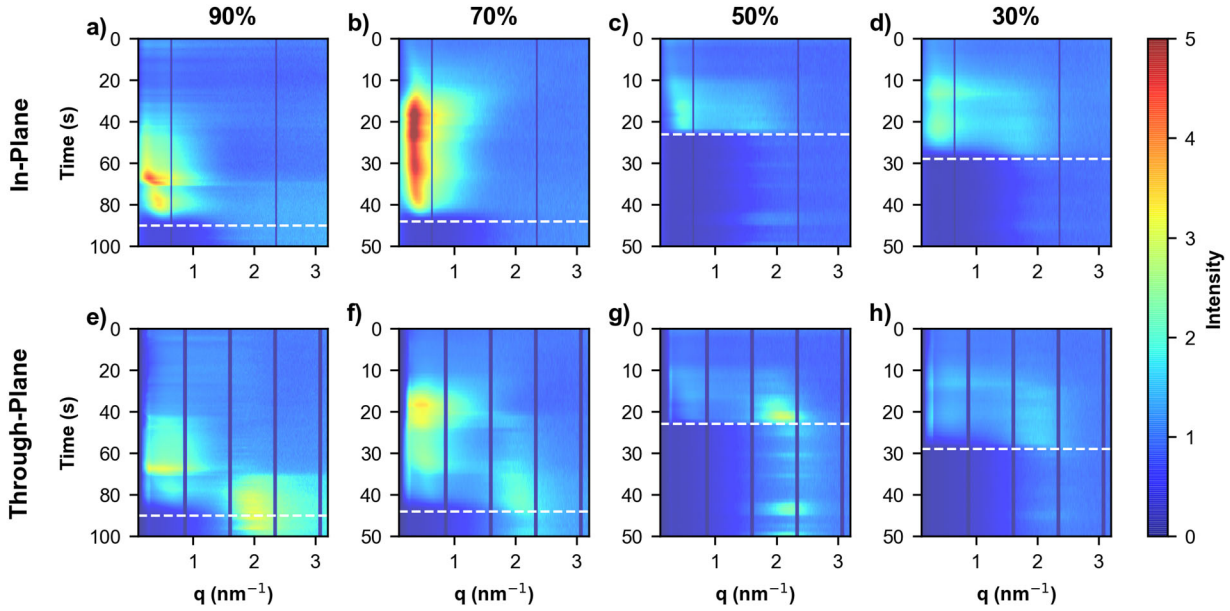

Figure 2.3. Effective structure factor (Seff) time evolution of the sol-gel transformation both (a)-(d) in-plane and (e)-(h) through-plane for the dispersions after casting for dispersion solvents containing (a, e) 90%, (b, f) 70%, (c, g) 50%, and (d, h) 30% water (balance *n*PA). Note the 90% sample has a different y-scale. Dashed white line indicates gel formation.

As shown in previous work, the first portion of the drying process is a solution-to-gel transformation.[103] Gelation is evidenced by the collapse of the primary structure factor peak around 0.3-0.4 nm^{-1} (noted by a lack of contrast) and is indicated by a dashed white line on each heat map in Figure 2.3. Immediately obvious is the fact that the high-water-concentration dispersions (HWD, 90% and 70%) take longer to form and dry than the low-water-concentration dispersions (LWD, 50% and 30%). The solution-to-gel transformation was determined for each water concentration as the time at which the following linecut does not change in this q-range. The primary structure-factor peak describes how the dispersion particles (both primary and secondary aggregates) are arranged in solution relative to one another.[103] As the dispersion gels, the particles begin to coalesce and the primary peak moves to higher q. As gelation completes, the main structure factor peak disappears.[103] The much longer drying time for the HWD as compared with the LWD is expected when considering the relative volatility of water and *n*PA.

Another qualitative observation can be made about the intensity of the structure factor peaks: the primary structure-factor evolution is much stronger for the HWD than the LWD. This increased intensity indicates a greater regularity to the arrangement of aggregates in solution, and stronger interaction between the aggregates. These Nafion/Nafion interactions were probed *ex situ* using rheology as shown in Figure 2.4, where the relative viscosity (measured viscosity of the dispersion

divided by the viscosity of the solvent) at the same shear rate that the dispersions were cast with the slot-die coater (see Figure S2.16 for the full measured viscosity range and shear-rate calculations). Figure 2.4 displays an increase in relative viscosity with dispersion water concentration. Generally, increased viscosity and non-Newtonian behavior indicates stronger polymer/polymer interactions;[120] the HWD exhibit greater degrees of shear-thinning than the LWD (as seen in Figure S2.16). Here, these stronger interactions are likely electrostatic in nature due to higher Nafion acidity in water-rich dispersions (as discussed in Chapter 3)[67] and longer electrostatic correlation lengths. Another reason for increased viscosity could be smaller particle sizes (since the dispersions all possess the same polymer concentration, this would cause a relative increase in volume fraction).[120] Smaller particles (less secondary aggregation) could also be a result of the greater electrostatic repulsion experienced by water-rich dispersions as compared with *n*-propanol-rich ones. While particle size versus particle/particle interaction contributions to the viscosity cannot be explicitly deconvoluted by this experiment, these results help explain the stronger structure factor peak in the HWD: increased interaction between particles enhances ordering.

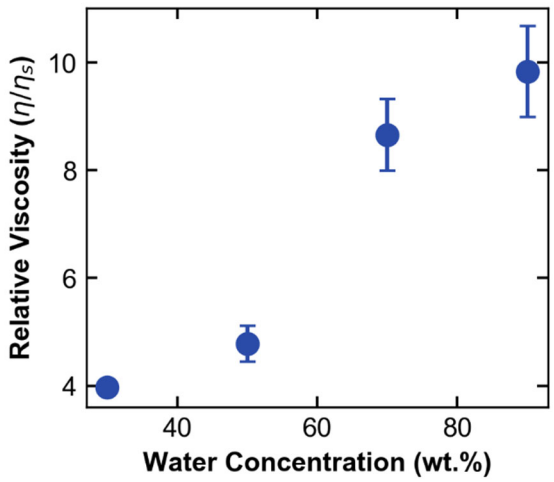

Figure 2.4. Measured viscosity of 4 wt. % Nafion dispersions (η) divided by the pure solvent viscosity (η_s) as a function of the water concentration in the dispersion (balance *n*-propanol) at ~12 Hz (the shear rate used to print the films for the *in situ* casting experiments).

We have so far discussed the primary structure-factor peak, but there is also a secondary structure-factor peak around 2 nm^{-1} corresponding to correlation lengths of 3 to 4 nm. This secondary structure-factor peak most likely describes the secondary aggregates in the system.[103] A further discussion of the assignment of structure factor peaks is presented in Section 2.6. Notably, this secondary structure-factor peak is absent at short drying times for the HWD through-plane, and does not appear in-plane, as opposed to the LWD, for which this secondary aggregate peak is present in both directions for a much longer portion of the drying time. When considering charged

particle aggregation theories, primary aggregates are stable (and do not become secondary aggregates) when there is sufficient electrostatic/coulombic repulsion to keep them apart. It is expected that the HWD would experience greater electrostatic repulsion, and therefore have a larger energy barrier to overcome in order to form secondary aggregates. The HWD display more acidic[67] (more charged) conformations, and the increased dielectric constant of the solvent media would similarly increase the magnitude of electrostatic repulsion experienced by the aggregates. Additionally, the smaller particle size as suggested by the viscosity measurements further indicate that the HWD have trouble forming secondary aggregates initially. However, as the solvent evaporates, Nafion concentration increases. This increases the relative ionic strength of the system, and therefore decreases the electrostatic repulsion and accordingly the height of the energy barrier, thus explaining why the secondary structure-factor peak does not appear until later times for the HWD.

Following the solution-to-gel transformation, Nafion particles continue to coalesce as solvent evaporates.[103] In the gel state, the secondary structure-factor peak collapses into the well-known ionomer peak.[103] Here, as the gel continues to dry, there are some oscillations in intensity, which may be due to heterogeneous drying (*i.e.* coffee-ring effect), or re-entrant solvent from the static headspace above the film. We can further explore the film-formation evolution from gel to final film by fitting the through-plane ionomer peak via the Teubner-Strey model to understand how the bicontinuous structure changes.[106-107] The ionomer peak is anisotropic; in-plane the intensity is very weak and does not exhibit the same dynamics observed through-plane (to see full GISAXS patterns please refer to Figure S2.15 in Section 2.6). Thus, only the through-plane data is analyzed. Figure S2.17 plots extracted parameters for the Teubner-Strey model as a function of time for a water:*n*PA ratio dispersions, which are related to the hydrophilic domain spacing (κ^{-1}), correlation length of the domains (ξ), volume fractions, and scattering length contrast. Similar as to in the solution state, kinetics in the gel state proceed on a timescale related to the ratio of water to *n*PA. The LWD quickly approach their final domain spacing, and dry to the point at which no ionomer peak is visible (as evidenced by the large error bars to the later portion of each fit in Figure S2.17). For HWD samples, the drying kinetics are slower, and the ionomer peak more slowly approaches its final values. Equilibration times for the Teubner-Strey fitting parameters (κ and ξ) are plotted in Figure 2.5 and show an increase in equilibration time with increasing water concentration.

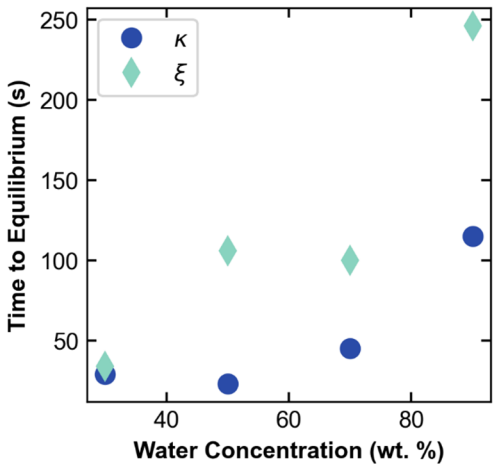

Figure 2.5. Tuebner-Strey fitting parameter apparent time to equilibrium versus weight percentage of water (the balance is *n*-propanol). κ^{-1} is the hydrophilic domain spacing and ξ represents the correlation between the domains.

At t = 200 s, the LWD were completely formed into a thin film, as demonstrated by the complete collapse of the ionomer peak (expected at~0.2 nm^{-1}) due to lack of contrast within the ionomer (see Figure 2.6). The films made from HWD, meanwhile, still exhibit a weak ionomer peak, indicating that some residual solvent remains. The 90% sample was measured out to 300 s with slight change in the ionomer peak. While the values have reached equilibrium values, residual solvent persists beyond the timescale of the experiment (see Figure S2.17 in Section 2.6). Further drying beyond this is expected to cause a similar complete ionomer peak collapse. Similarly, ξ in Figure 2.5 may continue to decay to its final value very slowly, but that is beyond the timescale of these experiments. Final film thicknesses are shown in Table 2.1.

Table 2.1. Final film thicknesses of the dried films from the casting experiments as measured by ellipsometry. At least 7 points are averaged over the width of the film.

	30%	**50%**	**70%**	**90%**
Thickness (nm)	93 ± 32	84 ± 16	107 ± 20	159 ± 71

At the above hard x-ray energy, absorbed water is needed to provide a contrast mechanism, and so differences in the final unhydrated structure cannot be probed. For this reason, the membrane structure experiments were performed at an energy near the sulfur K-edge to increase the electronic density contrast.

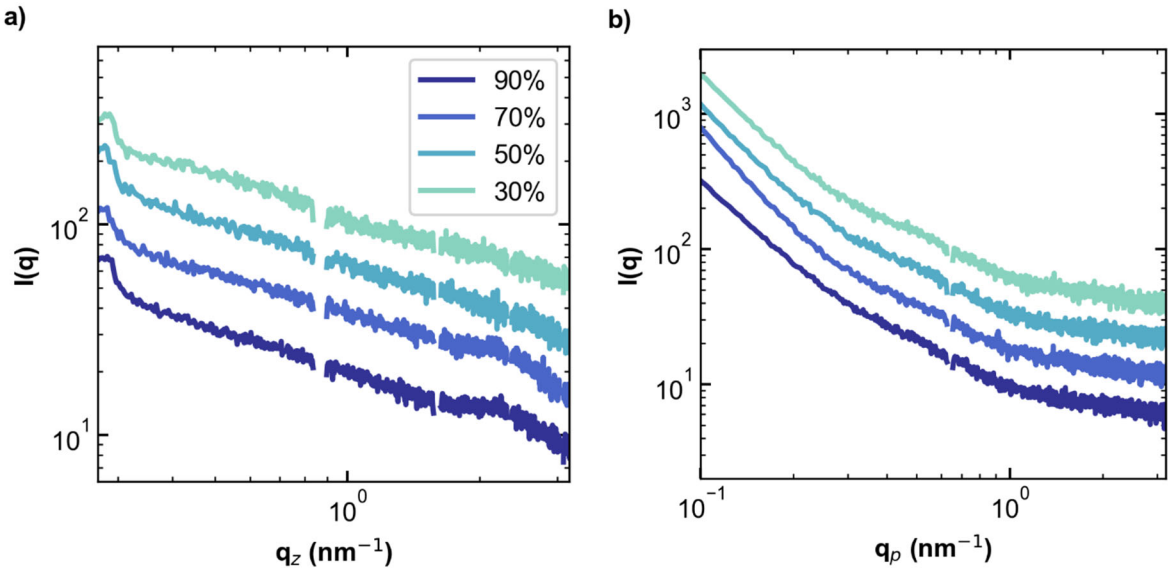

Figure 2.6. (a) Through-plane and (b) in-plane linecuts (offset for visual clarity) taken at the conclusion of film formation showing intensity (I) as a function of the scattering vector (q). Labels describe the weight percentage of water that makes up the dispersion solvent composition (the balance is *n*-propanol) from which these films were cast.

2.4.1.2 Annealed Membranes

To explore the effect of water:*n*PA ratio on membrane structure, membranes were prepared via solution-casting of dispersions containing the same solvent ratios as above. Because unannealed solution-cast membranes are extremely brittle[101-102, 121] (free-standing films are very difficult to isolate), and may not be fully formed, they lack application relevance. Therefore, these membranes were annealed at 150°C for one hour following drying as the thermal annealing process is known to improve the membranes' mechanical properties. This improvement is hypothesized to be because of an increase in chain entanglements when Nafion is raised above its α-transition temperature.[102]

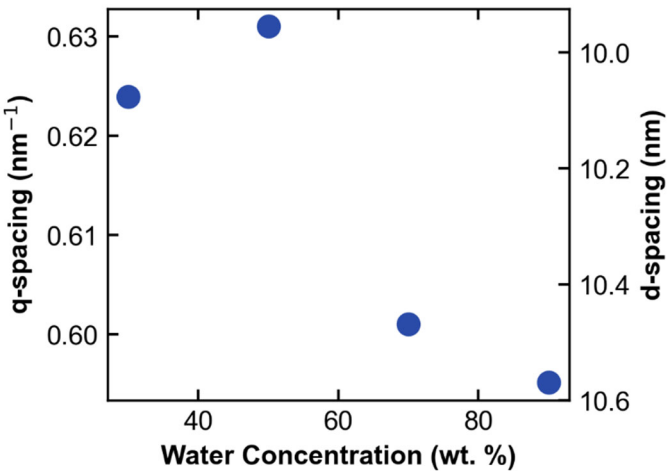

Figure 2.7. Inter-crystalline peak position (in reciprocal and real space) of the membranes as a function of the dispersion water concentration (balance *n*-propanol) at 2452 eV. Error bars are smaller than data points.

Annealed membranes were characterized using tender Wide-Angle X-ray Scattering (WAXS) at 2542 eV, to enhance scattering contrast in the film. These membranes were shot in vacuum, and while visible, the ionomer peak is very weak and does not display significant differences between samples. Interestingly, the inter-crystalline peak is quite strong at these energies. The inter-crystalline peak is indicative of how primary and secondary aggregates from solution have collapsed and arranged in the annealed film; the primary structure factor peak collapses into the inter-crystalline peak. Thus, it is representative of the network-like structure of the film. Figure 2.7 shows both the domain spacing (d-spacing, real space) and q-spacing (reciprocal space) as a function of dispersion water concentration from which the membranes were cast. The radially integrated scattering showing the inter-crystalline peak are shown in Figure S2.18 in Section 2.6. There are clear differences between the water concentrations: membranes made from HWD exhibit a larger characteristic network size than those made from LWD. This suggests that the mesh size of the backbone network (and correspondingly the hydrophilic domain network) is larger for membranes made from HWD. While these differences are small, these domain spacing changes will likely be magnified upon hydration and will impact the transport properties of the membrane. Importantly, this difference due to dispersion provenance is present post-annealing in vacuum, when there is no residual solvent left. Thus, the changes in dispersion aggregation and film formation persist with thermal annealing and impact membrane and thin-film morphology at all length scales (see Figure 2.8).

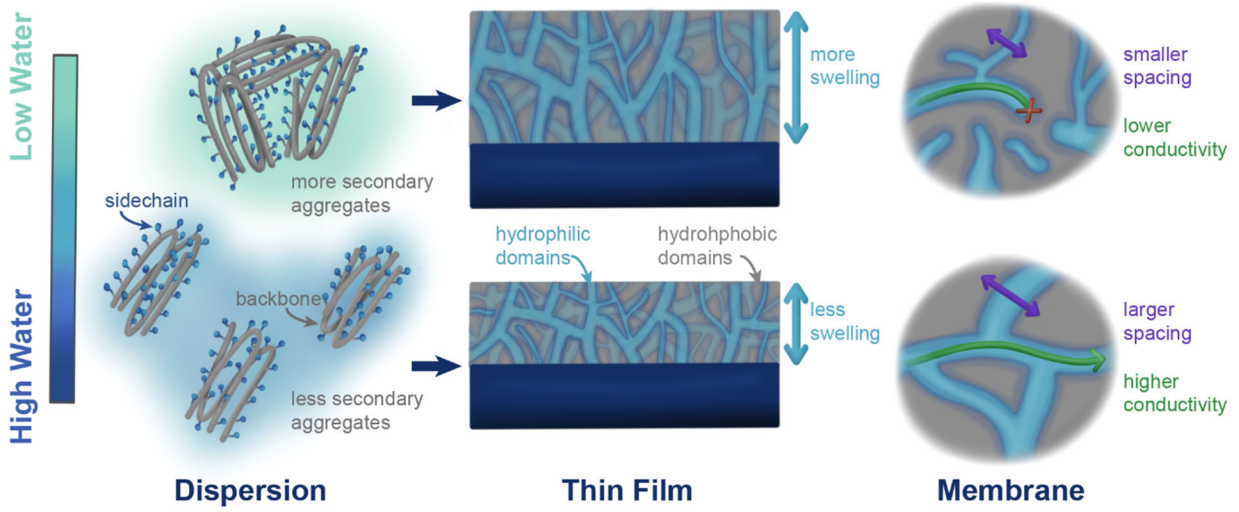

Figure 2.8. Proposed schematic depicting conclusions of data for dispersion aggregation, thin films, and membranes for high- and low-water concentrations. Features are not drawn to scale. Membrane diagram zooms into possible nanoscale/mesoscale structure (not meant to depict the entire membrane).

2.4.2 Properties

It is important to understand how these different thin-film and membrane structures affect application-relevant properties: the transport and mechanical properties in PFSAs are a function of their hydration, making water content the most critical parameter.[7]

2.4.2.1 Thin Films

For thin films, water uptake (or swelling) is measured using spectroscopic ellipsometry as a function of RH as shown in Figure 2.9. We investigate the impact of dispersion water:*n*PA ratio on both unannealed films (like those that were explored in the casting experiments above) as well as thin films of the same thickness that have been annealed at 150°C for one hour (the same annealing procedure used throughout this study for membranes).

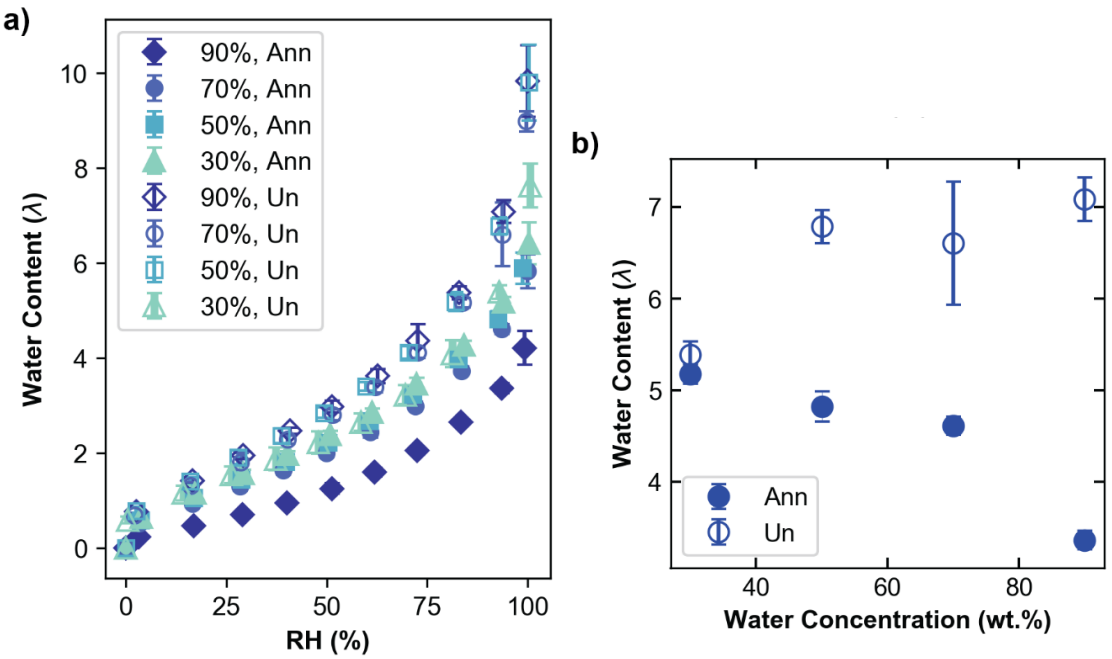

Figure 2.9. Thin-film (~145 nm thick on silicon) swelling measurements displaying water content (λ, mol water/mol SO_3^-) (a) as a function of relative humidity (RH). Labels describe the weight percentage of water that makes up the dispersion solvent composition (the balance is *n*-propanol) from which these films were cast. (b) Shows the swelling at 90% RH as a function of the dispersion solvent. Closed symbols (●) denote annealed (Ann) films, and open symbols (○) denote unannealed (Un) films.

As Figure 2.9 displays, more water is absorbed by unannealed samples than annealed samples. This observation is supported by previous studies comparing unannealed and annealed Nafion thin films.[108] However, for unannealed films, the differences among the films made from HWD is almost nonexistent; only the film made from the 30% dispersion has a noticeable difference in swelling. Previous work has shown that unannealed membranes dissolve in the presence of polar solvents.[101] It is possible that because these films are unannealed they revert to a pseudo-gel state at high hydration that is similar for all of them. These films are first exposed to 100% RH as a conditioning step and it is possible that this conditioning step wipes out differences in the original structure as they all swell with water, thus explaining why all but the 30% film (which would have the most different initial structure from a film cast from only water) possess similar swelling behavior upon RH cycling.

As opposed to the unannealed films, the annealed films do exhibit a trend with swelling as a function of the dispersion water concentration: swelling decreases as the water concentration in the dispersion the films were cast from increases. This trend suggests perhaps that the films have better chain entanglement, possibly due to the smaller secondary aggregates and a more regular arrangement of aggregates (as indicated by the stronger primary structure-factor peak) in the

dispersion as the film forms. This morphology may lead to a more cohesive network, restricting swelling.[122]

2.4.2.2 Membranes

As with the thin films, membrane water uptake was measured as shown in Figure 2.10. Unlike for the annealed thin films, the annealed membranes do not show a strong trend as a function of dispersion water concentration; perhaps the 90% film absorbs more water, but not significantly. Additional confinement effects experienced by the thin films may explain the difference in trend exhibited by the thin films versus the membranes. Confinement suppresses the water uptake in thin films to a regime that is comparable to the primary hydration of a membrane.[7, 108] For a fair comparison with thin-film hydration, the membrane residual water content is measured at 0% RH to determine the amount of water molecules strongly bound to the ionic groups in the primary solvation regime. Interestingly, the residual water in these membranes exhibits the same trend as the thin-film swelling: decreasing with increasing dispersion water concentration (see Figure S2.19 in Section 2.6). This suggests nanoscale changes in sidechain solvation and local water environment as dispersion water concentration varies. Thus, while dispersion effects are dominant in the entire hydration range for thin films, they are present mostly in the primary hydration environment for membranes (and hence justifies the dry-scattering exploration conducted above).

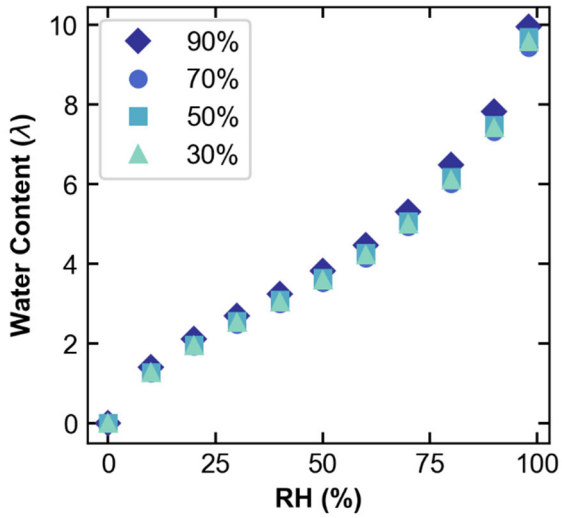

Figure 2.10. Membrane swelling measurements displaying water content (λ, mol water/mol SO_3^-) as a function of relative humidity (RH). Labels describe the weight percentage of water that makes up the dispersion solvent composition (the balance is *n*-propanol) from which these films were cast. Error bars are smaller than data points.

While we do know that the mesh size of the network is different among these membranes as evidenced in Figure 2.7, we cannot probe the network connectivity/tortuosity in scattering experiments. One way we can probe connectivity, however, is by measuring membrane conductivity; previous work has shown directly that conductivity (a macroscale property) is controlled by nano- and mesoscale properties like solvation and network connectivity, respectively.[123] The results of in-plane membrane conductivity in DI water are given in Figure 2.11. The measured conductivities fall in the expected range considering values exhibited by commercial Nafion and other solvent-cast Nafion systems.[7, 38, 100] Membrane conductivity increases with increasing dispersion water concentration, with a peak conductivity in the 70% sample. Why the 70% membrane possesses the highest conductivity is not immediately obvious. However, it likely is a result of a balance between the more swollen dispersion conformations produced by mixed water/propanol solvents,[37] and the enhanced ordering exhibited by the HWD. Additional work to determine this is required. Regardless, the membranes produced from the HWD clearly show enhanced conductivities over those prepared from the LWD, despite possessing similar water contents (see Figure 2.10). The conductivity data therefore suggests that the network organization is different (and better) in the membranes made from the HWD, particularly because water volume fraction is the same with changing conductivity. This demonstrates that the connectivity effects seen in the annealed thin films are also present the in membranes.

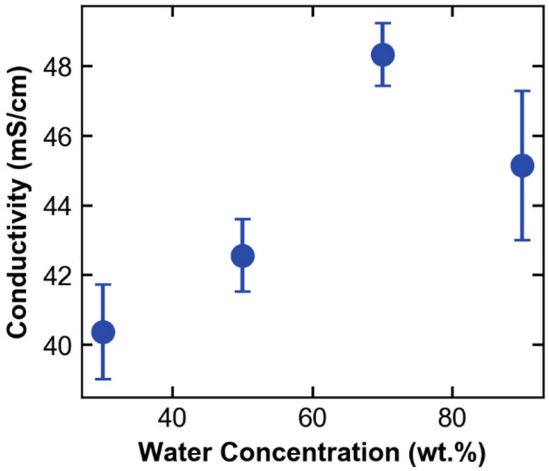

Figure 2.11. In-plane conductivity of membranes prepared from dispersions of varying water concentration (balance *n*-propanol).

2.4.3 Structure-Property Implications

Figure 2.8 schematically interprets the above data. The dispersion aggregation behavior changes as a function of water concentration, which affects how the films coalesce and the resultant nanoscale structure that in turn impacts macroscopic, observable properties.

The interactions between Nafion aggregates and the regularity of their ordering increases as water concentration in the dispersion increases. Furthermore, the equilibrium time to gelation and final formed film increases with increasing water concentration. However, it should be noted that there will be preferential *n*PA evaporation, and that the water:*n*PA ratio changes during the drying process.[102] Despite this, it is clear that the initial dispersion concentrations are deterministic of the film-formation process: timescales do not scale linearly with water concentration, and the intensities of the structure factor peaks are different across the four solvent ratios. Data cannot simply be normalized to water concentration and correlated with evaporation rate. These dispersion aggregation ordering differences are clearly translated to the membrane: changes in inter-crystalline peak position reflect the primary structure factor peak in solution.

Upon annealing, thin films cast from the HWD exhibit less swelling, and membranes exhibit a larger spacing between backbone regions. Despite this larger spacing, membranes show the same water content, suggesting better network connectivity/aggregate packing, perhaps due to the greater regularity of aggregates as the film forms. It is unclear how the varying water:*n*PA ratio affects the durability and mechanical properties of the ionomer, but from a transport-property perspective, the HWD films are preferable (although the longer equilibration time required for film formation may not be desirable at manufacturing scales).

Understanding specifically what is happening during the annealing process requires further investigation. It is believed that raising the membranes above their α-transition temperature disentangles the ionic domains and allows for rearrangement of the ionic network.[7] However, the backbone crystallite regions should remain relatively unaffected; it has been demonstrated there is little change with crystallinity at these temperatures (although there can be significant change at much higher temperatures).[124] Given this and the above data, it seems that the thermal annealing process here preserves the backbone domains and aggregate structures that coalesce during film formation. While the ionic domains can reorient and increase chain entanglement, meso- and macroscale changes to the network structure seem unlikely.

Therefore, annealing locks in the differences in film formation caused by the varying solvent composition in the dispersion, while the unannealed films can possibly eliminate their solvent history upon sufficient cycling in pure solvents (based on the swelling data from the unannealed films). Both findings have interesting implications for CLs in PEM fuel cells, electrolyzers, and similar devices. These CLs are created through different fabrication processes. Gas-diffusion electrodes (where the CL is deposited onto the diffusion media) and decal transfers are often hot pressed to the membrane at elevated temperatures to form a membrane-electrode assembly with minimized ohmic losses. Catalyst-coated membranes (in which the CL is deposited directly onto the membrane) on the other hand are often not hot pressed. Based on these findings, the differences between these two processes may further be compounded by the high-temperature treatment step:

hot-pressed samples may retain dispersion solvent differences, while samples that were not hot pressed may not. Furthermore, these devices often go through a temperature/RH/voltage break-in protocol before initial operation to condition the electrodes. Particularly for electrodes that have not been subjected to elevated temperatures, the ionomer swelling/reorganization during this break-in cycle is critical and may help explain some of the changes observed during break-in.

However, even post break-in, the effects of dispersion solvent are likely to remain whether the CL was hot-pressed or not. These films form quite differently, and likely will impact (and be impacted by) how the catalyst particles agglomerate. One could imagine the greater density of secondary aggregates in low-water-concentration inks affects how agglomerates of particles forms as compared to the lower density of aggregates in high-water-concentration inks. Indeed, ink-level studies have shown that water concentration changes catalyst/ionomer aggregation behavior,[88] and that low-water-concentration inks are less sensitive to ionomer content than high-water-concentration inks are (as shown in Chapter 3 and 5),[67] thereby suggesting that the changing ionomer/solvent interaction drives differing aggregation modes. Therefore, even though after RH cycling the unannealed thin films may behave similarly, large-scale catalyst particle reorganization is unlikely: the impact of solvent during CL formation will still be critical in controlling device performance.

2.5 Summary

In this study, the effects of solvent composition on PFSA states (dispersion, thin film, membrane) were examined. It was shown how dispersion solvent effects persist across the various states, length scales, and even annealing conditions. Specifically, we investigated the impact of water:*n*PA ratio on how thin films form from dispersions using time-resolved GISAXS, extended this understanding to probe structure in membranes with WAXS at tender X-ray energies, and then investigated the impact of these structures on thin-film swelling (of both annealed and unannealed films) and membrane swelling and conductivity. Notably, the dispersion water:*n*PA ratio altered how the films form by changing the timescale for the formation process, the strength of interactions of the dispersion aggregates, and how these aggregates come together within the film network. Membranes also demonstrated evidence of the impact of solvent: changing network spacing as a function of the solvent from which the membranes were cast. Furthermore, thin films prepared from high-water-concentration dispersions (HWD) exhibited less swelling than those prepared from low-water-concentration dispersions (LWD). Similarly, membranes cast from HWD had greater conductivities than LWD membranes. This structural data, coupled with the property data, suggest that HWD exhibit stronger aggregate interactions upon film formation for both membranes and thin films, and that these stronger interactions likely yield better network connectivity, thus explaining the trends for conductivity and water uptake. However, to probe network connectivity/tortuosity definitively, additional energy-resolved scattering work or cryo-electron microscopy is necessary to map sulfur/water channel distributions. As noted, thermal annealing seemed to preserve solvent-ratio effects rather than erase them. Unannealed thin films exhibited much weaker variation in properties between different water concentrations. Additionally, swelling-trend discrepancies between thin films and membranes were likely due to confinement

effects. These confinement effects are expected to be further impacted by substrate identity; additional research into how these solvent/ionomer interactions manifest on different substrates is required. Furthermore, the degree to which dispersion solvent impacts thin films and membranes post annealing is expected to change as a function of annealing temperature. This work presents an important step in understanding solvent/ionomer interactions. Dispersion-level interactions persist across all length scales, affect film formation and properties, and are maintained upon thermal annealing. With this knowledge, one can begin to understand how solvent choice nuances catalyst layer inks, CL microstructure, membrane properties, and other device-level metrics. More importantly, one can contemplate engineering dispersions and inks for specific PFSA properties, thus enabling higher-performing devices. This understanding of ionomer/solvent interactions will inform the work of Chapters 3 thru 5 as additional parameters are introduced (dispersion age and catalyst particles).

2.6 Supplementary Information

2.6.1 *In situ* GISAXS and Dispersion Properties

2.6.1.1 Initial Linecuts and Fitting

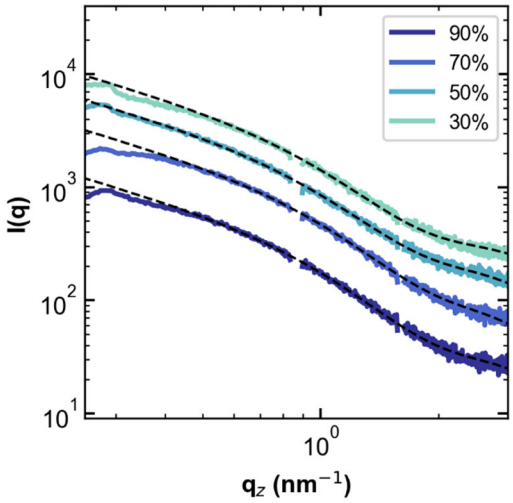

Figure S2.12. Through-plane intensity I(q) as a function of q linecuts obtained from GISAXS experiments of the dispersions immediately upon casting. Labels describe the weight percentage of water that makes up the dispersion solvent composition (the balance is *n*-propanol). Dashed lines show the core-shell form factor fit to the data. Lines are offset from one another for clarity.

Table S2.2. Core-shell form factor fitting parameters.

Parameter	30%	50%	70%	90%
Scale (in-plane; through-plane) (a.u)	0.256; 0.303	0.193; 0.301	0.187; 0.341	0.146; 0.234
Core Radius (Å)	8	8	8	8
Shell Thickness (Å)	18.26	19.34	18.61	17.71
Core Length (Å)	400	400	400	400
Core SLD ($Å^{-2}$)	5.05e-5	5.05e-5	5.05e-5	5.05e-5
Shell SLD ($Å^{-2}$)	1.14e-5	1.09e-5	1.09e-5	1.14e-5
Solvent SLD ($Å^{-2}$)	8.79e-6	8.79e-6	8.79e-6	8.79e-6
Background (in-plane; through-plane) (a.u)	5.37; 6.382	4.60; 4.80	3.67; 3.66	3.26; 3.30

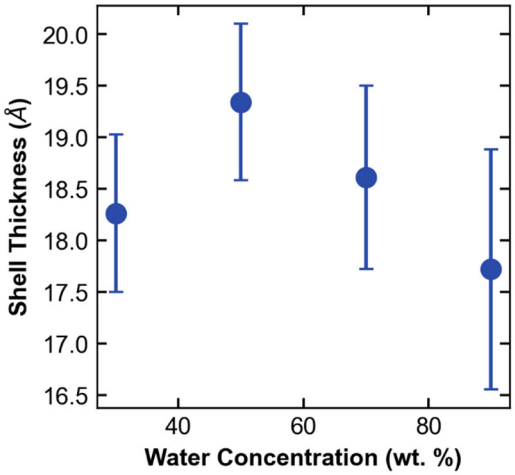

Figure S2.13. Shell thickness from core-shell form factor fit of initial linecuts. Error bars represent one standard deviation in fit uncertainty.

2.6.1.2 Structure Factors

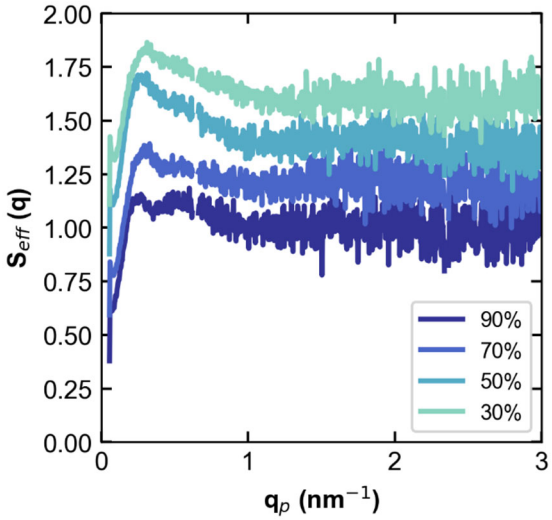

Figure S2.14. Initial effective structure factors (S_{eff}) of the dispersions immediately upon casting. This was obtained by dividing the line cuts in Figure 2.2 by the core-shell form factor. Labels describe the weight percentage of water that makes up the dispersion solvent composition (the balance is *n*-propanol). Lines are offset from one another for clarity.

One way to rationalize the two structure factor peaks discussed in Section 2.4.1 is to consider charged-particle aggregation phenomena. Charged particles exhibit heterogeneous aggregation states that can be described by theories such as Two-Yukawa, Darjaguin-Landau-Verwey-Overbeck (DLVO), and others that balance opposing forces such as electrostatic/coulombic repulsion and van der Waals attraction, *etc*.[125] These theories are all characterized by multiple local energy minima in an interaction energy landscape versus particle separation distance, and likely capture the primary physics governing Nafion particle aggregation, at least to a first degree. To summarize qualitatively the resulting energy profiles: the primary energy well at small separation distances governs the internal structure of secondary aggregates (flocs), while the secondary minima at larger separation distances describes separation between discrete aggregates (both secondary and lone primary). The two energy wells are separated by an energy barrier, the height of which dictates whether the primary aggregates can aggregate further (and therefore the stability of the suspension).[125] Within this framework, one can assign the primary structure-factor peak to the secondary energy minima (at larger length scales, smaller q), which describes the arrangement of aggregates in solution (and the characteristic long tail to this minima is indicative of multiple lengthscales/aggregate sizes that this averages over). The secondary structure-factor peak correlates to the primary energy minima (at smaller length scales, larger q). Additional structure-factor modeling work would be required to determine the relative strength of these local minima and how they vary with water:*n*PA ratio, but this framework provides a qualitative understanding of the data.

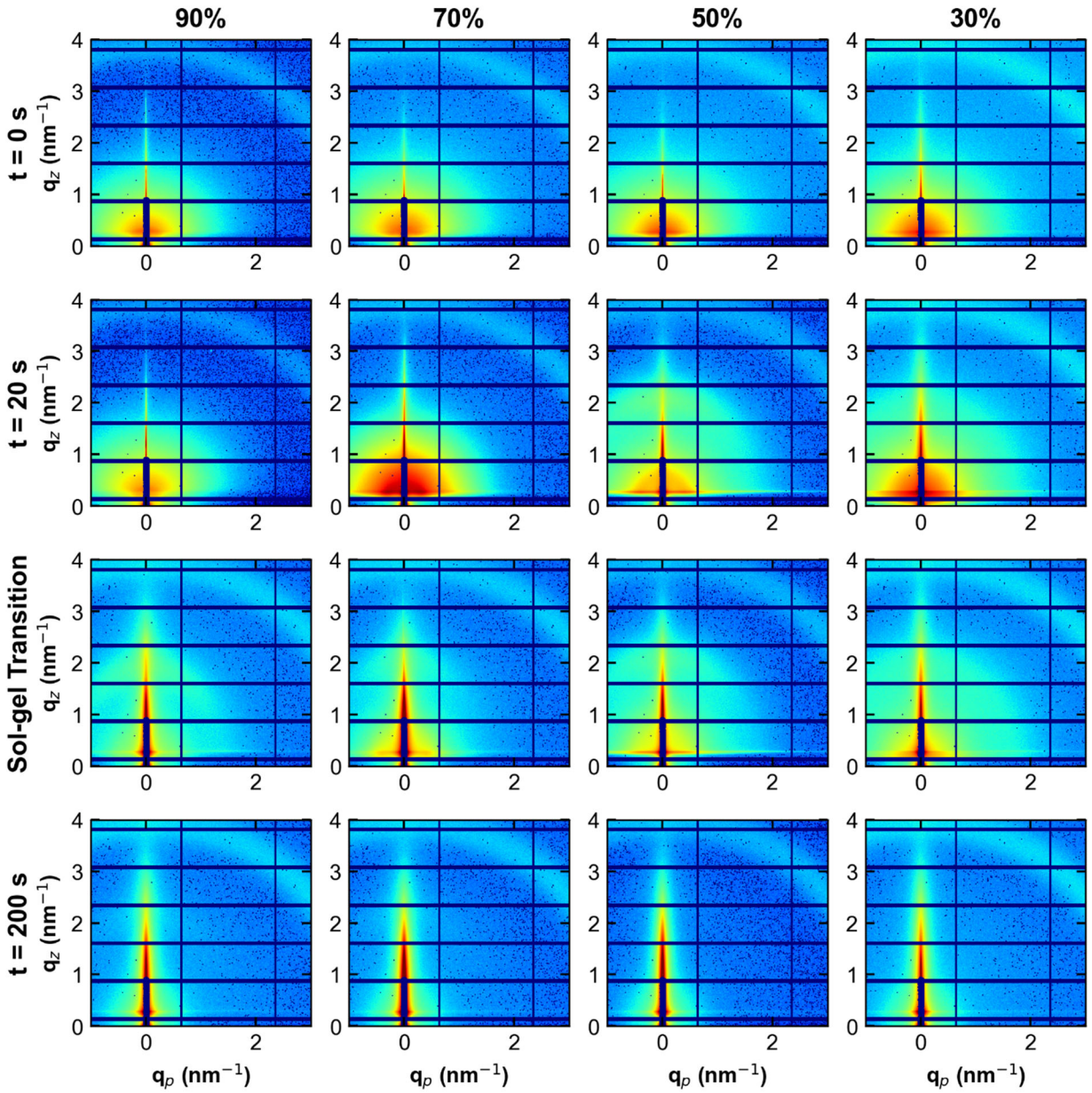

Figure S2.15. 2D GISAXS images for each water:*n*PA solvent ratio at select times. The sol-gel transition times shown are 88 s, 42 s, 22 s, and 27s for 90%, 70%, 50%, and 30%, respectively.

2.6.2 Rheology

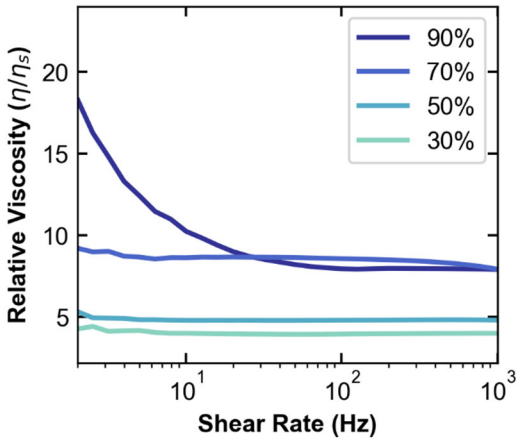

Figure S2.16. Measured viscosity of the dispersions (η) divided by the pure solvent viscosity (ηs) as a function of shear rate. Labels describe the weight percentage of water that makes up the dispersion solvent composition (the balance is *n*-propanol).

For flow through a slit, the shear rate at the wall ($\dot{\gamma}_{wall}$) is given by:

$$\dot{\gamma}_{wall} = \frac{6Q}{h^2 w} \tag{S2.6}$$

for a Newtonian fluid.[126] Here, Q is the volumetric flowrate, and h and w are the height and width of the slit, respectively. For the casting experiments, dispersions were printed at a rate of 5 µL/s through a slot-die printer head measuring 1 cm wide by 0.5 cm tall.[104] Even though the dispersions are not perfectly Newtonian, Equation S2.6 represents a good first approximation to estimate the shear rate experienced by the dispersions during casting experiments, especially for the lower water percentage dispersions. Accordingly, the shear rate is roughly 12 Hz. Data collected at 12.59 Hz (in Figure S2.16) is presented in Figure 2.4.

2.6.3 Teubner-Strey Fitting

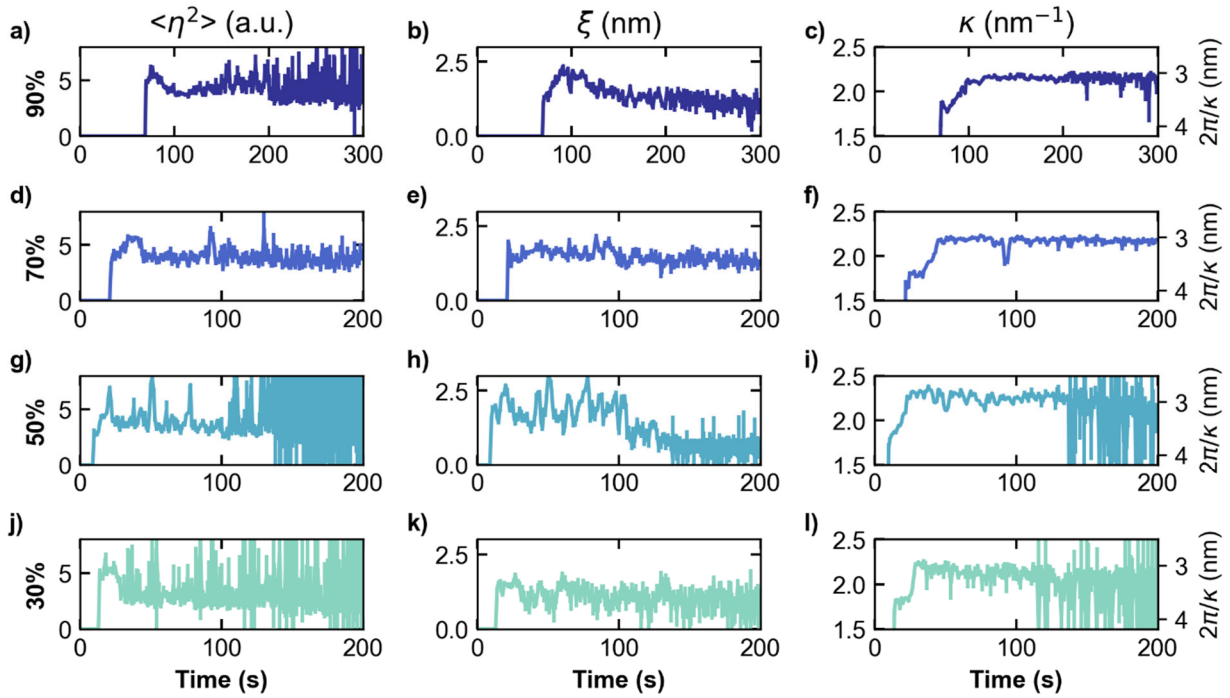

Figure S2.17. Gel to final film through-plane Teubner-Strey fitting parameters as a function of time, with error bars. Labels describe the weight percentage of water that makes up the dispersion solvent composition (the balance is *n*-propanol). Note the 90% goes out to 300 seconds.

The ionomer peak was fit to the Teubner-Strey Model[106-107]

$$I(q) = \frac{8\pi\langle\eta^2\rangle}{\xi(a - 2bq^2 + q^4} + background \tag{S2.7}$$

where

$$a = \left(\kappa^2 + \frac{1}{\xi^2}\right)^2 \qquad b = \left(\kappa^2 - \frac{1}{\xi^2}\right) \tag{S2.8}$$

The fitting parameters are $\langle\eta^2\rangle$, κ, ξ, and background. $\langle\eta^2\rangle$ is a function of volume fractions and the scattering length contrast, κ is inversely related to the spacing between domains, and ξ is the correlation length of domains.

Figure S2.17 shows parameters of the Teubner-Strey model versus time for the four water:*n*PA ratios. Both the 30% and 50% water films quickly approach their final parameter values within first 20 seconds after transitioning to the gel state. Between these two films, the 30% water film shows a lower correlation length, ξ, and the fits are considerably noisier because the ionomer peak falls below background. The 50% water film maintains a high correlation length, that oscillates in value through 100s, after which it similarly dries with no visible ionomer peak. The high-water-concentration dispersions (HWD; 70% and 90%), both begin gelation later because of the lower volatility solvent mixture. The HWD maintain a higher correlation length through the drying process and the ionomer peak in both more slowly proceed to their final values. At t = 200s, the LWD show no visible ionomer peak, while it is still visible in the HWD films.

2.6.4 Membrane Structure and Properties

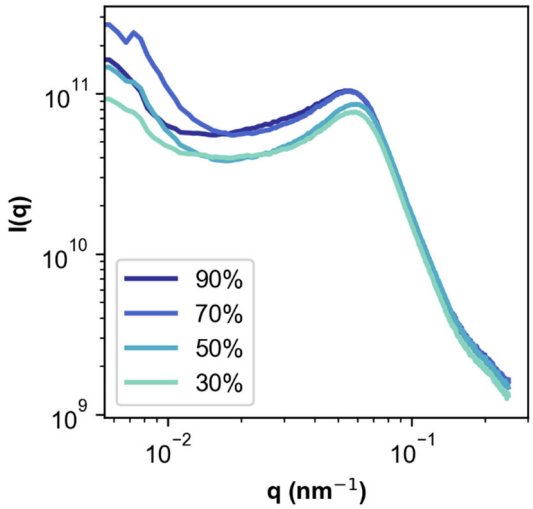

Figure S2.18. Inter-crystalline WAXS peak of the membranes at 2452 eV. Labels describe the weight percentage of water that makes up the dispersion solvent composition (the balance is *n*-propanol).

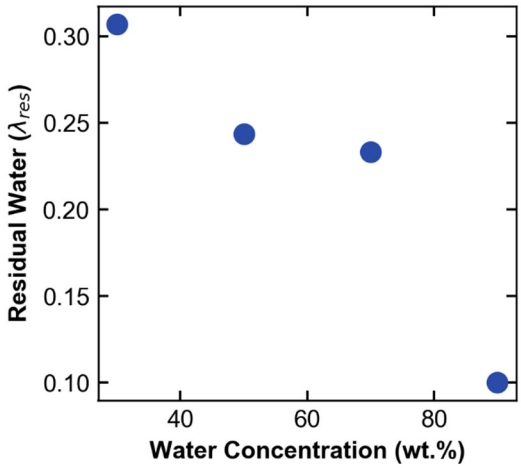

Figure S2.19. Residual water from membrane swelling measurements, as a function of the dispersion water concentration (balance *n*-propanol) from which the membranes were cast.

3 Inherent Acidity of PFSA Dispersions and Implications for Ink Aggregation‡

3.1 Abstract

In this chapter, we characterize dispersions of a common PFSA, Nafion, as well as inks of Nafion and carbon. It is shown that solvent choice affects a dispersion's measured pH, which is found to scale linearly with Nafion loading. Dispersions in water-rich solvents are more acidic than those in propanol-rich solvents: a 90% water versus 30% water dispersion can have up to a 55% measured proton deviation. Furthermore, because electrostatic interactions are a function of pH, these differences affect how particles aggregate in solution. Despite having different water contents, all inks studied demonstrate the same particle size and surface charge trends as a function of pH, thus providing insights into the relative influence of solvent and pH effects on these properties.

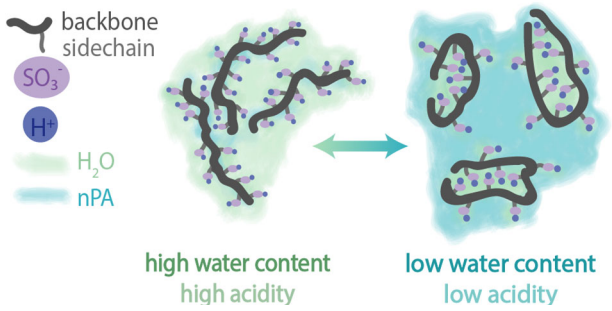

Figure 3.1. Schematic depicting a summary of Chapter 3: dispersion acidity is impacted by the solvent.

3.2 Introduction

Perfluorosulfonic acid (PFSA) is a random copolymer with a hydrophobic polytetrafluoroethylene backbone that provides mechanical support, and pendant hydrophilic sulfonic-acid sidechains (see Figure 1.4). PFSA films (like in a catalyst layer, CL) are typically prepared from commercial dispersions, which consist of PFSA (usually in its proton form) dispersed in a solvent (usually water/alcohol mixtures, although as will be discussed in Chapter 4, the stock dispersion composition influences the dispersion properties and may change depending on the manufacturer). PFSA dispersion morphology is greatly influenced by solvent choice. X-ray and neutron scattering experiments revealed that PFSA exists as rod-like aggregates with radii ~30Å in polar solvents.[54-55, 96] Moreover, different high dielectric constant (ε) solvents (including varying water/alcohol mixtures) can cause morphology to change dramatically (rods, swollen clusters, random-coil network, *etc.*).[37] The water-alcohol-PFSA mixture is particularly relevant because it is the typical

‡ This chapter was previously published as "Berlinger, S. A.; McCloskey, B. D.; Weber, A. Z., Inherent Acidity of Perfluorosulfonic Acid Ionomer Dispersions and Implications for Ink Aggregation. *J. Phys. Chem. B.* 2018, *122* (31), 7790-7796." and is adapted with permission from all co-authors.

solvent of commercial dispersions and CL inks. It has been demonstrated that these different solution-phase morphologies directly impact cast film properties;[6, 12, 38, 40, 60, 90, 100-102] ionomers maintain a memory of these structures[127] as discussed in Chapters 2 and 4.

These solvent effects must also change the interactions driving ionomer-particle aggregation/stability in an ink, because different water:alcohol ratio inks each exhibit different aggregate sizes, [60, 76, 79, 98, 128-131] and once dried, different CL morphology, water uptake, conductivity, *etc*. have been observed.[12-13, 39, 47, 71-72, 74-75, 90, 132-134] Unfortunately, none of these results are directly comparable to each other due to different components studied. While this solvent effect on cast properties has been established, there is currently a lack of understanding of the interactions between the catalyst, solvent, and PFSA present in the ink.[27] Initial attempts to model ink interactions used theories for general colloidal interactions of particles (DLVO theory) and polymers, with coulombic repulsion and surface-energy terms.[70, 95] However, these general polymer interaction forces are most applicable for uncharged polymers existing in good solvents, which is not the case for PFSA in alcohol/water systems. Due to the complicated biphasic nature of PFSA,[7] a complete model describing catalyst particle-PFSA interactions across all relevant concentration ranges does not exist.

Moreover, pH has not been considered explicitly in any previous PFSA dispersion or ink study. In the cast state, it is well documented that PFSA is a solid superacid, with the sidechain pKa reported to be around −6.[36] It is expected that PFSA will also have some acidity in the dispersion state. This inherent acidity is vitally important for understanding the electrostatic interaction in ink systems, because electrostatic repulsion is a function of surface charge, or zeta potential (ζ), and it is well documented that ζ is a strong function of pH (for the case where protons are potential determining ions, which is true for nearly all systems).[125] Therefore, pH is a determining parameter for particle aggregation. In addition, modifying the surface charge of a carbon substrate changes the affinity of PFSA for that surface.[135] However, no previous study has considered how inherent pH will alter surface charge in these systems or if it exists. In fact, the community previously believed that pH of dispersions would be near neutral, due to finite size effects of the ionomer aggregates. However, here we demonstrate that pH can be measured and plays an important role in determining ink interactions. This chapter remedies lack of understanding by decoupling solvent and pH effects, and examining how each alters the aggregation (electrostatic) behavior of a fuel-cell CL ink.

3.3 Experimental Methods

3.3.1 Materials

Nafion (a prototypical PFSA[7]) was used throughout this study to investigate PFSA behavior. Commercial Nafion dispersions (D2021) were obtained from Ion Power, Inc, and diluted to weight percentages varying from 0.05 to 4%. The structure of Nafion is shown in Figure 1.4. For each weight percent, multiple samples were prepared in different water to *n*-propanol (*n*PA) ratios, ranging from 90 to 30% water (balance consisting of *n*PA). Samples containing less than 30% water were not studied due to pH probe drift caused by dehydration of the glass membrane. *n*PA

(Sigma-Aldrich) was >99.9% purity, and 18 MΩ de-ionized water (MilliPore) was used. pH measurements were taken with an Orion Star A211 pH meter and a ROSS Ultra Triode pH/ATC probe (Thermo Fisher Scientific). The probe was calibrated before each use with appropriate known standards. Samples were stirred at 400 RPM for the course of the pH measurement; most samples equilibrated in less than thirty seconds. All measurements were repeated at least three times; error represents standard deviation of each sample.

3.3.2 pH Measurement

From a physical viewpoint, a pH measurement is a potential difference measurement, which is then converted to pH via the Nernst equation. This can create deviations from ideality, as junction potentials may influence the potential reading of the probe if the sample's solvent does not match that in the reference electrode. However, junction potentials are usually small (on the order of millivolts in water-alcohol systems).[136] Therefore, they can frequently be ignored, particularly in comparing between samples with the same solvent composition. From a theoretical viewpoint, pH is the negative logarithm of proton activity. In a dilute aqueous system with no added salt, the activity coefficient becomes one; only then is pH directly proportional to proton concentration. Activity may be influenced by a myriad of factors, including solvent Ɛ, degree of solvation/dissociation, *etc*. Consequently, the meaning of pH becomes a bit confusing as one moves away from aqueous systems; different solvents cannot be readily compared with each other due to different activities associated with those unique environments. Therefore, the pH measurement is a convolution of both proton concentration and solvent environment.

To alleviate this issue, an acid baseline was studied. Both perchloric (Sigma-Aldrich) and hydrochloric acids (MilliPore Sigma) were used to investigate different anions and confirm the relative insensitivity of the pH measurement with respect to the anion composition if a strong acid is used. The pH of each acid at different concentrations spanning from 0.001 to 0.1M was measured in solvents with water percentages ranging from 100 to 30%. There was little difference between these two acids. Furthermore, within the concentration range measured, there was no dependence of pH offset on concentration (*i.e*. the expected pH agreed with the measured pH for both 0.1M and 0.001M acid). Each point in the acid baseline (Figure S3.7) is an average of each concentration for both acids at that given solvent environment. The acid baseline allows one to decouple solvent environment and concentration effects, considering the expected pH deviation attributed to a proton existing in a different solvent environment. Total proton concentration is readily calculated given the equivalent weight and dispersion volume; this value was then corrected for solvent environment effects using the acid baseline. This correction is discussed in more detail in Section 3.6.

This pH measurement likely measures the average pH condition of the dispersion. In other words, all of the hydrogen ions are assumed to be measured, provided that they are external to the ionomer aggregates. Evidence for this is presented Figure 3.4, in which 100% of the protons (within error) are detected. A detailed exploration into the state of the electrical double layer and the proton concentration profile throughout the dispersion is beyond the scope of this study.

3.3.3 Inks

Simplified inks with 0.1 wt% carbon were prepared at ionomer to carbon (I:C) weight ratios from 0 to 1.5, in the same solvent ratios as above, using Vulcan XC72R (Fuel Cell Store). While it is expected that the addition of platinum will alter the results reported here, carbon and ionomer inks were initially chosen to understand the binary ionomer/carbon interaction. Primary carbon particles were 50 nm in diameter. All samples (dispersions and inks) were mechanically stirred for twenty minutes and then sonicated in a bath sonicator (Branson) for one hour. During the sonication, bath temperature remained constant via a water recirculator/chiller. Immediately after sonication, (within a minute) samples were measured via dynamic and electrophoretic light scattering (DLS, ELS, respectively, Nanoplus3, Micromeritics) to determine aggregation diameter and ζ. Five measurements were conducted over the course of fifteen minutes to gain good statistics and also acertain stability. Aggregate diameter was determined via the Stokes-Einstein equation (DLS measures a diffusion coefficient, which can then be related to a hydrodynamic radius via Stokes-Einstein), and ζ was modeled with the Smoluchowski equation (aggregates have sufficiently large values of κa such that the Smoluchowski equation is valid, in which κ is the inverse Debye length and a is the particle radius).[125] Other models do exist for soft particles (*i.e.* polymer layer covering a hard sphere) but they provide marginal corrections at the length scale of interest in this system.[137-139]

To decouple pH/solvent effects, dispersions in different solvent ratios were prepared, and acid ($HClO_4$) or base (NaOH) was added such that all dispersions had the same pH. Tested pHs were 0, 1, 2.5, and 9. pH 0 is below the isoelectric point of carbon (shown in Figure S3.8 to be around 1), and pH 2.5 is similar to that expected of a typical ink. Inks were then prepared from these pH-normalized dispersions. I:C ratios of 0 were not studied fully at all of these pHs because they were unstable and immediately aggregated (Figure S3.8). Meanwhile, all inks with appreciable ionomer levels show stability over the course of the measurement period (and larger particle diameters than pure carbon particle suspensions).

3.4 Results & Discussion

3.4.1 Dispersion pH

First, it is necessary to understand the ionomer/solvent interaction in terms of pH: to determine how varying water:*n*PA ratios change the pH of a dispersion for a given PFSA concentration, as well as how pH is affected by PFSA concentration for a given solvent ratio. The measured pH of PFSA dispersions diluted to different concentrations in solvents containing 90, 70, 50, and 30% water (balance *n*PA) is plotted in Figure 3.2. Each solvent ratio shows a linear dependence of pH on Nafion concentration, where the Nafion loadings are chosen to represent those occurring in different CL fabrication processes (with the high and low ranges typical of doctor-bladed and sprayed inks, respectively).[27] Furthermore, water-rich dispersions exhibit more acidic behavior,

while *n*PA-rich dispersions are less acidic. The difference between pH for each water ratio at a given Nafion concentration decreases as the amount of Nafion in the dispersion increases (*i.e.* at 0.05 wt%, the difference between the 90 and 30% water systems is 0.68 pH units, while at 4% the difference is only 0.25).

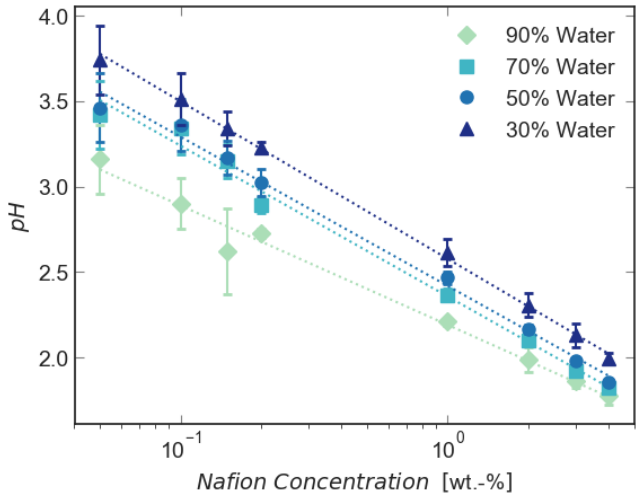

Figure 3.2. Measured pH of Nafion as a function of Nafion and water concentrations.

This difference is significant, and is better seen in Figure 3.3, where percent protons measured (PM) is plotted versus water concentration for given Nafion concentrations. PM is calculated by dividing the concentration of measured protons using a pH meter by the corrected total proton concentration expected from Nafion:

$$\mathrm{PM} = \frac{10^{-\mathrm{pH}}}{\left[\frac{\mathrm{g_{Nafion}}}{\mathrm{L}}\right] * \frac{1}{\mathrm{EW}} * \mathrm{ABC}} * 100 \tag{3.1}$$

where the equivalent weight (EW) used here is 1100 g_{Nafion}/mol_{SO3-}, the concentration of sulfonate groups is assumed to be equivalent to the concentration of protons, L is liters, and the ABC is the acid baseline correction (*i.e.* the fraction of protons expected to be measured for a small-molecule acid to account for solvent effects, as given in Figure S3.7).

For dilute Nafion concentrations (0.2 wt% in Figure 3.3) in 90% water, roughly all of the protons behave as would be expected from an ideal strong electrolyte solution of similar proton concentration (*i.e.*, the measured proton concentration is the same as the total proton concentration). As the fraction of *n*PA is increased in the solvent, fewer protons (~40% of the

theoretical expected amount) are detected at a given Nafion wt%. As Nafion concentration increases, PM decreases, and the difference between varying water contents decreases. Indeed, by 4 wt% Nafion, the PM (40-50%) is not substantially influenced by the solvent water:*n*PA ratio.

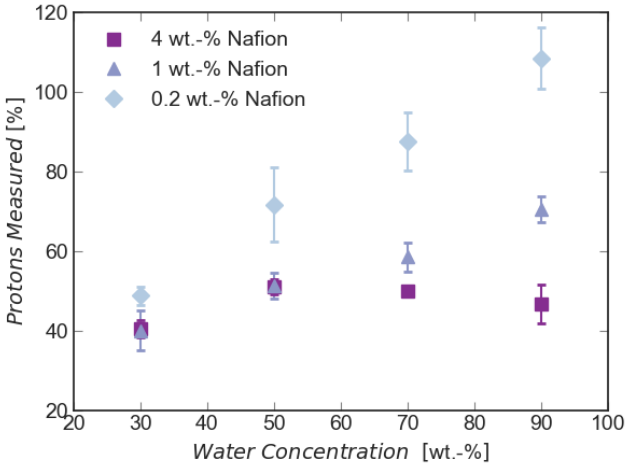

Figure 3.3. Measured proton divided by corrected theoretical proton concentration as a function of water concentration.

pH deviations seen cannot be due to the fact that propanol is slightly less acidic than water, because strong acids in the same propanol environment experienced little to no change in their pH (based on the acid baseline measurement). Furthermore, classical polyelectrolyte theories like Manning condensation do not account for deviations, because the charge spacing (taken to be the average backbone spacing between sidechains) is larger than the Bjerrum length for almost all of the samples.[140] Therefore, if change in measured protons is not due to solvent effects, it is proposed that they are attributed to changes in ionomer conformation.

It has already been discussed that the general structure of PFSA changes in different water:alcohol ratios. Perhaps, pH changes are a result of different sidechain orientations brought about by these different solvent contents. While most sulfonate-proton pairs should be dissociated in aqueous solutions, the protons will still remain within a Bjerrum length (~nm) of the sulfonate anions due to electroneutrality. It is suspected that protons that remain in proximity to sulfonate ions inside the PFSA structure will not participate as dissociated free protons as occur in small molecule strong acids (*e.g.*, HCl). However, in water-rich solvents, which have a higher affinity to the ionic sidechain than organic-rich solvents do, more sidechains will extend into the solvent and a more acidic bulk pH is expected. As propanol content is increased, there is less of a preference for sidechain orientation into solution (an inverted micellar structure has been proposed),[141] and less acidic pHs are measured. Therefore, PM in Figure 3.3 may be thought of as the number of total protons that are accessible to the bulk solution (versus those that are internal to the aggregate

structure). Interestingly, this also means that the pH probe can detect potential differences at this short lengthscale surrounding the ionomer. As stated earlier however, a detailed investigation into proton concentration profiles and the ionomer's electrical double layer is beyond the scope of this present study.

As ionomer concentration is increased, there is less of a difference in accessible protons between varying water contents than at lower concentrations. It is well known that Nafion can form secondary aggregates in solution;[6] at higher Nafion concentrations, a large portion of sidechains already exist inside the aggregate structure and therefore have buried sulfonate-proton pairs. Since there are less accessible protons, a lower percentage of the total protons in the dispersion is measured, even for very high water contents, and the effect of *n*PA content has a less dramatic effect than it does for very low Nafion concentrations. A schematic of the proposed preceding sidechain reorientation argument is shown in Figure 3.4. Additional experimental structural observations would be necessary to confirm this theory definitively, but current experimental techniques lack resolution required to resolve backbone and sidechain orientation. Cryo-transmission electron micrographs of Nafion dispersions are shown in Section 3.6. From the images, in propanol-rich solvents, PFSA forms narrow rod-like aggregates (with sidechains probably internal to the aggregate) and in water-rich solvents the hydrophobic backbone clusters in the middle of the aggregate.

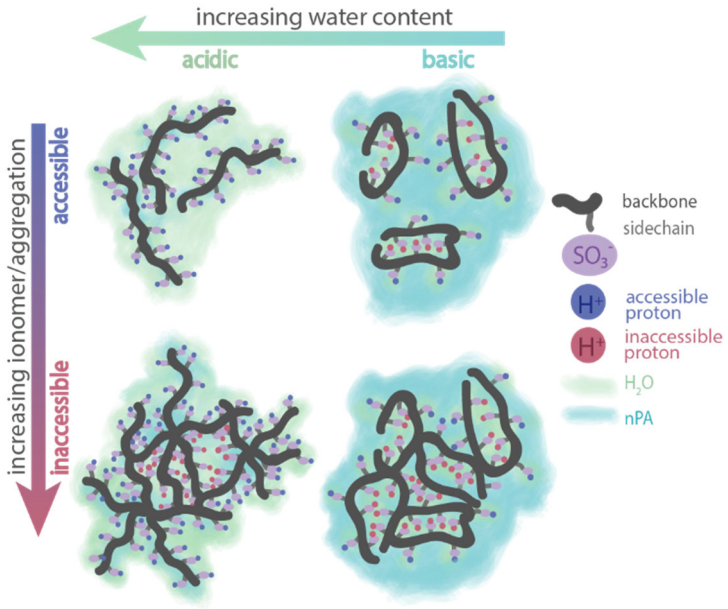

Figure 3.4. Schematic of 2D slice of potential structure representing individual chains and aggregates of Nafion, showing the sidechain orientation differences (pH differences) as a function of aggregation and solvent content.

3.4.2 Ink Aggregation

The above describes the interrelationship between pH and PFSA loading in dispersions, but there is a need to explore these effects in the tertiary ionomer/solvent/particle ink system. To do this, simplified inks containing Vulcan carbon, Nafion, and varying *n*PA:water and I:C ratios were fabricated as described in the Methods section.

The effect of Nafion concentration on pH in a carbon-solvent system is shown in Figure 3.5, where carbon suspensions are essentially titrated using a Nafion dispersion. Here, the measured pH of the total ink is plotted versus the number of measured protons (from Figure 3.3) associated with the addition of Nafion (at the same Nafion concentration). The neat carbon particle suspensions all have a pH around 7 to 8, which is expected given the very weakly basic character of typical oxygen defects present on carbon black surfaces.[142] If the Nafion did not interact at all with the carbon, we would expect a linear response similar to Figure 3.2. However, at low ionomer concentrations, we detect almost no ionomer: the pH is much higher (close to that of the neat suspension) than would be expected given the concentration of Nafion in the ink. That is due to adsorption of the Nafion to the carbon surface. As Nafion concentration is increased further, an equivalence point is observed between pH 7 and 4 for all solvent mixtures studied, at which point the ink pH displays expected values given the ionomer concentration. This equivalence point likely coincides with saturation of the carbon surface. The titration curve may essentially be thought of as an adsorption curve, representative of the ionomer free in solution (and therefore able to be detected by the pH probe). One may therefore transform this data into an adsorption isotherm. As a general back-of-the-envelope calculation, the equivalence point occurs around an I:C ratio of 1. If we assume 300 nm diameter (from Figure 3.6a) hard-sphere Vulcan carbon agglomerates (with a density of 0.264 g/cm^3), the ionomer layer covering these agglomerates (assuming all the ionomer adsorbs, with a density of 2 g/cm^3) would be roughly ~6 nm in thickness. This would be roughly monolayer thickness, given the size of the ionomer agglomerates in solution as measured by x-ray scattering (although of course the size is concentration dependent). Additional surface tension measurements (beyond the scope of this work) would provide insight into the free ionomer/aggregation in solution.

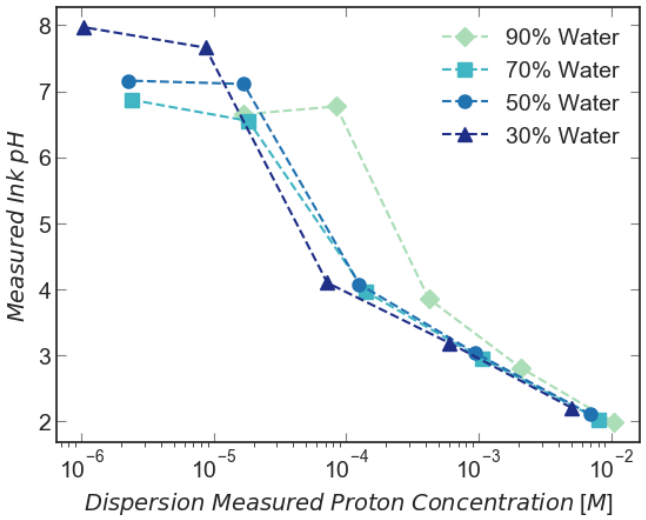

Figure 3.5. Titration of a 0.1 wt% XC72 Vulcan carbon particle solution by the addition of Nafion (plotted as measured proton concentration) at different water:*n*PA ratios.

Interestingly, as the water content in the ink increases, the total Nafion required to reach the equivalence point also increases (around an order of magnitude measured proton concentration difference between 30 and 90% water for the same Nafion concentration). From Figure 3.6a, this is actually in direct disagreement with surface area arguments: as the water concentration increases, the carbon agglomerate diameter increases (and therefore at the same carbon concentration, the carbon surface area decreases). One might expect that the amount of ionomer to reach the equivalence point and saturate the surface would scale with surface area; more ionomer would then be required to reach the equivalence point as water concentration decreases (not increases). Because we observe the opposite trend (meaning the adsorbed ionomer layer is thicker at the equivalence point as water content increases), this indicates that the magnitude of the electrostatic forces controlling ionomer/carbon interactions are fundamentally different for different solvent types (more charged groups on the ionomer and carbon surface interact with each other in water-rich solvents than propanol-rich). Optimal I:C ratios have previously been thought to be related to how the ionomer covers the carbon. However, ideal I:C ratios seem to vary slightly between groups that report using different solvents and carbon particles.[6, 81, 84, 132, 143-144] Considering this titration behavior, ionomer coverage is most likely related to pH (and different electrostatic magnitude) as a result of changing charge density (ionic strength). The varying equivalence points for each water concentration are likely also related to optimal I:C ratios. Similar titration curves are measured in Chapter 6 as a function of platinum content.

These varying electrostatic interactions will also affect the aggregation behavior of the ink, as shown in Figure 3.6. High magnitudes of zeta potential (ζ) indicate particles with high electrostatic repulsion, whereas lower values indicate particles are more susceptible to aggregation. With no PFSA, the carbon aggregate diameter increases with increasing water content, probably driven by hydrophobic effects. Upon addition of Nafion, aggregate size continues to increase, while

displaying the same water content/size relationship. Because each of these inks is at a different ionomer concentration and solvent ratio, each is at a different pH (and therefore different charge concentration and magnitude of electrostatic interaction). This is seen in Figure 3.6b: each ink has a different ζ.

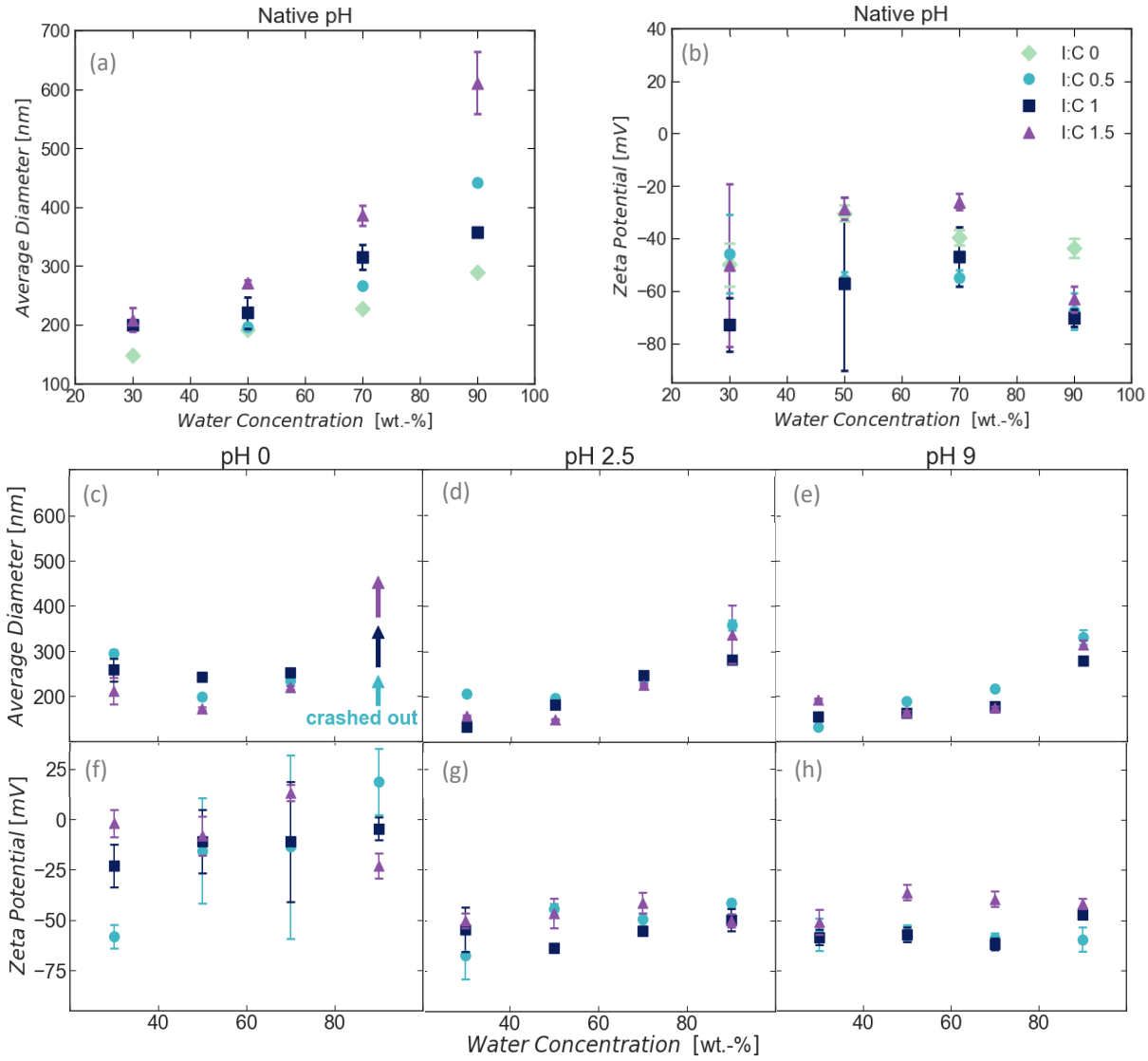

Figure 3.6. (a) The diameter as measured by dynamic light scattering and (b) zeta potential of the carbon/ionomer aggregates at different water percentages for Ionomer:Carbon (I:C) ratios between 0 and 1.5, without adjusting pH. (c)-(e) The average diameter of inks made by first adjusting the dispersion pH to 0, 2.5, and 9, respectively. (f)-(h) The average zeta potential of the same inks in (c)-(e).

To distinguish between pH and solvent effects on aggregation, dispersion pH (total measured protons) was adjusted to the same value (0, 2.5, or 9) using $HClO_4$ or NaOH, before adding carbon

particles. Aggregate size is shown in Figure 3.6c-e, and ζ in 4f-h for each pH. I:C of zero was not able to be studied fully at any of these pHs because it immediately aggregated and condensed (shown in the Section 3.6). This is evidence that Nafion acts as a stabilizing agent for carbon particles (or perhaps a buffering agent), in agreement with previously findings that Nafion addition increases stability.[70, 95] pH-normalized inks exhibit the same size and ζ trends as a function of I:C. Indeed, there is almost no difference between the I:C ratios, whereas in the native pH state there was over a 300 nm size difference between I:C 0.5 and 1.5 for 90% water.

It is important to note that a number of factors may be influencing the aggregation behavior, including changing dielectric constant and ionic strength. Both of these may be brought about by the addition of either ionomer or acid.[145] However, both of these are closely related to pH in these systems. Dielectric constant and ionic strength may both be changing because of ionic group addition, which is reflected in the dispersion pH. Therefore, even though there may be other indirect effects driving aggregation behavior, they are all ultimately linked to the ionomer dispersion behavior.

Furthermore, similarities between Figure 3.6d and e could be explained by similarities in ionic strength. Ionic strength is representative of the number of charged ionic species in the system. When the inks are normalized to the same pH, they should also therefore have the same effective ionic strength (they will have different number of accessible protons from the Nafion, and different amounts of added protons from the acid, but they will ultimately have the same acid concentration, and therefore the same ionic strength). Interestingly, when adding base, much more was required than calculated based solely on measured proton concentration. A possible explanation could be sodium ion exchange with the inaccessible protons, thus making the dispersion more acidic than initially measured (and hence more base required to neutralize). Due to this increased amount of base, the ionic strength of the alkaline and acidic normalized inks was very similar, perhaps explaining similarities in observed aggregate diameters.

For each ink, the ζ is very similar for all I:C ratios, indicating comparable levels of electrostatic interactions. Furthermore, as acid content increases, ζ trends toward zero, even becoming positive for some samples at pH 0, in agreement with typical electrostatically-controlled system behavior. However, it is also evident that hydrophobic effects play a large role in aggregation. As an example, consider the pH 0 graphs (Figure 3.6c,f) where all of the 90% water samples crash out of solution. The ζ for the 90% water dispersions becomes more negative with increasing I:C (which is also consistent with the idea that sidechains are facing outward and therefore contribute more negative groups once adsorbed to the carbon surface). However, the unstable 1.5 I:C 90% water ink has a larger magnitude ζ than, for example, the stable 1.5 I:C 70% water ink. If the system was purely electrostatically dominated, then the 1.5 I:C 70% water ink should be unstable as well; however, it was stable on the measured timescale (3 hours).

Of additional interest, for the 30% water case, the I:C- ζ trend is reversed, with the lowest I:C ratio exhibiting the most negative ζ. This is consistent with the sidechains having less affinity for *n*PA than water, and therefore are not exposed on the surface. It is clear that both solvent (in the form of hydrophobic forces) and pH (as a manifestation of PFSA conformation) are coupled and each contribute significantly to the resulting ink-aggregation behavior.

3.5 Summary

PFSAs have an inherent pH that is dependent on solvent composition, and may be a result of solvent-induced morphology changes. Indeed, pH could be a simple screening tool for PFSA structural parameters. These different dispersions have varying numbers of accessible protons, which alter the ionic strength and magnitude of electrostatic interactions. In a fuel-cell ink, this manifests in different aggregation behavior that collapses when inks are reduced to the same pH. The findings presented herein have potentially far-reaching implications for enhanced control over ink properties and engineering for various electrochemical technologies, enabling one to tune both solvent (viscosity, evaporation rate, hydrophobicity) and pH (electrostatic aggregation) effects independently.

3.6 Supplementary Information

3.6.1 pH Measurement Corrections

To calculate percent protons measured, the concentration of measured protons was divided by theoretical proton concentration. The number of theoretical protons is readily calculated from the concentration of Nafion added to the dispersion, the number of sidechains expected from that concentration using the equivalent weight (grams of polymer per mole sulfonic acid groups), the assumption that every SO_3^- is associated with one proton, and the volume of solvent. The measured proton concentration is determined from the measured pH value, assuming a unity activity coefficient. This is inherently an incorrect assumption, but not a bad one as discussed below.

The measured pH value depends on activity coefficients, concentration, and junction potentials, the latter of which is minimal. Therefore, it is necessary to determine whether the observed pH changes are a result of concentration differences (*i.e*. morphology changes) or activity coefficient differences. To distinguish the two cases, an acid baseline was studied, as shown in Figure S3.7. Solutions containing less than 20% *n*PA seem to be nearly ideal; the measured proton value matches the theoretical proton value with >95% accuracy, suggesting the activity coefficients do not alter pH values in this system. For solvents containing more propanol, the measured proton value plateaus to around 80%. The values for Nafion systems however, reach as low as 30%. While a detailed study of proton activity coefficients in these systems is outside the scope of this work, this demonstrates that up to 50% of the deviations expected cannot be explained solely by the effect of protons existing in different solvent environments (only about 20% can), and therefore the majority must be attributed to the influence of solvent water:*n*-propanol ratio on the sidechain orientation in the aggregate structures. The percent protons measured data in Figure 3.3 therefore represents a corrected version of the data in Figure S3.7, in which the theoretical proton concentration has been scaled by the amount you would expect to measure in that solvent environment (taking into account these activity coefficient differences of the acid baseline).

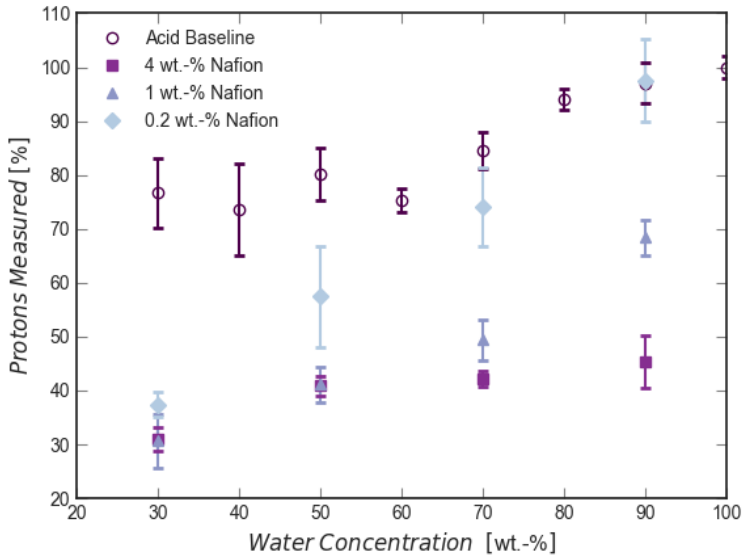

Figure S3.7. Uncorrected data of percent protons measured of acids and different Nafion loadings as a function of water concentration.

3.6.2 Inks

The data for pH 1 is shown in Figure S3.8. The bare carbon ink crashes out of solution and has a zeta potential of around 0 (indicative of instability). Above pH 1, the bare carbon is stable, indicating that the isoelectric point occurs around pH 1.

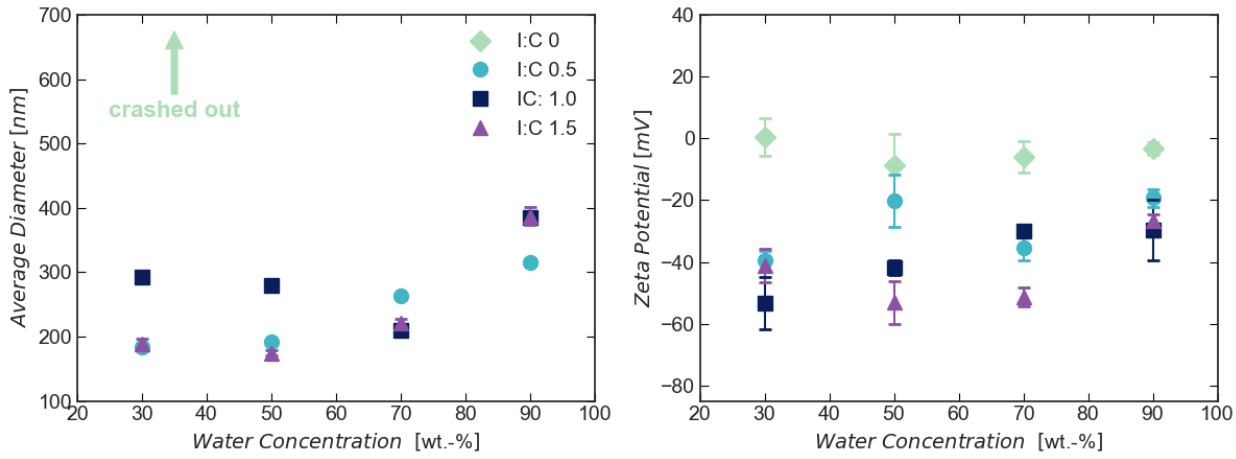

Figure S3.8. The average diameter and zeta potential of the aggregates in inks adjusted to pH 1. Comparing no ionomer to higher ionomer-to-carbon (I:C) ratios shows that ionomer stabilizes the dispersions.

3.6.3 Dispersion Aggregate Structure

Cryo transmission electron microscopy images were taken on Talos Arctica (Thermo Scientific) and JEOL 3100 FFC microscopes, each equipped with Gatan K2 Summit detectors. Samples were cast onto holey carbon grids and frozen in liquid ethane.

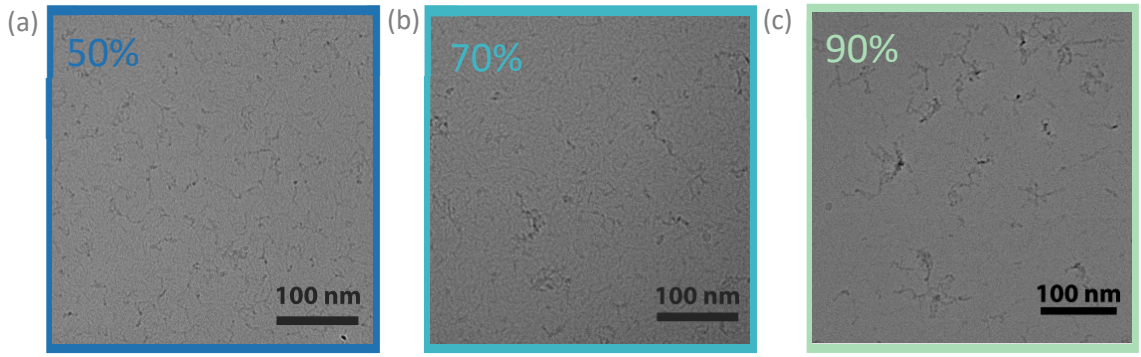

Figure S3.9. cryo-TEM images of 0.2% Nafion solutions in (a)-(c) 50, 70, and 90% water, respectively.

Figure S3.9a-c show the cryo-TEM images of 0.2 wt% Nafion dispersions. The *n*PA-rich dispersions form extended rods, while the water-rich dispersions exhibit more clustered structure, with high density (dark colored) points in the middle. Combining micrograph images and pH data allows us to hypothesize the ionomer aggregate conformation in solution, particularly the sidechain

versus backbone orientation. This is shown schematically in Figure 3.4: at low concentrations in high water contents, the backbone clusters in the middle, and then extends outward, allowing nearly all of the sidechains to be solvated. In propanol-rich solvents, there is less driving force for the backbones to aggregate, or for the sidechains to extend into solution, so the ionomer forms a rod-like aggregate structure that exhibits a more basic pH. Furthermore, as ionomer concentration is increased and more secondary aggregates form, there are less accessible protons. This explains why higher weight percent dispersions exhibit lower percent protons measured (Figure 3.3) for all water contents.

4 Aging Influences Structure and Properties of Ionomer Dispersions

4.1 Abstract

It has recently been established that different solvents alter the properties of ionomer dispersions; these different dispersion conformations affect the structure and resulting properties of thin films and membranes once cast and dried (as discussed in Chapter 2). Importantly however, ionomer used in inks is often diluted from a stock dispersion. This dilution causes the ionomer to change solvent environments and concentrations compared to those of the stock dispersion. No previous investigation has studied changes that occur due to this dilution process, or how the time from dilution affects dispersion properties or films cast from them. Herein, we use pH measurements to probe dispersion behavior and demonstrate that all dispersions studied become more acidic with time from dilution, stabilizing after approximately two weeks. Importantly, the more dissimilar the new dispersion conditions are (in terms of solvent composition and ionomer concentration), the more the ionomer dispersion changes over time. When the time from dispersion preparation/dilution is increased (aged), scattering peaks due to hydrophilic domains (the ionomer peak) change from their "new" values depending on solvent composition. Interestingly, membranes cast from both solvent extremes studied become more conductive as the dispersion used to cast them is aged because of these structural differences. In total, this study explores dispersion aging as an important variable (dispersion age) that controls ionomer structure-property-processing relationships, creating the possibility to use aging to tune cast ionomer properties during manufacturing.

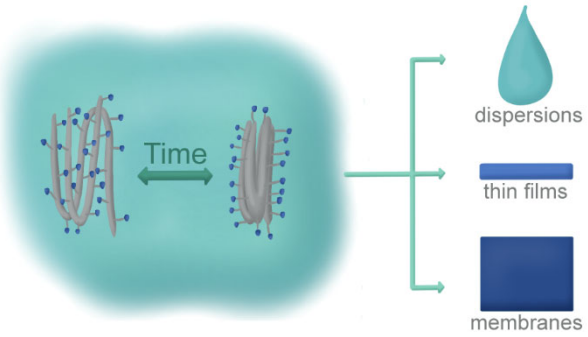

Figure 4.1. Schematic depicting a summary of Chapter 0: dispersion conformation changes with age, propagating to affect the properties of dispersions, thin films, and membranes.

4.2 Introduction

Catalyst layers (CLs) are prepared through solution-processing techniques, in which the catalyst particles and ionomer are first dispersed in an ink, before casting and drying the electrode.[27] The interaction between these components in-solution determines the final structure and properties of the CL, as discussed in Chapter 1.[82] Notably, the ionomer conformation is dramatically influenced by the dispersing solvent.[37, 56-57, 59, 146-147] In Chapter 2,[148] we showed that these differences in dispersion conformation affect how ionomer aggregates coalesce and form films. Different thin-film and membrane structures arise after casting, and these solvent-induced differences persist even after thermal annealing, propagating to affect device-relevant metrics such as conductivity and water uptake.

Generally, polyelectrolyte dispersion aggregation/conformation is determined by a balance between entropic/hydrophobic interactions and electrostatic repulsion,[149] often resulting in the formation of core-shell particles[150] (as has been observed for PFSA[103, 148]). Notably, these interactions are modulated by solvent properties[150], and depending on the solvent, the polymer may be unstable or meta-stable (*i.e.* changing conformation with time). Time-dependent aggregation has been observed for various ionomer and polyelectrolyte systems, including polyurethane ionomers,[151] S-P3MEET,[152] Carbopol,[153] and poly(allylamine),[154] among others.

This time-dependent behavior also persists once these polymers are cast. Physical aging due to changes in ionic domains have been observed for sulfonated polystyrene[155] and ethylene-based ionomers.[156] This phenomenon (often termed hygrothermal aging) has been extensively studied for PFSA membranes.[7, 157-163] Therefore, because PFSAs are subject to membrane-based temporal instabilities, dispersion-level dependences likely also exist.

Evidence suggesting that dispersions change with time may be gathered from ink-aging studies. Ink aggregate sizes,[70, 95] viscosity,[164] and hydrophobicity[165] change with time, impacting CL microstructure[166] and electrochemical surface area,[167] catalyst mass activity,[167] and selectivity.[168] Although there are certainly many complex interactions occurring in these ink systems as a function of time, likely the behavior is in part due to ionomer differences in solution. Isolating the effect of ionomer dispersion aging is critical to understanding ink structure-property-processing relationships and controlling CL microstructure and performance.

In this chapter, we systematically explore how PFSA dispersions change with time from dilution. The strong effect of solvent on PFSA conformation and solvent interactions has previously been demonstrated to be due to changes in electrostatic persistence length;[67, 97] time-dependent behavior is likely to be a function of solvent environment. Therefore, we extend Chapter 2's investigation on the impact of solvent on PFSA properties[148] by introducing time from dilution as an additional variable. We probe the dispersion behavior in this solvent-time parameter space via pH measurements (as established in Chapter 3), and then cast membranes of different solvent compositions at various time points to unravel how structure (via x-ray scattering) is influenced by dispersion age. Finally, we correlate the effects of these different structures on membrane conductivity. In this way, we elucidate the intricacies of ionomer/solvent processing, and find that aging is an important, underappreciated parameter that strongly impacts dispersion properties.

4.3 Experimental Methods

4.3.1 Dispersions

All ionomer dispersions were prepared by diluting stock 20 wt% Nafion dispersion (D2021, Ion Power, Inc.) to either 0.5, 2, or 4 wt/v% ($g_{Nafion}/mL_{solvent}$, *i.e.* 0.005, 0.02, or 0.04 $g_{Nafion}/mL_{solvent}$, hereafter referred to as "0.5, 2, and 4%" Nafion). The dilution used various ratios of water (18 MΩ, Milli-Q) and *n*-propanol (>99.9% purity, Sigma-Aldrich), considering the inherent water and propanol in the stock dispersion (D2021 is approximately 20% Nafion, 46% water, and 34% *n*-

propanol, by weight), to bring the total solvent composition to either 30, 50, 70, or 90 wt% water. We also investigate the use of a 5wt% stock dispersion (Nafion D521, Ion Power, Inc.). Dispersion ionomer concentrations were chosen to encompass a range of industrially-relevant and practically-constrained values (*i.e.* thin films and spray-coated CL inks are always prepared from lower concentrations, membranes and more viscous inks used in doctor blading/roll-to-roll are prepared from higher concentrations, etc.). Upon dilution, dispersions were mechanically mixed for 1 minute, followed by bath sonication (Branson) for 30 minutes. The sonicator was equipped with a water recirculator set at 10°C to ensure the dispersion did not increase in temperature during the course of sonicaton. Dispersions were either used immediately (within thirty minutes from the end of sonication) or stored at room temperature for a specified amount of time. All dispersions were remixed (but not resonicated) for one minute if they were used again (to measure pH, cast membranes, *etc.*)

The pH of the dispersions (0.5, 2, and 4% Nafion dispersed in 90, 70, 50, and 30% water, balance *n*-propanol) was measured over the course of two weeks with an Orion Star A211 pH meter and a ROSS Ultra Triode pH/ATC probe (Thermo Fisher Scientific). Before each measurement, the probe was calibrated with appropriate standards. During the measurement, the dispersion was stirred at 400 RPM with a magnetic stir bar. Multiple replicate dispersions were measured each day; error bars represent standard deviations among the samples.

4.3.2 Membranes

To fabricate membranes, 4% Nafion dispersions prepared as above (dispersed in a range of 30-90% water, balance *n*-propanol) were poured into custom-made glass wells such that the same mass of ionomer was added to each. They were then heated at 35°C for 1 hour and annealed at 150°C for an additional hour in a vacuum oven, before slowly cooling back to room temperature overnight (still under vacuum). They were then carefully removed from the glass, and the dry thickness of all membranes was measured at 16 +/- 5 μm with a thickness gauge (Heidenhain). The same dispersions were used to fabricate membranes on day 0 and on day 7. The membranes will hereafter be referred to by the age of the dispersion used to cast the membranes (*e.g.* Day 7). Note that this does not mean the membrane itself is 7 days old.

Hydrated membrane structure was probed with small angle x-ray scattering (SAXS) at beamline 7.3.3. of the Advanced Light Source (ALS) at Lawrence Berkeley National Laboratory (LBNL). The X-ray wavelength used was $\lambda = 0.124$ nm, with a monochromator energy resolution of E/dE of 100, and the presented patterns were collected using a 2D Dectris Pilatus 2M CCD detector (172 μm x 172 μm pixel size). The scattering wave vector, $q = 4\pi \sin(\theta/2)/\lambda$, where θ is the scattering angle, was in the range of 0.001 to 0.04 $Å^{-1}$. SAXS images were collected by immersing the samples in DI water in custom-made solution cells with X-ray transparent Kapton™ windows. All of the experiments were carried out at 25°C immersed in liquid water; the samples were equilibrated at least 24 hours prior to imaging.

The collected two-dimensional scattering patterns were azimuthally integrated to generate 1-D intensity profiles, I(q), which were corrected for background scattering. From the SAXS data, hydrophilic-domain spacing and inter-crystalline spacing, and full-width half-max (FWHM), were calculated using a Gaussian fit to the (ionomer scattering) peaks.

Day 0 and day 7 membranes used for the conductivity measurements were equilibrated in DI-water for at least 24 hours before their wet thickness and width were measured. The resistance of the membranes was then measured using a four-point probe (BekkTech) and potentiostat (BioLogic) to sweep the voltage from –0.1 to 0.1 V and record the current as described previously.[119] Conductivity was calculated from the resistance measurement using the dimensions of the cross-sectional area of the membrane and the spacing between the electrodes. Three different membranes for each solvent ratio were measured.

4.4 Results & Discussion

4.4.1 Dispersions

pH measurements are a fast and facile way to probe ionomer/solvent interactions (discussed previously in Chapter 3).[67] Here, we use pH to screen all of the ionomer dispersions studied (three concentrations of four solvent ratios each) as a function of time. Figure 4.2A-C gives the pH of 0.5, 2, and 4% Nafion dispersed in 90, 70, 50, and 30% water as a function of time. As has been previously established, higher water-content dispersions are more acidic than low-water-content dispersions, and this difference cannot be attributed solely to changes in dielectric permittivity/ion pairing (likely suggesting conformational ionomer differences).[67] Interestingly though, these pH values are not stable. All dispersions become slightly more acidic with time. In panels D-F of Figure 4.2, we plot the percentage proton increase defined as

$$\%\ \text{proton increase} = \frac{[\mathrm{H}_i^+] - [\mathrm{H}_0^+]}{[H_0^+]} * 100 = \frac{10^{-\mathrm{pH_i}} - 10^{-\mathrm{pH_0}}}{10^{-\mathrm{pH_0}}} * 100 \tag{4.1}$$

where subscripts *i* and 0 refer to the *i*th and initial day of the measurement, respectively. As a reference, the pH of the stock D2021 dispersion is roughly 1.01 (and D521 is 1.57). Additionally, if all protons contributed to bulk pH (which we know they don't from Chapter 3) the minimum theoretical pH is 2.34, 1.74, and 1.44 for the 0.5, 2, and 4% Nafion dispersions, respectively, assuming an EW of 1100.

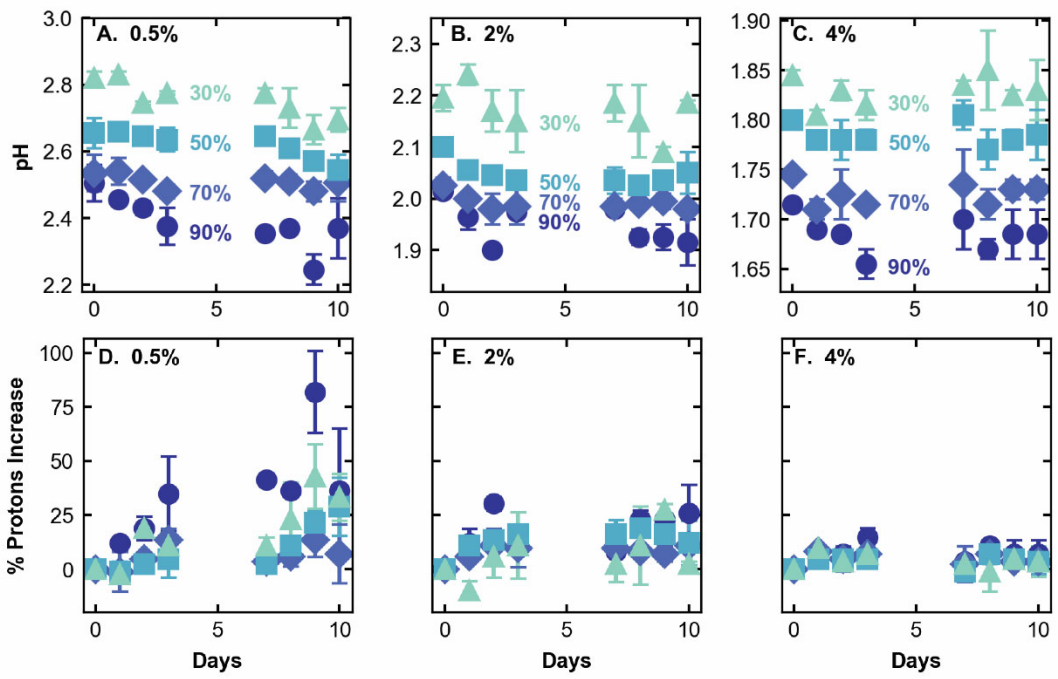

Figure 4.2. pH of (A.) 0.5, (B.) 2, and (C.) 4% Nafion dispersions, dispersed in various water to *n*-propanol ratios, reported as the percentage water in the figures (30 to 90%). Panels (D.-F.) correspond to (A.-C.) respectively, transforming the pH data into percentage increase in proton concentration as calculated from the pH measurement, normalized to the initial day 0 concentration.

Figure 4.2 reveals a few notable points. First, the dispersions do not uniformly become more acidic with time. Generally, the solvent extremes (90 and 30% water) experience greater changes than do the intermediate water-concentration dispersions. This has previously been observed with 3M PFSA dispersions: 100% water dispersions exhibited much greater changes than 50% water dispersions.[169] Additionally, low-concentration dispersions (Figure 4.2D) become much more acidic with time than do high-concentration dispersions (Figure 4.2F). 0.5% Nafion dispersed in 90 and 30% water becomes roughly 30 to 40% more acidic over ten days, while 4% Nafion in the same solvent becomes only 5% more acidic.

pH measurements have previously been suggested to be a proxy for dispersion conformation, as described in Chapter 3. If this is true, the change in pH with time suggests changing conformation in response to ionomer/solvent interactions. Ideally, solution structural information of these dispersions would also be gathered (with resonant x-ray scattering or neutron scattering). However, pH represents a facile screening tool that would complement these data. When the dispersions are prepared, the ionomer is moved from a high concentration state dispersed in intermediate water concentrations (roughly 50% water) to a lower concentration in various water/alcohol ratios. Higher concentrations would promote more aggregation (and therefore less accessible protons/higher pH values compared to a strong mineral acid at the same

concentration).[67] As the ionomer adapts to its new solvent environment, the aggregate size may shrink. This is consistent with the fact that lower concentrations and solvents that are more dissimilar to the initial state experience greater changes over time. Therefore, the equilibration time of the ionomer to adapt to this new solvent environment is longer than the mixing time and continues to evolve over the course of many days.

Figure 4.3 shows the behavior of Nafion dispersions prepared from D521 (rather than D2021 as in Figure 4.2). As discussed above, D521 is a stock dispersion containing 5 wt% ionomer, rather than 20 wt% as in D2021. When using D521 to dilute, the same pH behavior is observed as when using D2021: increasing acidity with time, with more pronounced acidity changes for low ionomer concentrations and water content extremes. However, the D521 dispersions are all initially more acidic than the D2021 dispersions. This makes sense given the above hypothesis: the initial lower stock dispersion concentrations (and smaller aggregates) would yield more acidic dispersions when diluted to similar concentrations as a dispersion prepared from a higher-concentration stock (with larger aggregates). The two dispersion types do converge to the same pH values within a few days.

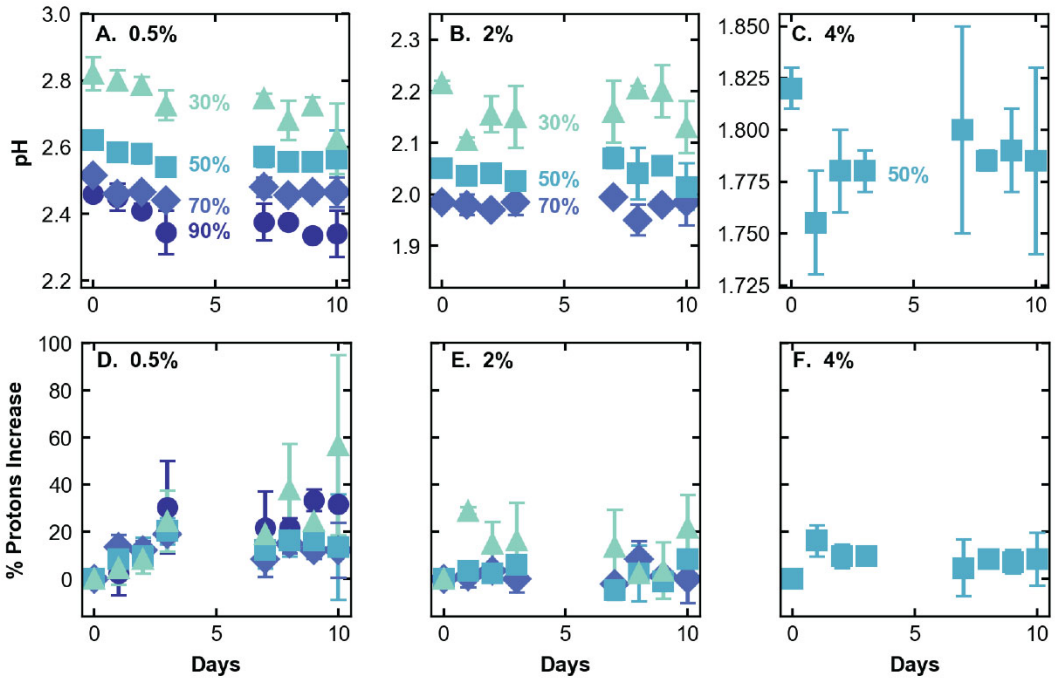

Figure 4.3. pH of (A.) 0.5, (B.) 2, and (C.) 4% Nafion dispersions prepared from Nafion D521, dispersed in various water to *n*-propanol ratios, reported as the percentage water in the figures (30 to 90%). Panels (D.-F.) correspond to (A.-C.) respectively, transforming the pH data into percentage increase in proton concentration as calculated from the pH measurement, normalized to the initial day 0 concentration.

The changes in pH over time have important implications for CLs. It was recently reported that inks with high water contents experienced more cobalt leaching from alloyed-platinum catalysts, due to the more acidic environment.[170] Because the pH will continue to become more acidic, the nature of the catalyst, in addition to the ionomer, may change over time with aged inks.

Furthermore, the electrostatic interaction between the ionomer and catalyst particles will change with time due to the increase in charges. As will be demonstrated in Chapter 5, the ionomer's charge strongly affects its adsorption behavior: ionomers with a higher charge density adsorb less to carbon surfaces and more to platinum surfaces under typical mixed water/propanol ink conditions.[169] This will ultimately affect how the ionomer coats the catalyst particles, and the ionomer distribution in the final CL. CL performance (electrochemical surface area,[88] mass-transport resistance,[86] *etc*.) and durability (CL cracking)[171] are directly impacted by ionomer distributions. Aging therefore offers opportunities to both understand and directly control this distribution.

4.4.2 Membranes

We next analyze membranes cast from dispersions of different ages (0 and 7 days): first exploring structure via SAXS, and then investigating how that structure impacts metrics like conductivity. Figure 4.4 displays the scattering linecuts of hydrated membranes (in liquid water) cast at 0 days or 7 days from varying water/propanol compositions after thermal annealing. The typical inter-crystalline (representing crystalline domain spacing) and ionomer (representing the hydrophilic water domains) peaks[7] are observed. Notably, the peaks change both as a function of dispersion water content and dispersion age. Even more importantly, how they change with age is a function of dispersion water content, in agreement with the data presented earlier.

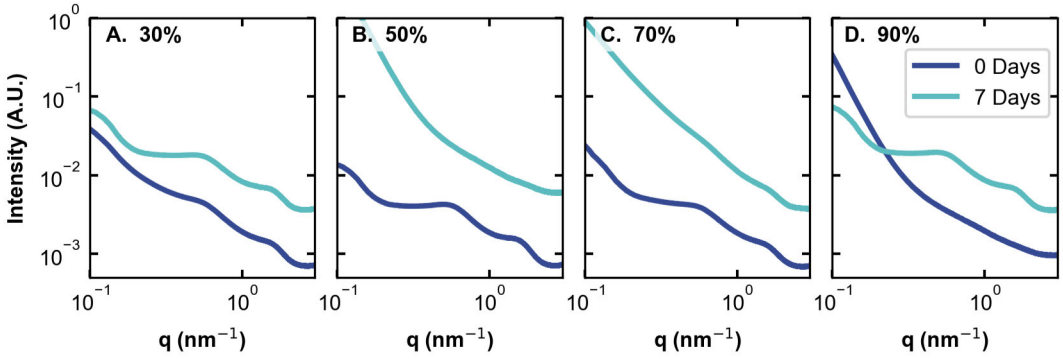

Figure 4.4. Small-angle x-ray scattering linecuts of Nafion membranes cast from 4% Nafion dispersions in (a.) 30, (B.) 50, (C.) 70, or (D.) 90% water (balance *n*-propanol). The same dispersions were used to cast membranes on the initial day and 7 days later.

Initially, the membranes cast from 90% water on day 0 display almost no observable phase separation, while the membranes prepared from the other water compositions do. The d-spacing of the ionomer peak also increases as dispersion water content increases from 30 to 70% (see Table 4.1). When membranes are cast from the same dispersions one week later, very different structures arise. Both of the extremes (90 and 30% water) display higher ionomer peak intensities with larger full-width half max (FWHM) values, indicating greater phase separation with a larger distribution of domains, as compared with both their day 0 counterparts, as well as the other day 7 water composition membranes (50 and 70%). These diverging trends with time (middle versus extreme water compositions) parallel the dispersion pH measurements, where the extreme compositions had different behavior than the middle compositions.

Table 4.1. domain (d) spacing and full-width half max (FWHM) of the ionomer peak, and FWHM of the inter-crystalline peak calculated from SAXS membrane experiments. Some cells are empty (--) because the peak was to weak to fit, as seen in Figure 4.4.

	90%, 0 Days	**90%, 7 days**	**70%, 0 Days**	**70%, 7 Days**	**50%, 0 Days**	**50%, 7 Days**	**30%, 0 Days**	**30%, 7 Days**
d-spacing ionomer peak (nm)	--	4.02 ± 0.75	4.05 ± 0.67	3.86 ± 0.35	4.03 ± 0.77	--	4.00 ± 0.67	4.02 ± 0.75
FWHM ionomer peak (nm^{-1})	--	0.048	0.042	0.024	0.049	--	0.043	0.048
FWHM inter-crystalline peak (nm^{-1})	--	0.030	0.028	--	0.031	--	0.037	0.031

While in-plane conductivity does not correlate exactly with ionomer peak measurements (conductivity will also be a convolution of tortuosity/connectivity, which is not probed in scattering experiments), conductivity is a useful indicator of how the ionomer domains are connected, and can serve to complement SAXS data. Figure 4.5 displays the results of in-plane conductivity measurements on similar membranes that were measured above in Figure 4.4. Conductivity of day 0 membranes increases with increasing water content, in agreement with previously observed trends in Chapter 2.[148] Differences in quantitative values between these results and previous ones could be due to differences in environmental conditions during the casting process (temperature has previously been shown to affect dispersion pH).[172]

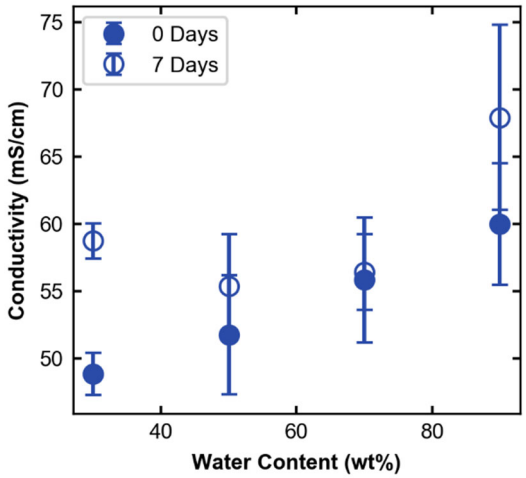

Figure 4.5. In-plane conductivity of Nafion membranes cast from 4% Nafion dispersions in various water to *n*-propanol ratios (reported as a function of water content). The same dispersions were used to cast membranes on the initial day (0) and 7 days later. Error bars represent the values of multiple unique samples.

When considering membranes prepared from 7-day-old dispersions, a familiar trend arises: membranes cast from extreme water-content dispersions have similar behavior, as do intermediate water-content dispersions. More specifically, the extreme water compositions both become more conductive with time (although the increase for the high-water content may be within error), while the intermediate concentrations remain the same. The increase in conductivity is consistent with the increase in phase separation and increased FWHM experienced by these membranes as calculated form the SAXS data. However, it is unclear why the intermediate concentrations remain the same (rather than decreasing in conductivity in accordance with the expected trends from the SAXS data). This again suggests that there are additional differences between these membranes related to connectivity of water domains that cannot be probed from SAXS alone. Additionally, these differences may manifest in other transport-property measurements (*e.g.*, through-plane conductivity, gas permeability) that are influenced by membrane domain tortuosity.

4.5 Summary

In summary, we have shown that dispersion acidity changes as a function of time from dilution. This is particularly true for water/propanol ratio extremes, and very dilute dispersions. From a practical standpoint, this may also mean using Nafion D2021 vs D521 may result in different ionomer and perhaps catalyst-layer behavior, and care must be taken to ensure that experimental replicates have the same processing history. Importantly, the differences in dispersion behavior

propagate to membranes: when comparing one solvent composition, different structures are observed before and after aging. Notably, the pH changes for the high concentrations used to cast the membranes were minimal, but the structural changes were still present. This suggests that high concentration dispersions may experience conformational changes that are not detected by pH measurements, and also implies membranes or thin films cast from lower ionomer concentrations may experience even greater structural differences. Similarly, this raises an important question: are the high-concentration stock dispersions themselves stable? Further investigation into dispersion structures (via neutron scattering or resonant x-ray scattering techniques) is necessary to understand fully how time affects the ionomer "equilibrium" conformation. Additionally, thin-film studies are necessary to understand how this time-dependent process impacts catalyst layers. Despite these gaps, this chapter raises critical processing considerations that undoubtedly influence all data using these types of materials. Additionally, one may contemplate leveraging these aging effects (such as improved conductivity) to age dispersions selectively to obtain appropriate metastable states for enhanced performance.

5 Probing Ionomer Interactions with Electrocatalyst Particles in Solution‡

5.1 Abstract

The interaction between ionomer (ion-conducting polymer) and catalyst particles in porous electrodes of electrochemical energy-conversion devices is a critical yet poorly understood phenomenon that controls device performance: electrode morphology is controlled by ionomer/particle interactions in precursor inks during electrode formation. In this chapter, we probe the origin of this interaction in inks to unravel the complexities of the ionomer/particle adsorption interactions. Quartz-crystal microbalance studies detail ionomer adsorption (with a range of charge densities) to model surfaces under a variety of solvent environments, and isothermal-titration-calorimetry experiments extract thermodynamic binding information to platinum- and carbon-black nanoparticles. Results reveal that under the conditions tested, ionomer binding to platinum is governed by a similar mechanisms but weaker magnitude as adsorption to carbon, suggesting that adsorption to platinum-on-carbon catalyst particles in inks is likely dictated mostly by entropic interactions with the carbon surface. Furthermore, water-rich solvents (relative to mixed water/propanol) promote ionomer adsorption, as first indicated by ink aggregation studies in Chapter 3. Finally, ionomer dispersions change with time as discussed in Chapter 4, yielding dynamic ionomer/particle binding interactions.

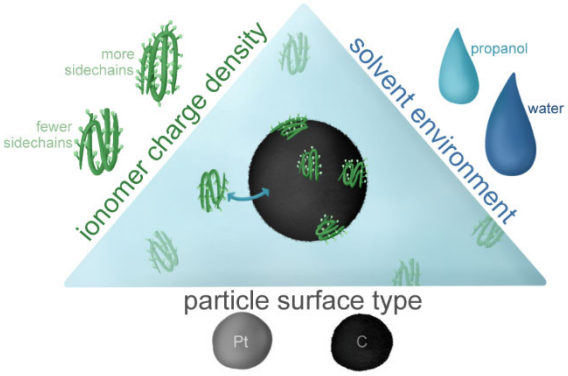

Figure 5.1. Schematic depicting a summary of Chapter 5: ionomer adsorption onto nanoparticles is affected by the charge density of the ionomer, the particle surface chemistry, and the surrounding solvent environment.

5.2 Introduction

Many studies have characterized dried catalyst layers (CLs) to understand structure-property-performance relationships.[8-10, 41, 88] However, little is known about how to direct specific structures during fabrication, which to date has been primarily empirical and thus non predictive. Enabling next-generation CLs and designing them *a priori* necessitates understanding the forces controlling

‡ This chapter was previously published as "Berlinger, S. A.; McCloskey, B. D.; Weber, A. Z., Probing Ionomer Interactions with Electrocatalyst Particles in Solution. *ACS Energy Lett.* 2021, *6*, 2275-2282." and is adapted with permission from all co-authors.

formation and structure, especially the ionomer/particle interaction (as discussed in Chapter 1).[82, 173] This ink-to-CL progression is depicted in Figure 5.2.

Solvent identity is a critical parameter that impacts ink properties and CL microstructure. The contrasting hydrophobic backbone and hydrophilic sidechains of perfluorosulfonic acid (PFSA, structure shown in Figure 1.4) have competing preferences in solution, and changing solvent type (including the water:propanol ratio, two common ink solvents) causes PFSA to adopt conformations that reflect this.[37, 54-56, 59, 67, 96-98, 146] (Here and throughout we mean "in solution" to mean dispersed in a solution of solvents. This does not suggest that the ionomer or nanoparticles are fully solubilized.) These different ionomer conformations (*i.e*. dispersion structures) affect the self-assembly of ionomer aggregates and the properties of their films post-drying (Chapters 2 and 3).[103, 148] Furthermore, different conformations will alter how the ionomer adsorbs to catalyst particles. Changing the water:propanol ratio affects the acidity of dispersions, impacting electrostatic interactions between the ionomer and particles.[67] Atomistic molecular-dynamics (MD) simulations reveal that both solvent and ionomer charge density (equivalent weight, EW, g polymer/mol SO_3^-) control ionomer adsorption to model carbon surfaces.[143] Additionally, there seems to be a hydrophobic interaction between the ionomer backbone and the carbon surface. Because the sidechains extend from the ionomer aggregate, this suggests that the sidechains are very flexible and can move out of the way during adsorption to allow the backbone the be accessible, the aggregate rearranges upon adsorption, or that smaller individual chains (and not large aggregates) are the adsorbing entities. The impact of solvent[50, 67, 70, 88, 95, 174-175] and particle type[68, 176] on ink aggregation is attributed to differences in ionomer/particle interactions, which propagate to impact the overall current-voltage behavior of the device.[12, 40, 47, 50, 60, 72, 75, 88, 90-91, 175] Metrics like ink zeta potential correlate well with mass activity, non-Fickian resistance, and limiting current density and depend on ink water:propanol ratios: maximum performance of each of these parameters is observed at intermediate water concentrations.[88] This can be explained by competing microstructural changes: increasing ionomer coverage of the agglomerates and increasing agglomerate size as ink water content increases.[88] Clearly, ionomer/particle agglomerates are impacted by the interactions between these components in solution. However, decoupling particle type, solvent, and EW influences on ionomer adsorption behavior remains a challenge.

In short, CL performance depends greatly on the ionomer/particle interaction. Despite the various previous investigations, fundamental questions remain regarding the specifics of this ink interaction: what is the mechanism for ionomer adsorption to particles? Does the ionomer preferentially interact with certain materials rather than others? How does the presence of different solvents alter this interaction? Answering these questions is vital toward understanding CL inks and eventual control of CL structure and performance. In this chapter, we explore these interplays by systematically measuring ionomer adsorption onto model surfaces (to understand the impact of platinum and surface hydrophobicity) with quartz-crystal microbalance (QCM) to screen adsorption as a function of solvent (water and *n*-propanol), EW, and surface type, as illustrated in Figure 5.2. For the majority of this study, we use 3M PFSA as a model ionomer due to the range of EWs available (refer to Figure 1.4 for 3M PFSA structure). To complement the QCM adsorption screening, we ascertain quantitative thermodynamic binding information (binding strength and mechanism) using isothermal titration calorimetry (ITC) on carbon and platinum nanoparticles.

We conclude by discussing how other important parameters, including dispersion age and sidechain chemistry alter binding behavior.

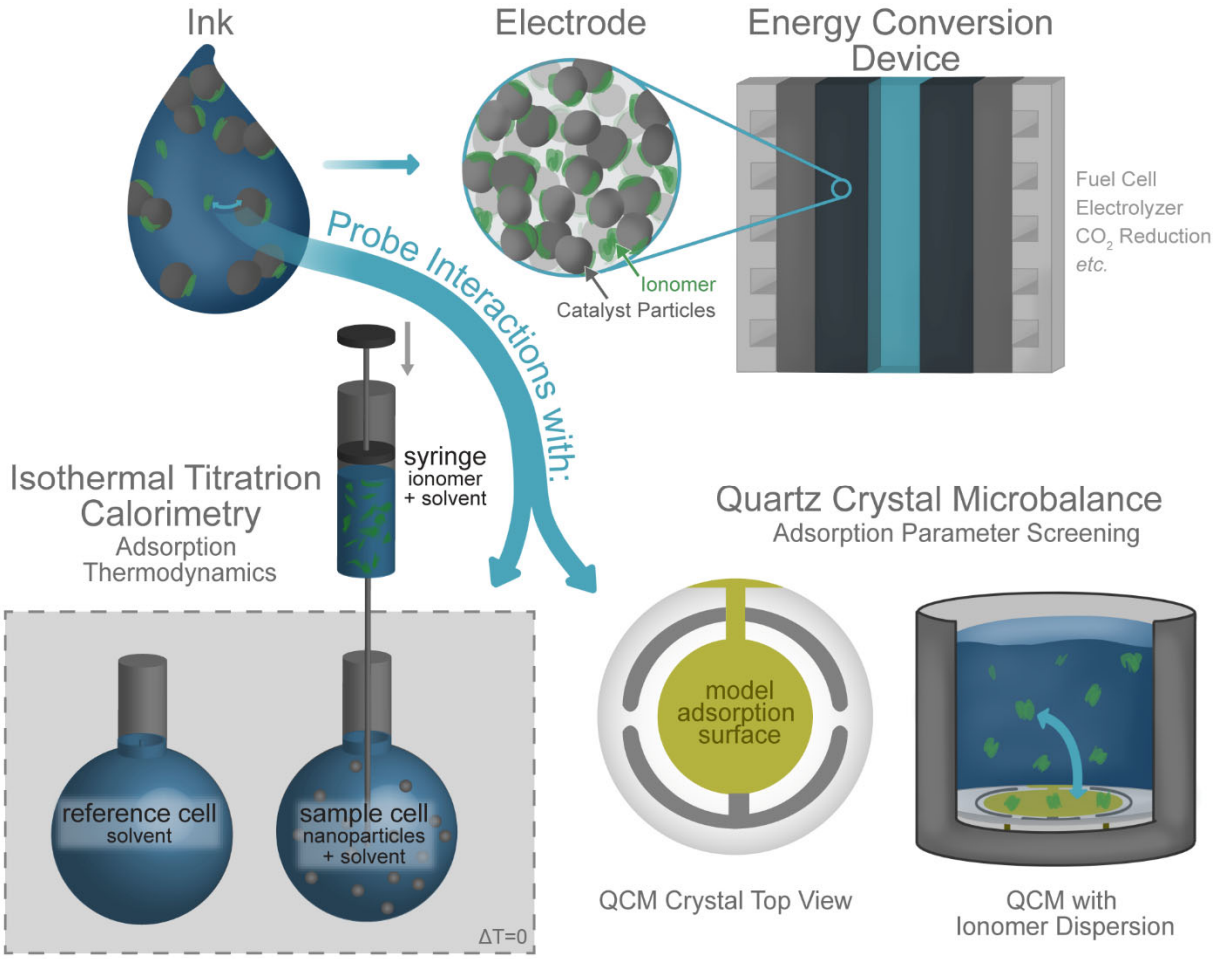

Figure 5.2 Ink-to-electrode progression, depicting that ionomer adsorption to catalyst particles impacts electrode structure. In this chapter, we probe these interactions with both isothermal titration calorimetry (adsorption thermodynamics) and quartz crystal microbalance (QCM, to screen the influence of solvent, surface type, and ionomer charge density parameters on adsorption) as illustrated.

5.3 Experimental Methods

5.3.1 Ionomers

For this study, two types of perfluorosulfonic-acid (PFSA) ionomers are used. The majority of the study employs 3M PFSA (structure shown in Figure 1.4) at three different equivalent weights (EW) to investigate the effect of sidechain density: 620, 825, and 1000 g polymer/mol SO_3^-. The tetrafluoroethylene (TFE) backbone spacing (x in Figure 1.4, where x indicates the number of TFE groups) is roughly 2.4, 4.5, and 6.2, respectively. The molecular weight (M_W) of the 3M polymers is roughly on the order of 250 kDa. We also compare 3M 1000 against Nafion 1100 (Ion Power, Inc.), shown in Figure 1.4 (x is 6.5). All dispersions were prepared by diluting the stock dispersion provided by 3M (or purchased from Ion Power, Inc. for Nafion) to the appropriate wt/v% in solvent (mixtures of water and *n*-propanol, *n*PA) as detailed below. All water used was 18 MΩ Milli-Q deionized (DI) water (Millipore). *n*PA was purchased from Sigma Aldrich (99.9% HPLC grade).

5.3.2 Quartz Crystal Microbalance (QCM) Experiments

5.3.2.1 Crystal Surface Functionalization

Adsorption of different 3M PFSA EWs (620, 825, 1000) in a variety of solvents (water:*n*PA ratios) onto model surfaces was studied using QCM (full parameter matrix reported in Table 5.1). The QCM technique relies on measuring the resonant frequency of the quartz crystal. Adsorbates on the crystal surface dampen the crystal's resonant frequency by increasing the force experienced by the crystal surface as it oscillates. Using a model (*e.g.* Sauerbrey or Voigt) one can convert frequency changes (Δf) to mass changes (Δm) with ng/cm^2 resolution. Frequently, the crystal surface is functionalized in some way to probe specific adsorbate/surface interactions. Here, to understand the impact of particle hydrophobicity (relevant for carbon supports) and metal type, model surfaces were chosen to encompass a range of surface wettability. 5 surfaces were studied: platinum, gold, one model hydrophobic, and two model hydrophilic surfaces. 1-inch 5 MHz AT-cut quartz crystals (Maxtek) were purchased with either polycrystalline gold or platinum surfaces. Platinum and gold crystals were used as received, following a DI-water rinse, ethanol rinse, and plasma-cleaning protocol. Model hydrophilic and hydrophobic surfaces were created on gold electrodes by first cleaning in the same manner, and then creating self-assembled thiol-based monolayers using 1-decanethiol (hereafter referred to as alkane-modified, hydrophobic), 11-mercaptoundecanoic acid (carboxyl-modified), and 11-mercapto-1-undecanol (hydroxyl-modified). The model hydrophilic surfaces were chosen to mimic the charged aspect of the carbon surface: Vulcan has a negative surface charge, and carboxylic acid is one of the most common functional groups on Vulcan. All thiols had greater that 97% purity and were purchased from Sigma Aldrich. Functionalization occurred in a custom-built cell that allowed only the front of the QCM crystal to contact the thiol solution. The front of the crystal was immersed in a 2 mM thiol solution in 200 proof ethanol (Koptek) for 24 hours in an inert nitrogen environment, before rinsing thoroughly in ethanol. For the carboxylic-acid thiol, pH of the thiol solution was also adjusted to

2 using 37% hydrochloric acid (OmniTrace, EMD Millipore), but otherwise had the same functionalization procedure. Upon rinsing, crystals were used immediately. Before every QCM experiment, the water contact angle of the crystal was verified using a goniometer with at least three droplets of ~100 μL each at different locations across the surface (to verify surface uniformity). Droplets were placed by contacting the droplet (released from a pipet) with the crystal surface. Contact angles and associated water-droplet images are shown in Table 5.1 and Figure 5.3, respectively.

Table 5.1. Parameter matrix of the 3M EWs studied (+ Nafion) in each solvent (reported as wt% water, balance *n*-propanol) per QCM surface type studied. Equilibrium water contact angles of the five surfaces are also reported in the last row.

Solvent (% Water)	platinum	hydroxyl-modified	gold	carboxyl-modified	alkane-modified
100	620, 825, 1000 (+Nafion 1100)	620, 825, 1000	620, 825, 1000	620, 825, 1000	620, 825, 1000 (+Nafion 1100)
70	620, 1000				620, 1000
50	620, 825, 1000				620, 825, 1000
30	620, 1000				620, 1000
Water Contact Angle (º)	19 ± 2	24 ± 4	52 ± 3	55 ± 5	105 ± 4

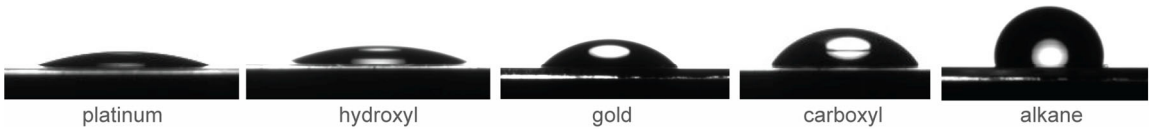

Figure 5.3. Water droplets (~100 μL) used to determine water-contact angles on the five QCM surfaces studies. Platinum and gold surfaces were supplied by the manufacturer. Hydroxyl, carboxyl, and alkane surfaces were prepared by creating self-assembled monolayers on the gold surface of 11-mercapto-1-undecanol (hydroxyl-modified), 11-mercaptoundecanoic acid (carboxyl-modified), and 1-decanethiol alkane-modified).

5.3.2.2 Experimental Protocol

All ionomer dispersions were prepared by diluting the stock dispersion (provided by 3M) with the appropriate solvents to 5 mg/mL, and sonicating for 20 minutes in a bath sonicator (Branson) equipped with custom temperature control set at 10°C such that the dispersions experienced no temperature rise during sonication. They were then used immediately. The low weight-percent value was chosen such that there were no discernible viscosity or density changes between the

pure solvent and the ionomer dispersion in the same solvent. (As will be described below, the frequency change due to adsorption is referenced to the frequency of the crystal in pure solvent. If the densities/viscosities were not matched, this frequency change upon flowing in ionomer dispersion would be a convolution of both the liquid property changes as well as adsorption.) Additionally, this ionomer concentration was not too high or too low such that the data depended on the ionomer concentration, but rather was dictated by the surface interactions. The solvents used to dilute the dispersions were 100, 70, 50, and 30 wt% water, balance *n*PA, and the final dispersions are referred to by these percentages. However, because the stock solution provided by 3M contained 25% polymer in a 75:25 ethanol:water mixture, the actual solvent composition of the dispersions is slightly different, because the native solvent of the stock dispersion must be accounted for. The actual solvent volume percentages are reported in Table 5.2.

Table 5.2. The composition of the final dispersion solvent, and the associated name used. Components are reported in weight percentages of the total solvent, rounded to the nearest half percent.

Dispersion Name	100% Water	70% Water	50% Water	30% Water
Water (%wt)	99	69	49.5	30
n-Propanol (%wt)	0	30	49.5	69
Ethanol (%wt)	1	1	1	1

After contact-angle verification, the crystal was loaded into the sensor cell, which was kept in an environmental oven (Thermotron) set at 25°C +/- 0.2°C. The sensor cell used for all experiments was a closed flow-cell holder with a sample chamber volume of roughly 200 µL (openQCM).

All experiments were conducted in an identical manner: the solvents, ionomer dispersions, and the sensor module (with the crystal) were equilibrated in the oven for 45 minutes. Then, the frequency of the bare crystal was recorded (and used as f_0 below in Equation S5.1) before pure solvent was introduced into the sensor chamber at a rate of 0.1 mL/min. The cell was flushed at the same rate for 30 min, to allow for mechanical equilibration. The frequency value at the end of this time period was set as the reference frequency to which further frequency change (Δf) was measured against. Example raw data are shown in Figure 5.4 (these are data for 3M 1000 on a gold crystal in 100% water, but they are representative for all experiments discussed). The equilibration time is seen prior to the dotted line in the region labeled “solvent,” with a Δf of zero.

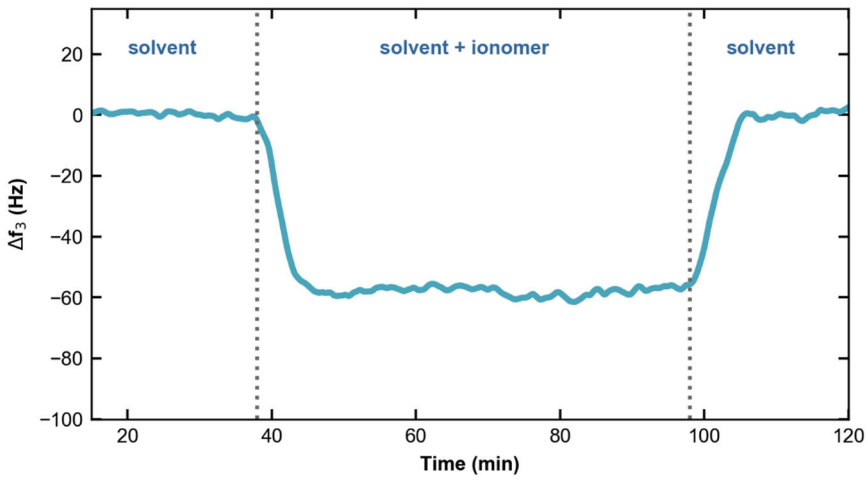

Figure 5.4. Example raw QCM data (for 3M 1000 on a gold crystal adsorbing from 100% water) depicting the frequency shift at the third overtone (Δf_3) relative to the pure solvent (here water) frequency and dissipation. Dashed vertical lines around 38 and 98 minutes indicate where feed solution was changed.

Taking care not to introduce any air bubbles into the feed lines, the 5 mg/mL 3M PFSA solution (dispersed in the same solvent used in the initial 30 minutes), was fed in at the same flow rate. This period is shown by the section designated "solvent + ionomer" between the two dashed vertical lines in Figure 5.4. The ionomer solution pumped through the cell for one hour while monitoring frequency continuously at the third overtone. This time period was purposefully longer than the initial adsorption period to ensure equilibrium was attained. The overtone was chosen to maximize the balance between signal-to-noise ratio and measurement sensitivity. The frequency change was taken to be the difference between the shift upon adsorption once the signal plateaued of the whole adsorption region, and the steady-state value of the crystal in contact with the solvent alone. After the one-hour adsorption (during which the signal plateaued indicating adsorption was complete), pure solvent was again pumped through the cell to monitor desorption. In all cases, the ionomer desorbed, indicated reversible adsorption, as seen in Figure 5.4.

To transform frequency data into mass data, both the Sauerbrey[177] and Voigt[178] viscoelastic models were assessed. While the viscoelastic properties of each of these EWs has not been fully characterized, they are likely not too dissimilar from Nafion, where there have been extensive mechanical-property measurements.[7] Using the shear modulus and viscosity of Nafion to guide a sensitivity analysis (discussed in Section 5.6), the Voigt model gave almost identical results to the Sauerbrey model (within 1 ng/cm^2). While the Sauerbrey model was originally derived for a rigid, solid layer, it gave very similar results to the viscoelastic model, and was therefore chosen to use for data analysis because of its transparent, linear transformation of frequency into mass. The Sauerbrey equation (Equation S5.1 in Section 5.6) requires only the frequency change (Δf) at a given overtone (n) order (as well as the bare crystal frequency which is a constant) to calculate the mass change (*i.e.* no additional assumptions); both the measured frequency change ($\Delta f/n$) and

calculated mass change (Δm) from Equation S5.1 in Section 5.6 are reported for the QCM plots in Section 5.4.1. Error bars represent propagated error of noise in one experiment (of the adsorption plateau region) and the standard deviation of multiple unique experiments.

By assuming an ionomer aggregate shape in solution, one can also calculate surface coverages on the QCM crystal. If we estimate the ionomer is a ~3nm x 10nm cylinder[96], with a density of 2.1 g cm^{-3} [113-114], we can predict 50 ng cm^{-2} (*i.e.* the areal mass measured in the QCM experiment) would correspond to a roughly 10% surface coverage, 400 ng cm^{-2} is 80% coverage, and 800 ng cm^{-2} is 160% coverage (values encompassing the range seen in Figure 5.6 and Figure 5.7). This greater-than-100% coverage could indicate multilayer adsorption. However, it is known that PFSA aggregate shape changes with solvent, and it is possible the aggregate density and shape also change with EW. No studies have measured the solution structures/densities of these ionomers in these solvent ratios at these concentrations; such an analysis is beyond the scope of this study. More accurate coverage estimates would require this information. Therefore, these predicted coverages are imprecise, and should be used only to observe general trends.

5.3.3 Isothermal Titration Calorimetry (ITC) Experiments

5.3.3.1 Experimental Details

The QCM data explore adsorption to model planar surfaces. This is important to understand the relative impact of surface type, EW, and solvent on the adsorption behavior of PFSA, but does not yield quantitative information regarding binding. Therefore, we conducted isothermal titration calorimetry (ITC) experiments in water using nanoparticles likely to be found in ink systems, to gain thermodynamic information regarding the ionomer/particle interaction. While ITC is traditionally employed as a biological tool to study macromolecule/ligand binding, it had been successfully used in similar systems,[179] and recently demonstrated with another PFSA chemistry.[180] The ITC technique allows one to calculate association constants (K_A), as well as decouple entropic and enthalpic contributions to binding free energy. In our ITC experiments, ionomer dispersions are titrated into a sample cell containing nanoparticles (in pure water) while the power required to keep the cell at a constant temperature is monitored. By integrating the power over time, adsorption heats and binding isotherms are measured. The data shown here are parameters (association constant, K_A, adsorption enthalpy and entropy) extracted from an independent (Langmuir) binding model fit with appropriate subtraction to remove heats of mixing/dilution. Additional fitting details are presented in Section 5.6.

Importantly, the QCM data suggests that the thermodynamics of binding are reversible (Figure 5.4), due to the relatively facile complete desorption profiles observed. This condition is necessary to apply appropriately ITC binding isotherms. The ITC sample matrix is shown in Table 5.3. For each of these conditions, we studied both fresh dispersions (prepared that day) and dispersions that were prepared two weeks prior and sonicated before using.

Table 5.3. Parameter matrix of the 3M EWs studied (+ Nafion) per nanoparticle type studied with ITC.

	Platinum black nanoparticles	Vulcan carbon nanoparticles
100% Water	620, 825, 1000 (+Nafion 1100)	620, 825, 1000 (+Nafion 1100)

To minimize noise in the measurement, all ionomer samples for ITC were dialyzed in water in 2000 MWCO cartridges (Thermo Fisher) prior to use and consisted of the same EW series used for the QCM data. Experiments were conducted on a NanoITC (TA Instruments). All ITC experiments used only water as the solvent to remove any heat of mixing solvent effects. The syringe contained 3.25 mg/mL ionomer, and the cell 0.5 mg/mL nanoparticle. Nanoparticle types included platinum black powder (TKK) and Vulcan XC-72 carbon (Fuel Cell Store), and were used as received. Every ITC binding experiment (polymer into particle) consisted of twelve 8 μL injections of polymer into particles, with an injection time of 900 seconds. The injection interval was determined by trial-and-error to ensure that all measurements returned to the baseline after each subsequent injection. A 4 μL injection preceding every experiment, to ensure no bubbles or diffusion during equilibration impact the results (this data point was omitted from subsequent analysis). Stir rate was kept constant at 150 RPM. The reference cell was filled with deionized water. Temperature was set to 25°C. Example representative binding data (for 3M 1000 into platinum black) is shown in Figure 5.5a. In all cases, minimal baseline drift was observed, indicating minimal secondary particle aggregation. This suggests that the added ionomer adsorbs to the nanoparticle aggregates, and does not induce excessive further aggregation (due to the lack of baseline drift). This is important to properly interpret the ITC data; if the nanoparticles were continuously aggregating during the course of the experiment, the surface area of the substrate would continuously change, rending interpretation difficult.

For every binding experiment (ionomer into nanoparticle), background controls (water into nanoparticle, ionomer into water, water into water) were measured to account for heats of dilution/mixing, and were subtracted from the binding experiment. Each peak was then integrated to obtain energy (enthalpy) per injection, and the total adsorption enthalpy was calculated. These data were fit to an independent binding isotherm, excluding the first injection (in TA Instruments NanoAnalyze software). The fit and data are shown in Figure 5.5b. From the isotherm fit, binding constants were determined (discussed more in Section 5.6). Error bars in the represent confidence intervals of this fit.

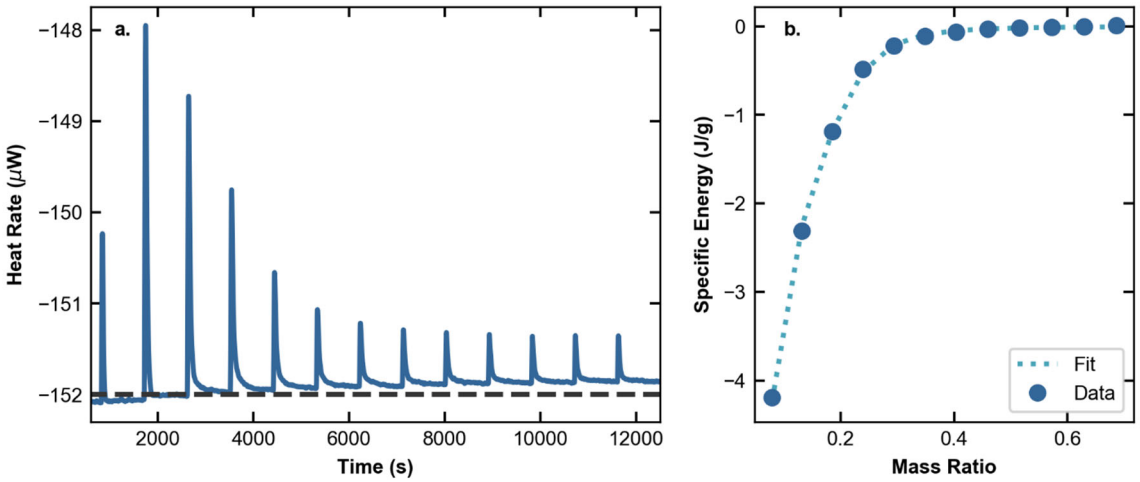

Figure 5.5. Example ITC data of 3M 1000 binding to platinum black. (a.) Raw ITC data, before background subtraction. The first injection is omitted in the fitting to ensure no air bubbles/diffusion of polymer during equilibration impacts the measurement. Minimal baseline drift (baseline indicated by dashed gray line) is observed. (b.) The same data, and the independent binding model isotherm fit to that data, as a function of mass ratio of polymer to particle.

The concentrations used in determining the binding constants are units of L/g; as such, the binding constants reported in Section 5.4.2 and 5.4.3 are specific, rather than molar, properties. These specific properties are useful to the community because literature reports ink properties on a weight basis, and it requires no assumptions to obtain these values. However, it is important to note that because a gram of platinum and a gram of carbon have a very different number of binding sites, one should not compare the binding-constant magnitude across different material types.

5.4 Results & Discussion

5.4.1 Adsorption Screening

Different solvents impact how the ionomer interacts with the catalyst particles and how these ionomer/particle aggregates interact with each other. In most ink-level studies, these two effects are extremely difficult to decouple. QCM is uniquely suited to study the ionomer/particle interaction: by holding the surface constant, thereby removing the impact of solvent on particle aggregation, one can systematically investigate the impact of solvent on ionomer adsorption to a surface. The most common surfaces found in these classes of electrocatalyst nanoparticles are platinum and carbon. Therefore, we use model platinum and functionalized-gold QCM surfaces to probe the ionomer/platinum and ionomer/substrate interactions across a range of different substrate hydrophobicities (a key parameter for carbon supports): hydrophobic (alkane-thiol self-assembled monolayers, SAMs) and hydrophilic (hydroxyl- and carboxyl-terminated SAMs) functionalized gold, as well as pristine gold and platinum surfaces. For each surface studied, the ionomer EW

(620, 825, or 1000 g/mol SO_3^-) and the solvent used to disperse the ionomer are varied, creating a substrate/EW/solvent parameter matrix (shown in Table 5.1). Although the planar QCM geometry differs from the spherical aspect ratio of nanoparticles, these results elucidate the relative importance of each parameter on PFSA adsorption from solution. By looking at the raw data, one can determine that ionomer adsorption to these surfaces is reversible (an example is shown in Figure 5.4), and that adsorption kinetics for all tested conditions proceed at the same rate Figure S5.12).

To explore the effect of solvent, the two EW (620 and 1000) and substrate (in terms of contact angle: alkane-thiol and platinum) extremes are used. Higher EWs indicate relatively fewer sidechains per gram of polymer, or greater sidechain spacing (more backbone tetrafluoroethylene groups, see Figure 1.3). 3M 1000 has the maximum spacing (equal to Nafion explored later) of the ionomers studied. The ionomers are dispersed in various water:*n*-propanol ratios. The frequency change of the quartz crystal due to ionomer adsorption in solvent, relative to the frequency of the crystal in pure solvent, and the associated adsorbed polymer mass is plotted in Figure 5.6.

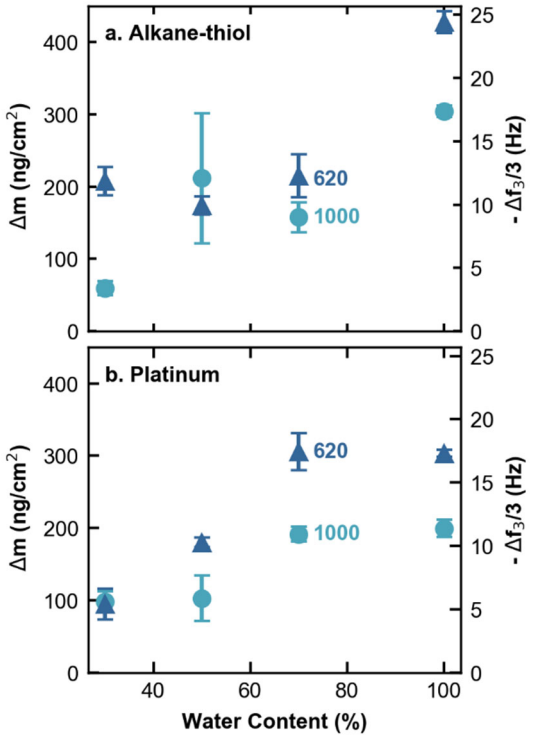

Figure 5.6. Frequency change (Δf) measured at the third overtone and associated mass change (Δm) due to ionomer adsorption in solution (as compared with pure solvent) on (a.) alkane-thiol and (b.) platinum model surfaces, respectively, for ionomers with EWs of 620 and 1000 g/mol SO_3^- dispersed in a range of water:*n*-propanol ratios, reported as weight percentage water.

Adsorption depends strongly on EW and solvent, in agreement with MD simulations.[143] Increasing water content from 30 to 100% promotes ionomer adsorption, likely a result of entropic hydrophobic interactions (as discussed below and consistent with the ITC results). This also agrees with the data presented in Chapter 3 Figure 3.6 which showed increasing aggregation of ionomer and catalyst particles at higher water contents.

If the interaction between the surfaces and the ionomer is driven by hydrophobic interactions, more water in the dispersion would induce hydrophobic entities in solution to minimize their contact area with water. This would cause both more ionomer backbone aggregation/association in the dispersion (*i.e*. phase partitioning of hydrophobic components), and also cause the ionomer to be less well-solubilized, driving adsorption to other surfaces (*i.e*. nanoparticles, the crystal surface, *etc*.). Because the adsorption trend holds across different surfaces types (the platinum and alkane-thiol surface), this suggests adsorption is controlled by solvent-driven interactions (*i.e*. hydrophobic interactions), rather than specific ionomer/surface interactions (although the magnitude of adsorption is indeed affected by surface type – and is greater on the hydrophobic alkane surface than the platinum surface). Previous Chapters established the micellar nature of the ionomer aggregates. To be consistent with that picture, hydrophobic association between the backbone and the particle or crystal surface indicates that either the sidechains are long and mobile enough to move out of the way during adsorption, smaller aggregates (or individual chains) are the adsorbates, or the ionomer conformation completely rearranges upon adsorption. Because adsorption is reversible (Figure 5.4), the latter option is likely not true, suggesting that either the smaller aggregates preferentially adsorb, or the sidechains are mobile enough to move and expose the backbone. Centrifugation adsorption studies to fractionate the ionomer aggregates according to size could reveal this, but that is beyond the scope of this study.

The conformation of the ionomer (as a result of ionomer/solvent interactions) also likely impacts adsorption behavior. Moving to the propanol extreme (0% water), adsorption again increases (see Figure S5.11). This increase is likely due to changing ionomer conformation: at the solvent extremes, the ionomer adopts a denser, smaller structure,[37, 59] that is likely able to pack and adsorb more readily than the swollen structures at intermediate water contents.

When comparing the 30% water-content results to the >80% water-content, 3M 1000 adsorbs roughly 200% more onto platinum surfaces and 3M 620 adsorbs about 300% more. These values correspond to ~20% coverage on the crystal at low-water contents to near-complete coverage at high-water contents (coverage estimates discussed in Section 5.6). A similar trend has been observed by AFM studies: more ionomer aggregates adsorb on platinum at higher water concentrations.[181] These adsorption differences are significant and dictate the amount of ionomer interacting with catalyst particle surfaces versus free in solution, the latter of which likely leads to large ionomer agglomerates upon drying and CL formation. Therefore, tuning the water:alcohol ratio directs how much ionomer adsorbs to particles, thereby controlling CL morphology/performance.[88, 175]

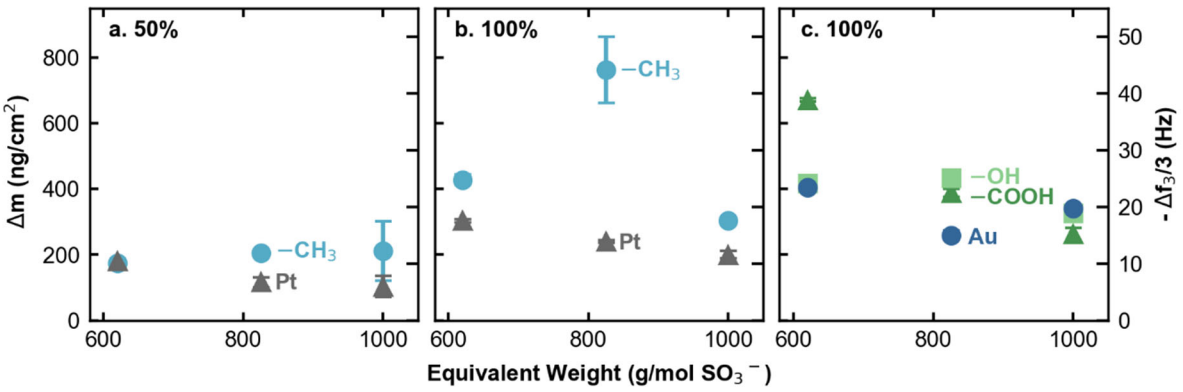

Figure 5.7. Frequency change (Δf) measured at the third overtone and associated mass change (Δm) due to ionomer adsorption in solution (as compared with pure solvent) for a range of EWs on surfaces with alkane (-CH_3), platinum (Pt), gold (Au), hydroxyl (-OH), and carboxyl (-COOH) functionality in (a.) 50:50 (wt%) water:*n*-propanol and (b.,c.) 100% water.

Figure 5.7 examines the relationship between EW and surface type. By comparing Figure 5.7a with Figure 5.7b, it is evident for all EW that more ionomer adsorbs to alkane-thiol and platinum surfaces in 100% water than in 50:50 (wt%) water:*n*-propanol (see Figure 5.6). In both solvent mixtures, as EW decreases, ionomer adsorption to platinum increases. This same trend is observed for the other hydrophilic surfaces studied in Figure 5.7c. Importantly, PFSA adsorption to platinum represents the lowest adsorption magnitude among the surfaces studied (in agreement with other studies that showed the PFSA/platinum interaction was weaker than the PFSA/gold interaction[62, 182]). Some hypothesize that there is a strong specific interaction between PFSA sulfonate groups and platinum, and that this interaction drives PFSA adsorption to catalyst particles in inks. However, we do not see indications of this (due to low adsorption), counter to other experimental evidence[61-63, 135] that shows sulfonate adsorption to platinum surfaces. This is rationalized because the platinum in those experiments was polarized (relative to the potential of zero charge),[183-186] while ours is under no applied potential. Additionally, in the *operando* PFSA/platinum interaction studies, the platinum is likely in a metallic state; conversely, the platinum surfaces here (and found in inks) will have some native oxide coverage, which has been shown to impact PFSA behavior.[187] Therefore, the PFSA/platinum interaction in solution versus in operating CLs is different, likely due to different surface charge states. An explanation as to why PFSA adsorption increases with decreasing EW could be that as the ionomer becomes more hydrophilic (as shown by increased acidity in Chapter 3),[59, 67] it can more readily interact with platinum; scattering studies show PFSA backbone chains orient on hydrophobic surfaces differently than they do on hydrophilic ones.[188-189] The PFSA/platinum interaction is discussed further below.

Based on the platinum adsorption trend, one might expect the opposite trend for the hydrophobic surface: as ionomer EW increases, so would adsorption. This is seen weakly in the 50% solvent environment, but the trend very obviously deviates for 100% water. In the 50% solvent, the ionomer has a loose, lamellar structure (given phase-diagram dielectric-constant predictions[59]), in

contrast with the tight, condensed rods observed at higher water contents.[37, 59, 67] This loose structure could result in high sidechain mobility, allowing for adsorption to scale with EW in a more linear manner than at higher water contents. With more collapsed conformations in pure water,[67, 96] it is reasonable to expect different trends. While additional solution structure data is needed to confirm this, it is possible that 3M 825 possesses an appropriate ratio of hydrophilic and hydrophobic moieties such that its conformation in water is optimal for adsorption to hydrophobic surfaces; ITC data presented in the next section confirms that 3M 825 also possesses the strongest binding constant among the ionomers studied to hydrophobic surfaces. Indeed, this may be consistent with the fact that 3M 825 is 3M's commercial dispersion for fuel cells. Additional reasons for the nonlinear EW trend could be due to differences in molecular weight[24] between the ionomers. However, because the trends change as a function of surface type and solvent, and because the molecular weights are so large (~250 kDa), we expect molecular weight effects to be secondary to the impact of EW. Of note, it is possible that in highly concentrated polymer regimes, these effects may have more influence.[190-191] To decouple EW and molecular weight effects, systematic studies of polymer series of the same EW with varying molecular weights should be conducted.

5.4.2 Thermodynamics of Binding

To gain quantitative thermodynamic binding information and delineate the ionomer/particle interactions, ITC is performed with the various ionomers and platinum or Vulcan-carbon nanoparticles, where the latter is typically used in CLs and, as will be shown, is approximated by alkane-thiol SAMs in the QCM experiments. Both freshly prepared dispersions (like those used in the QCM experiments) and aged dispersions (prepared two weeks prior and remixed before using) are studied. Figure 5.8 shows K_A for the three EWs on Vulcan carbon and platinum-black nanoparticles. Because the binding constants are on a gram basis, one should not compare values across different particle types (they will have a different number of binding sites per gram, molar data is presented in Figure S5.15). We first consider the new dispersion data. Notably, the EW trends on carbon and platinum are the same as those observed in the QCM experiments (Figure 5.7b): weaker binding is observed on platinum as EW increases, and binding to carbon has the same nonlinear EW dependence; the alkane-thiol surface is therefore a good proxy for Vulcan.

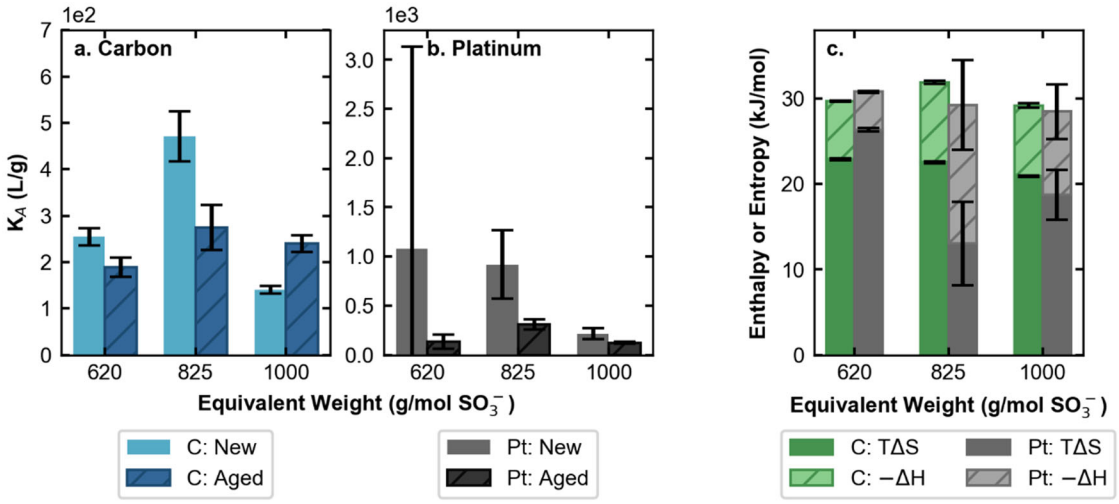

Figure 5.8. Association constants (K_A) of ionomer binding to (a.) carbon or (b.) platinum nanoparticles for freshly prepared (New) or older (Aged) dispersions as a function of ionomer EW in water. Note quantitative comparisons should not be made between (a.) and (b.) because K_A is on a gram basis. (c.) Stacked plot displaying the absolute value of the enthalpic and entropic contributions to the positive binding free energy for the New dispersions (all values indicate spontaneous adsorption).

The enthalpic (−ΔH) and entropic (TΔS) contribution to the positive free energy (|ΔG|=RTln[K_A]) for PFSA binding is plotted in Figure 5.8c (fitting discussed more in Section 5.6). Energy values are in agreement with those calculated for other ionomer isotherms,[180] and are similar or weaker than those observed for protein/surface interactions,[192-194] although quantitative values depend on molar-conversion assumptions (see Section 5.6). Immediately evident is that the entropic contribution is larger than the enthalpic contribution, regardless of EW or particle identity. Enthalpic signatures are representative of specific-binding, hydrogen bonding, *etc*., while spontaneous entropically-driven binding in aqueous solutions is often due to hydrophobic interactions.[192, 194] These entropic hydrophobic interactions arise (at small distances) because liberated water molecules (excluded solvent) gain entropy when surfaces come together, offsetting the loss in conformational entropy of the adsorbate. The entropically-driven ITC data are consistent with previous MD[143, 174, 176] and experimental[195] results that conclude adsorption to carbon surfaces is driven by hydrophobic interactions with the backbone. Interestingly, PFSA adsorption to platinum is also entropically-dominated, suggesting specific-binding between sulfonate and platinum (which would manifest as an enthalpic ITC signature) is not the primary ionomer/platinum interaction under these (non-polarized) conditions. This agrees with one study that noted the co-adsorption of fluorocarbon groups in addition to sulfonate at elevated potentials.[62] These results indicate that the ionomer/platinum interaction is not especially strong (at least compared to the ionomer/carbon interaction) in inks, and that adsorption to platinum is controlled by a similar mechanism as to carbon.

Therefore, given the larger surface area of carbon relative to platinum in most electrocatalyst particles, PFSA/particle adsorption (and subsequent aggregation) in inks is likely dominated by the PFSA/carbon interaction. Indeed, carbon treatment methods to tune the PFSA/carbon interaction have been successfully employed to control CL performance.[77, 196] Similarly, one metric often reported is the ionomer-to-carbon (I/C) ratio, where optimal ratios[23, 80, 83-84, 86, 144, 197] seem dependent on carbon type; given the results herein, ideal ratios will also likely vary with solvent and EW. The effect of particle surface functionality will be explored in Chapter 6.

5.4.3 Additional Parameters

Another consideration is how these PFSA/particle interactions vary with time. As discussed in Chapter 4, the dispersions change over time (from time of dilution), which will likely also impact how they interact with nanoparticles. PFSA conformational changes are evidenced by the significant change in dispersion pH[67] as a function of time (Figure S5.17), following the same trends exhibited by the Nafion data presented in Chapter 4. This corroborates the hypothesis that there is a slow equilibrium timescale for reorganization when these dispersions are prepared, and that they maintain some memory of their previous state (considering that pH changes are greater the more dissimilar the dispersion solvent is from its initial solvent). This is likely true for all PFSA systems, given the same behavior displayed by Nafion and 3M. Additional factors that could influence dispersion conformation over time could result from radical formation during sonication[198], although this is unlikely given the sonication power used here. These time-dependent results have critical implications for CLs cast from inks of different age, and may help explain changes in CL microstructure and performance.[166]

This increase in acidity indicates that there is a greater density of sidechains on the exterior of the ionomer aggregates. This would cause greater electrostatic repulsion between them, and perhaps limit the adsorption interaction strength onto nanoparticles. If the binding behavior of these dispersions is measured two weeks later, the interaction strength and trends change, as seen for the aged data in Figure 5.8. Indeed, the ionomer/particle interaction generally becomes weaker with time. However, the binding mechanism remains entropically driven (in fact, even more so as shown in Figure S5.16).

Finally, it is of interest to understand the role sidechain length and chemistry play on these interactions. To examine this, Figure 5.9 compares Nafion 1100 and 3M 1000 as they have same sidechain spacing but Nafion has a longer sidechain with an extra ether oxygen (see Figure 1.4). Within error, binding of these two ionomers to both particle types and adsorption to both QCM surfaces is the same. This indicates that EW is a stronger predictor of binding affinity than sidechain length, in agreement with model thin-film[199] and CL studies.[200]

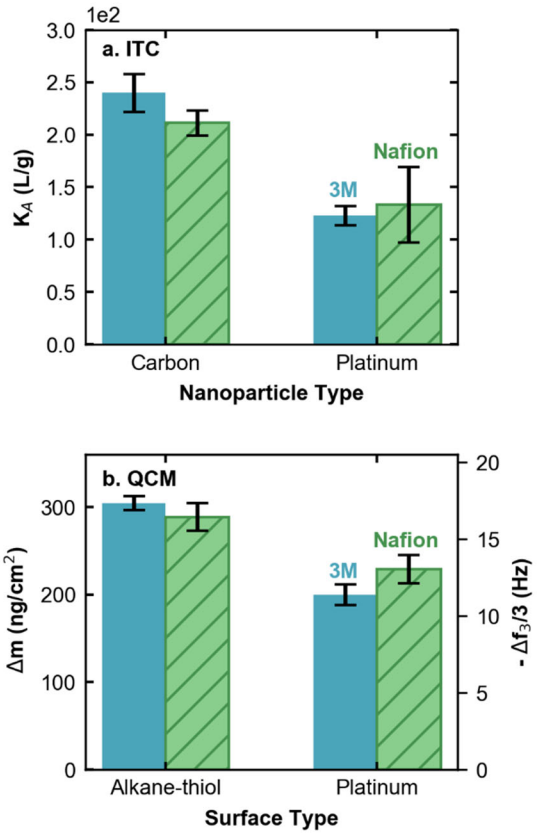

Figure 5.9. (a.) Association constants (K_A) of 3M 1000 versus Nafion 1100 binding on carbon and platinum black nanoparticles from ITC measurements. (b.) Frequency change (Δf) measured at the third overtone and associated mass change (Δm) due to ionomer adsorption (3M 1000 or Nafion 1100) in 100% water onto alkane-thiol-modified and platinum QCM surfaces.

5.5 Summary

In summary, we used both QCM and ITC data to understand the influence of solvent environment, EW, surface type, and sidechain length on PFSA adsorption. PFSA adsorption strongly depends on solvent environment: as the water:propanol ratio increases from intermediate water concentrations to high water concentrations, PFSA adsorption increases regardless of surface type, suggesting both that hydrophobic partitioning and ionomer conformation drive adsorption in water/alcohol solvents. When holding solvent constant, adsorption depends on EW and surface type. Interestingly, ITC data suggest the binding mechanism to platinum versus carbon is similar (entropic/hydrophobically driven). Given this, and considering that adsorption from ink-relevant solvents is lower on platinum versus hydrophobic QCM surfaces, it is likely that ionomer/particle aggregation in inks is dominated by ionomer/carbon rather than ionomer/platinum interactions, especially when considering the larger carbon surface area relative to platinum in many platinum-on-carbon nanoparticles. This is contrary to the hypothesis that sulfonate group/platinum

interactions control ink adsorption. While these sulfonate interactions dominate in operating devices, the QCM and ITC data presented herein suggest these interactions are not controlling in ink systems, where surface charge states of platinum (oxide) are different. Importantly, these ink interactions will control agglomerate microstructure formation, and thus will also control the amount of ionomer (and sulfonate groups) available to interact with the platinum surface once under applied potential. While additional work is needed to understand more completely how dispersions change with time, these ionomer/particle interactions are dynamic and have the potential to significantly influence ink aggregate structures (and eventual CL structures/interfaces).

The complex surface/EW/solvent parameter space explored in this chapter controls the forces between ink constituents and determines the CL microstructure upon drying; thus, the data presented herein is critical in unraveling the governing interactions and phenomena. More importantly, with this new understanding we can now engineer inks to promote (or demote) adsorption to specific surfaces in order to control optimal CL performance and electrode designs for many energy-conversion technologies.

5.6 Supplementary Information

5.6.1 QCM Model Sensitivity Analysis

To convert the frequency signal to a mass response, a model is required. The two most common are the Sauerbrey and Voigt Models. The Sauerbrey model is appropriate for thin, rigid solids in a vacuum, though is often used for many other systems. Here, the frequency response (Δf) is linearly related to a change in mass per area (Δm):[177]

$$\Delta m = -\frac{\sqrt{\rho_q \mu_q}}{2 f_0^2}\frac{\Delta f}{n} \tag{S5.1}$$

by a proportionality constant that depends of the material properties of the quartz crystal (the density, ρ, and the shear modulus, μ), the frequency of the unloaded crystal, f_0, and the overtone the crystal is driven at, n. This model is often used because of its simplicity.

The Voigt model is more complex. For thin polymer layers adsorbed to a surface, immersed in a liquid, the frequency response may be written as[178]

$$\Delta f \approx \frac{1}{2\,\pi \rho_q h_q}\left(\frac{\eta_l}{\delta_l} + h_p \rho_p \omega - 2h_p \left(\frac{\eta_l}{\delta_l}\right)^2 \frac{\eta_p\,\omega^2}{\mu_p^2 + \omega^2 \eta_p^2}\right) \tag{S5.2}$$

Here, subscripts l, p, and q, denote properties of the liquid overlayer, polymer adsorbed layer, and quartz crystal, respectively. h represents the layer thickness (so $h_p \rho_p$ represents the areal mass density Δm given by Sauerbrey). The viscoelastic properties are given by the shear viscosity, η,

and shear modulus, μ. ω is the angular frequency of oscillation, and δ is the viscous penetration depth (how far the shear-wave propagates), given by

$$\delta = \sqrt{2\frac{\eta}{\rho\omega}} \tag{S5.3}$$

According to the Voigt model, the viscoelastic properties of the polymer, as well as the properties of the solvent overlayer, affect the frequency response. To assess how much they alter the results as compared with using the Sauerbrey, we performed a sensitivity analysis.

For this sensitivity analysis, we simulated the frequency response of a film with properties similar to ours (as described below), to understand what the frequency response would be for identical films if fit by either the Voigt model or the Sauerbrey model. First, we evaluated the impact of polymer viscoelastic properties. The properties of hydrated 3M at each of these EWs have not been measured, however, extensive mechanical tests have been conducted on similar PFSAs (largely Nafion).[7] Likely, the addition of more sidechains (in the case of 3M 620 and 825) will alter the shear modulus, and so using Nafion properties as a guide, we chose values that are much lower and higher than would be expected for similar systems[7] (in order to ensure we cover the whole range of possible values) using Poisson's ratio[201] to convert from Young's modulus to shear modulus. We performed a similar sensitivity analysis on shear viscosity, using value ranges extrapolated from literature,[202] and there was minimal impact on the frequency response (viscoelastic properties are dominated by the high modulus). Therefore, to assess the impact of viscoelastic properties, viscosity was held constant, the overlayer was set to water, and modulus was varied as described above. The results of this are shown in Figure S5.10a, where the y-axis displays the calculated frequency difference between the two models. The Voigt model did not change the expected frequency response in an appreciable manner (perhaps one or two Hz for thin layers).

To assess impact of liquid overlayer properties, we held the polymer layer properties constant (using an intermediate value of shear modulus), and varied solvent properties, as shown in Figure S5.10b. The Voigt model correction to Sauerbrey is even smaller in this case. Obviously, these effects can compound each other, but should only provide a minor correction of a few Hz that is within error of the measurement. These polymers are sufficiently stiff such that the solid approximation used by Sauerbrey is sufficient.

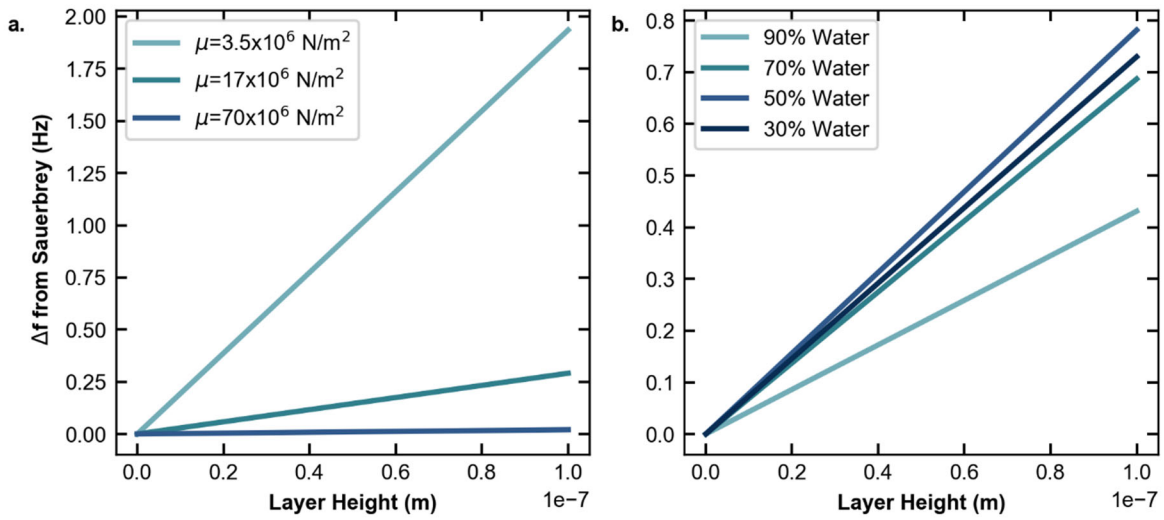

Figure S5.10. Calculated deviation from the Sauerbrey model as a function of layer thickness for a thin polymer layer immersed in an infinite liquid overlayer. (a.) Varies the value of shear modulus, while holding the shear viscosity constant at 2 x 10^{-1} Ns/m^2. The overlayer properties are that of water. (b.) Examines the effect of changing the solvent overlayer using the properties of water and *n*-propanol mixtures (water percentages are balanced by propanol), setting the polymer layer properties to μ = 17 x 10^6 N/m^2 and η = 2 x 10^{-1} N/m^2. Density of the PFSA film was assumed to be 2 g/cm^3.[113-114]

It is worth noting that the modulus of the adsorbed film may not be that of a thin film, and that the layer may not be homogeneous. However, there is no QCM theory model currently that accounts for this two-phase physics.

5.6.2 Adsorption Behavior

5.6.2.1 Water Content

To complement the data in the chapter's main text, we also extended the 3M 1000 adsorption data to the propanol extreme (0% water, 100% propanol) as shown in Figure S5.11. Only 3M 1000 was explored at the propanol extreme due to limited availability of 3M 620. Here, we see a U-shaped behavior, where adsorption magnitudes start increasing again in the absence of water. The beginning of this upturn can also be observed for 3M 620 in the 30% water environment. This increase at both extremes is likely due to changing ionomer conformations: at the extremes, the ionomer adopts a smaller, more micellar structure,[37, 59] which is likely able to pack and adsorb more readily than the swollen structure at intermediate water contents.

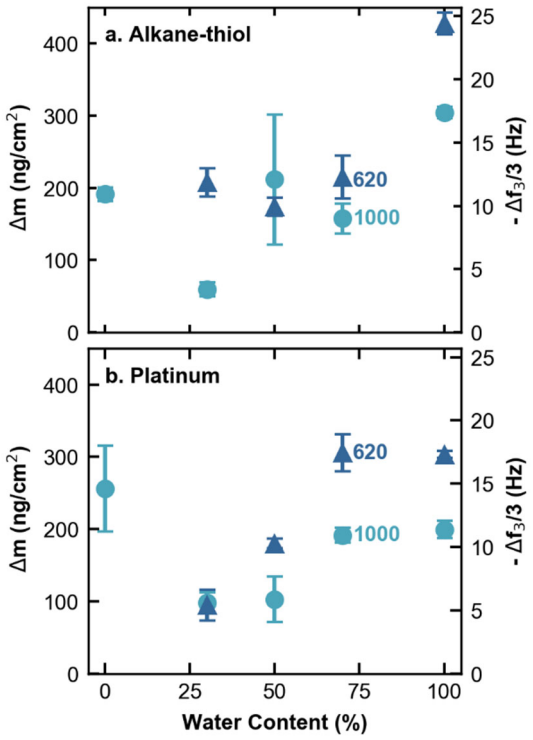

Figure S5.11. Frequency change (Δf) measured at the third overtone and associated mass change (Δm) due to ionomer adsorption in solution (as compared with pure solvent) on (a.) alkane-thiol and (b.) platinum model surfaces, respectively, for ionomers with EWs of 620 and 1000 g/mol SO3- dispersed in a range of water:*n*-propanol ratios, reported as weight percentage water.

5.6.2.2 Adsorption Kinetics

By looking at the adsorption kinetics, one may also learn something about the PFSA binding behavior. In Figure S5.12, we plot the raw QCM data, in which solvent flows in before time zero, and, at time zero, solvent/ionomer dispersion is introduced into the feed lines. The initial lag is due to the time it takes for the ionomer to move through the tubing and reach the sensor cell. The frequency change (Δf) of the adsorbed ionomer (*i.e.* frequency of ionomer/solvent dispersion minus that of pure solvent) is normalized to the maximum frequency change (adsorption plateau value) such that all the frequency changes scale between zero and one. Figure S5.12 shows an overlay of data from many representative experiments, spanning the entire range of solvent/EW/surface-type parameter space studied here. Based on this, it is clear that the slopes of all the adsorption curves, as well as the point where they plateau, are very similar, suggesting the adsorption kinetics are not controlled by any of the experimental parameters. It is also not limited by the amount of ionomer flowing into the cell. In fact, the amount that adsorbs is significantly less than the total ionomer flowing through the cell. The dispersion flows at a rate of 5 x 10^5 $ng_{ionomer}$/min, which is significantly in excess of the amount that adsorbs (on the order of 100 s of

nanograms). Therefore, adsorption of PFSA to the QCM crystal, regardless of EW, surface type, or solvent, proceeds in a similar manner.

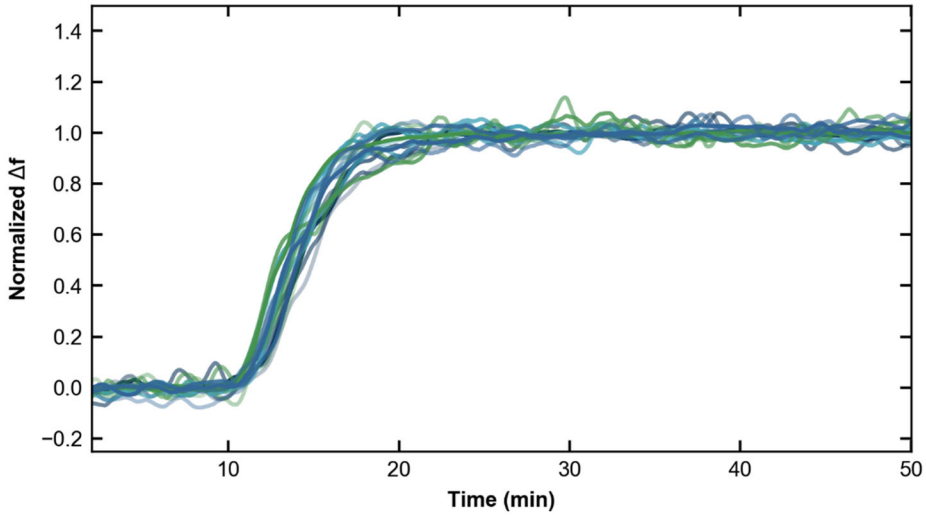

Figure S5.12. Frequency change divided by maximum frequency change (normalized Δf) for fifteen representative experiments encompassing all solvents, equivalent weights, and surfaces studied as a function of time from which dispersion is introduced.

5.6.2.3 Surface Contact Angle Screening

From the ITC data, it is clear that hydrophobic interactions are important in dictating PFSA adsorption. Therefore, we transform the adsorption data in Figure 5.7 by plotting adsorption as a function of the contact angle of the surface for PFSA adsorption (see Table 5.1) in pure water, as shown in Figure S5.13.

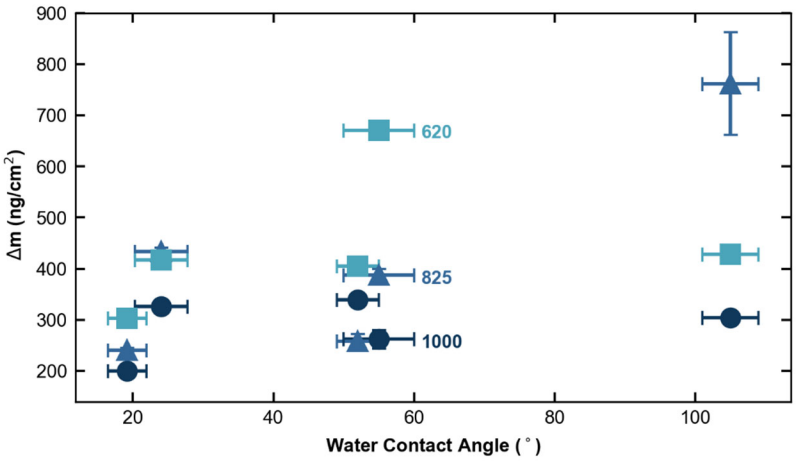

Figure S5.13. The calculated mass change (Δm) for adsorption of 3M PFSA of different EWs in pure water, as a function of the water contact angle of the surface it adsorbs to.

Generally, when comparing the contact-angle extremes, more ionomer regardless of EW adsorbs onto the highest contact-angle than the lowest contact-angle surfaces. In the intermediate contact-angle regions, 825 displays no clear trend, while 3M 620 and 1000 are mostly constant as a function of surface type, with the exception of the carboxylic-acid surface (around 55°). Likely, the carboxylic-acid surface deviates from this trend due to hydrogen-bonding effects, consistent with the fact that the binding enhancement increases with the number of sidechains. The lack of strong trend with contact angle corroborates the data in Figure 5.6 and Figure 5.7 that adsorption is primarily dictated by ionomer/solvent interactions. Of note, these trends are in pure water and may change when dispersed in different solvents.

5.6.3 ITC Fitting

As discussed in Section 5.3, in an ITC experiment, we measure power as a function of time during sequential injections (refer to Figure 5.5). These power spikes can be integrated to get the energy as a function of how total injection amount. Example data for 3M 1000 binding to carbon (Vulcan carbon black nanoparticles) are shown in Figure S5.14. Data are fit to an independent binding isotherm model in NanoAnalyze (TA Instruments).

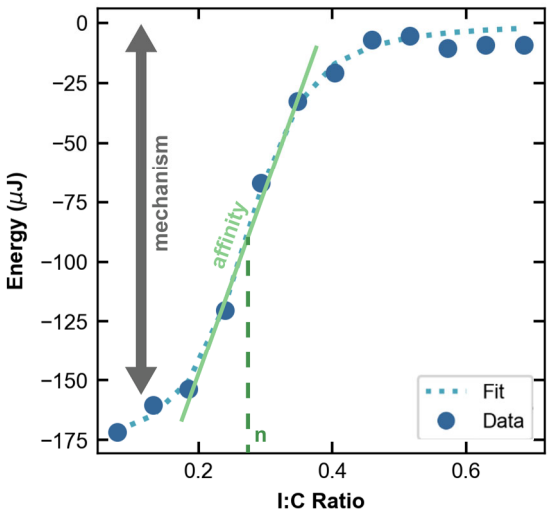

Figure S5.14. Data of sequential injections of ionomer (3M 1000) into carbon nanoparticles, as a function of the ionomer-to-carbon (I:C) weight ratio in the sample cell. The dotted light blue line is the independent binding model fit to the data. The total energy (enthalpy) change is indicative of the binding mechanism, the slope of the curve gives the binding affinity (K_A) and the concentration to reach 50% saturation gives the binding stoichiometry, n.

Generally, the adsorption may be written as a reaction

$$\mathrm{I} + \mathrm{P} \overset{K_A}{\Leftrightarrow} \mathrm{IP} \tag{S5.4}$$

in which ionomer (I) and particles (P) combine to form an ionomer-particle complex (IP), with a forward reaction given by the association constant, K_A (the reverse reaction is given by the dissociation constant, K_D). K_A is given by the concentrations of all species:

$$K_A = \frac{[\mathrm{IP}]}{[\mathrm{I}][\mathrm{P}]} \tag{S5.5}$$

The units of the association constant are therefore inverse concentration. One may write the particle fractional coverage, θ

$$\theta = \frac{K_A[\mathrm{I}]}{1 + K_A[\mathrm{I}]} \tag{S5.6}$$

The heat released, Q, is related to the heat of adsorption, ΔH_{ads}

$$Q = Vn\Delta H_{ads}[P]\theta \tag{S5.7}$$

where V is volume and n denotes any binding stoichiometry (that may modify the above reaction equations). Each differential heat,

$$\Delta Q_i = Q_i - Q_{i-1} \tag{S5.8}$$

is regressed. The association constant is related to the slope of the fit line, and the total energy change reveals information about the binding mechanism. The above analysis holds whether the units are defined on a gram or mole basis. However, to calculate the free energy (ΔG_{ads}) and entropy (ΔS_{ads}) of adsorption, one must use molar units and the following equations:

$$\Delta G_{ads} = RT \ln K_A * [1\ M] \tag{S5.9}$$

$$\Delta S_{ads} = \frac{\Delta H_{ads} - \Delta G_{ads}}{T}$$

where T is temperature, R is the ideal gas constant, and the free energy is calculated using a reference concentration of 1 M.

5.6.4 Molar Conversion of ITC Data

To extract the entropy of adsorption, concentrations used in the binding isotherm must be on a molar basis. However, converting the mass concentration of PFSA (with an unknown and possibly changing molecular weight across the EWs) and nanoparticles to molar concentration is not straightforward. Therefore, we used the molar concentration of monomers for the PFSA concentration, by dividing the mass concentration by EW. 3.25 mg/mL PFSA yields 3.25 mM 3M 1000, 3.94 mM 3M 825, and 5.24 mM 3M 620. To obtain moles of nanoparticles, we calculated the moles of binding sites, effectively normalizing the mass concentration by surface area. By taking into account density of platinum (21.45 kg/m^3) and Vulcan (2.64 kg/m^3) nanoparticles, particle size (primary particle diameter for Vulcan set at 50 nm and for platinum black at 30 nm), and binding site size (we assumed this was the projected area of the solution aggregate size,[54-55, 96] as discussed in the coverage section above), we calculate the carbon and platinum concentrations to be 0.054 mM and 0.0011 mM binding sites, respectively. These molar concentrations were then used to extract the entropic and enthalpic contributions to the free energy. Importantly, the quantitative values of these parameters may change as a function of the molar-conversion

assumptions. For this reason, binding constant data in the main text are reported in mass units (requiring no assumptions) rather than molar units. However, the trends extracted from the molar conversion should remain the same, regardless of exact quantitative values used as model inputs. The molar binding constants (association constants, K_A) extracted from the independent binding model are presented in Figure S5.15 for both fresh and two-week old dispersions. These complement the gram-basis K_A values shown in Figure 5.8.

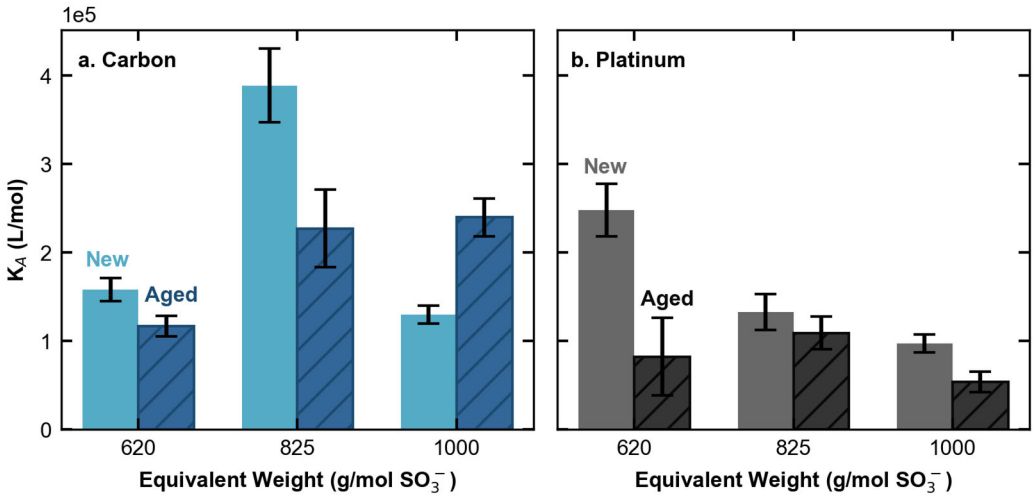

Figure S5.15. Association constants (K_A) of ionomer binding to (a.) carbon or (b.) platinum nanoparticles for freshly prepared (New) or older (Aged) dispersions as a function of ionomer EW in water.

It is important to note that all ITC experiments were conducted in pure water. Additional experiments in other solvents are necessary to understand fully the thermodynamics of binding as a function of solvent concentration.

5.6.5 Dispersion Ageing

To see if the binding mechanism changes for dispersions measured two weeks after sample preparation, the entropic and enthalpic contributions to the free energy are shown in Figure S5.16 (new dispersions shown in Figure 5.8c). The aged dispersions exhibit the same trends as the new dispersions: namely, that the entropic contribution dominates over the enthalpic one. In fact, when comparing this data with Figure 5.8c, it is seen that the entropic fraction is actually slightly larger in these aged dispersions.

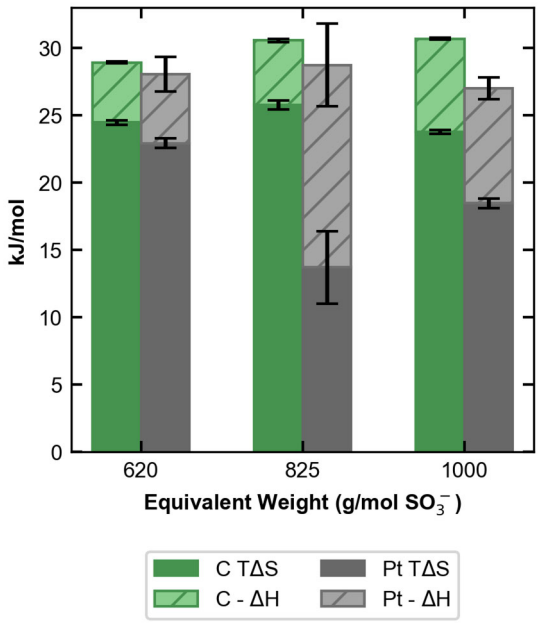

Figure S5.16. The enthalpic and entropic contributions to the binding free energy to carbon and platinum for aged dispersions of varying EW.

Clearly, these dispersions change with time. To probe this further, we looked at the 3M dispersion pH (proxy for ionomer conformation, as shown in Chapter 3[67]) as a function of time, as we did in Chapter 4 with Nafion. To do so, we prepared dispersions of 5 mg/mL 3M PFSA (either 3M 1000 or 3M 620) in 100% water or a mixture of 50 wt% water:50 wt% *n*PA. They were sonicated for 30 minutes, and then allowed to equilibrate for 45 minutes at room temperature. The pH of the dispersions was then measured with an Orion Star A211 pH meter and a ROSS Ultra Triode pH/ATC probe (Thermo Fisher Scientific). The probe was calibrated before each use with appropriate known standards. Samples were stirred at 400 RPM for the course of the pH measurement. The dispersions were then stored at room temperature, and their pH was measured each day over the course of ten days. Three unique dispersions for each sample set were measured and monitored for this length of time. The results of this are shown in Figure S5.17. As seen in Chapter 4, the dispersions in 100% water become quite a bit more acidic over time, while the 50% water:*n*PA dispersions exhibit less of a change. All dispersions seem to stabilize after approximately one week, and their final pH values are consistent with those previously reported for Nafion as a function of water concentration (Chapter 3).[67] As discussed in Chapter 4, it is possible that these dispersions maintain a memory of their previous solvent environment and take a while (longer than the mixing time) to equilibrate to the new solvent. However, unlike the Nafion dispersions explored in Chapter 4, the stock 3M dispersions come in 25% water/75% ethanol. Because higher alcohol concentrations are expected the exhibit less acidic behavior, that could explain why the dispersions prepared in 100% water display a large increase in acidity (solvent

environment is very different initially), while those in 50% do not (*i.e.,* solvent environment is more similar).

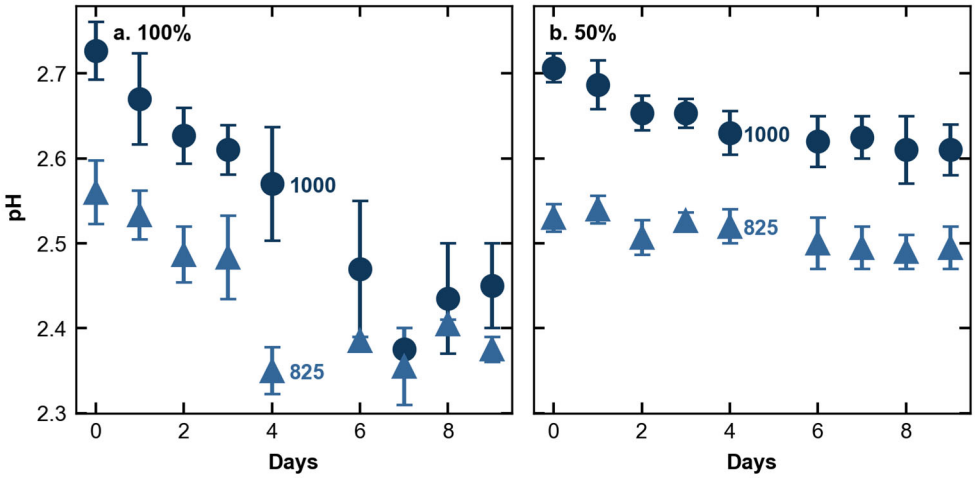

Figure S5.17. pH of 3M 1000 and 3M 825 in either (a) 100% water or (b) 50% water/50% *n*-propanol measured as a function of the days after sample preparation.

6 Fuel-Cell High-Current-Density Performance and Platinum Loading: Insights from Catalyst/Ionomer Ink Interactions‡

6.1 Abstract

Catalyst layers (CLs) are heterogeneous structures, often with uneven ion-conducting polymer (ionomer) coverage and underutilized catalyst. Various platinum-supported-on-carbon nanoparticles are used, but little is known about how or why changing the primary particle loading (PPL, or weight fraction of platinum on a carbon support) impacts performance. By investigating CL gas-transport resistance and zeta potential (ζ) of corresponding inks as a function of PPL, a direct correlation between CL high-current-density performance and ink ζ is revealed. This correlation stems from changes in ionomer distribution as a function of PPL as observed by pH, ζ, and impedance measurements. These findings are critical to unraveling ionomer distribution heterogeneity in the CL and enabling enhanced Pt utilization and improved device performance for fuel cells and related electrochemical devices.

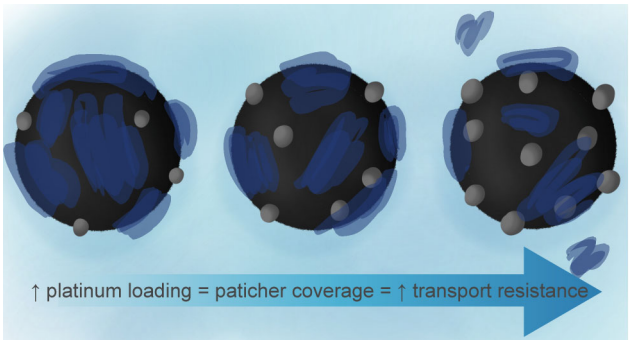

Figure 6.1. Schematic depicting a summary of Chapter 6: as platinum primary particle loading increases, ionomer coverage on the particle's surface becomes patchier thus increasing transport resistance in catalyst layers.

6.2 Introduction

As discussed in the preceding chapters, polymer-electrolyte fuel cells (PEFCs) present an attractive clean-energy alternative to conventional energy sources in myriad sectors, especially transportation. However, their wide-scale commercialization is limited due to high costs associated with the use of platinum (Pt) in their catalyst layers (CLs). Unfortunately, reducing CL Pt loading induces significant transport losses and poor performance, particularly gas-transport losses in the

‡ This chapter will be published as, "Berlinger, S. A.*; Chowdhury, A.*; Van Cleve, T.; He, A.; Dagan, N.; Neyerlin, K.C.; McCloskey, B. D.; Radke, C. J.; Weber, A.Z., Fuel-Cell High Current-Density Performance and Platinum Loading: Insights from Catalyst/Ionomer Ink Interactions, *in preparation*." and is adapted with permission from all co-authors. * indicates co-first author.

cathode CL.[17, 86] Mitigating these losses while maintaining low Pt loadings is paramount to the widespread deployment of this technology.

As described in Chapter 1, CLs in PEFCs are complex porous-electrode structures consisting of agglomerates of Pt-supported-carbon catalyst particles (referred to hereafter as catalyst particles) and ion-conducting polymer (ionomer) binder.[6, 11] Of note, the platinum loading on this carbon support (termed primary particle loading, PPL) and the ionomer-to-particle weight ratio (typically expressed as ionomer-to-carbon, I:C) can vary. The carbon, platinum, ionomer, and void-space pathways create a triple percolated network for the transport of various species to and from the reaction sites: reactant gas (H_2, O_2), product water, protons (H^+), and electrons (e^-). Using microscopy,[203-208] ptychography,[209] and tomography[8, 21, 210] techniques, studies have revealed the heterogeneous nature of CL structures: there are non-uniform ionomer distributions (with a significant fraction of Pt not in direct contact with ionomer), isolated ionomer domains, and wide variability of agglomerate sizes and ionomer film thicknesses. When platinum particles are not near or in contact with the ionomer, they do not contribute to the electrochemical surface area (ECSA). Optimizing CL structure with well-distributed phases is essential to allow for efficient species transport and high Pt utilization (and therefore reduced capital costs).

As described in Chapters 1 thru 5, CLs are fabricated from inks containing catalyst particles and ionomer dispersed in solvent (typically water:alcohol mixtures). The interactions between the components in solution govern how these agglomerates self-assemble (Chapter 3) and how the ionomer adsorbs to the catalyst particles (Chapter 5).[27, 70, 211] Upon drying, these ink-level interactions manifest and control the eventual CL microstructure, the nature of the ionomer/particle interface, and the properties of the ionomer (Chapters 2 and 4). Ink properties (*e.g.*, ink zeta potential, ζ, agglomerate size, *etc.*) have been shown to correlate well with CL performance (mass activity, gas-transport resistance, *etc.*) as a function of ink water:alcohol ratio[46] and I:C ratio[212]. Importantly, the surface chemistry of the catalyst particles (platinum content and distribution, carbon identity, *etc.*) alters how the ionomer interacts with them, as evidenced by rheological measurements.[68] Furthermore, the calorimetry and adsorption measurements of Chapter 5 reveal that when subject to no applied potentials, binding strengths of ionomer are higher on hydrophobic (carbon) surfaces than on platinum surfaces when using Nafion (a prototypical ionomer, although depending on ionomer charge density this relationship may change, as discussed in the preceding chapter).[169] One would therefore expect that as the PPL varies (*i.e.* the surface area of platinum relative to carbon), ionomer/particle interaction strengths would differ (decreasing interaction with increasing platinum surface area), which could propagate to impact device power output. Higher PPL is also known to result in larger Pt nanoparticle size.[22, 213]

In this study, we probe the influence of PPL on both ink and CL properties, using Vulcan-supported particles and Nafion as a model support and ionomer, respectively. Ink ionomer/particle interactions are explained with ζ and pH measurements as a function of I:C. We link ink interactions to CL properties by investigating both gas-transport resistance and ζ of corresponding inks as a function of PPL. Additionally, CL findings are validated by double-layer capacitance and H^+ transport-resistance measurements. In this way, we probe the influence of carbon and platinum surface area (SA) on ink properties to understand how they determine CL transport, revealing important implications for controlling ionomer distribution heterogeneity and Pt utilization.

6.3 Experimental Methods

Ink preparation and measurements: Inks for electrode fabrication were prepared by dispersing ionomer dispersions* (Nafion®, D521, Ion Power, Delaware, USA) and Pt-nanoparticle catalyst supported on Vulcan carbon (TEC10V10E, TEC10V30E and TEC10V50E from TKK, Tokyo, Japan) in a solvent mixture of 18 MΩ deionized water (Millipore Milli-Q® IQ 7000 Water Purification System, Millipore Sigma, Massachusetts, USA) and *n*-propyl alcohol (>99.9 % purity, Sigma Aldrich, Missouri, USA) in a 1:1 weight ratio. For bare carbon samples, Vulcan XC72 was used (Fuel Cell Store). The carbon-to-solvent weight ratio was kept constant at 0.03 wt. % for low Pt-loading electrode samples (0.05mg/cm^2 electrode geometric surface area) and zeta-potential measurements. For higher Pt loading samples (0.1mg/cm^2 electrode area), the carbon-to-solvent weight ratio was increased to 0.1 wt.%. All inks were manually agitated followed by sonication for 30 minutes in a bath sonicator (Branson) maintained at 10°C using a water recirculatory/chiller (F25-HL Refrigerated - Heating Circulator, Julabo Inc, Pennsylvania, USA). Zeta potentials of the inks were measured immediately after sonication via electrophoretic light scattering (NanoPlus3, Micromeritics, Georgia, USA), modeled using the Smoluchowski equation.[67] To understand ionomer/particle interactions in inks fundamentally, pH measurements were conducted of inks containing a wide range of I:C ratios. Inks were prepared in a similar manner as above, with a fixed carbon-to-solvent ratio of 0.1%, dispersed in varying ionomer concentrations using diluted ionomer (Nafion®, D2021, Ion Power, Delaware, USA). pH measurements were taken with an Orion Star A211 pH meter and a ROSS Ultra Triode pH probe with automatic temperature compensation (ATC) (Thermo Fisher Scientific). The probe was calibrated before each use with appropriate known standards. Samples were stirred at 400 RPM for the course of the pH measurement; most samples equilibrated in less than thirty seconds.

Electrode fabrication: Electrodes were prepared by spray coating inks using a Sono-Tek ultrasonic spray coater and a 25 kHz AccuMist nozzle (Sono-Tek Exacta Coat, New York, USA). The working electrode (WE) was spray-coated onto a NR212 Nafion membrane (Ion Power, Delaware, USA) while the counter electrode (CE) was spray-coated on the gas-diffusion layer (GDL) (Sigracet 25BC, SGL Wiesbaden, Germany). In the WE, the total Pt mass loading was maintained at 0.05 mg/cm^2 and 0.1mg/cm^2 for CL gas-transport resistance and EIS measurements, respectively. CE utilized a total Pt loading of 0.3mg/cm^2. Nafion ionomer binder at an I:C ratio of 0.7 and 0.9 was utilized for all WEs and CEs, respectively.

Cell Assembly for CL gas-transport resistance measurements: Membrane-electrode assemblies (MEAs) were prepared by stacking the CE sprayed onto the GDL against the Nafion membrane

* Consistent with the rest of this thesis and the terminology in the field, we use the term ionomer "dispersion" to mean an ionomer and solvent system. Importantly however, given the ζ trends presented in the rest of this chapter and the pH data of Chapter 3, "solution" may be a more appropriate term based on observed tendency of the ionomer to uniformly distribute in the ink at high I:C and control "bulk" behavior.

with the WE sprayed on the other side. Additional GDL sheets were added on the WE-side during measurements. The active cross-sectional area, determined by the WE electrode cross-sectional area directly in contact with the GDL, was limited to 2 cm^2. The remaining area was covered by impermeable Teflon gaskets (PTFE, McMaster Carr, Illinois, USA) to prevent gas exposure. Teflon gaskets also help seal the cell, achieve desired GDL compression, and maintain their position. The entire assembly was mounted in a single cell with graphite flow-fields (total area 5 cm^2) and single serpentine flow-channels (Fuel Cell Technologies Inc, New Mexico, USA). The cell was operated using a commercial test stand (850e Multi-Range Fuel Cell Test System, Scribner Associates, North Carolina, USA) that allowed control of gas flowrates, humidity, cell temperature, and cell backpressure. Cyclic voltammograms and limiting-current measurements were recorded via a Biologic VSP potentiostat (Biologic, Seyssinet-Pariset, France).

Cell Assembly for EIS and polarization-curve measurements: MEAs as described above were sandwiched between two 25 cm^2 SGL29 BC GDLs, at 25% compression and placed between the flow fields with the cell bolts tightened to 40 in-pounds. 25 cm^2 double/triple (CE/WE) serpentine flow fields were used.

Break-in protocol: A modified version of the break-in protocol described by Ono *et al*.[214] was adopted for this study. The samples were maintained at a constant potential (0.2 V referenced to the CE) for 12 hours at 80°C, 100% relative humidity (RH), and 50 kPa gauge pressure while flowing pure H_2 (flowrate of 400 std cm^3/minute) on CE side and air (flowrate of 800 std cm^3/minute) on WE side.

ECSA measurement: Electrochemical surface area (ECSA) was estimated by CO-stripping voltammetry as described by Schuler *et al*.[215] at 40°C, 80% RH, and ambient pressure (same operating conditions as limiting-current measurements). Both electrodes were flushed using humidified Ar for 1 h to hydrate the sample at the desired RH. The CE feed was then switched to 2% H_2 in Ar, and 20 cleaning cycles were performed between 0.08 to 0.95 V (referenced to the CE) at a scan-rate of 50 mV/s, followed by additional 20 cleaning cycles over the same potential range at a scan-rate of 100 mV/s. The WE was thereafter fed with 1% CO diluted in Ar at 500 std cm^3/min for CO adsorption for 5 min to allow CO adsorption. Next, Ar purged the WE at 500 std cm^3/min for 15 min to remove any excess CO and obtain monolayer adsorption. Finally, three CVs were recorded by sweeping the WE potential between 0.08 to 0.95 V (referenced to CE) at a scan-rate of 100 mV/s. ECSA was calculated from the charge integration of the CO peak. The second and third CVs served as a baseline for charge integration of the CO peak. A CO-monolayer oxidation charge of 420 mC/cm^2 was assumed in all the calculations. The surface-area roughness factor r_f, commonly used to characterize electrodes and defined as the ECSA normalized to electrode geometric area, was estimated from the ratio of ECSA to WE active area (2 cm^2). r_f values are reported in Table S6.4 of Section 6.6.

Transport-resistance measurement: Electrode transport resistances were estimated from limiting-current measurements using the H_2-pump configuration and test protocol as described by Spingler *et al*.[216] and Schuler *et al*.[215] A 2% H_2 in Ar mixture was fed to the CE to minimize crossover current while maintaining a stable potential. To achieve the mass-transport limit on the WE, low concentration gas mixtures of 1000 ppm H_2 in Ar were utilized. The flowrates maintained were

1000 std cm^3/min on the WE, and 500 std cm^3/min on the CE. The setup was maintained at 40°C, 80 % RH, and ambient pressure during the measurements.

To record the limiting current, the cell was flushed using humidified Ar for 45 min. The CE feed was then switched to 2% H_2 in Ar, and 20 cleaning cycles were performed between 0.08 to 0.95 V (referenced to CE) at a scan-rate of 50 mV/s, followed by additional 20 cleaning cycles over the same potential range at scan-rate of 100 mV/s. Thereafter, the potential on the WE was maintained constant at 0.3 V (referenced to the CE) to record the crossover current. The WE gas was then switched to 1000 ppm H_2 to record the total steady-state current density. Limiting current density is obtained by subtracting the crossover current density from the total current density.

The total cell resistance R_{Total} is given by the ratio of average feed reactant concentration (on the WE) to the measured limiting current i_{lim} as

$$R_{Total} = \frac{nFC_{Feed}^{Avg}}{i_{lim}} \tag{6.1}$$

where $n\,(=2)$ is the number of electrons in the overall reaction. R_{Total} for the H_2-pump configuration is composed of transport resistances from the GDL and the WE,

$$R_{Total} = NR_{GDL} + R_{CL} \tag{6.2}$$

where N is the number of GDLs stacked on the WE, R_{GDL} is the transport resistance of a single GDL, and R_{CL} is the WE transport resistance. R_{GDL} is determined from GDL stacking experiments where R_{Total} is measured as a function of N and other system parameters are kept constant.[216] The slope of R_{Total} versus N represents R_{GDL}. R_{CL} is determined by subtracting the total GDL resistance NR_{GDL} from R_{Total}. Measurement precision is maintained since both R_{CL} and NR_{GDL} have similar magnitudes (much higher than experimental error).

Impedance Measurements: Electrochemical impedance spectroscopy (EIS) experiments were prepared on fully conditioned 25 cm^2 MEAs with WE Pt loading of 0.1 mg Pt/cm^2 using a Gamry Reference 3000 Potentiostat connected to a Gamry 30k Booster. EIS experiments were conducted at 80°C with 1 atm pure H_2 and N_2 flowing at 100 cm^3/min at CE and WE gas lines, respectively. Experiments were run at 10, 25, 50, 75, and 100 % RH with 30 to 60 min equilibration time before each measurement. EIS was measured 50 kHz to 50 mHz at 0.45 and 0.2 V versus RHE with ±10 mV oscillations for CO-free and CO-doped experiments, respectively. The WE was exposed to 1% CO/N_2 feed for 15 min to allow for CO adsorption, then purged with pure N_2 prior to CO-doped experiments. Residual CO was oxidized after CO-doped EIS experiments and before CO-free EIS measurements via CO stripping voltammetry.

Double-Layer Capacitance (C_{dl}): As previously described,[46, 217] double-layer capacitance for an individual EIS spectra was determined by finding the y-intercept of ω^{-2} vs $-1/\omega Z_{img}$ plot using the linear region present at low frequency (typically 0.1 to $0.5 < \omega^{-2} < 2.5$ rad^2/s^2). Ionomer fractional capacitance on Pt and C surfaces were determined by comparing the changes in C_{dl} taken under wet and dry conditions with and without CO exposure[46, 217]. Uncertainty of the *y*-intercept associated with the least square linear regression fit were propagated through both ionomer coverage calculations.

Sheet Resistance Determination: The CL sheet resistance (R_{sheet}) was determined by fitting EIS data (between 50 kHz and 0.5 Hz) from 100% RH H_2/N_2 EIS spectra to a spherical diffusion model[218] (Equation 6.3) with an Open Source Impedance Fitter (OSIF)[219] tool,

$$Z = (i\omega)^{\theta}\ell + R_{hfr} + \frac{R_{sheet}}{\sqrt{R_{sheet}Q_{dl}(i\omega)^{\phi}}\coth\sqrt{R_{sheet}Q_{dl}(i\omega)^{\phi}} - 1} \tag{6.3}$$

where Z is complex impedance, ℓ is inductance of nonideal inductor, ω is frequency (rad/s), R_{hfr} is high frequency resistance element, R_{sheet} is CL sheet resistance, Q_{dl} is double layer capacitance of nonideal capacitor, and θ, ϕ are phase elements corresponding to nonideal inductor and capacitors, respectively. Due to the relative thinness of these CLs, the spherical diffusion model gave better fits compared to an analogous transmission-line model with capacitive and inductive elements modeled as constant-phase elements.

H_2/Air Polarization Curves: The cell was maintained at 80°C, 150 kPa total pressure and varying RH. H_2 and air were fed to the counter electrode (CE) and working electrode (WE), respectively. The test protocol involved measuring the current versus voltage curves from 0.3 V to open-circuit voltage (OCV) for 4 min per point (average of last 1 min used). Currents were normalized by ECSA to account for differences in Pt surface area with varying PPL loading.

SEM Imaging (Electrode and electrode thickness): SEM images of the CLs were obtained using a SEM FEI Quanta 250 FEG equipped with a Bruker Quantax 200 EDX detector. For CL thickness measurements, the samples were freeze-fractured under liquid nitrogen. Average thickness from three different CL locations is reported.

6.4 Results & Discussion

6.4.1 Particle Description

Varying PPL changes the relative amounts of carbon and Pt surface area (SA) of the catalyst particles: estimates indicate that the carbon SA decreases from 100% to 70 to 80% while the Pt SA increases from 0% to 20 to 30% as Pt PPL increases from 0 to 46 wt.% These estimates are

adapted from from Padgett et. al., as follows.[35] As a reference, unloaded Vulcan Brunauer-Emmett Teller (BET) surface area is roughly ~ $250\ m^2/g_{carbon}$. The BET surface area of loaded catalyst particles is attributed to both carbon and platinum surface area, and the total surface area should not change significantly. Pt surface area is reported from ECSA measurements.[35]

We consider two extreme cases to bound the expected surface area values. First, we assume all the surface area measured from BET is external surface area, and that the Pt particles are spherically shaped. We can therefore decouple platinum and carbon surface area by considering the projected circular Pt area (equal to 1/4th the total Pt surface area, assuming spherical particles). The projected Pt area is subtracted from the total BET surface area to calculate carbon surface area.

Table 6.1. Relative platinum and carbon surface area estimates, assuming zero percent internal porosity.

	Pt Surface Area (per gram carbon)	**Carbon surface area (corrected for Pt) (per gram carbon)**	**Pt:C surface area ratio**
10 wt. %	$68\ m^2/g_{Pt} = 7.56\ m^2/g_{carbon}$	$248.1\ m^2/g_{carbon}$	~0.03
46 wt. %	$45\ m^2/g_{Pt} = 38.33\ m^2/g_{carbon}$	$240.4\ m^2/g_{carbon}$	~0.16

Although Vulcan carbon is considered fairly compact and non-porous, one can ascribe an extreme of ~30% porosity to the particles as an upper bound.[35] The above calculations can thus be corrected for this porosity and internal surface area, considering an external BET surface area of ~ $175\ m^2/g_{carbon}$.

Table 6.2. Relative platinum and carbon surface area estimates, assuming 30% internal porosity.

	Pt Surface Area (per gram carbon)	**Carbon surface area (corrected for Pt) (per gram carbon)**	**Pt:C surface area ratio**
10 wt. %	$68\ m^2/g_{Pt} = 7.56\ m^2/g_{carbon}$	$173.1\ m^2/g_{carbon}$	~0.04
46 wt. %	$45\ m^2/g_{Pt} = 38.33\ m^2/g_{carbon}$	$165.4\ m^2/g_{carbon}$	~0.23

While there is a large spread in the values between Table 6.1 and Table 6.2, they illustrate that typically the carbon surface area is much larger than the platinum surface area, and that the Pt:C surface area ratio increases as loading increases. The actual surface areas will likely be between these two extreme cases.

It is worth noting that SA does will vary linearly with Pt content since carbon and Pt have drastically different specific (mass-normalized) SAs. Additionally, because Pt is slightly hydrophilic and Vulcan carbon (C) is slightly hydrophobic, varying PPL alters the hydrophobic/hydrophilic nature of catalyst particles, thereby influencing ionomer adsorption onto catalyst particles (see Chapter 5).[169]

6.4.2 Ink Characterization

ζ can be thought of as an effective surface potential of the agglomerates in the ink and is also an indicator of colloidal stability: higher-magnitude-ζ particles will experience more electrostatic repulsion and will therefore tend to aggregate less than low-ζ particles. It has previously been established that ζ is closely coupled with I:C ratio (see Chapter 3),[67] indicating ζ is strongly dependent on ionomer/particle interactions. Therefore, it is expected that the ζ/I:C dependence should change as a function of PPL. To probe this, Figure 6.2 shows the ink ζ as a function of I:C ratio (Nafion is used as the ionomer) for bare C (0% Pt), 10, and 30% Pt/C. A 1:1 water:*n*-propanol solvent composition is used for all inks in this study. We observe a U-shaped dependence of ζ on the I:C ratio for the three PPLs. Figure S6.7 also plots ζ for a much wider range of I:C using bare carbon particles (without platinum). Generally, ζ is proportional to the charge on particle and inversely proportional to the ionic strength of the surrounding medium.[125] While there should certainly be a correction to classical double-layer theory due to the large size of Nafion (discussed more in Section 6.6), these general trends with charge and ionic strength should still hold.

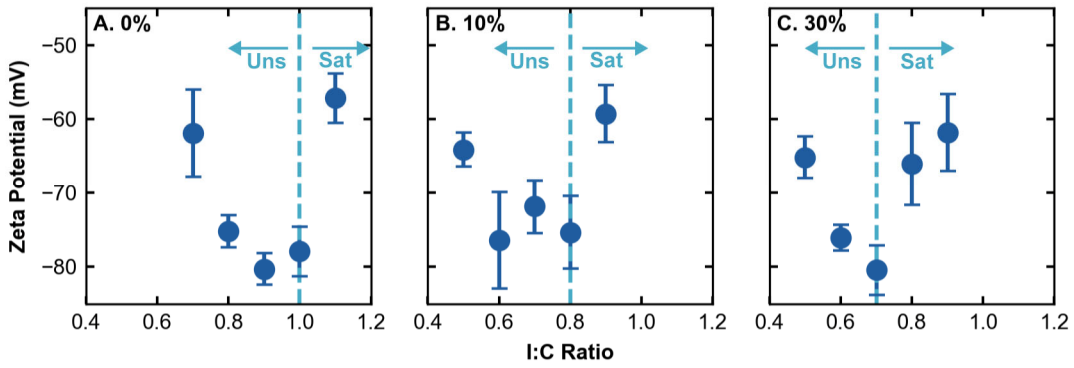

Figure 6.2. Zeta potential of inks of varying ionomer-to-carbon (I:C) ratios, containing (A.) 0 wt.% Pt (bare carbon) (B.) 10 wt.% Pt, or (C). 30 wt.% Pt-on-carbon catalyst particles. The dashed light blue vertical line indicates where the marginal ionomer added switches from adsorbing to the catalyst-particle surface (because the surface is unsaturated, Uns) versus no longer adsorbing (because the surface is saturated, Sat). (B.) and (C.) are reproduced with permission from Anamika Chowdhury.[212]

We will first examine the initial part of the U-shaped curve at low I:C ratios in Figure 6.2A. In a dispersion, the acid group in the sulfonate sidechain dissociates to form H^+ and negatively charged SO_3^- groups.[36, 67] ζ of pure Nafion in this solvent is difficult to measure (indeterminate experimentally via electrophoretic light scattering). The increase in ζ magnitude (more negative) therefore cannot be simply due to the addition of ionomer, but because the agglomerates are becoming more negatively charged. In other words, ionomer adsorption onto the agglomerate surface initially causes a more negative ζ as I:C increases due to negatively charged SO_3^- groups associated with the adsorbed ionomer.

At a certain I:C ratio, the ζ value plateaus, and then decreases in magnitude. This I:C transition ratio occurs at ionomer saturation points confirmed by other adsorption studies,[169, 180] and at a similar saturation point as measured from the ITC adsorption isotherms of Chapter 5. Therefore, it is likely that transition occurs when the agglomerate surface is saturated by ionomer. After the transition, additional ionomer behaves like the addition of small-molecule salts and acids (Figure S6.7B): the ionomer is likely no longer interacting strongly with the agglomerate surface, and instead adding to the ionic strength of the surrounding solvent medium. In other words, the additional ionomer added beyond the transition point dissociates and behaves like dissolved ions in the bulk solvent. This increase in ionic strength causes ζ to trend toward zero.

Interestingly, the I:C transition ratio is a function of PPL. For bare carbon (0% Pt, Figure 6.2A), this transition region occurs at an I:C of 1. As PPL increases, the jump in ζ progressively shifts to lower I:C ratios: 0.8 for 10 wt.% Pt and I:C ratio of 0.7 for 30 wt.% Pt, as indicated by the light-blue dashed vertical lines in Figure 6.2. As discussed in Chapter 5, Nafion adsorbs more strongly onto Vulcan than onto Pt under similar conditions.[169] As the carbon SA available for the ionomer to interact with decreases (Table 6.1 and Table 6.2), the amount of ionomer the catalyst-particle surface can accommodate also decreases, in agreement with the decreasing threshold I:C with increasing PPL.

To explore the relationship between PPL and ionomer/particle ink interactions further, pH is measured during ink titration with ionomer (as in Figure 3.5),[67] and compared with the pH of ionomer-only dispersions at the same ionomer concentrations. The pH of both the ink (with 0, 30, and 46 Pt wt. % catalyst particles) and the dispersion (no particles) are plotted on the y- and x-axis, respectively in Figure 6.3. The raw data of ink pH versus I:C is shown in Figure S6.9.

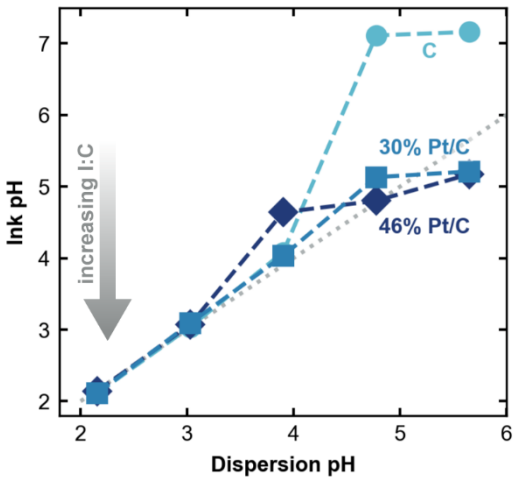

Figure 6.3. Measured pH titrating in ionomer of an ink containing either bare carbon (C), 30, or 46 wt.% platinum on carbon (Pt/C) as a function of the measured pH of ionomer-solvent dispersions of the same composition containing no particles. Dashed lines are meant to guide the eye. The dotted gray line indicates a one-to-one correlation.

Because the ionomer is acidic, low pH values (bottom left of Figure 6.3) represent the highest ionomer concentrations (highest I:C). In this regime, the pH of the ink and the ionomer dispersions agree directly, thus indicating that the ionomer contributes to the bulk pH in a similar manner with and without nanoparticles. However, at low ionomer concentrations (moving to the top right of the figure), a clear deviation from this linear behavior (evidenced by a slope change) from this relationship between the ink and dispersion pH is observed. This difference could be due to the nanoparticles or the ionomer/particle interactions. For bare carbon, we see the low I:C ink pH is quite a bit higher than the dispersion pH, likely due to the slightly basic nature of Vulcan (without platinum deposition). Notably, the ink pH is relatively insensitive to ionomer concentration when ionomer is first increased. Figure S6.9 replots the ink pH data as a function of I:C. This insensitivity could only be because the ionomer is not contributing to the bulk pH in this region, suggesting that it is bound/adsorbed to the nanoparticle, and therefore the ions cannot freely distribute in the bulk solution. Below pH ~4, a noticeable slope change occurs; the dispersion and ink pH values converge because the particles are saturated. Again, the deviation between ink and dispersion pH is due to adsorption of the ionomer to the catalyst-particle surface, as seen in Figure 3.5, and pH may be thought of as a measure of bulk (free) ionomer.

This same trend is seen for the Pt/C data: all inks display relatively insensitive pH responses with increasing ionomer concentration at low I:C ratios. The Pt/C values are also initially more acidic than bare C due to differences in surface chemistry induced by the acidic platinum deposition process. (It should be noted therefore that the bare carbon did not undergo a similar treatment process, and the ionomer/carbon interactions are likely inherently slightly different between untreated bare carbon and the carbon. The data are presented however to understand the intrinsic ionomer/Vulcan interaction.) For the Pt/C ink pH data, the adsorption of ionomer on the catalyst

particles scavenges ionomer from solution. Below pH ~4, enough ionomer is present to overcome adsorption loss of ionomer on catalyst particles

In our inks, the fact that ionomer does not contribute to bulk pH at low ionomer concentrations (likely due to interactions with the nanoparticle surface) and does at high concentrations corroborates the U-shaped ζ behavior, in which at low concentrations the ionomer does not add to ionic strength but rather lowers ζ due to adsorption. At high ionomer concentrations, the additional ionomer (beyond the saturation point) remains dispersed in the solvent, thereby increasing the bulk ionic strength. Furthermore, the pH transition region occurs at similar I:C ratios (Figure S6.9) as the ζ-transition values. However, it is important to note that the ζ trend may not hold for inks with very low carbon concentration (*i.e.* if the amount of ionomer adsorbed to the carbon surface area negligibly affects the bulk ionomer concentration).

6.4.3 CL Investigation

To understand how these varying PPL-influenced ink interactions affect CL performance, Figure 6.4A shows the effect of PPL on CL gas-transport resistance and corresponding ink ζ, using bare C (0% Pt), 10, 30, and 46 wt% Pt/C catalysts. Gas transport was not measured for bare carbon because it is a poor H_2 catalyst. CL gas-transport resistance is composed of the total transport resistance for the gas to diffuse through the CL thickness to the Pt reaction sites. At low Pt CL loadings (as is the case here), the overall CL gas-transport resistance is dominated by local gas-transport resistance which is composed of ionomer thin-film transport resistance and an interfacial resistance at the Pt/ionomer interface.[86] We therefore attribute trends in CL gas-transport resistance to local gas-transport resistance. All inks/CLs were prepared in an identical manner with the same total platinum loading and solvent composition (1:1 water:*n*-propanol*)*. All CLs were fabricated with a fixed I:C of 0.7 to capture behavior on either side of the ζ-plateau value for the varying PPLs (*i.e.,* 10% should be to the left of, 30% should be on, and 46% should be to the right of the plateau values as seen in Figure 6.2). Because total platinum loading was maintained constant (0.05 mg/cm^2), each CL had a different nominal thickness due to the varying PPL used: CLs fabricated from high primary particle loadings have less total carbon (and are therefore thinner). Additionally, ECSA varied widely across the CLs with different PPL (Table S6.4). This probably results from changes in Pt nanoparticle size as a function of PPL.[22, 213] The CL gas-transport-resistance data presented in Figure 6.4A is therefore normalized to the average ECSA (see Section 6.6).

As mentioned above, ζ has previously been shown to correlate well with CL high current-density performance[46, 212]; changes in CL structure are triggered by differences in ionomer/particle interactions. In Figure 6.4, we see this strong relationship as a function of PPL. CLs with low PPL demonstrate low CL gas-transport resistance and high ζ magnitudes. At 46 Pt wt.% PPL, a sharp increase in CL gas-transport resistance occurs concurrently with a sharp decrease in ζ magnitude. The gas-transport resistance data agree with previous studies that report decreases in CL high current-density performance with increased PPL.[16] The previous studies attributed these trends to crowding of carbon surface by Pt particles, resulting in low flux per Pt particle. [16] However, the

coincidental ζ trends with high gas-transport resistances indicate microstructural changes of the CL (more aggregation).

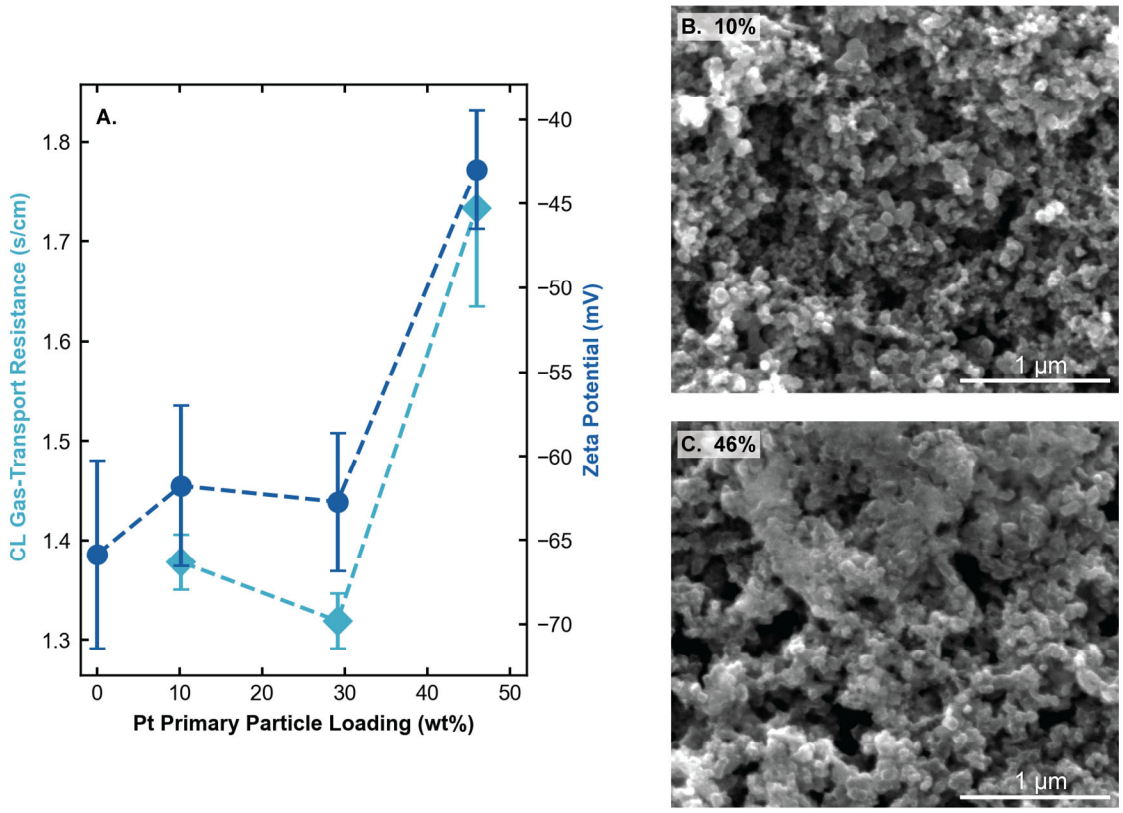

Figure 6.4. (A.) Gas-transport resistance of catalyst layers (CLs) containing the same total platinum loading (0.05 mg/cm^2), but varying primary particle platinum loading. The zeta potentials of the inks used to cast these CLs are also shown. Scanning electron microscopy images of CLs manufactured with (B.) 10 wt% Pt/C and (C.) 46 wt% Pt/C (the same samples measured in (A.)).

From the ζ measurements, we would expect the majority of ionomer to adsorb to the nanoparticles at low PPL because we are on the left side of the U-shaped adsorption curve (I:C of 0.7). At high PPL, we would conversely expect to have some free ionomer, since we have already passed the I:C ζ transition value. This non-uniform ionomer coverage (discussed further below) at high PPL correlates with the increases local transport resistances observed in Figure 6.4A.

Both low-magnitude ζ and high gas-transport resistances indicate microstructural changes of the CL, likely more/larger agglomerates. A lower magnitude ζ dictates less repulsion between the catalyst particles in the ink. This likely results in aggregation and the formation of larger agglomerates, in turn, increasing the local transport resistance due to the more tortuous pathways

the gas must take to reach buried platinum on the inside of the aggregate. To verify this hypothesis and study the structure, SEM was used to image the CLs via as shown in Figure 6.4B-C for CLs fabricated with PPL of 10 and 46 Pt wt.%, respectively. The 10 wt.% sample exhibits a highly porous structure with well-formed pores while the 46 Pt wt.% sample displays a more aggregated structure, in agreement with the gas-transport resistance and ζ data.

Double-layer capacitance (C_{dl}) is used to verify the ionomer distribution within the CL, as previously described.[46] Briefly: under dry conditions only the particle surface covered by ionomer contributes to C_{dl}. Under wet conditions, likely the entire surface of the catalyst particles contribute to C_{dl} due to the presence of both water and ionomer pathways. Capacitive measurements are related to ionomer coverage and the dry-to-wet ratio of C_{dl} is indicative of the fraction of particle SA covered by ionomer (though there may not be a strictly linear relationship due to differences in the dielectric permittivity of hydrated versus dry Nafion). When this measurement is repeated with CO (adsorbed on Pt), the capacitance is attributed primarily to carbon (it is assumed that adsorbed CO insulates the platinum surface area)[46]. The Pt capacitance contribution under dry and wet conditions is isolated by subtracting the C_{dl} with CO adsorbed from the total C_{dl}. The results are presented in Figure 6.5. Note that these data are related to the percentage surface of carbon and platinum, respectively, covered by ionomer, and the two values should not necessarily sum to one (both could be 1).

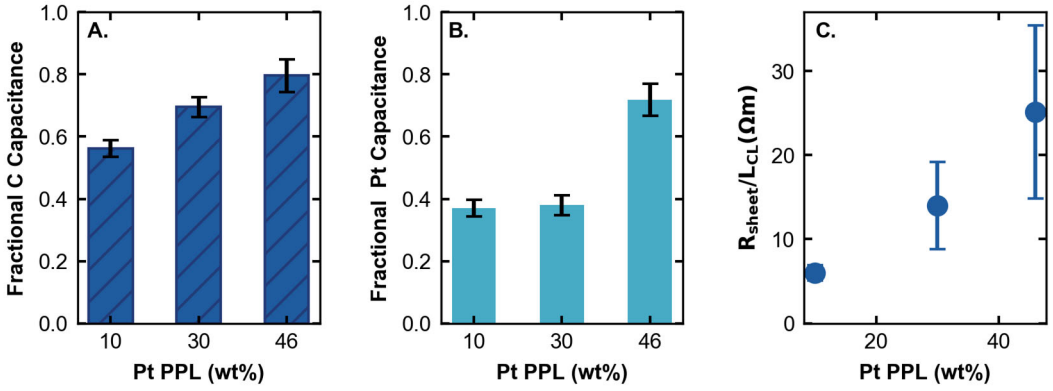

Figure 6.5. Fractional (A.) carbon and (B.) platinum double-layer capacitance due to ionomer coverage on those respective surfaces. (C.) Bulk catalyst layer (CL) sheet resistance (R_{CL}), normalized by thickness of the CL (L_{CL}). All data are for electrodes containing 0.1 mg/cm^2 platinum loading, achieved while varying the Pt PPL.

The ionomer coverage on carbon is within a small range across all samples, suggesting similar ionomer/carbon interactions across all samples. However, there is a clear steady increase in fractional carbon capacitance as PPL increases (Figure 6.5A). Concurrently, the total carbon surface area available for ionomer to interact with steadily decreases as PPL increases. Because

the surface area decrease is larger than the capacitance increase, the overall amount of ionomer adsorbed to C actually decreases, consistent with ζ predictions. This trend is also consistent with the hypothesis that the carbon surface becomes more saturated faster with increasing PPL (due to lower total available carbon SA).

The Pt fractional capacitance exhibits a sharp change in magnitude between 30 and 46% Pt PPL, which is where we would expect a behavior change from the ζ measurements (because the 46% is to the right of the U-shaped curve). This higher coverage on Pt at higher PPL is not evident from ink ζ or prior adsorption studies.[169] This trend could be due to spillover from adsorption onto carbon. Alternatively, higher ionomer coverage on Pt at high PPL could potentially result from the drying step in CL fabrication. As the solvent evaporates, the free ionomer (for high PPL samples that are on the right side of the U-shaped ζ curve) is forced to deposit on available free SA (including Pt SA). Such induced deposition in a relatively fast drying step that occurs during spray deposition can result in non-uniform ionomer coverage or isolated ionomer aggregates, in agreement with the SEM images (Figure 6.4B-C). Combined with patchier coverage due to less carbon SA, this may yield poor ionic conductivity.

This is consistent with observed high CL sheet resistance (R_{sheet}) at high PPL. CL R_{sheet} measures through-plane H^+ transport resistance. Since high PPL CLs are thinner at fixed nominal Pt loadings (0.1mg/cm^2), CL R_{sheet} values were normalized in Figure 6.5C by the thickness of CL (L_{CL}) cross sections measured by SEM (summarized in Table 6.3). When normalized by the thickness, differences in R_{sheet} are a direct result of changes in ionomer distribution (since the ionomer should have the same intrinsic conductivity in all electrodes and the same amount). A high R_{sheet}/L_{CL} indicates a heterogeneous ionomer distribution with poor ionomer connectivity, such as ionomer aggregates connected by thin ionomer strands and/or a highly tortuous ionomer network (although R_{sheet} will be dominated by the path of least resistance throughout the layer, and not necessarily all of the paths).

Table 6.3. CL thickness (L_{CL}) measured from CL cross-sectional SEM.

Pt/C wt%	**10 wt. %**	**30 wt. %**	**46 wt. %**
CL Thickness (µm)	11.75±1.38	5.08±1.86	1.61±0.65

It is important to note however, that despite the larger normalized resistances (Figure 6.4A and Figure 6.5C), higher PPLs allow for thinner electrodes, which will reduce the total through-plane gas and H^+-transport resistance, allowing for higher Pt utilization throughout the CL thickness. The nominal resistance values may be more important than normalized values for dictating performance under certain PEFC operating conditions with high water production. Polarization curve plots (corrected by multiplying with the sample r_f and dividing by average r_f) in Figure 6.6 demonstrate superior performance of CLs with higher PPL compared to 10 wt.% PPL, likely due

to these thickness differences (Table S6.4). CLs with 30 wt.% PPL seem to provide the optimal CL structure, balancing between the local and through-plane transport resistances, and thus the best performance. Trade-offs between local interactions and macroscopic processes must both be considered.

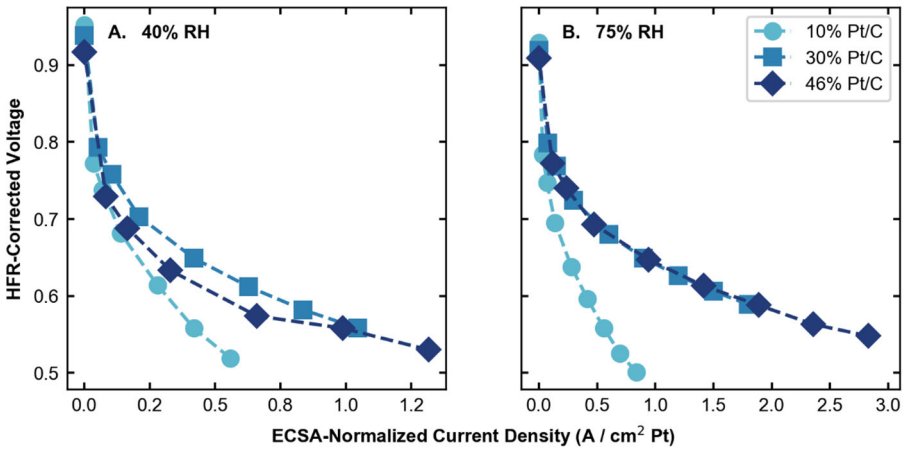

Figure 6.6. H_2-Air polarization curves obtained from CLs using different PPL on the WE, with a total Pt loading of 0.1 mg/cm^2. Operating conditions were 80°C, 150 kPa backpressure, and either (A.) 40% relative humidity (RH) or (B.) 75% RH. The voltage is corrected for high-frequency ohmic resistance (HFR), and the current density is normalized to Pt specific surface area.

The results in this chapter agree with prior studies in which low PPL catalysts demonstrated superior current-voltage behavior when CL thickness was held constant across all samples by carbon dilution, likely due to improved local transport.[16] Even when polarization curves are corrected for ohmic resistance and hydrogen crossover, low PPL still demonstrate better performance, confirming that the polarization curve differences arise due to varying local transport resistance. However, Schuler et. al. did not observe much impact of PPL on local resistance likely because they used a high-surface-area carbon support in which a significant fraction of Pt particles are located in interior micropores.[86] Thus, the carbon versus platinum exterior surface area is not significantly impacted by PPL for these types of catalyst particles. This again highlights the interplay between various CL parameters such as PPL and carbon support type and the need to account comprehensively for all CL parameters to achieve optimal CL design/structure.

6.5 Summary

Inks for PEFC CLs consist of various components (solvent, ionomer, and catalyst particles) and the interactions between the components can critically influence CL microstructure and

performance. In this current study, the impact of platinum primary particle loading (PPL) on catalyst/ionomer ink interactions and subsequent effects on CL microstructure and thus gas- and H^+-transport resistance was explored. Nafion ionomer preferentially adsorbs to carbon surfaces in the inks (rather than platinum) as discussed in Chapter 5. As PPL is increased and the available carbon surface area (SA) decreases, the carbon surface saturates at a lower ionomer content and additional non-adsorbed ionomer remains dispersed in the solvent. This results in higher ionic strength (therefore lower ink ζ), and thus a more agglomerated CL structure. These trends agree with results from ink ζ and pH investigations, SEM imaging, and capacitance measurements. This non-adsorbed ionomer may deposit non-uniformly during the CL fabrication process, resulting in observed poor H^+ conductivity. Hence, low PPL catalysts are preferred to improve local transport processes. However, higher PPL catalysts with low CL thickness are advantageous with respect to reducing through-plane reactant gas- and H^+-transport resistances, thereby providing better Pt utilization. The two different transport resistances (local and bulk) need to be optimized, and this optimum point undoubtedly varies depending on the target operating conditions. Based on the above results, it seems moderate PPLs with I:C ratios, where the zeta-potential magnitude is maximized, provide an optimal balance between all of the effects studied in this chapter. Of note, the ionomer/catalyst interactions probed here are known to depend on solvent composition (as discussed in the previous chapters), highlighting the large ink variable space that can be manipulated to alter CL structure. Further studies are required to understand this parameter space and their impact on final CL performance, including the delineation between local and macroscopic properties. Importantly, this study demonstrated a direct link between ink interactions and CL performance metrics, revealing critical insights into how ionomer coverage and transport processes are affected by carbon and platinum SAs. Such information is imperative to optimize inks for enhanced CL transport and improved platinum utilization.

6.6 Supplementary Information

6.6.1 Ink Zeta Potential and pH

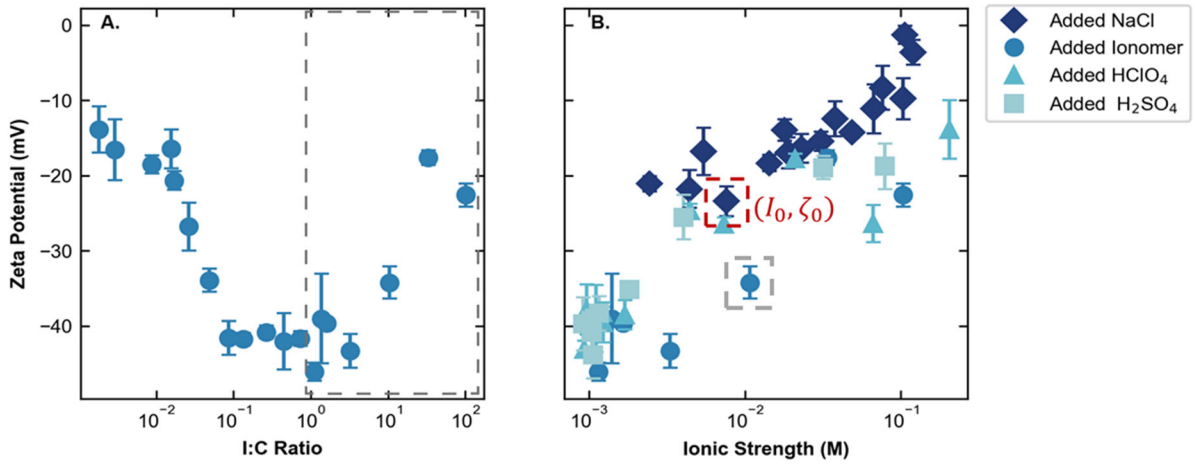

Figure S6.7. (A.) Zeta potential of 0 wt% Pt/Carbon (bare carbon) inks containing 0.1 wt% nanoparticles as a function of ionomer to carbon weight ratio, exhibiting U-shaped behavior (B.) Zeta potential of 0 wt% Pt/Carbon (bare carbon) inks with constant I:C ratio of 1 and additional electrolyte/acid to increase ionic strength (corresponding to the range enclosed by the dashed gray box in Figure A). Figure A. data is plotted for reference. All ink dispersions show similar behavior of increasing zeta potential (decreasing magnitude) with higher ionic strength. Ionic strength for the ionomer dispersions was calculated assuming all charges contribute to the ionic strength. The dashed boxes in (B.) are used in further analysis below.

Debye-Hückel (DH) theory predicts that ζ is directly proportional to the Debye length λ

$$\varepsilon\zeta = q\lambda \propto I^{-1/2} \tag{S6.4}$$

where ε is the medium dielectric permittivity, q is the charge density on the particle surface, and I is the solvent ionic strength. For dilute solutions with small electrolyte ions (such as NaCl), λ is given by:

$$\lambda = \sqrt{\frac{\varepsilon RT}{F^2 \sum_i z_i^2 C_i^{Bulk}}} \tag{S6.5}$$

z_i and C_i^{Bulk} is the valence and bulk phase concentration of ion i. $\sum_i z_i^2 C_i^{Bulk}$ represents the ionic strength, I, of the dispersion. Therefore, ζ is also inversely proportional to the square-root of I. We can thus write the following equation for the ratio of ζ and corresponding I at constant particle surface charge:

$$\frac{\zeta}{\zeta_0} = \sqrt{\frac{I_0}{I}} \tag{S6.6}$$

where the subscript "0" indicates a reference ionic strength.

Figure S6.8 plots the ratio of ζ versus the square-root of inverse of I for NaCl-ink dispersions from the values in Figure S6.7. We ignore the contribution of ionomer added until the transition region (I:C ratio 1) since it primarily adsorbs to the carbon particles and does not contribute significantly to the bulk ionic strength. The data point at I of ~$7x10^{-3}$M (highlighted in Figure S6.7 in the red box) is used as the references (ζ_0, I_0). Overall, we observe a good agreement between ratio of ζ and the square-root of inverse of I.

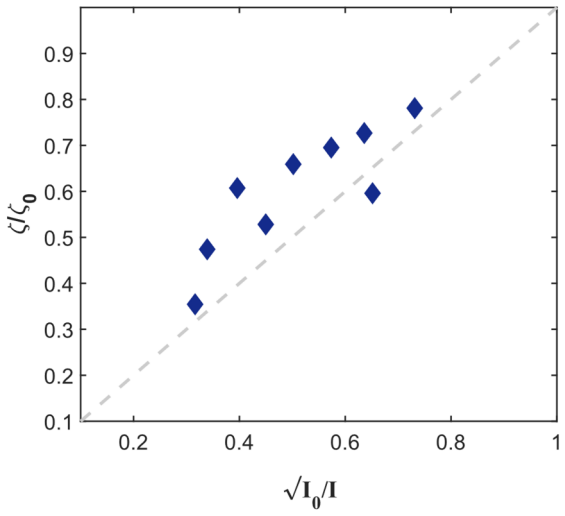

Figure S6.8. ζ versus $1/\sqrt{I}$, normalized by reference point ζ_0 and I_0 (highlighted in Figure S6.7). The dashed grey line represents 1:1 correlation.

Data points with I higher than 0.1M and lower than 0.007M did not follow the trend and are excluded from the plot. At high I, this is probably due to ion condensation or crowding effects. The cause of deviations at low I is unknown and could result from experimental error.

For large molecules such as polymer chains, it is essential to modify the DH λ equation to consider finite-size effects. Using the modified Poisson Boltzmann and Bickermann equation, $\lambda_{\text{size-corr}}$ for dispersions with large ions is[220-221]

$$\lambda_{\text{size-corr}}^{-2} = \frac{F^2}{\varepsilon RT}\left[I - \frac{\left(\sum_i z_i v_i C_i^{Bulk}\right)^2}{\sum_i v_i^2 C_i^{Bulk}}\right] \tag{S6.7}$$

where v_i is the volume occupied by ion i and is calculated using the hard-sphere assumption, corrected by the packing coefficient p.

$$v_i = \frac{\frac{4}{3}\pi R_i^3 N_A}{p} \tag{S6.8}$$

R_i is the radius of ion i. $p = 0.64$ for random close packing.

The second term on the right of Equation S6.7 is greater than zero and reduces the impact of I. $\lambda_{\text{size-corr}}$ estimated using Equation S6.7 is thus larger than λ calculated from Equation S6.5, resulting in a higher magnitude ζ. This is also observed experimentally in Figure S6.7B where the inks with added ionomer demonstrate higher ζ compared to ink with added acids or salts.

To verify that the differences in ζ between ink dispersions with ionomer and with added NaCl is due to ion size, we calculate the ratio of $\lambda_{\text{size-corr}}$ for ionomer-ink dispersions to λ for NaCl-ink dispersion and compare it to the ratio of ζ. We use the data points with I$\sim 10^{-2}$M for this analysis (highlighted in Figure S6.7B) as it is above the transition region but is lower than high $I = 10^{-1}$M where other effects such as ion condensation can become important. Once again, we ignore the contribution of ionomer added up to the transition region (I:C ratio 1) to bulk solvent ionic strength I and assume that the I is contributed only by ionomers added beyond the transition region (I:C ratio 1).

By denoting the ionomer monomer charge as m and bulk ionomer monomer concentration as $C_{ionomer}^{Bulk}$, the concentration of the counterion H^+ is then equal to m times $C_{ionommer}^{Bulk}$. Equation S6.7 is re-written for the ionomer-ink dispersion as

$$\lambda_{\text{size-corr}}^{-2} = \frac{F^2}{\varepsilon RT}\left[m(1+m)C_{ionomer}^{Bulk} - \frac{C_{ionomer}^{Bulk} m^2 (R_+^3 - R_-^3)^2}{(mR_+^6 + R_-^6)}\right] \tag{S6.9}$$

where R_+ and R_- are the effective radius of cation (H^+) and anion (monomer), respectively. Since $R_+ \ll R_-$, the above equation can be further simplified to be:

$$\lambda_{\text{size-corr}}^{-2} = \frac{F^2}{\varepsilon RT}\left[m(1+m)C_{ionomer}^{Bulk} - C_{ionomer}^{Bulk}m^2\right] = \frac{F^2}{\varepsilon RT}mC_{ionomer}^{Bulk} \quad \text{(S6.10)}$$

$$\lambda_{\text{size-corr}} = \sqrt{\frac{\varepsilon RT}{F^2 mC_{ionomer}^{Bulk}}}$$

The equivalent NaCl-ink dispersion (at the same I) will have bulk ion concentration of $mC_{ionomer}^{Bulk}$ (both ions) and $I = 2mC_{ionomer}^{Bulk}$. λ thus is

$$\lambda = \sqrt{\frac{\varepsilon RT}{F^2 2mC_{ionomer}^{Bulk}}} \quad \text{(S6.11)}$$

The ratio $\lambda_{\text{size-corr}}$ to λ is thus equal to $\sqrt{2}$. This ratio is in excellent agreement with experimental data at $I \sim 10^{-2}$ M where the ζ of NaCl and ionomer-ink dispersions are ~ 23.49 mV and ~34.22 mV respectively and confirms that the lower ζ of ionomer-ink dispersions is due to size effects.

The above analysis importantly confirms that the ζ data (and the pH data) at high I:C may be explained by the ionomer's ability to distribute uniformly and affect the bulk ionic strength.

The titration data of Figure 6.3 may be replotting to more explicitly show how ink pH changes as a function of I:C ratio, as displayed in Figure S6.9.

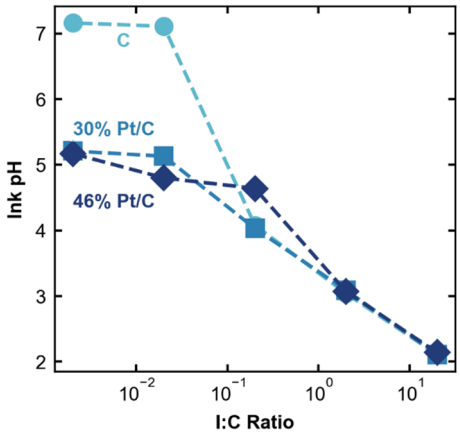

Figure S6.9.The measured pH titrating in ionomer of an ink containing either bare carbon (C), 30 wt%, or 46 wt% platinum on carbon (Pt/C) as a function of the added ionomer, reported as ionomer-to-carbon weight ratio (I:C). Dashed lines are meant to guide the eye.

6.6.2 ECSA Correction

The CL gas-transport resistance includes through-plane diffusion resistance, and a local gas-transport resistance (R_{Local}) due to transport resistance through the ionomer film and is given by:

$$R_{CL} = \frac{L}{3D_{CL}} + \frac{1}{r_f} R_{Local} \tag{S6.12}$$

For low Pt-loadings, the through-plane resistance is minimal and R_{Local}, which includes diffusion resistance through the ionomer film and an interfacial resistance at the ionomer/Pt interface, dominates, *i.e.*[215]

$$R_{CL} \sim \frac{1}{r_f} R_{Local} \tag{S6.13}$$

where r_f is the CL roughness factor, defined as ECSA per unit CL geometric area. To account for differences in ECSA across various samples, the measured CL gas-transport resistance is multiplied with the corresponding sample r_f and divided by the average r_f (averaged across all samples).

For the polarization-curve data reported in Figure 6.6, the current is corrected by multiplying with the sample r_f and dividing by average r_f. This correction however does not consider the different thicknesses of CLs with varying PPL. At high total Pt loadings, such as 0.1 mg/cm^2, the through-plane gas-transport resistance, *i.e.,* the transport resistance through the thickness of the CL can become dominant. This likely underestimates the current output of CLs with low PPL and overestimates the current output at high PPL.

Table S6.4. r_f (ECSA normalized to CL geometric area) at various total Pt loadings of WE.

	10 wt. %	**30 wt. %**	**46 wt. %**
0.05 mg/cm^2	22.64 ± 0.2	37.98 ± 1.06	54.48 ± 1.55
0.10 mg/cm^2	30.57	48.10	72.03

6.6.3 CL Thickness Measurement

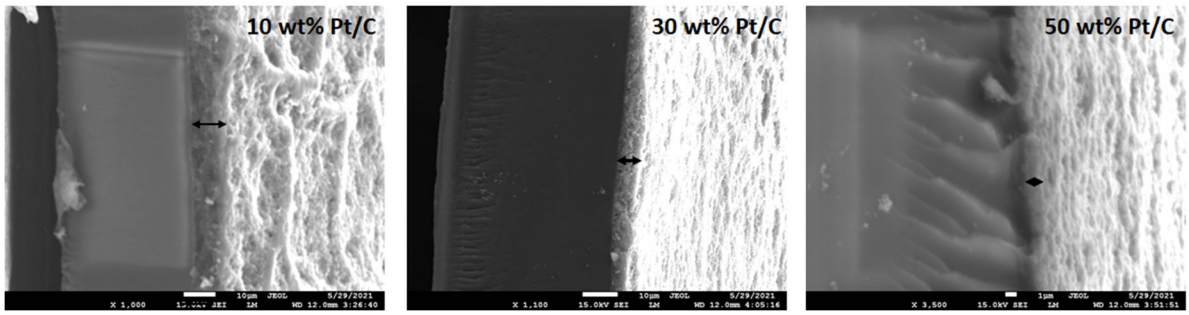

Figure S6.10. Freeze-fractured cross-sectional SEM images of CLs with varying primary particle Pt wt% loadings, and a total loading of 0.1 mg/cm^2. Cross-sectional thickness is indicated by black arrow in images. CL thickness measurements were averaged from three different locations. Results are reported in Table S6.4.

6.6.4 H^+ Transport Resistance Correction

Using EIS from the 100% H_2/N_2 experiments, we measure the total H^+-transport resistance through the thickness of the CL. However, as highlighted in Table S6.4, the CLs with different PPLs exhibit varying thicknesses and porosity. Since the I:C ratio was maintained constant, different porosity would result in varying ionomer volume fraction. We correct for these variations in CL sheet-resistance measurements:

$$R_{\mathrm{H}^+,CL}(corrected) = \frac{R_{sheet}}{L_{CL}} = \frac{1}{\phi_{ionomer}\sigma_{ionomer}} \tag{S6.14}$$

where L_{CL} is the CL thickness (measured from cross-sectional SEM). Assuming the intrinsic ionomer conductivity $\sigma_{ionomer}$ is a constant, the differences in $R_{H^+,CL}$ are due to differences in ionomer distribution and porosity of CLs.

7 Summary & Outlook[‡]

The electrochemical performance of energy-conversion devices, including fuel cells, depends on the properties of their catalyst layers (CLs). The size of the agglomerates of catalyst particles that form, the catalyst particle/ionomer interface, ionomer coverage, and additional deterministic microstructural signatures directly depend on the interaction between these components in precursor CL inks. To understand and control the CL fabrication process, this dissertation investigated the fundamental governing interactions between the ionomer, the particles, and the solvents in CL inks.

Beginning with Chapter 1, we detailed why this problem is so complex. Namely:

(1) The parameter space is massive. Figure 1.2 details a subset of the most commonly altered variables, but this list is not exhaustive. Catalyst type (carbon support and platinum loading), ionomer chemistry (equivalent weight, sidechain length, and side-chain functional group), solvent type (solvent identity and mixture ratio if multiple are used), and processing parameters (total ink solids loading, ionomer-to-carbon ratio [I:C], deposition method [ultra-sonic spray, slot-die, gravure coating, *etc.*], drying/heating protocols) all vary.
(2) Traditionally, focus has been placed on analyzing CL microstructures and relating them to performance. Emphasis on explicitly and transparently reporting ink parameters has been missing in the community. Therefore, while CLs have been used and researched for decades, these studies are not easily relatable to each other or reproducible due to lack of reported fabrication details; they reveal little insight into how ink parameters affect reported properties. Furthermore, there is a larger question of explicitly which metadata are actually sufficient/necessary to reproduce data.
(3) Within recent years, there has been a shift toward ink-focused papers. However, there is no standard ink recipe or protocol in the research literature. Therefore, when comparing ink papers across different groups, many variables change, and it is extremely difficult to isolate the effect of just one.

The above issues necessitate the fundamental investigation undertaken in this dissertation. The two most important interactions (ionomer/solvent and ionomer/particle) identified in Chapter 1 are explored throughout this dissertation and are summarized below.

[‡] Portions of this chapter were previously published as "Berlinger, S. A.; Garg, S.; Weber, A. Z., Multicomponent, multiphase interactions in fuel-cell inks. *Current Opinion in Electrochemistry* **2021,** *29*, 100744," and are adapted with permission from all co-authors.

7.1 Ionomer/Solvent Interactions

Due to the ionomer's hydrophobic backbone and hydrophilic sidechains, solvent identity affects the ionomer dispersion conformation in accordance with these competing sidechain/backbone preferences. Rods, random coils, blobs, micelles, and core-shell particles have all been used to describe these solvent-influenced dispersion structures.[37, 54-55, 96, 103] Water-alcohol mixtures are some of the most commonly studied solvents due to ease of processability; this is the solvent system explored in this dissertation.

As revealed in Chapter 2, these dispersion conformations modulate the properties of films and membranes once cast.[99-100, 102, 148] *In situ* scattering was employed to understand the dispersion-to-film transition, and how different solvents determine the evolution of thin-film morphology during drying.[103, 148] Conductivity and water-uptake measurements show that as the water content in the dispersion increases relative to propanol, the transport properties of the cast film improve.[148] It is possible the enhanced limiting-current density in Figure 1.5 witnessed at higher dielectric permitivities (ε, higher ratios of water relative to propanol) could be due in part to this effect.

Chapter 3 investigated how changing the water:propanol ratio changes the relative acidity of ionomer dispersions. This is hypothesized to be due to sidechain-versus-backbone/solvent interactions.[67] Namely, the sidechains of PFSA may preferentially extended outwards into solution in water-rich solvents, whereas in propanol-rich solvents PFSA conformation may have a more hydrophobic exterior. Similar structures were predicted using MD simulations, whereby explicitly considering both solvents demonstrated that different solvents partition inside versus outside the ionomer aggregate.[59]

The fact that solvent type alters the final structure and properties of thin films has additional implications. PFSA used in ink formulations and thin-film studies is often diluted from stock dispersions that come in various different solvents themselves. One must consider both the solvent used to dilute (*i.e.* the ink solvent) as well as the native stock solvent, as these will both alter PFSA behavior.

Additionally, the time from and magnitude of dilution is critical. As explored in Chapter 4, the pH of dispersions (discussed more in Chapter 3) decreases as time from dilution increases. Solvent ratios (extremes on the water/propanol spectrum), and dilution concentrations that are dissimilar from the stock dispersions are affected more. This suggests that these ionomers have a very slow equilibration time to adapt to new solvent environments. If films are cast from dispersions prepared at different times, their structure is influenced both by dispersion solvent (as in Chapter 2) and how that solvent-induced morphology is influenced with time. These structures then impact ionomer performance metrics. Importantly, these dispersion conformation changes impact how the ionomer interacts with nanoparticles. The direct results of Chapter 4 were studied in Chapter 5: ionomer/solvent/temporal effects propagated to weaken ionomer/particle interaction strengths.

The above studies have revealed important insights into the nature of the ionomer. While the literature typically considers the ionomer as a dispersion due to the presence of ionomer aggregates, these aggregates are concentration (and solvent) dependent. One might not expect that

these aggregates can behave like small molecules, but the investigations in Chapters 3 and 6 demonstrate that the ionomer at low and moderate concentrations can affect bulk properties like pH and ionic strength in a manner similar to small molecules (with deviations from small-molecule values attributed to conformation/size effects). Therefore, the ionomer in solvent behaves both like a "dispersion" with a non-solubilized backbone, and like a "solution" affecting bulk electrostatic behavior. Of course, the degree to which it affects that bulk behavior depends on the ionomer conformation, which is directly impacted by solvent and concentration.

Importantly, these different solution conformations (aggregate size, degree of hydrophilicity/hydrophobicity, acidity, *etc.*) will influence how the ionomer adsorbs to catalyst particles in solution (altering the ionomer/particle interaction, discussed in the next section, and further detailed in Chapter 3). Modified Derjaguin-Landau-Verwey-Overbeek (DLVO) theory has been applied to ink systems to try to understand aggregation processes.[70, 95] While these are important first steps in modeling ink interactions, they overlook some important physics. In DLVO theory, solvent modifies the Hamaker attraction term and the electrostatic repulsion potential through changes in ε. However, in addition to changing ε, solvent alters the physical characteristics of the ionomer aggregate as discussed above. Both of these effects will influence overall aggregation behavior, and the coupling between them cannot be ignored. Figure 1.5 demonstrates this point: solvent ε definitively changes CL performance, but the ionomer/catalyst particle aggregation process is not governed solely by classical (electrostatic) DLVO forces (exemplified by lack of correlation between the aggregate-size and zeta-potential trends).

7.2 Ionomer/Particle Interactions

The ionomer/particle interaction encompasses both the ionomer/platinum and the ionomer/support (carbon) interaction. In terms of the ionomer/carbon interaction, MD simulations have shown that PFSA interacts with carbon surfaces via backbone adsorption;[143, 174] this interaction is likely hydrophobic in nature.[174] Importantly, adsorption was predicted to be a strong function of solvent environment and EW.[143] This was verified experimentally by quartz-crystal-microbalance (QCM) experiments in Chapter 5.[169] Higher ratios of water to propanol promote adsorption to carbon surfaces. Additionally, PFSA binding behavior to carbon was probed with isothermal titration calorimetry (ITC), where analysis of the entropic and enthalpic contributions to the binding free energy reveal that the binding process is entropically-dominated.[169, 180] This also points to hydrophobic interactions between PFSA and the carbon surface.

Ionomer/platinum interactions have received much attention in operating fuel cells, due to sulfonate/platinum interactions that effectively poison the catalyst. A number of groups have extrapolated the results of these *operando* studies, and have assumed there is a strong, inherent platinum/sulfonate interaction; they postulate this interaction drives adsorption to agglomerates in the ink. However, it is important to note that this interaction is potential-dependent, and primarily noted at potentials above the potential of zero charge. [62, 183-184] Additionally, spectroscopic studies have shown that in addition to sulfonate groups, there is co-adsorption of fluorocarbon[62-63, 181] and ether-oxygen groups.[65] In inks, Chapter 5 demonstrates that while binding strength does increase

with decreasing EW, the amount of ionomer that adsorbs to platinum under no applied potential is less than the amount that adsorbs to a hydrophobic (carbon-like) surface.[169] Moreover, the binding mechanism is entropically driven, similar to that seen with carbon.[169]

All of the above information suggests that the ionomer/platinum ink interaction is different than that in operating fuel cells: in inks it is not particularly strong, as compared with the other interactions present. While *ex-situ* thin-film studies have revealed different behavior on platinum versus on silicon,[161, 187] it is possible this is merely due to changes in substrate hydrophobicity, rather than due to strong specific-ion binding between sulfonate and platinum. In fact, ionomer structures have been shown to order differently on substrates of varying hydrophobicity.[188] These ionomer/platinum ink interactions are also subject to dispersion solvent effects: atomic-force-microscopy studies reveal that ionomer films are smoother when they adsorb from mixed water-propanol solvents onto platinum, rather than from high-water concentration solvents,[181] and the QCM experiments of Chapter 5 exhibit increased ionomer adsorption at higher water contents.[169]

Given the differences (and similarities) between the ionomer/platinum and ionomer/carbon ink interactions, and due to the larger surface area of carbon relative to platinum on the exterior of catalyst particles, it is likely that solution-level interactions are primarily controlled by ionomer/carbon interactions. This indicates that different carbon types or functionalization should manifest different ionomer/carbon interactions; the impact this has on CL performance should be evident when exploring I:C ratio. This is seen in Figure 1.6: parameters have different trends as a function of I:C when using Vulcan carbon versus high-surface-area carbon supports (that have varying surface hydrophobicity).

Because ionomer/carbon interactions are stronger than ionomer/platinum interactions, the ionomer/catalyst particle interaction strength will vary (weaken) as platinum loading on the particle surface is increased. As studied in Chapter 6, higher platinum loading results in weaker ink zeta potentials, likely patchier ionomer coverage, larger CL agglomerates, and worse local transport resistances due to altered ink interactions. This further demonstrates the direct link between ink properties and CL performance and exemplifies how ink components may be strategically selected to tune interactions. Possible avenues to do so will rely on altering either the hydrophobic or electrostatic interaction between the ionomer and the particles. Treating the carbon or imbuing it with a surface layer to make it more hydrophobic (or hydrophilic) would alter the strength of interaction between the backbone and the carbon surface. Similarly, adding charged groups to the catalyst particle would cause additional electrostatic repulsion (or attraction, depending on the polarity) between the ionomer and the particles. These concepts can also be extended to altering the ionomer chemistry either by changing the backbone, or by adding additional ionic groups to the sidechains. Already in the last three years, researchers are employing these techniques to affect ionomer/particle interactions[222] with modified supports,[77, 223-224] additives[196] (including ionic liquids),[225-226] and novel ionomers.[227]

7.3 Concluding Remarks

Ultimately, the goal is to predict catalyst-layer (CL) performance given certain ink parameters, or even better, to determine how an ink would need to change to achieve optimal CL performance via optimized structure. If a more active catalyst type is created, or a more conductive and stable ionomer is synthesized, one could know *a priori* how it would affect CL properties and how to tune ink ratios and processing conditions without the need for months of empirical optimization. To make this a reality, we must understand how ink parameters impact ink interactions (and identified interaction descriptors), and in turn how these interactions dictate CL parameters. However, due to disparate material sets used and often incomplete experimental methods detailing CL fabrication, it is difficult to make use of the wealth of CL literature. Rather, systematic, ink-focused research is needed, and the community must make a concerted effort to report all relevant ink details (*i.e.* metadata) moving forward.

Despite these challenges, this dissertation has made significant progress toward understanding how ink parameters influence ink interactions, in particular, ionomer/particle and ionomer/solvent interactions. Key in both of these interactions is the ionomer itself. Small angle x-ray and neutron scattering has greatly aided in understanding the general conformation of the ionomer. However, molecular-level information is still missing, and is required to understand truly the ionomer/particle interface both in inks and during fuel-cell operation. pH measurements (corroborated by molecular-dynamics simulations) may be a way to elucidate sidechain structure, but additional direct experimental observation is necessary. How do the sidechains orient in solution? What is the exact structure of an ionomer aggregate? Importantly, does this aggregate structure rearrange upon adsorption? What is the ionomer orientation when adsorbed on a particle, both in an ink and dried in a CL? Advances in chemically-resolved microscopy and scattering techniques are necessary to probe ionomer structure on a molecular level with elemental and orientational specificity. Additionally, the protein community has answered many of these questions to unravel protein structure; there are significant opportunities to apply similar techniques to ionomer studies.

On a more macroscopic level, it is imperative to link measurable ink interaction descriptors (*i.e.* zeta potential, agglomerate size, pH) to CL parameters, moving beyond the correlations presented in Chapter 1. This linkage will undoubtedly involve modeling/simulation of some kind. Possibilities include modifying a DLVO-type framework to consider additional ionomer physics, or larger-scale phase-field or particle-dynamics simulations. Importantly, this dissertation has not considered the deposition method or drying process, which will influence the final CL structure. This drying step will also need to be incorporated into modeling efforts. In this way, we can completely understand (and therefore control) the ink-to-CL fabrication process, enabling ink engineering for smarter CL design for a wide range of energy-conversion devices.

8 References

1. The Future of Hydrogen. https://www.iea.org/reports/the-future-of-hydrogen.

2. Hydrogen Economy Outlook. https://data.bloomberglp.com/professional/sites/24/BNEF-Hydrogen-Economy-Outlook-Key-Messages-30-Mar-2020.pdf.

3. Road Map to a US Hydrogen Economy. http://www.fchea.org/us-hydrogen-study.

4. Cullen, D. A.; Neyerlin, K. C.; Ahluwalia, R. K.; Mukundan, R.; More, K. L.; Borup, R. L.; Weber, A. Z.; Myers, D. J.; Kusoglu, A., New roads and challenges for fuel cells in heavy-duty transportation. *Nature Energy* **2021**.

5. DOE Launches Two Consortia to Advance Fuel Cell Truck and Electrolyzer R&D. https://www.energy.gov/eere/articles/doe-launches-two-consortia-advance-fuel-cell-truck-and-electrolyzer-rd.

6. Holdcroft, S., Fuel Cell Catalyst Layers: A Polymer Science Perspective. *Chem. Mater.* **2014,** *26* (1), 381-393.

7. Kusoglu, A.; Weber, A. Z., New Insights into Perfluorinated Sulfonic-Acid Ionomers. *Chem. Rev.* **2017,** *117* (3), 987-1104.

8. Cetinbas, F. C.; Ahluwalia, R. K.; Kariuki, N. N.; Myers, D. J., Agglomerates in Polymer Electrolyte Fuel Cell Electrodes: Part I. Structural Characterization. *J. Electrochem. Soc.* **2018,** *165* (13), F1051-F1058.

9. Epting, W. K.; Gelb, J.; Litster, S., Resolving the Three-Dimensional Microstructure of Polymer Electrolyte Fuel Cell Electrodes using Nanometer-Scale X-ray Computed Tomography. *Advanced Functional Materials* **2012,** *22* (3), 555-560.

10. Cullen, D. A.; Koestner, R.; Kukreja, R. S.; Liu, Z. Y.; Minko, S.; Trotsenko, O.; Tokarev, A.; Guetaz, L.; Meyer, H. M.; Parish, C. M.; More, K. L., Imaging and Microanalysis of Thin Ionomer Layers by Scanning Transmission Electron Microscopy. *J. Electrochem. Soc.* **2014,** *161* (10), F1111-F1117.

11. Karan, K., PEFC catalyst layer: Recent advances in materials, microstructural characterization, and modeling. *Current Opinion in Electrochemistry* **2017,** *5* (1), 27-35.

12. Uchida, M.; Aoyama, Y.; Eda, N.; Ohta, A., New Preparation Method for Polymer-Electrolyte Fuel Cells. *J. Electrochem. Soc.* **1995,** *142* (2), 463-468.

13. Litster, S.; McLean, G., PEM fuel cell electrodes. *J. Power Sources* **2004,** *130* (1–2), 61-76.

14. Rajalakshmi, N.; Dhathathreyan, K. S., Catalyst layer in PEMFC electrodes—Fabrication, characterisation and analysis. *Chem. Eng. J.* **2007,** *129* (1–3), 31-40.

15. Obut, S.; Alper, E., Numerical assessment of dependence of polymer electrolyte membrane fuel cell performance on cathode catalyst layer parameters. *J. Power Sources* **2011,** *196* (4), 1920-1931.

16. Owejan, J. P.; Owejan, J. E.; Gu, W., Impact of Platinum Loading and Catalyst Layer Structure on PEMFC Performance. *Journal of the Electrochemical Society* **2013,** *160* (8), F824-F833.

17. Weber, A. Z.; Kusoglu, A., Unexplained transport resistances for low-loaded fuel-cell catalyst layers. *J. Mater. Chem. A* **2014,** *2* (41), 17207-17211.

18. Takahashi, S.; Mashio, T.; Horibe, N.; Akizuki, K.; Ohma, A., Analysis of the Microstructure Formation Process and Its Influence on the Performance of Polymer Electrolyte Fuel-Cell Catalyst Layers. *ChemElectroChem* **2015,** *2* (10), 1560-1567.

19. Kariuki, N.; Myers, D. J.; Fongalland, D.; Bonastre, A. M.; Sharman, J., Microstructure Analysis of Polymer Electrolyte Membrane Fuel Cell Catalyst-Ionomer Inks and Cathode Catalyst Layers By Ultra Small Angle X-Ray Scattering. *Meeting Abstracts* **2016,** *MA2016-01* (35), 1735.

20. Cetinbas, F.; Ahluwalia, R.; Kariuki, N.; More, K. L.; Cullen, D. A.; Sneed, B.; Winarski, R. P.; Ilavsky, J.; De Andrade, V.; Myers, D. J., Structural Characterization and Transport Modeling of Pt and Pt Alloy Polymer Electrolyte Fuel Cell Cathode Catalyst Layers. *Meeting Abstracts* **2016,** *MA2016-02* (38), 2598.

21. Cetinbas, F. C.; Ahluwalia, R. K.; Kariuki, N.; De Andrade, V.; Fongalland, D.; Smith, L.; Sharman, J.; Ferreira, P.; Rasouli, S.; Myers, D. J., Hybrid approach combining multiple characterization techniques and simulations for microstructural analysis of proton exchange membrane fuel cell electrodes. *J. Power Sources* **2017,** *344*, 62-73.

22. Padgett, E.; Andrejevic, N.; Liu, Z.; Kongkanand, A.; Gu, W.; Moriyama, K.; Jiang, Y.; Kumaraguru, S.; Moylan, T.; Kukreja, R.; Muller, D., Connecting Fuel Cell Catalyst Nanostructure and Accessibility Using Quantitative Cryo-STEM Tomography. *Journal of the Electrochemical Society* **2018,** *165* (3), F173-F180.

23. Alink, R.; Singh, R.; Schneider, P.; Christmann, K.; Schall, J.; Keding, R.; Zamel, N., Full Parametric Study of the Influence of Ionomer Content, Catalyst Loading and Catalyst Type on Oxygen and Ion Transport in PEM Fuel Cell Catalyst Layers. *Molecules* **2020,** *25* (7), 1523.

24. Nagappan, R.; Swami, K.; Roland, K.; Timothy, F.; Wenbin, G.; Nancy, N. K.; Deborah, J. M.; Peter, J. D.; Ahmet, K., Editors' Choice—Ionomer Side Chain Length and Equivalent Weight Impact on High Current Density Transport Resistances in PEMFC Cathodes. *J. Electrochem. Soc.* **2021,** *168*, 024518.

25. Borup, R. L.; Kusoglu, A.; Neyerlin, K. C.; Mukundan, R.; Ahluwalia, R. K.; Cullen, D. A.; More, K. L.; Weber, A. Z.; Myers, D. J., Recent developments in catalyst-related PEM fuel cell durability. *Current Opinion in Electrochemistry* **2020,** *21*, 192-200.

26. Borup, R.; Meyers, J.; Pivovar, B.; Kim, Y. S.; Mukundan, R.; Garland, N.; Myers, D.; Wilson, M.; Garzon, F.; Wood, D.; Zelenay, P.; More, K.; Stroh, K.; Zawodzinski, T.; Boncella, J.; McGrath, J. E.; Inaba, M.; Miyatake, K.; Hori, M.; Ota, K.; Ogumi, Z.; Miyata, S.; Nishikata, A.; Siroma, Z.; Uchimoto, Y.; Yasuda, K.; Kimijima, K.-i.; Iwashita, N., Scientific Aspects of Polymer Electrolyte Fuel Cell Durability and Degradation. *Chem. Rev.* **2007,** *107* (10), 3904-3951.

27. Hatzell, K. B.; Dixit, M. B.; Berlinger, S. A.; Weber, A. Z., Understanding inks for porous-electrode formation. *J. Mater. Chem. A* **2017,** *5* (39), 20527-20533.

28. Thompson, S. T.; Wilson, A. R.; Zelenay, P.; Myers, D. J.; More, K. L.; Neyerlin, K. C.; Papageorgopoulos, D., ElectroCat: DOE's approach to PGM-free catalyst and electrode R&D. *Solid State Ionics* **2018,** *319*, 68-76.

29. Serov, A.; Artyushkova, K.; Niangar, E.; Wang, C.; Dale, N.; Jaouen, F.; Sougrati, M.-T.; Jia, Q.; Mukerjee, S.; Atanassov, P., Nano-structured non-platinum catalysts for automotive fuel cell application. *Nano Energy* **2015,** *16*, 293-300.

30. Shao, Y.; Dodelet, J.-P.; Wu, G.; Zelenay, P., PGM-Free Cathode Catalysts for PEM Fuel Cells: A Mini-Review on Stability Challenges. *Advanced Materials* **2019,** *31* (31), 1807615.

31. Antolini, E., Carbon supports for low-temperature fuel cell catalysts. *Appl. Catal., B* **2009,** *88* (1), 1-24.

32. Yarlagadda, V.; Carpenter, M. K.; Moylan, T. E.; Kukreja, R. S.; Koestner, R.; Gu, W.; Thompson, L.; Kongkanand, A., Boosting Fuel Cell Performance with Accessible Carbon Mesopores. *ACS Energy Letters* **2018,** *3* (3), 618-621.

33. Samad, S.; Loh, K. S.; Wong, W. Y.; Lee, T. K.; Sunarso, J.; Chong, S. T.; Wan Daud, W. R., Carbon and non-carbon support materials for platinum-based catalysts in fuel cells. *Int. J. Hydrogen Energy* **2018,** *43* (16), 7823-7854.

34. Liu, Y.; Ji, C.; Gu, W.; Jorne, J.; Gasteiger, H. A., Effects of Catalyst Carbon Support on Proton Conduction and Cathode Performance in PEM Fuel Cells. *J. Electrochem. Soc.* **2011,** *158* (6), B614.

35. Padgett, E.; Andrejevic, N.; Liu, Z.; Kongkanand, A.; Gu, W.; Moriyama, K.; Jiang, Y.; Kumaraguru, S.; Moylan, T. E.; Kukreja, R.; Muller, D. A., Editors' Choice—Connecting Fuel Cell Catalyst Nanostructure and Accessibility Using Quantitative Cryo-STEM Tomography. *J. Electrochem. Soc.* **2018,** *165* (3), F173-F180.

36. Sondheimer, S. J.; Bunce, N. J.; Lemke, M. E.; Fyfe, C. A., Acidity and catalytic activity of Nafion-H. *Macromolecules* **1986,** *19* (2), 339-343.

37. Welch, C.; Labouriau, A.; Hjelm, R.; Orler, B.; Johnston, C.; Kim, Y. S., Nafion in Dilute Solvent Systems: Dispersion or Solution? *ACS Macro. Lett.* **2012,** *1* (12), 1403-1407.

38. Silva, R. F.; De Francesco, M.; Pozio, A., Solution-cast Nafion® ionomer membranes: preparation and characterization. *Electrochim. Acta* **2004,** *49* (19), 3211-3219.

39. Fernández, R.; Ferreira-Aparicio, P.; Daza, L., PEMFC electrode preparation: Influence of the solvent composition and evaporation rate on the catalytic layer microstructure. *J. Power Sources* **2005,** *151*, 18-24.

40. Johnston, C. M.; Lee, K.-S.; Rockward, T.; Labouriau, A.; Mack, N.; Kim, Y. S., Impact of Solvent on Ionomer Structure and Fuel Cell Durability. *ECS Trans.* **2009,** *25* (1), 1617-1622.

41. Lei, C.; Fan, Y.; Natalia, M.; Magali, S.; Geraldine, M. P.; Jasna, J.; David, C.; Karren, L. M.; Yu Seung, K.; Hui, X., Impact of Catalyst Ink Dispersing Solvent on PEM Fuel Cell Performance and Durability. *J. Electrochem. Soc.* **2021,** *168*, 044517.

42. Du, S.; Li, W.; Wu, H.; Abel Chuang, P.-Y.; Pan, M.; Sui, P.-C., Effects of ionomer and dispersion methods on rheological behavior of proton exchange membrane fuel cell catalyst layer ink. *Int. J. Hydrogen Energy* **2020,** *45* (53), 29430-29441.

43. Wang, M.; Park, J. H.; Kabir, S.; Neyerlin, K. C.; Kariuki, N. N.; Lv, H.; Stamenkovic, V. R.; Myers, D. J.; Ulsh, M.; Mauger, S. A., Impact of Catalyst Ink Dispersing Methodology on Fuel Cell Performance Using in-Situ X-ray Scattering. *ACS Applied Energy Materials* **2019,** *2* (9), 6417-6427.

44. Mauger, S. A.; Pfeilsticker, J. R.; Wang, M.; Medina, S.; Yang-Neyerlin, A. C.; Neyerlin, K. C.; Stetson, C.; Pylypenko, S.; Ulsh, M., Fabrication of high-performance gas-diffusion-electrode based membrane-electrode assemblies. *J. Power Sources* **2020,** *450*, 227581.

45. Millington, B.; Whipple, V.; Pollet, B. G., A novel method for preparing proton exchange membrane fuel cell electrodes by the ultrasonic-spray technique. *J. Power Sources* **2011,** *196* (20), 8500-8508.

46. Van Cleve, T.; Khandavalli, S.; Chowdhury, A.; Medina, S.; Pylypenko, S.; Wang, M.; More, K. L.; Kariuki, N. N.; Myers, D. J.; Weber, A. Z.; Mauger, S.; Ulsh, M.; Neyerlin, K. C., Dictating Pt-based Electrocatalyst Performance in Polymer Electrolyte Fuel Cells; from Formulation to Application. *ACS Appl. Mater. Interfaces* **2019**.

47. Huang, D. C.; Yu, P. J.; Liu, F. J.; Huang, S. L.; Hsueh, K. L.; Chen, Y. C.; Wu, C. H.; Chang, W. C.; Tsau, F. H., Effect of Dispersion Solvent in Catalyst Ink on Proton Exchange Membrane Fuel Cell Performance. *Int. J. Electrochem. Sci.* **2011,** *6* (7), 2551-2565.

48. Mauger, S. A.; Neyerlin, K. C.; Yang-Neyerlin, A. C.; More, K. L.; Ulsh, M., Gravure Coating for Roll-to-Roll Manufacturing of Proton-Exchange-Membrane Fuel Cell Catalyst Layers. *J. Electrochem. Soc.* **2018,** *165* (11), F1012-F1018.

49. Saha, M. S.; Paul, D. K.; Peppley, B. A.; Karan, K., Fabrication of catalyst-coated membrane by modified decal transfer technique. *Electrochemistry Communications* **2010,** *12* (3), 410-413.

50. Orfanidi, A.; Rheinländer, P. J.; Schulte, N.; Gasteiger, H. A., Ink Solvent Dependence of the Ionomer Distribution in the Catalyst Layer of a PEMFC. *J. Electrochem. Soc.* **2018,** *165* (14), F1254-F1263.

51. Suzuki, T.; Tsushima, S.; Hirai, S., Effects of Nafion® ionomer and carbon particles on structure formation in a proton-exchange membrane fuel cell catalyst layer fabricated by the decal-transfer method. *Int. J. Hydrogen Energy* **2011,** *36* (19), 12361-12369.

52. Xu, R.; Wu, C.; Xu, H., Particle size and zeta potential of carbon black in liquid media. *Carbon* **2007,** *45* (14), 2806-2809.

53. Berlinger, S. A.; McCloskey, B. D.; Weber, A. Z., Understanding Binary Interactions in Fuel-Cell Catalyst-Layer Inks. *ECS Trans.* **2017,** *80* (8), 309-319.

54. Loppinet, B.; Gebel, G., Rodlike Colloidal Structure of Short Pendant Chain Perfluorinated Ionomer Solutions. *Langmuir* **1998,** *14* (8), 1977-1983.

55. Loppinet, B.; Gebel, G.; Williams, C. E., Small-Angle Scattering Study of Perfluorosulfonated Ionomer Solutions. *J. Phys. Chem. B.* **1997,** *101* (10), 1884-1892.

56. Mabuchi, T.; Huang, S.-F.; Tokumasu, T., Dispersion of Nafion Ionomer Aggregates in 1-Propanol/Water Solutions: Effects of Ionomer Concentration, Alcohol Content, and Salt Addition. *Macromolecules* **2020,** *53* (9), 3273-3283.

57. Kuo, A.-T.; Urata, S.; Nakabayashi, K.; Watabe, H.; Honmura, S., Coarse-Grained Molecular Dynamics Simulation of Perfluorosulfonic Acid Polymer in Water–Ethanol Mixtures. *Macromolecules* **2021,** *54* (2), 609-620.

58. Ghelichi, M.; Malek, K.; Eikerling, M. H., Ionomer Self-Assembly in Dilute Solution Studied by Coarse-Grained Molecular Dynamics. *Macromolecules* **2016,** *49* (4), 1479-1489.

59. Tarokh, A.; Karan, K.; Ponnurangam, S., Atomistic MD Study of Nafion Dispersions: Role of Solvent and Counterion in the Aggregate Structure, Ionic Clustering, and Acid Dissociation. *Macromolecules* **2020,** *53* (1), 288-301.

60. Ngo, T. T.; Yu, T. L.; Lin, H.-L., Influence of the composition of isopropyl alcohol/water mixture solvents in catalyst ink solutions on proton exchange membrane fuel cell performance. *J. Power Sources* **2013,** *225*, 293-303.

61. Subbaraman, R.; Strmcnik, D.; Stamenkovic, V.; Markovic, N. M., Three Phase Interfaces at Electrified Metal−Solid Electrolyte Systems 1. Study of the Pt(hkl)−Nafion Interface. *J. Phys. Chem. C.* **2010,** *114* (18), 8414-8422.

62. Masuda, T.; Sonsudin, F.; Singh, P. R.; Naohara, H.; Uosaki, K., Potential-Dependent Adsorption and Desorption of Perfluorosulfonated Ionomer on a Platinum Electrode Surface Probed by Electrochemical Quartz Crystal Microbalance and Atomic Force Microscopy. *J. Phys. Chem. C.* **2013,** *117* (30), 15704-15709.

63. Kendrick, I.; Kumari, D.; Yakaboski, A.; Dimakis, N.; Smotkin, E. S., Elucidating the Ionomer-Electrified Metal Interface. *Journal of the American Chemical Society* **2010,** *132* (49), 17611-17616.

64. Liu, C.; Uchiyama, T.; Nagata, N.; Arao, M.; Yamamoto, K.; Watanabe, T.; Gao, X.; Imai, H.; Katayama, S.; Sugawara, S.; Shinohara, K.; Oshima, K.; Sakurai, S.; Uchimoto, Y., Operando X-ray Absorption Spectroscopic Study on the Influence of Specific Adsorption of the Sulfo Group in the Perfluorosulfonic Acid Ionomer on the Oxygen Reduction Reaction Activity of the Pt/C Catalyst. *ACS Applied Energy Materials* **2021**.

65. Kodama, K.; Motobayashi, K.; Shinohara, A.; Hasegawa, N.; Kudo, K.; Jinnouchi, R.; Osawa, M.; Morimoto, Y., Effect of the Side-Chain Structure of Perfluoro-Sulfonic Acid Ionomers on the Oxygen Reduction Reaction on the Surface of Pt. *ACS Catalysis* **2018,** *8* (1), 694-700.

66. Fan, L.; Wang, Y.; Jiao, K., Oxygen Permeation Resistances and Routes in Nanoscale Ionomer Thin Film on Platinum Surface. *J. Electrochem. Soc.* **2021,** *168* (1), 014511.

67. Berlinger, S. A.; McCloskey, B. D.; Weber, A. Z., Inherent Acidity of Perfluorosulfonic Acid Ionomer Dispersions and Implications for Ink Aggregation. *The Journal of Physical Chemistry B* **2018,** *122* (31), 7790-7796.

68. Khandavalli, S.; Park, J. H.; Kariuki, N. N.; Myers, D. J.; Stickel, J. J.; Hurst, K.; Neyerlin, K. C.; Ulsh, M.; Mauger, S. A., Rheological Investigation on the Microstructure of Fuel Cell Catalyst Inks. *ACS Appl. Mater. Interfaces* **2018,** *10* (50), 43610-43622.

69. Balu, R.; Choudhury, N. R.; Mata, J. P.; de Campo, L.; Rehm, C.; Hill, A. J.; Dutta, N. K., Evolution of the Interfacial Structure of a Catalyst Ink with the Quality of the Dispersing Solvent: A Contrast Variation Small-Angle and Ultrasmall-Angle Neutron Scattering Investigation. *ACS Appl. Mater. Interfaces* **2019,** *11* (10), 9934-9946.

70. Dixit, M. B.; Harkey, B. A.; Shen, F.; Hatzell, K. B., Catalyst Layer Ink Interactions That Affect Coatability. *J. Electrochem. Soc.* **2018,** *165* (5), F264-F271.

71. Jung, C.-Y.; Kim, W.-J.; Yi, S.-C., Optimization of catalyst ink composition for the preparation of a membrane electrode assembly in a proton exchange membrane fuel cell using the decal transfer. *Int. J. Hydrogen Energy* **2012,** *37* (23), 18446-18454.

72. Kim, T.-H.; Yi, J.-Y.; Jung, C.-Y.; Jeong, E.; Yi, S.-C., Solvent effect on the Nafion agglomerate morphology in the catalyst layer of the proton exchange membrane fuel cells. *Int. J. Hydrogen Energy* **2017,** *42* (1), 478-485.

73. Millington, B.; Du, S.; Pollet, B. G., The effect of materials on proton exchange membrane fuel cell electrode performance. *J. Power Sources* **2011,** *196* (21), 9013-9017.

74. Thanasilp, S.; Hunsom, M., Effect of MEA fabrication techniques on the cell performance of Pt–Pd/C electrocatalyst for oxygen reduction in PEM fuel cell. *Fuel* **2010,** *89* (12), 3847-3852.

75. Therdthianwong, A.; Ekdharmasuit, P.; Therdthianwong, S., Fabrication and Performance of Membrane Electrode Assembly Prepared by a Catalyst-Coated Membrane Method: Effect of Solvents Used in a Catalyst Ink Mixture. *Energy Fuels* **2010,** *24* (2), 1191-1196.

76. Yang, F.; Xin, L.; Uzunoglu, A.; Qiu, Y.; Stanciu, L.; Ilavsky, J.; Li, W.; Xie, J., Investigation of the Interaction between Nafion Ionomer and Surface Functionalized Carbon Black Using Both Ultrasmall Angle X-ray Scattering and Cryo-TEM. *ACS Appl. Mater. Interfaces* **2017,** *9* (7), 6530-6538.

77. Orfanidi, A.; Madkikar, P.; El-Sayed, H. A.; Harzer, G. S.; Kratky, T.; Gasteiger, H. A., The Key to High Performance Low Pt Loaded Electrodes. *J. Electrochem. Soc.* **2017,** *164* (4), F418-F426.

78. Doo, G.; Lee, J. H.; Yuk, S.; Choi, S.; Lee, D.-H.; Lee, D. W.; Kim, H. G.; Kwon, S. H.; Lee, S. G.; Kim, H.-T., Tuning the Ionomer Distribution in the Fuel Cell Catalyst Layer with Scaling the Ionomer Aggregate Size in Dispersion. *ACS Appl. Mater. Interfaces* **2018,** *10* (21), 17835-17841.

79. Ngo, T. T.; Yu, T. L.; Lin, H.-L., Nafion-based membrane electrode assemblies prepared from catalyst inks containing alcohol/water solvent mixtures. *J. Power Sources* **2013,** *238*, 1-10.

80. Sasikumar, G.; Ihm, J. W.; Ryu, H., Optimum Nafion content in PEM fuel cell electrodes. *Electrochim. Acta* **2004,** *50* (2–3), 601-605.

81. Sasikumar, G.; Ihm, J. W.; Ryu, H., Dependence of optimum Nafion content in catalyst layer on platinum loading. *J. Power Sources* **2004,** *132* (1–2), 11-17.

82. Berlinger, S. A.; Garg, S.; Weber, A. Z., Multicomponent, multiphase interactions in fuel-cell inks. *Current Opinion in Electrochemistry* **2021,** *29*, 100744.

83. Passalacqua, E.; Lufrano, F.; Squadrito, G.; Patti, A.; Giorgi, L., Nafion content in the catalyst layer of polymer electrolyte fuel cells: effects on structure and performance. *Electrochim. Acta* **2001,** *46* (6), 799-805.

84. Ishikawa, H.; Sugawara, Y.; Inoue, G.; Kawase, M., Effects of Pt and ionomer ratios on the structure of catalyst layer: A theoretical model for polymer electrolyte fuel cells. *J. Power Sources* **2018,** *374*, 196-204.

85. Kongkanand, A.; Mathias, M. F., The Priority and Challenge of High-Power Performance of Low-Platinum Proton-Exchange Membrane Fuel Cells. *The Journal of Physical Chemistry Letters* **2016,** *7* (7), 1127-1137.

86. Schuler, T.; Chowdhury, A.; Freiberg, A. T.; Sneed, B.; Spingler, F. B.; Tucker, M. C.; More, K. L.; Radke, C. J.; Weber, A. Z., Fuel-Cell Catalyst-Layer Resistance via Hydrogen Limiting-Current Measurements. *J. Electrochem. Soc.* **2019,** *166* (7), F3020-F3031.

87. Sadeghi, E.; Putz, A.; Eikerling, M., Effects of ionomer coverage on agglomerate effectiveness in catalyst layers of polymer electrolyte fuel cells. *Journal of Solid State Electrochemistry* **2014,** *18* (5), 1271-1279.

88. Van Cleve, T.; Khandavalli, S.; Chowdhury, A.; Medina, S.; Pylypenko, S.; Wang, M.; More, K. L.; Kariuki, N.; Myers, D. J.; Weber, A. Z.; Mauger, S. A.; Ulsh, M.; Neyerlin, K. C., Dictating Pt-Based Electrocatalyst Performance in Polymer Electrolyte Fuel Cells, from Formulation to Application. *ACS Appl. Mater. Interfaces* **2019,** *11* (50), 46953-46964.

89. Osmieri, L.; Wang, G.; Cetinbas, F. C.; Khandavalli, S.; Park, J.; Medina, S.; Mauger, S. A.; Ulsh, M.; Pylypenko, S.; Myers, D. J.; Neyerlin, K. C., Utilizing ink composition to tune bulk-electrode gas transport, performance, and operational robustness for a Fe–N–C catalyst in polymer electrolyte fuel cell. *Nano Energy* **2020,** *75*, 104943.

90. Shin, S. J.; Lee, J. K.; Ha, H. Y.; Hong, S. A.; Chun, H. S.; Oh, I. H., Effect of the catalytic ink preparation method on the performance of polymer electrolyte membrane fuel cells. *J. Power Sources* **2002,** *106* (1–2), 146-152.

91. Xie, Z.; Navessin, T.; Zhao, X.; Adachi, M.; Holdcroft, S.; Mashio, T.; Ohma, A.; Shinohara, K., Nafion Ionomer Aggregation and its Influence on Proton Conduction and Mass Transport in Fuel Cell Catalyst Layers. *ECS Trans.* **2008,** *16* (2), 1811-1816.

92. Sharma, R.; Grahl-Madsen, L.; Andersen, S. M., Influence of dispersion media on Nafion® ionomer distribution in proton exchange membrane fuel cell catalyst carbon support. *Materials Chemistry and Physics* **2019,** *226*, 66-72.

93. Lee, J. H.; Doo, G.; Kwon, S. H.; Choi, S.; Kim, H.-T.; Lee, S. G., Dispersion-Solvent Control of Ionomer Aggregation in a Polymer Electrolyte Membrane Fuel Cell. *Scientific Reports* **2018,** *8* (1), 10739.

94. Yang, F.; Xin, L.; Uzunoglu, A.; Stanciu, L.; Ilavsky, J.; Son, S.; Xie, J., Investigation of Solvent Effects on the Dispersion of Carbon Agglomerates and Nafion Ionomer Particles in Catalyst Inks Using Ultra Small Angle X-Ray Scattering Method. *ECS Trans.* **2016,** *75* (14), 361-371.

95. Shukla, S.; Bhattacharjee, S.; Weber, A. Z.; Secanell, M., Experimental and Theoretical Analysis of Ink Dispersion Stability for Polymer Electrolyte Fuel Cell Applications. *J. Electrochem. Soc.* **2017,** *164* (6), F600-F609.

96. Gebel, G.; Loppinet, B., Colloidal structure of ionomer solutions in polar solvents. *J. Mol. Struct.* **1996,** *383* (1), 43-49.

97. Aldebert, P.; Gebel, G.; Loppinet, B.; Nakamura, N., Polyelectrolyte effect in perfluorosulfonated ionomer solutions. *Polymer* **1995,** *36* (2), 431-434.

98. Lee, S.-J.; Yu, T. L.; Lin, H.-L.; Liu, W.-H.; Lai, C.-L., Solution properties of nafion in methanol/water mixture solvent. *Polymer* **2004,** *45* (8), 2853-2862.

99. Lin, H.-L.; Yu, T. L.; Huang, C.-H.; Lin, T.-L., Morphology study of Nafion membranes prepared by solutions casting. *J. Polym. Sci., Part B: Polym. Phys.* **2005,** *43* (21), 3044-3057.

100. Ma, C.-H.; Yu, T. L.; Lin, H.-L.; Huang, Y.-T.; Chen, Y.-L.; Jeng, U. S.; Lai, Y.-H.; Sun, Y.-S., Morphology and properties of Nafion membranes prepared by solution casting. *Polymer* **2009,** *50* (7), 1764-1777.

101. Moore, R. B.; Martin, C. R., Chemical and morphological properties of solution-cast perfluorosulfonate ionomers. *Macromolecules* **1988,** *21* (5), 1334-1339.

102. Kim, Y. S.; Welch, C. F.; Hjelm, R. P.; Mack, N. H.; Labouriau, A.; Orler, E. B., Origin of Toughness in Dispersion-Cast Nafion Membranes. *Macromolecules* **2015,** *48* (7), 2161-2172.

103. Dudenas, P. J.; Kusoglu, A., Evolution of Ionomer Morphology from Dispersion to Film: An in Situ X-ray Study. *Macromolecules* **2019,** *52* (20), 7779-7785.

104. Liu, F.; Ferdous, S.; Schaible, E.; Hexemer, A.; Church, M.; Ding, X.; Wang, C.; Russell, T. P., Fast printing and in situ morphology observation of organic photovoltaics using slot-die coating. *Advanced materials (Deerfield Beach, Fla.)* **2015,** *27* (5), 886-91.

105. Kline, S., Reduction and analysis of SANS and USANS data using IGOR Pro. *Journal of Applied Crystallography* **2006,** *6* (39), 895-900.

106. Teubner, M.; Strey, R., Origin of the scattering peak in microemulsions. *The Journal of Chemical Physics* **1987,** *87* (5), 3195-3200.

107. Chen, S. H.; Chang, S. L.; Strey, R. In *On the interpretation of scattering peaks from bicontinuous microemulsions*, Darmstadt, Steinkopff: Darmstadt, 1990; pp 30-35.

108. Kusoglu, A.; Kushner, D.; Paul, D. K.; Karan, K.; Hickner, M. A.; Weber, A. Z., Impact of Substrate and Processing on Confinement of Nafion Thin Films. *Advanced Functional Materials* **2014,** *24* (30), 4763-4774.

109. Dishari, S. K.; Hickner, M. A., Antiplasticization and Water Uptake of Nafion Thin Films. *ACS Macro Lett.* **2012,** *1* (2), 291-295.

110. Kongkanand, A., Interfacial Water Transport Measurements in Nafion Thin Films Using a Quartz-Crystal Microbalance. *J Phys Chem C* **2011,** *115* (22), 11318-11325.

111. Paul, D. K.; Fraser, A.; Karan, K., Towards the understanding of proton conduction mechanism in PEMFC catalyst layer: Conductivity of adsorbed Nafion films. *Electrochemistry Communications* **2011,** *13* (8), 774-777.

112. Eastman, S. A.; Kim, S.; Page, K. A.; Rowe, B. W.; Kang, S.; Soles, C. L.; Yager, K. G., Effect of Confinement on Structure, Water Solubility, and Water Transport in Nafion Thin Films. *Macromolecules* **2012,** *45* (19), 7920-7930.

113. Gebel, G.; Lambard, J., Small-Angle Scattering Study of Water-Swollen Perfluorinated Ionomer Membranes. *Macromolecules* **1997,** *30* (25), 7914-7920.

114. Takamatsu, T.; Eisenberg, A., Densities and expansion coefficients of nafion polymers. *J. Appl. Polym. Sci.* **1979,** *24* (11), 2221-2235.

115. Zhernenkov, M.; Canestrari, N.; Chubar, O.; DiMasi, E. In *Soft matter interfaces beamline at NSLS-II: geometrical ray-tracing vs. wavefront propagation simulations*, September 01, 2014; 2014; p 92090G.

116. Pandolfi, R. J.; Allan, D. B.; Arenholz, E.; Barroso-Luque, L.; Campbell, S. I.; Caswell, T. A.; Blair, A.; Carlo, F. D.; Fackler, S.; Fournier, A. P.; Freychet, G.; Fukuto, M.; Gürsoy, D.; Jiang, Z.; Krishnan, H.; Kumar, D.; Kline, R. J.; Li, R.; Liman, C.; Marchesini, S.; Mehta, A.; N'Diaye, A. T.; Parkinson, D. Y.; Parks, H.; Pellouchoud, L. A.; Perciano, T.; Ren, F.; Sahoo, S.; Strzalka, J.; Sunday, D.; Tassone, C. J.; Ushizima, D.; Venkatakrishnan, S.; Yager, K. G.; Zwart, P.; Sethian, J. A.; Hexemer, A., *Xi-cam:* a versatile interface for data visualization and analysis. *Journal of Synchrotron Radiation* **2018,** *25*, 1261-1270.

117. Kusoglu, A.; Savagatrup, S.; Clark, K. T.; Weber, A. Z., Role of Mechanical Factors in Controlling the Structure-Function Relationship of PFSA Ionomers. *Macromolecules* **2012,** *45* (18), 7467-7476.

118. Kusoglu, A.; Weber, A. Z., Water Transport and Sorption in Nafion Membrane. In *Polymers for Energy Storage and Delivery: Polyelectrolytes for Batteries and Fuel Cells*, American Chemical Society: 2012; Vol. 1096, pp 175-199.

119. Scribner *BekkTech's Procedures For Performing In-Plane Membrane Conductivity Testing*

120. Dealy, J. M.; Wissbrun, K. F., *Melt Rheology and Its Role in Plastics Processing*. Springer: 1990.

121. Gebel, G.; Aldebert, P.; Pineri, M., Structure and related properties of solution-cast perfluorosulfonated ionomer films. *Macromolecules* **1987,** *20* (6), 1425-1428.

122. Kusoglu, A.; Savagatrup, S.; Clark, K. T.; Weber, A. Z., Role of Mechanical Factors in Controlling the Structure–Function Relationship of PFSA Ionomers. *Macromolecules* **2012,** *45* (18), 7467-7476.

123. Crothers, A. R.; Radke, C. J.; Weber, A. Z., Impact of Nano- and Mesoscales on Macroscopic Cation Conductivity in Perfluorinated-Sulfonic-Acid Membranes. *J. Phys. Chem. C.* **2017,** *121* (51), 28262-28274.

124. Gao, X.; Yamamoto, K.; Hirai, T.; Uchiyama, T.; Ohta, N.; Takao, N.; Matsumoto, M.; Imai, H.; Sugawara, S.; Shinohara, K.; Uchimoto, Y., Morphology Changes in Perfluorosulfonated Ionomer from Thickness and Thermal Treatment Conditions. *Langmuir* **2020,** *36* (14), 3871-3878.

125. Israelachvili, J. N., *Intermolecular and Surface Forces*. Academic Press: 2011; Vol. 3.

126. Bird, R. B.; Stewart, W. E.; Lightfoot, E. N., *Transport Phenomena, Second Edition*. John Wiley & Sons, Inc.: 2002.

127. Lundberg, R. D.; Phillips, R. R., Influence of sample history on ionomer properties. *J. Polym. Sci., Part C: Polym. Lett* **1984,** *22* (7), 377-384.

128. Zhang, H.; Pan, J.; He, X.; Pan, M., Zeta potential of Nafion molecules in isopropanol-water mixture solvent. *J. Appl. Polym. Sci.* **2008,** *107* (5), 3306-3309.

129. Li, S.; Terao, K.; Sato, T., Colloidal Dispersion of a Perfluorosulfonated Ionomer in Water–Methanol Mixtures. *Polymers* **2018,** *10* (1), 72.

130. Takahashi, S.; Shimanuki, J.; Mashio, T.; Ohma, A.; Tohma, H.; Ishihara, A.; Ito, Y.; Nishino, Y.; Miyazawa, A., Observation of ionomer in catalyst ink of polymer electrolyte fuel cell using cryogenic transmission electron microscopy. *Electrochim. Acta* **2017,** *224*, 178-185.

131. Xu, F.; Zhang, H.; Ilavsky, J.; Stanciu, L.; Ho, D.; Justice, M. J.; Petrache, H. I.; Xie, J., Investigation of a Catalyst Ink Dispersion Using Both Ultra-Small-Angle X-ray Scattering and Cryogenic TEM. *Langmuir* **2010,** *26* (24), 19199-19208.

132. Zamel, N., The catalyst layer and its dimensionality – A look into its ingredients and how to characterize their effects. *J. Power Sources* **2016,** *309*, 141-159.

133. Sung, K. A.; Jung, H.-Y.; Kim, W.-K.; Cho, K.-Y.; Park, J.-K., Influence of dispersion solvent for catalyst ink containing sulfonated poly(ether ether ketone) on cathode behaviour in a direct methanol fuel cell. *J. Power Sources* **2007,** *169* (2), 271-275.

134. Kim, J.-H.; Ha, H. Y.; Oh, I.-H.; Hong, S.-A.; Lee, H.-I., Influence of the solvent in anode catalyst ink on the performance of a direct methanol fuel cell. *J. Power Sources* **2004,** *135* (1–2), 29-35.

135. Koestner, R.; Roiter, Y.; Kozhinova, I.; Minko, S., Effect of Local Charge Distribution on Graphite Surface on Nafion Polymer Adsorption as Visualized at the Molecular Level. *J. Phys. Chem. C.* **2011,** *115* (32), 16019-16026.

136. Gelsema, W. J.; de Ligny, C. L.; Remijnse, A. G.; Blijleven, H. A., pH-Measurements in alcohol-water mixtures, using aqueous standard buffer solutions for calibration. *Recueil des Travaux Chimiques des Pays-Bas* **1966,** *85* (7), 647-660.

137. Dukhin, S. S.; Zimmermann, R.; Werner, C., Electrokinetic phenomena at grafted polyelectrolyte layers. *J. Colloid Interface Sci.* **2005,** *286* (2), 761-773.

138. Hiroyuki, O., Theory of electrostatics and electrokinetics of soft particles. *Science and Technology of Advanced Materials* **2009,** *10* (6), 063001.

139. Ohshima, H., Electrophoresis of soft particles: Analytic approximations. *ELECTROPHORESIS* **2006,** *27* (3), 526-533.

140. Manning, G. S., Limiting Laws and Counterion Condensation in Polyelectrolyte Solutions I. Colligative Properties. *The Journal of Chemical Physics* **1969,** *51* (3), 924-933.

141. Rubatat, L.; Gebel, G.; Diat, O., Fibrillar Structure of Nafion: Matching Fourier and Real Space Studies of Corresponding Films and Solutions. *Macromolecules* **2004,** *37* (20), 7772-7783.

142. O'Reilly, J. M.; Mosher, R. A., Functional groups in carbon black by FTIR spectroscopy. *Carbon* **1983,** *21* (1), 47-51.

143. Mashio, T.; Ohma, A.; Tokumasu, T., Molecular Dynamics Study of Ionomer Adsorption at a Carbon Surface in Catalyst Ink. *Electrochim. Acta* **2016,** *202*, 14-23.

144. Antolini, E.; Giorgi, L.; Pozio, A.; Passalacqua, E., Influence of Nafion loading in the catalyst layer of gas-diffusion electrodes for PEFC. *J. Power Sources* **1999,** *77* (2), 136-142.

145. Fahrenberger, F.; Hickey, O. A.; Smiatek, J.; Holm, C., Importance of Varying Permittivity on the Conductivity of Polyelectrolyte Solutions. *Phys. Rev. Lett.* **2015,** *115* (11), 118301.

146. Mabuchi, T.; Huang, S.-F.; Tokumasu, T., Nafion Ionomer Dispersion in Mixtures of 1-Propanol and Water Based on the Martini Coarse-Grained Model. *Journal of Polymer Science* **2020,** *58* (3), 487-499.

147. Hoffmann, E.; Fischer, D.; Thoma, M.; Damm, C.; Lobaz, V.; Zhigunov, A.; Peukert, W., Impact of DAA/water composition on PFSA ionomer conformation. *J. Colloid Interface Sci.* **2021,** *582*, 883-893.

148. Berlinger, S. A.; Dudenas, P. J.; Bird, A.; Chen, X.; Freychet, G.; McCloskey, B. D.; Kusoglu, A.; Weber, A. Z., Impact of Dispersion Solvent on Ionomer Thin Films and Membranes. *ACS Applied Polymer Materials* **2020,** *2* (12), 5824-5834.

149. Potemkin, I. I.; Vasilevskaya, V. V.; Khokhlov, A. R., Associating polyelectrolytes: Finite size cluster stabilization versus physical gel formation. *The Journal of Chemical Physics* **1999,** *111* (6), 2809-2817.

150. Nomula, S.; Cooper, S. L., Hydrophobic Aggregation in Polyurethane Ionomer Solutions. *J. Colloid Interface Sci.* **1998,** *205* (2), 331-339.

151. Tielemans, M.; Roose, P.; Groote, P. D.; Vanovervelt, J.-C., Colloidal stability of surfactant-free radiation curable polyurethane dispersions. *Progress in Organic Coatings* **2006,** *55* (2), 128-136.

152. Li, J.; Jacobs, I. E.; Friedrich, S.; Stroeve, P.; Moulé, A. J., Solution aging and degradation of a transparent conducting polymer dispersion. *Organic Electronics* **2016,** *34*, 172-178.

153. Agarwal, M.; Joshi, Y. M., Signatures of physical aging and thixotropy in aqueous dispersion of Carbopol. *Physics of Fluids* **2019,** *31* (6), 063107.

154. Park, J.-J.; 최영욱; Kim, K.-B.; Chung, H.; Sohn, D., Aggregation Processes of a Weak Polyelectrolyte, Poly(allylamine) Hydrochloride. *Bulletin of the Korean Chemical Society* **2008,** *29* (1), 104-110.

155. Weiss, R. A., The effect of aging on the thermal behavior of sulfonated polystyrene. *Journal of Polymer Science: Polymer Physics Edition* **1982,** *20* (1), 65-72.

156. Kohzaki, M.; Tsujita, Y.; Takizawa, A.; Kinoshita, T., The crystallization and formation of cluster of ethylene ionomer during physical aging. *J. Appl. Polym. Sci.* **1987,** *33* (7), 2393-2402.

157. Kwon, O.; Kang, Y.; Wu, S.; Zhu, D.-M., Characteristics of Microscopic Proton Current Flow Distributions in Fresh and Aged Nafion Membranes. *J. Phys. Chem. B.* **2010,** *114* (16), 5365-5370.

158. Collette, F. M.; Thominette, F.; Mendil-Jakani, H.; Gebel, G., Structure and transport properties of solution-cast Nafion® membranes subjected to hygrothermal aging. *J. Memb. Sci.* **2013,** *435*, 242-252.

159. Shi, S.; Liu, D.; Liu, D.; Tae, P.; Gao, C. Y.; Yan, L.; An, K.; Chen, X., Mechanical properties and microstructure changes of proton exchange membrane under immersed conditions. *Polymer Engineering & Science* **2014,** *54* (10), 2215-2221.

160. Coms, F. D.; Fuller, T. J.; Schaffer, C. P., A Mechanistic Study of Perfluorosulfonic Acid Membrane Water Permeance Degradation in Air. *J. Electrochem. Soc.* **2018,** *165* (6), F3104-F3110.

161. Tesfaye, M.; Kushner, D. I.; Kusoglu, A., Interplay between Swelling Kinetics and Nanostructure in Perfluorosulfonic Acid Thin-Films: Role of Hygrothermal Aging. *ACS Applied Polymer Materials* **2019,** *1* (4), 631-635.

162. Naudy, S.; Collette, F.; Thominette, F.; Gebel, G.; Espuche, E., Influence of hygrothermal aging on the gas and water transport properties of Nafion® membranes. *J. Memb. Sci.* **2014,** *451*, 293-304.

163. Clapham, S. M.; Coms, F. D.; Fuller, T. J.; Zou, L., Degradation of Perfluorosulfonic Acid Membrane Water Permeance via Formation of Sulfonic Acid Anhydrides. *ECS Trans.* **2013,** *50* (2), 1011-1020.

164. Komoda, Y.; Okabayashi, K.; Nishimura, H.; Hiromitsu, M.; Oboshi, T.; Usui, H., Dependence of polymer electrolyte fuel cell performance on preparation conditions of slurry for catalyst layers. *J. Power Sources* **2009,** *193* (2), 488-494.

165. Uemura, S.; Kameya, Y.; Iriguchi, N.; Yoshida, T.; Shinohara, K.; Hirai, S., Communication—Investigation of Catalyst Ink Degradation by X-ray CT. *J. Electrochem. Soc.* **2018,** *165* (3), F142-F144.

166. Uemura, S.; Yoshida, T.; Koga, M.; Matsumoto, H.; Yang, X.; Shinohara, K.; Sasabe, T.; Hirai, S., Ink Degradation and Its Effects on the Crack Formation of Fuel Cell Catalyst Layers. *J. Electrochem. Soc.* **2019,** *166* (2), F89-F92.

167. Koh, S.; Strasser, P., Dealloyed Pt Nanoparticle Fuel Cell Electrocatalysts: Stability and Aging Study of Catalyst Powders, Thin Films, and Inks. *J. Electrochem. Soc.* **2010,** *157* (4), B585.

168. Biddinger, E. J.; von Deak, D.; Marsh, H. S.; Ozkan, U. S., RRDE Catalyst Ink Aging Effects on Selectivity to Water Formation in ORR. *Electrochemical and Solid-State Letters* **2010,** *13* (8), B98.

169. Berlinger, S. A.; McCloskey, B. D.; Weber, A. Z., Probing Ionomer Interactions with Electrocatalyst Particles in Solution. *ACS Energy Letters* **2021**, 2275-2282.

170. Myers, D. J.; Kropf, A. J.; Wegener, E. C.; Mistry, H.; Kariuki, N.; Park, J., Degradation of Platinum-Cobalt Alloy PEMFC Cathode Catalysts in Catalyst-Ionomer Inks. *J. Electrochem. Soc.* **2021,** *168* (4), 044510.

171. Kumano, N.; Kudo, K.; Suda, A.; Akimoto, Y.; Ishii, M.; Nakamura, H., Controlling cracking formation in fuel cell catalyst layers. *J. Power Sources* **2019,** *419*, 219-228.

172. Berlinger, S. A.; Dagan, N.; McCloskey, B. D.; Weber, A. Z., The Effect of pH on Fuel-Cell Catalyst-Layer Inks. *ECS Trans.* **2018,** *86* (13), 133-140.

173. Woo, S.; Lee, S.; Taning, A. Z.; Yang, T.-H.; Park, S.-H.; Yim, S.-D., Current understanding of catalyst/ionomer interfacial structure and phenomena affecting the oxygen reduction reaction in cathode catalyst layers of proton exchange membrane fuel cells. *Current Opinion in Electrochemistry* **2020,** *21*, 289-296.

174. Malek, K.; Eikerling, M.; Wang, Q.; Navessin, T.; Liu, Z., Self-Organization in Catalyst Layers of Polymer Electrolyte Fuel Cells. *J. Phys. Chem. C.* **2007,** *111* (36), 13627-13634.

175. Van Cleve, T.; Wang, G.; Mooney, M.; Cetinbas, C. F.; Kariuki, N.; Park, J.; Farghaly, A.; Myers, D.; Neyerlin, K. C., Tailoring electrode microstructure via ink content to enable improved rated power performance for platinum cobalt/high surface area carbon based polymer electrolyte fuel cells. *J. Power Sources* **2021,** *482*, 228889.

176. Mashio, T.; Malek, K.; Eikerling, M.; Ohma, A.; Kanesaka, H.; Shinohara, K., Molecular Dynamics Study of Ionomer and Water Adsorption at Carbon Support Materials. *J. Phys. Chem. C.* **2010,** *114* (32), 13739-13745.

177. Sauerbrey, G., Verwendung von Schwingquarzen zur Wägung dünner Schichten und zur Mikrowägung. *Zeitschrift für Physik* **1959,** *155* (2), 206-222.

178. Voinova, M. V.; Rodahl, M.; Jonson, M.; Kasemo, B., Viscoelastic Acoustic Response of Layered Polymer Films at Fluid-Solid Interfaces: Continuum Mechanics Approach. *Physica Scripta* **1999,** *59* (5), 391-396.

179. Chiad, K.; Stelzig, S. H.; Gropeanu, R.; Weil, T.; Klapper, M.; Müllen, K., Isothermal Titration Calorimetry: A Powerful Technique To Quantify Interactions in Polymer Hybrid Systems. *Macromolecules* **2009,** *42* (19), 7545-7552.

180. Thoma, M.; Lin, W.; Hoffmann, E.; Sattes, M.; Segets, D.; Damm, C.; Peukert, W., A simple and reliable method for studying the adsorption behavior of Aquivion® ionomers on carbon black surfaces. *Langmuir* **2018,** *34* (41), 12324–12334.

181. Devivaraprasad, R.; Masuda, T., Solvent-Dependent Adsorption of Perfluorosulfonated Ionomers on a Pt(111) Surface Using Atomic Force Microscopy. *Langmuir* **2020,** *36* (46), 13793-13798.

182. Masuda, T.; Ikeda, K.; Uosaki, K., Potential-Dependent Adsorption/Desorption Behavior of Perfluorosulfonated Ionomer on a Gold Electrode Surface Studied by Cyclic Voltammetry, Electrochemical Quartz Microbalance, and Electrochemical Atomic Force Microscopy. *Langmuir* **2013,** *29* (7), 2420-2426.

183. Muzaffar, T.; Kadyk, T.; Eikerling, M., Physical Modeling of the Proton Density in Nanopores of PEM Fuel Cell Catalyst Layers. *Electrochim. Acta* **2017,** *245*, 1048-1058.

184. Garrick, T. R.; Moylan, T. E.; Yarlagadda, V.; Kongkanand, A., Characterizing Electrolyte and Platinum Interface in PEM Fuel Cells Using CO Displacement. *J. Electrochem. Soc.* **2016,** *164* (2), F60-F64.

185. Huang, J.; Malek, A.; Zhang, J.; Eikerling, M. H., Non-monotonic Surface Charging Behavior of Platinum: A Paradigm Change. *J. Phys. Chem. C.* **2016,** *120* (25), 13587-13595.

186. Zenyuk, I. V.; Litster, S., Modeling ion conduction and electrochemical reactions in water films on thin-film metal electrodes with application to low temperature fuel cells. *Electrochim. Acta* **2014,** *146*, 194-206.

187. Tesfaye, M.; MacDonald, A. N.; Dudenas, P. J.; Kusoglu, A.; Weber, A. Z., Exploring substrate/ionomer interaction under oxidizing and reducing environments. *Electrochemistry Communications* **2018,** *87*, 86-90.

188. Modestino, M. A.; Kusoglu, A.; Hexemer, A.; Weber, A. Z.; Segalman, R. A., Controlling Nafion Structure and Properties via Wetting Interactions. *Macromolecules* **2012,** *45* (11), 4681-4688.

189. Karan, K., Interesting Facets of Surface, Interfacial, and Bulk Characteristics of Perfluorinated Ionomer Films. *Langmuir* **2019,** *35* (42), 13489-13520.

190. Janardhan, R.; Gedam, P. H.; Sampathkumaran, P. S., The effect of polymer molecular weight in the adsorption process. *J. Colloid Interface Sci.* **1990,** *140* (2), 391-400.

191. De Gennes, P., Scaling theory of polymer adsorption. *J. Phys. France* **1976,** *32* (12), 1445-1452.

192. Norde, W., ENERGY AND ENTROPY OF PROTEIN ADSORPTION. *Journal of Dispersion Science and Technology* **1992,** *13* (4), 363-377.

193. Johnson, R. D.; Arnold, F. H., The temkin isotherm describes heterogeneous protein adsorption. *Biochimica et Biophysica Acta (BBA) - Protein Structure and Molecular Enzymology* **1995,** *1247* (2), 293-297.

194. Prozeller, D.; Morsbach, S.; Landfester, K., Isothermal titration calorimetry as a complementary method for investigating nanoparticle–protein interactions. *Nanoscale* **2019,** *11* (41), 19265-19273.

195. Takuya, M.; Hideo, N.; Satoru, T.; R., S. P.; Kohei, U., Formation and Structure of Perfluorosulfonated Ionomer Thin Film on a Graphite Surface. *Chem. Lett.* **2009,** *38* (9), 884-885.

196. Pramounmat, N.; Loney, C. N.; Kim, C.; Wiles, L.; Ayers, K. E.; Kusoglu, A.; Renner, J. N., Controlling the Distribution of Perfluorinated Sulfonic Acid Ionomer with Elastin-like Polypeptide. *ACS Appl. Mater. Interfaces* **2019,** *11* (46), 43649–43658.

197. Zhao, X.; Li, W.; Fu, Y.; Manthiram, A., Influence of ionomer content on the proton conduction and oxygen transport in the carbon-supported catalyst layers in DMFC. *Int. J. Hydrogen Energy* **2012,** *37* (12), 9845-9852.

198. Pollet, B. G., Let's Not Ignore the Ultrasonic Effects on the Preparation of Fuel Cell Materials. *Electrocatalysis* **2014,** *5* (4), 330-343.

199. Kusoglu, A.; Dursch, T. J.; Weber, A. Z., Nanostructure/Swelling Relationships of Bulk and Thin-Film PFSA Ionomers. *Advanced Functional Materials* **2016,** *26* (27), 4961-4975.

200. Nagappan, R.; Swami, K.; Roland, K.; Timothy, F.; Wenbin, G.; Nancy, N. K.; Deborah, J. M.; Peter, J. D.; Ahmet, K., Editors' Choice—Ionomer Side Chain Length and Equivalent Weight Impact on High Current Density Transport Resistances in PEMFC Cathodes. *J. Electrochem. Soc.* **2021**.

201. Page, K. A.; Shin, J. W.; Eastman, S. A.; Rowe, B. W.; Kim, S.; Kusoglu, A.; Yager, K. G.; Stafford, G. R., In Situ Method for Measuring the Mechanical Properties of Nafion Thin Films during Hydration Cycles. *ACS Appl. Mater. Interfaces* **2015,** *7* (32), 17874-17883.

202. Daly, K. B.; Panagiotopoulos, A. Z.; Debenedetti, P. G.; Benziger, J. B., Viscosity of Nafion Oligomers as a Function of Hydration and Counterion Type: A Molecular Dynamics Study. *J. Phys. Chem. B.* **2014,** *118* (48), 13981-13991.

203. Xie, J.; Wood, D. L.; More, K. L.; Atanassov, P.; Borup, R. L., Microstructural Changes of Membrane Electrode Assemblies during PEFC Durability Testing at High Humidity Conditions. *J. Electrochem. Soc.* **2005,** *152* (5), A1011.

204. More, K.; Borup, R.; Reeves, K., Identifying Contributing Degradation Phenomena in PEM Fuel Cell Membrane Electride Assemblies Via Electron Microscopy. *ECS Trans.* **2019,** *3* (1), 717-733.

205. Lei, C.; Yang, F.; Macauley, N.; Spinetta, M.; Purdy, G.; Jankovic, J.; Cullen, D. A.; More, K. L.; Kim, Y. S.; Xu, H., Impact of Catalyst Ink Dispersing Solvent on PEM Fuel Cell Performance and Durability. *J. Electrochem. Soc.* **2021,** *168* (4), 044517.

206. Lopez-Haro, M.; Guétaz, L.; Printemps, T.; Morin, A.; Escribano, S.; Jouneau, P. H.; Bayle-Guillemaud, P.; Chandezon, F.; Gebel, G., Three-dimensional analysis of Nafion layers in fuel cell electrodes. *Nature Communications* **2014,** *5*, 5229.

207. Morawietz, T.; Handl, M.; Oldani, C.; Friedrich, K. A.; Hiesgen, R., Quantitative in Situ Analysis of Ionomer Structure in Fuel Cell Catalytic Layers. *ACS Applied Materials & Interfaces* **2016,** *8* (40), 27044-27054.

208. Wu, J.; Melo, L. G. A.; Zhu, X.; West, M. M.; Berejnov, V.; Susac, D.; Stumper, J.; Hitchcock, A. P., 4D imaging of polymer electrolyte membrane fuel cell catalyst layers by soft X-ray spectro-tomography. *J. Power Sources* **2018,** *381*, 72-83.

209. Wu, J.; Zhu, X.; West, M. M.; Tyliszczak, T.; Shiu, H.-W.; Shapiro, D.; Berejnov, V.; Susac, D.; Stumper, J.; Hitchcock, A. P., High-Resolution Imaging of Polymer Electrolyte Membrane Fuel Cell Cathode Layers by Soft X-ray Spectro-Ptychography. *J. Phys. Chem. C.* **2018,** *122* (22), 11709-11719.

210. Litster, S.; Epting, W. K.; Wargo, E. A.; Kalidindi, S. R.; Kumbur, E. C., Morphological Analyses of Polymer Electrolyte Fuel Cell Electrodes with Nano-Scale Computed Tomography Imaging. *Fuel Cells* **2013,** *13* (5), 935-945.

211. Berlinger, S. A.; Garg, S.; Weber, A. Z., Multicomponent, multiphase interactions in fuel cell inks. *Current Opinion in Electrochemistry* **2021**, 100744.

212. Chowdhury, A. Investigating Transport Resistances in Fuel-Cell Catalyst Layers. University of California, Berkeley, 2021.

213. Sneed, B. T.; Cullen, D. A.; Reeves, K. S.; Dyck, O. E.; Langlois, D. A.; Mukundan, R.; Borup, R. L.; More, K. L., 3D Analysis of Fuel Cell Electrocatalyst Degradation on Alternate Carbon Supports. *Acs Appl Mater Inter* **2017,** *9* (35), 29839-29848.

214. Ono, Y.; Ohma, A.; Shinohara, K.; Fushinobu, K., Influence of Equivalent Weight of Ionomer on Local Oxygen Transport Resistance in Cathode Catalyst Layers. *J Electrochem Soc* **2013,** *160* (8), F779-F787.

215. Schuler, T.; Chowdhury, A.; Freiberg, A. T. S.; Sneed, B. T.; Spingler, F. B.; Tucker, M. C.; More, K.; Radke, C. J.; Weber, A. Z., Fuel-Cell Catalyst-Layer Resistance via Hydrogen Limiting-Current Measurements. *J Electrochem Soc* **2019,** *166* (7), F3020-F3031.

216. Spingler, F. B.; Phillips, A.; Schuler, T.; Tucker, M. C.; Weber, A. Z., Investigating fuel-cell transport limitations using hydrogen limiting current. *Int J Hydrogen Energ* **2017,** *42* (19), 13960-13969.

217. Iden, H.; Ohma, A., An in situ technique for analyzing ionomer coverage in catalyst layers. *J. Electroanal. Chem.* **2013,** *693*, 34-41.

218. Diard, J.-P.; Le Gorrec, B.; Montella, C., *Handbook of Electrochemical Impedance Spectroscopy. DIFFUSION IMPEDANCES*. 2020.

219. Open Source Impedance Fitter. https://github.com/NREL/OSIF

220. Li, B.; Liu, P.; Xu, Z.; Zhou, S., Ionic size effects: generalized Boltzmann distributions, counterion stratification and modified Debye length. *Nonlinearity* **2013,** *26* (10), 2899.

221. Lopez-Garcia, J. J.; Horno, J.; Grosse, C., Poisson–Boltzmann description of the electrical double layer including ion size effects. *Langmuir* **2011,** *27* (23), 13970-13974.

222. Breitwieser, M.; Klingele, M.; Vierrath, S.; Zengerle, R.; Thiele, S., Tailoring the Membrane-Electrode Interface in PEM Fuel Cells: A Review and Perspective on Novel Engineering Approaches. *Advanced Energy Materials* **2018,** *8* (4), 1701257.

223. Ott, S.; Orfanidi, A.; Schmies, H.; Anke, B.; Nong, H. N.; Hübner, J.; Gernert, U.; Gliech, M.; Lerch, M.; Strasser, P., Ionomer distribution control in porous carbon-supported catalyst layers for high-power and low Pt-loaded proton exchange membrane fuel cells. *Nature Materials* **2019**.

224. Wang, Y.-J.; Fang, B.; Li, H.; Bi, X. T.; Wang, H., Progress in modified carbon support materials for Pt and Pt-alloy cathode catalysts in polymer electrolyte membrane fuel cells. *Progress in Materials Science* **2016,** *82*, 445-498.

225. Avid, A.; Zenyuk, I. V. In *Ionic Liquid Modified Pt/C Electrocatalysts for the Oxygen Reduction Reaction in Polymer Electrolyte Fuel Cells*, The Electrochemical Society ECS Meetings Abstracts: 2020.

226. Li, Y.; Van Cleve, T.; Sun, R.; Gawas, R.; Wang, G.; Tang, M.; Elabd, Y. A.; Snyder, J.; Neyerlin, K. C., Modifying the Electrocatalyst–Ionomer Interface via Sulfonated Poly(ionic liquid) Block Copolymers to Enable High-Performance Polymer Electrolyte Fuel Cells. *ACS Energy Letters* **2020,** *5* (6), 1726-1731.

227. Katzenberg, A.; Chowdhury, A.; Fang, M.; Weber, A. Z.; Okamoto, Y.; Kusoglu, A.; Modestino, M. A., Highly Permeable Perfluorinated Sulfonic Acid Ionomers for Improved Electrochemical Devices: Insights into Structure–Property Relationships. *Journal of the American Chemical Society* **2020,** *142* (8), 3742-3752.